

# Mathematical Modeling of D.C. Electric Arc Furnace Operations

by

Marco Aurelio Ramírez

B.S., Chemical Metallurgical Engineering  
Universidad Nacional Autónoma de México, (1993)

S.M., Metallurgical Engineering  
CINVESTAV, México, (1996)

Submitted to the Department of Materials Science and Engineering  
in Partial Fulfillment of the Requirements for the Degree of

DOCTOR OF PHILOSOPHY IN  
METALLURGY  
at the  
MASSACHUSETTS INSTITUTE OF TECHNOLOGY

September, 2000

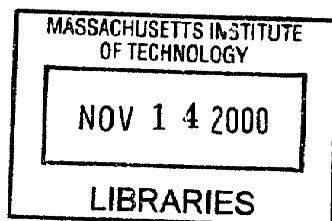
© Massachusetts Institute of Technology, 2000  
All Rights Reserved

Signature of Author: \_\_\_\_\_  
Department of Materials Science and Engineering  
August 4, 2000

Certified by: \_\_\_\_\_  
Merton C. Flemings  
Toyota Professor of Materials Processing  
Thesis Supervisor

\_\_\_\_\_  
Gerardo Trapaga  
Principal Research Associate  
Thesis Supervisor

Accepted by: \_\_\_\_\_  
Carl V. Thompson  
Stavros Salapatas Professor of Materials Science and Engineering  
Chair, Departmental Committee on Graduate Students



ARCHIVES :

# Mathematical Modeling of D.C. Electric Arc Furnace Operations

by

Marco Aurelio Ramirez

Submitted to the Department of Materials Science and Engineering on August 4, 2000, in Partial Fulfillment of the Requirements for the degree of Doctor of Philosophy in Metallurgy

## ABSTRACT

A fundamental study of the Direct Current Electric Arc Furnace (DC-EAF) for steel-making has been carried out through the development of a rigorous mathematical model. The mathematical representation involves the simultaneous solution of Maxwell's equations for the electromagnetic fields, and the turbulent fluid flow and heat transfer equations. In solving the arc and bath regions it was assumed (and justified) that the arc-bath interactions are dominated by the behavior of the arc.

In contrast to previous modeling investigations, this work relaxes some critical assumptions and provides a more realistic and comprehensive representation of the system. This work also examines and compares the relative merits of alternative electromagnetic and turbulence formulations, and addresses the role of induced currents and compressibility effects in the representation of the arc. Furthermore, due allowance was made to represent and analyze the effect of gas injection, the presence of a slag layer in the bath and changes in anode configuration at the bottom of the reactor.

Because of a lack of experimental information on actual or pilot plant DC-EAF systems, different aspects of the model were validated using several sources of experimental data reported in the literature for related systems. These included measurements on welding arcs, laboratory scale high-intensity carbon arcs, electromagnetically driven metallic systems, and ladle metallurgy physical models. It was found that, in general, the agreement between measurements and predictions was good.

A detailed analysis was carried out to examine the effect of process parameters (e.g., arc current, arc length, bath dimensions, anode arrangements, etc) on the behavior of the furnace (e.g., heat transfer to the bath, heating efficiency, mixing times in the bath, etc).

Predictions from the arc model show that all the arc characteristics are strongly coupled and that the arc physics is governed by the expansion of the arc. From a parametric study it was found that when the arc region (defined by the 10,000 K isotherm) is plotted in dimensionless form, a universal shape for the arc can be defined, regardless of the values of arc current or arc length. This universality was restricted to the range of conditions analyzed in this thesis, to arcs struck between graphite cathodes in air, and does not include the jet impingement region on the bath surface. This common arc expansion behavior suggested the universal nature of other arc characteristics. Universal maps of temperature, magnetic flux density, and axial velocity are also reported in terms of simple analytical expressions.

The practical effects of the two main process parameters of the arc region, i.e. the arc current and the arc length, were analyzed. It was found that increasing the arc length significantly increases the arc resistance and, consequently, the arc power, although this behavior reached asymptotic values at larger arc lengths. Increasing the arc current, however, does not affect the arc voltage. Thus, it is found that increasing the arc power increases the amount of energy transferred into the bath, but the heat transfer efficiency decreases. Therefore, the shorter the arc the more efficient is the heat transfer to the bath. It is also recognized that heat transfer from the arc to the bath is controlled by convection, although radiation can become an important mechanism, especially for large arc lengths.

Results of the bath model indicate that, in the absence of inert gas stirring and with no slag present in the system, electromagnetic body forces dominate and are responsible for the fluid flow patterns in the system. The effects of the arc determine the distributions of temperature and other mixing characteristics in the bath. The bath model was used to evaluate the effect of the main process parameters and design variables on mixing, refractory wear, temperature stratification, and heat transfer efficiency. An increase in the arc length is detrimental to mixing but increases the rate of heating in the melt as a result of the increased arc power. Increasing arc current improves mixing and the heat transferred to the bath, but is likely to be detrimental to the life of the bottom refractory. The results also suggest that high furnace aspect ratios (taller and thinner arc furnaces) are highly recommended because an increase in the aspect ratio increases mixing, prevents refractory wear, and promotes arc heating efficiency. The arc configuration in the furnace can be changed to control fluid flow patterns in the bath to meet specific needs, such as better mixing, or to prevent refractory wear.

The presence of a top layer of slag reduces mixing and increases overall liquid temperatures. Injection of gases through the bottom in eccentric operations generates complex flow patterns that improve mixing in regions away from the symmetry axis.

It is the author's belief that this model is a useful tool for process analysis in the DC-EAF. It has the capability to address many issues of current and future concern and represents one component of a fundamental approach to the optimization of DC-EAF operations.

Thesis Supervisor: Professor Merton C. Flemings  
Title: Toyota Professor of Materials Processing

Thesis co-supervisor: Dr. Gerardo Trapaga  
Title: Principal Research Associate

## Table of Contents

	Abstract	2
	Table of Contents	4
	List of Figures	6
	List of Tables	17
	Acknowledgments	18
<b>1</b>	<b>Introduction</b>	<b>19</b>
1.1	Motivation	19
1.2	Scope	23
1.3	State of the art in EAF modeling	24
1.4	Objectives	29
1.5	Approach	30
1.6	Layout of the Thesis	32
<b>2</b>	<b>Arc Modeling</b>	<b>34</b>
2.1	Mathematical Model of the Arc Region	34
2.1.1	Description of the Arc Physics	34
2.1.2	Assumptions	36
2.1.3	Governing Equations	39
2.1.4	Boundary Conditions	44
2.1.5	Cathode and Bath Representations	45
2.1.6	Physical Properties	47
2.2	Arc Model Validation	49
2.2.1	Welding Arc Process (GWTA)	50
2.2.1.1	Physical Description of the Welding Process (Differences with EAF)	50
2.2.1.2	Mathematical Representation of the Welding Arc: Potential and Magnetic Approaches	51
2.2.1.3	Comparison between the Two Formulations	56
2.2.1.4	Comparison against Experimental Data and other Numerical Studies	62
2.2.2	Bowman Experimental Information	68
2.2.2.1	Comparison of Model Predictions with Experimental Measurements by Bowman	68
2.3	Arc Results	73
2.3.1	Grid Sensitivity	73
2.3.2	Physics Involved in the Arc Process Based on the Standard Case (40 KA Arc Current and 0.25 m Arc Length)	76
2.3.3	Sensitivity Analysis: Effect of Model Parameters and Assumptions	87
2.3.3.1	Effect of the Current Density at the Cathode ( $J_c$ )	87
2.3.3.2	Effect of the Turbulence Model	90
2.3.3.3	Effect of the Anode Temperature	98
2.3.3.4	Effect of Compressibility	100
2.3.3.5	Effect of Neglecting Induced Currents	106
2.3.4	Process Analysis: Effect of the Process Variables on the Arc Behavior	111
2.3.4.1	Effect of the Arc Current on Arc Characteristics and Arc-Bath Interactions	111
2.3.4.2	Effect of the Arc Length on Arc Characteristics and Arc-Bath Interactions	119
2.4	Discussion and Summary of the Arc Process	127
<b>3</b>	<b>Bath Modeling</b>	<b>149</b>
3.1	Physical Representation of the Bath	149
3.2	Mathematical Model of the Bath Region	150
3.3	Bath Model Validation	161
3.3.1	Electromagnetic Driven Flow (Kang's Experimental Setup)	161

3.3.2	Physical Models of Ladles	165
3.4	Bath Model Results	175
3.4.1	Results for Single-Phase Model	175
3.4.1.1	Grid Sensitivity	175
3.4.1.2	Standard Case (Arc Current of 40 KA and Arc Length of 25 cm): General Description	177
3.4.1.3	Effect of Buoyancy, Shear Stress and Electromagnetic Body Forces on Fluid Dynamics and Heat Transfer in the Bath Region	184
3.4.1.4	Effect of the Arc Length and Arc Current on Fluid Dynamics and Heat Transfer in the Bath Region	188
3.4.1.5	Effect of the Wall Function: Equilibrium versus Non-equilibrium Wall Function	199
3.4.1.6	Effect of the Turbulence Models	200
3.4.1.7	Effect of the Size of the Reactor on the Fluid Dynamics and Temperature Field	204
3.4.1.8	Effect of the Anode Electrode Configuration on Fluid Dynamics and Temperature Field	211
3.4.2	Results of the Gas Injection Model	219
3.4.2.1	Isolated Effect of the Inert Gas Injection on Velocity and Temperature Fields of the Steel (Gas-Steel Model)	220
3.4.2.2	Effect of the Inert Gas Injection on the Bath Behavior (Gas-Steel Model)	221
3.4.2.3	Effect of the Gas Flow Rate on the Velocity and Temperature Fields (Gas-Steel Model)	223
3.4.3	Simplified Formulation to Represent a Top Slag layer	225
3.4.3.1	Effect of the Slag Layer on Velocity and Temperature Fields (Slag-Steel Model)	225
4	<b>Conclusions</b>	<b>227</b>
5	<b>Future Work</b>	<b>234</b>
6	<b>References</b>	<b>236</b>
	<b>Appendix A: DC Arc Furnaces of the World</b>	<b>241</b>
	Biographical Note	244

## List of Figures

1.1.1	World crude steel production from all processes and EAF [1].	19
1.1.2	AC Electric Arc Furnace.	21
1.1.3	DC Electric Arc Furnace.	21
1.1.4	EAF evolution [4]. Operational cost expressed by power consumption (KWh per ton of steel) and electrode consumption (kg of carbon per ton of steel). Productivity is expressed by the tap-to-tap time in minutes.	22
1.5.1	The DC-EAF system. Schematic representation of the approach followed in this work.	32
2.1.1	Schematic representation of the arc region in a DC-EAF. The main phenomena are depicted in the figure.	35
2.1.2	2D cylindrical polar coordinate representation of the computation domain in the arc region. The figure shows the non-uniform grid employed and all boundaries. The boundaries are: symmetry axis (AF), cathode surface (AC) which contains the cathode spot (AB), bath surface boundary (EF) and the entrainment (fixed pressure) boundaries (CD) and (DE).	39
2.1.3	Physical properties of air at 1 atm as a function of temperature. (a) density, (b) viscosity, (c) thermal conductivity, (d) specific heat, (e) electric conductivity, (f) radiation losses. Line represents calculations done by Murphy [88], filled dots are computations reported by Boulos [85] and unfilled dots are data used by Szekely et al. [92]. Radiation losses are taken from Morris et al. [93].	48-49
2.2.1	Argon physical properties as a function of temperature at 1 atm (Boulos et. al [85]) (a) density, (b) specific heat, (c) thermal conductivity, (d) electric conductivity, (e) viscosity, (f) radiation losses (Radiation losses are taken from Tampkin and Evans [95]).	55
2.2.2	Comparison of computed results for an argon welding arc with 200 A and 10 mm using two approaches: Potential approach (PA) and magnetic approach (MA). (a) Velocity field. (b) Pressure field. (c) Temperature field. (d) Current density field. (e) Magnetic flux density field. (f) Electromagnetic body force field.	57-59
2.2.3	Comparison between potential and magnetic approaches for an argon welding arc of 200 A current and 10 mm arc length. (a) Magnetic flux density radial profiles at $Z/L=0$ , $Z/L=0.25$ , $Z/L=0.5$ , $Z/L=0.75$ and $Z/L=1$ . (b) Radial current density profiles at $Z/L=0.25$ , $Z/L=0.5$ and $Z/L=0.75$ . (c) Axial current density profiles at $Z/L=0.25$ , $0.5$ and $0.75$ axial positions. (d) Arc velocity, arc pressure and arc temperature along the symmetry axis. (e) Shear stress and arc pressure at the anode. (f) Heat fluxes at the anode.	61
2.2.4	Comparison between experimental temperature maps by Hsu et. al. (cases A, B and C in Table 2.2.4) and computations. Upper plots present the Potential approach while lower plots present the Magnetic approach.	64-66
2.2.5	Comparison between results from the potential and magnetic approaches against experimental and other numerical simulations reported in the welding literature. (a) Temperature along the symmetry axis (case A in Table 2.2.4). (b) Velocity profile along the symmetry axis (case A in Table 2.2.4). (c) Arc pressure along the axis (case	67

	A and D in Table 2.2.4). (d) Arc pressure at the anode surface (case D in Table 2.2.4). (e) Current distribution at the anode (case F and H in Table 2.2.4). (f) Heat flux distribution at the anode (case F and H in Table 2.2.4).	
2.2.6	Computed fields for an electric arc with 2160 A and 7 cm arc length as in Bowman experiments. (a) Velocity and Temperature fields. (b) Turbulent kinematic viscosity and magnetic flux density fields.	70
2.2.7	Comparison between simulations and experimental measurements by Bowman for a 520 A and 7 cm electric arc in air. Radial profiles of axial velocity at (a) 2 cm, (b) 3.8 cm and (c) 5.5 cm from cathode. (d) Axial velocity profile along the symmetry axis.	71
2.2.8	Comparison between simulations and experimental measurements by Bowman for a 1150 A and 7 cm electric arc in air. Radial profiles of axial velocity at (a) 2 cm, (b) 3.8 cm and (c) 5.5 cm from cathode. (d) Axial velocity profile along the symmetry axis.	71-72
2.2.9	Comparison between simulations and experimental measurements by Bowman for a 2160 A and 7 cm electric arc in air. Radial profiles of axial velocity at (a) 2 cm, (b) 3.8 cm and (c) 5.5 cm from cathode. (d) Axial velocity profile along the symmetry axis.	72
2.3.1	Computed magnetic flux density profile along the cathode spot for three different grids.	74
2.3.2	Grid sensitivity: (a) axial velocity along the axis; (b) temperature along the axis; (c) arc pressure along the axis; and (d) current density along the axis.	75
2.3.3	Grid sensitivity: (a) current density at the bath surface; (b) pressure profile at the bath surface; (c) Shear stress at the bath surface.	75-76
2.3.4	Computed results for the standard electric arc (40 KA arc current and 0.25 m arc length). (a) Arc velocity field; (b) Arc pressure field; (c) Axial velocity along the symmetry axis; (d) Pressure distribution along the symmetry axis.	77
2.3.5	Computed results for the standard electric arc (40 KA arc current and 0.25 m arc length). (a) Potential field. (b) Total current density field. (c) Potential derived current density field. (d) Induced current density field. (e) Axial current density profiles along the radius at 5, 12.5, 20 and 22 cm from cathode.	79-80
2.3.6	Computed results for the standard electric arc (40 KA arc current and 0.25 m arc length). (a) Magnetic flux density field, $B_{\theta}$ ; (b) Electromagnetic body force vector field; (c) $B_{\theta}$ radial profiles at 5, 12.5, 20 cm from cathode and at the bath surface.	81
2.3.7	Computed results for the standard electric arc (40 KA arc current and 0.25 m arc length). (a) Temperature field; (b) Temperature distribution along the symmetry axis.	82
2.3.8	Computed results for the standard electric arc (40 KA arc current and 0.25 m arc length). (a) Kinematic viscosity; (b) Density; (c) Electric conductivity.	83
2.3.9	Computed results for the standard conditions (40 KA arc current and 0.25 m arc length). (a) Turbulent kinetic energy; (b) Turbulent energy dissipation rate; (c) Turbulent kinematic viscosity.	84
2.3.10	Arc-bath interactions at the bath surface. (a) Current density and (b) Heat flux distribution. (c) Cumulative heat flux. (d) Shear stress. (e) Arc pressure. (f) Arc	86-87

	temperature.	
2.3.11	Computed electric quantities with two different $J_c$ 's (a) Computed current density fields for a $J_c$ of $4.4 \times 10^7$ A/m <sup>2</sup> . (b) Computed current density fields for a $J_c$ of $1.0 \times 10^7$ A/m <sup>2</sup> . (c) Axial current density profiles along the radius at distances from the cathode of 5, 12.5 and 20 cm. (d) Magnetic flux density radial profiles at 5, 12.5 and 20 cm from cathode.	88
2.3.12	Effect of $J_c$ on arc characteristics. Temperature, pressure and velocity fields are plotted along the axis for two different cathode spot current densities ( $4.4 \times 10^7$ A/m <sup>2</sup> and $1.0 \times 10^7$ A/m <sup>2</sup> ).	89
2.3.13	Effect of $J_c$ on arc-bath interactions. (a) Heat fluxes for $J_c$ of $4.4 \times 10^7$ A/m <sup>2</sup> and $J_c$ of $1.0 \times 10^7$ A/m <sup>2</sup> . (b) Shear stress distribution at the bath for $J_c$ of $4.4 \times 10^7$ A/m <sup>2</sup> and $J_c$ of $1.0 \times 10^7$ A/m <sup>2</sup> .	90
2.3.14	Comparison between standard k- $\epsilon$ and RNG turbulence models. (a) Computed turbulent kinematic energy, $k$ . (b) Energy dissipation rate, $\epsilon$ . (c) Turbulent kinematic viscosity, $\nu_t$ .	91-93
2.3.15	Turbulence parameters computed from the two-scale k- $\epsilon$ model (a) Turbulent kinetic energy in the production region, $K_p$ . (b) Turbulent kinetic energy in the transfer region, $K_t$ . (c) Energy dissipation rate in the production region, $E_p$ . (d) Energy dissipation rate in the transfer region, $E_t$ . (e) Turbulent kinematic viscosity, $\nu_t$ . (f) Turbulent kinematic viscosity, $\nu_t$ obtained from the standard k- $\epsilon$ model.	94-96
2.3.16	Effect of the turbulence model on arc characteristics and arc-bath interactions. (a) Temperature along the axis. (b) Axial velocity along the arc axis. (c) Pressure along the axis. (d) Heat fluxes at the bath. (e) Shear stress at the bath surface.	97-98
2.3.17	Effect of bath temperature on arc-bath interactions. (a) Arc current. (b) Shear stress. (c) Heat flux. (d) Gas temperature at the bath.	99
2.3.18	Computed Mach number field for the standard arc case (40 KA and 0.25 m) without considering compressibility effects.	101
2.3.19	Effect of compressibility on velocity and temperature in the arc. (a) Arc Temperature without compressibility. (b) Arc Temperature with compressibility. (c) Arc velocity without compressibility. (d) Arc velocity with compressibility.	102
2.3.20	Effect of compressibility on density fields. (a) Density without compressibility. (b) Density with compressibility.	103
2.3.21	Effect of compressibility on electric parameters. (a) Potential without compressibility. (b) Potential with compressibility. (c) Current density without compressibility. (d) Current density with compressibility	103-104
2.3.22	Effect of compressibility on turbulent kinematic viscosity, $\nu_t$ . (a) Without compressibility. (b) With compressibility.	104-105
2.3.23	Effect of compressibility on arc-bath interactions. (a) Heat fluxes. (b) Pressure. (c) Shear stresses.	105
2.3.24	Effect of induced currents on arc properties. (a) Arc temperature field with induced currents. (b) Arc temperature field without induced currents. (c) Arc velocity field	107



	with induced currents. (d) Arc velocity field without induced currents.	
2.3.25	Effect of induced currents on arc properties. (a) Electric potential with induced currents. (b) Electric potential without induced currents. (c) Current density field with induced currents. (d) Current density field without induced currents. (e) Magnetic flux density field with induced currents. (f) Magnetic flux density field without induced currents.	109
2.3.26	Effect of induced currents on arc-bath interactions. (a) Heat fluxes at the anode. (b) Shear stresses at the anode.	110
2.3.27	Effect of the arc current on axial velocity profile along the axis for constant arc length of 25 cm.	112
2.3.28	Effect of the arc current on temperature profile along the axis for an arc length of 25 cm.	112
2.3.29	Effect of the arc current on arc pressure for a constant arc length of 25 cm.	113
2.3.30	Effect of the arc current on axial current density for arc length of 25 cm. In the plots axial current density at three different positions is presented for each current: (a) 4.5 cm, (b) 14.5 cm, (c) 23.1 cm.	113
2.3.31	Effect of the arc current on $B_{\theta}$ radial profiles for an arc length of 0.25 m at four different axial positions: (a) 5 cm, (b) 12.5 cm, (c) 20 cm, (d) at bath surface.	114
2.3.32	Effect of the arc current on current density at the bath surface for the four arc currents employed and an arc length of 25 cm.	115
2.3.33	Effect of the arc current on heat flux at the bath surface for the different arc currents employed in this study and an arc length of 25 cm. (a) 36, (b) 40, (c) 44, and (d) 50 KA.	115-116
2.3.34	Effect of the arc current on cumulative heat flow at the bath surface for all the currents employed in this study and an arc length of 25 cm. (a) 36KA. (b) 40 KA. (c) 44 KA. (d) 50 KA.	117
2.3.35	Effect of the arc current on shear stress at the bath surface for the four arc currents employed in this study and a constant arc length of 25 cm.	118
2.3.36	Effect of the arc current on temperature at the bath surface for the four arc currents employed in this study and a constant arc length of 25 cm.	118
2.3.37	Effect of the arc current on arc pressure at the bath surface for the four arc currents employed in this study and a constant arc length of 25 cm.	119
2.3.38	Effect of the arc length on the axial velocity profile along the symmetry axis with a constant arc current of 40 KA.	120
2.3.39	Effect of the arc length on the temperature profile along the symmetry axis with a constant arc current of 40 KA.	120
2.3.40	Effect of the arc length on the pressure profile along the axis with a constant arc current of 40 KA.	121
2.3.41	Effect of the arc length on the current density profile along the axis with a constant	121

	arc current of 40 KA.	
2.3.42	Effect of the arc length on the current density profile at the bath surface with a constant arc current of 40 KA.	122
2.3.43	Effect of the arc length on the heat flux at the bath surface for an arc current of 40 KA and different arc lengths: (a) 15 cm, (b) 20 cm, (c) 25 cm, (d) 30 cm, (e) 35 cm.	123-124
2.3.44	Effect of the arc length on the heat flow at the bath surface for an arc current of 40 KA and different arc lengths: (a) 15 cm, (b) 20 cm, (c) 25 cm, (d) 30 cm, (e) 35 cm	124-125
2.3.45	Effect of the arc length on the shear stress at the bath surface with a constant arc current of 40 KA.	125
2.3.46	Effect of the arc length on the arc temperature at the bath surface with a constant arc current of 40 KA.	126
2.3.47	Effect of the arc length on the pressure at the bath surface with a constant arc current of 40 KA.	127
2.4.1	Maximum heat fluxes at the bath as a function of the two main process parameters: (a) Arc current. (b) Arc length.	128
2.4.2	Total heat flow from the arc to the bath as a function of the two main process parameters: (a) Arc current. (b) Arc length.	128
2.4.3	Total voltage drop in the electric arc as a function of the two main process parameters: (a) Arc current. (b) Arc length	129
2.4.4	Maximum arc pressure at the bath as a function of the two main process parameters: (a) Arc current. (b) Arc length.	130
2.4.5	Maximum arc current density at the bath as a function of the two main process parameters: (a) Arc current. (b) Arc length.	130
2.4.6	Maximum shear stress at the bath surface as a function of the two main process parameters: (a) Arc current. (b) Arc length.	131
2.4.7	Maximum plasma velocities as function of arc current. Line represents Maecker equation and symbols are maximum velocities predicted in this study for all arc lengths.	132
2.4.8	Maximum pressure below cathode as function of arc current. Solid line represents Maecker equation and dots are maximum arc pressures predicted in this study for all arc lengths. Dashed line is Maecker equation augmented 13.2% (equation 2.4.1 multiplied by 1.132).	133
2.4.9	Computed maximum dimensionless current densities at the bath surface as function of dimensionless arc length. Variables in dimensionless form are: $J_{max}/J_c$ and $L/R_c$ .	134
2.4.10	Arc shape expressed in dimensionless form. Dimensionless arc radius ( $R_a/R_c$ ) position along dimensionless axial distance ( $Z/R_c$ ) is reported for the complete set of arcs computed in this study. Dots are experimental data reported by Jordan [21]. The arc radius was determined to correspond to the 10,000 K isotherm.	135
2.4.11	$B_\theta$ radial profiles at the same dimensionless axial distances for the three arcs	137

	presented in Table 2.4.1. The profiles correspond to the dimensionless axial distances of (a) $Z/R_c=0$ . (b) $Z/R_c=2$ . (c) $Z/R_c=5$ . (d) $Z/R_c=7$ .	
2.4.12	Dimensionless magnetic flux density radial profiles ( $B_\theta/B_{max}^0$ against $R/R_a$ ) for the three arcs presented in Table 2.4.1. The profiles correspond to the same dimensionless axial distances of (a) $Z/R_c=0$ . (b) $Z/R_c=2$ . (c) $Z/R_c=5$ . (d) $Z/R_c=7$ . (e) All distances plotted together to show the universal nature of the radial profile.	138
2.4.13	The $B_{max}^0/B_{MAX}$ profile along the dimensionless distance of $Z/R_c$ for the arcs presented in Table 2.4.1.	139
2.4.14	Temperature radial profiles for the arcs presented in Table 2.4.1. The profiles correspond to the same dimensionless distances of (a) $Z/R_c=2$ . (b) $Z/R_c=5$ . (c) $Z/R_c=7$ . (d) Temperature radial profiles are plotted at six different axial distances from cathode for an arc of 36 KA and 35 cm.	139-140
2.4.15	Dimensionless temperature radial profiles for the arcs presented in Table 2.4.1. The profiles correspond to those in Figure 2.4.14: (a) $Z/R_c=2$ . (b) $Z/R_c=5$ . (c) $Z/R_c=7$ . (d) Dimensionless temperature radial profiles are plotted at six different axial distances from cathode for the arc of 36 KA and 35 cm. (e) Lines from Figures (a), (b), (c) and (d) are plotted together.	141-142
2.4.16	Temperature axial profiles along the symmetry axis for the arcs in Table 2.4.1. (a) Dimensional axial profiles. (b) Dimensionless profiles obtained when $T_{max}^0$ is divided by the maximum temperature in the domain, $T_{MAX}$ , while $Z$ is divided by $R_c$ .	143
2.4.17	Axial velocity profiles along the radius for the arcs presented in Table 2.4.1. The profiles correspond to dimensionless distances of (a) $Z/R_c=2$ . (b) $Z/R_c=5$ . (c) $Z/R_c=7$ . (d) $Z/R_c=11$ . (e) Axial velocities along the radius at dimensionless distances of 2, 5, 7, and 11 (36 KA and 35 cm arc).	144
2.4.18	Dimensionless axial velocity profiles along the radius for the arcs presented in Table 2.4.1. The profiles correspond to dimensionless distances of (a) $Z/R_c=2$ . (b) $Z/R_c=5$ . (c) $Z/R_c=7$ . (d) $Z/R_c=11$ . (e) Dimensionless axial velocity profiles for the 36 KA and 35 cm arc. (f) All lines are plotted together to show the universal fashion of the profile.	145
2.4.19	Axial velocity profiles along the symmetry axis for the arcs in Table 2.4.1. (a) Dimensional axial profiles. (b) Dimensionless profiles obtained when $V_{max}^0$ is divided by the maximum velocity in the domain, $V_{MAX}$ , while $Z$ is divided by $R_c$ .	146
2.4.20	Total heat flow input to the bath from the arc as a function of arc power.	147
2.4.21	Electric arc heating efficiency. The efficiency is defined as the fraction of total arc power reaching the bath region.	148
3.1.1	Schematic representation of the bath region in a DC-EAF.	150
3.2.1	Schematic representation of the computation domain for the bath region in a DC-EAF.	151
3.3.1	Schematic representation of the experimental setup by Kang. Phenomena occurring in the system are also shown in figure.	162
3.3.2	Velocity field computed for the Kang system. (a)Current of 300 A. (b)Current of 600 A.	163

3.3.3	Comparison between experiments and predictions of mean liquid velocities at 2cm from top surface along the radius. Three different turbulence models are presented: Standard k- $\epsilon$ , RNG and Two-scale k- $\epsilon$ . (a) Current of 300 A. (b) Current of 600 A.	163
3.3.4	Comparison between experiments and predictions of turbulent kinetic energy at 0.5 cm from top surface along the radius. Three different turbulence models are presented: Standard k- $\epsilon$ , RNG and Two-scale k- $\epsilon$ . (a) Current of 300 A. (b) Current of 600 A.	164
3.3.5	Comparison between experiments and predictions of energy dissipation rate (in logarithmic scale) at 2 cm from top surface along the radius. Three different turbulence models are presented: Standard k- $\epsilon$ , RNG and Two-scale k- $\epsilon$ . (a) Current of 300 A. (b) Current of 600 A.	165
3.3.6	Schematic representation of the ladle systems simulated in this work.	166
3.3.7	Predicted and experimental liquid axial velocity profiles as a function of the radial position for different experimental systems. (a) Sheng and Irons with $0.5 \times 10^{-4} \text{ m}^3/\text{s}$ at 0.21 m from nozzle. (b) Sheng and Irons with $1.5 \times 10^{-4} \text{ m}^3/\text{s}$ at 0.21 m from nozzle. (c) Grevet with $1.33 \times 10^{-4} \text{ m}^3/\text{s}$ at 0.408 m from nozzle. (d) Grevet with $2.66 \times 10^{-4} \text{ m}^3/\text{s}$ at 0.408 m from nozzle. (e) Iguchi at 0.1398 m from nozzle.	169
3.3.8	Comparison between predicted (a) and measured (b) liquid velocity fields (case F in Table 3.3.2)	170
3.3.9	Radial profiles of liquid axial velocity at different axial positions (case F in Table 3.3.2). Distance from the bottom: (a) 5 cm; (b) 15 cm; (c) 25 cm; (d) 35 cm	170
3.3.10	Radial profiles of gas hold up at different axial positions (case F in Table 3.3.2). Distance from the bottom: (a) 5 cm; (b) 15 cm; (c) 25 cm; (d) 35 cm	171
3.3.11	Comparison between predicted (a) and measured (b) liquid velocity fields for eccentric injection of nitrogen in woods metal (case E in Table 3.3.2)	172
3.3.12	Comparison between predicted and measured gas fraction distributions for eccentric injection of nitrogen in Woods metal (case E in Table 3.3.2). The r-z plane shown corresponds to the plane containing both the symmetry axis and the center of the nozzle. The different axial locations are 5, 10, 15, 20, 25, 30, and 35 cm from the bottom.	172
3.3.13	Tracer concentration history at three different positions for an eccentric injection of air into a water ladle (case D in Table 3.3.2). The concentration is represented in dimensionless form, where $C_{av}$ is the concentration at full mixing condition and C is the instantaneous concentration.	174
3.4.1	Grid sensitivity using 5 different non-uniform grids of 15x10, 30x20, 45x30, 60x40 and 75x50. (a) Potential distribution along the symmetry axis. (b) Axial velocity along the symmetry axis.	176
3.4.2	Grid sensitivity using 5 different non-uniform grids of 15x10, 30x20, 45x30, 60x40 and 75x50. (a) Axial velocity along the radius at 0.25 m from top surface. (b) Radial velocity along the radius at the cell next to the bottom of the reactor.	176
3.4.3	Computational grid of 60x40 cells selected for calculations based on the grid sensitivity analysis.	177

3.4.4	Bath region characteristics for the standard case (40 KA and 25 cm): (a) Velocity field. (b) Stream lines. (c) Axial velocity profiles along the radius at different axial distances of 0.125, 0.25, 0.375 and 0.5 m from top surface. (d) Radial velocity profiles along radius at different axial distances of 0, 0.125, 0.25, 0.375 and 0.5 m from top surface.	178
3.4.5	Bath region characteristics for the standard case (40 KA and 25 cm): (a) Temperature field. (b) Radial temperature profiles along radius at axial distances of 0.125, 0.25, 0.375 and 0.5 m from top surface.	179-180
3.4.6	Bath region characteristics for the standard case (40 KA and 25 cm): (a) Potential field. (b) Temperature field. (c) Magnetic flux density field. (d) Electromagnetic body force field.	181
3.4.7	Bath region characteristics for the standard case (40 KA and 25 cm): (a) Turbulent kinetic energy field. (b) Energy dissipation rate field. (c) Turbulent kinematic viscosity field. (d) Turbulent kinematic viscosity radial profiles at 0, 0.125, 0.25, 0.375 and 0.5 m from top surface.	182-183
3.4.8	Axial bath properties along the symmetry axis: temperature, axial velocity and potential distributions.	184
3.4.9	Temperature and velocity fields in the bath region under the influence of different effects driving the flow. (a) Combined effect (shear stress, buoyancy, and electromagnetic forces), (b) Buoyancy only, (c) Shear stress only, and (d) Electromagnetism only.	186-187
3.4.10	Axial profiles of bath characteristics along the symmetry axis for different arc lengths of 15, 20, 25, 30 and 35 cm and 40 KA of arc current. (a) Temperature. (b) Axial velocity.	189
3.4.11	(a) Radial steel velocities along radius at the bottom surface for different arc lengths of 15, 20, 25, 30, and 35 cm and 40 KA of arc current. (b) Maximum velocity in the domain as a function of the arc length.	189
3.4.12	Radial profiles of the turbulent characteristics in the bath at 0.25 m from top surface for different arc lengths of 15, 20, 25, 30, and 35 cm and 40 KA of arc current. (a) Turbulent kinetic energy. (b) Energy dissipation rate. (c) Turbulent kinematic viscosity.	190
3.4.13	Average Temperature in the bath region as a function of arc length. The average temperature represents the enthalpy of the melt in the bath region.	191
3.4.14	Mixing time maps for the bath regions under electric arcs current of 40 KA and arc lengths of (a) 15 cm, (b) 20 cm, (c) 25 cm, (d) 30 cm, and (e) 35 cm. Mixing times are expressed in seconds and 95% of uniformity is the criteria to define mixing.	192
3.4.15	Concentration history at six different positions in the bath domain when injection is place in: (a) top free surface at the symmetry axis and (b) in the center of the circulation loop. The melt is influenced by an arc of 40 KA arc current and 25 cm arc length. The plots show a schematic representation of the injection and measuring positions.	193
3.4.16	Comparison of the heat balances in the bath region for the different arc lengths tested (15, 20, 25, 30 and 35 cm) keeping the same arc current of 40 KA. In the plot five	194

	elements contribute to the heat balance: (a) Heat from lateral wall, (b) Heat from bottom wall, (c) Heat from the arc, (d) Radiation losses and (e) Joule heat.	
3.4.17	Effect of the arc current on several bath properties along the symmetry axis under the influence of electric arcs of 25 cm arc length and 36, 40, 44 and 50 KA arc currents. (a) Temperature. (b) Axial velocity.	195
3.4.18	Effect of the arc current on several bath properties along the radius axis under the influence of electric arcs of 25 cm arc length and 36, 40, 44 and 50 KA arc currents. (a) Temperature radial profile at 0.25 m from top surface. (b) Radial velocity profile along the radius at the bottom surface.	195
3.4.19	Radial profiles of the turbulent characteristics in the bath at 0.25 m from top surface for different arc currents of 36, 40, 44, and 50 KA, and 25 cm arc length. (a) Turbulent kinetic energy. (b) Energy dissipation rate. (c) Turbulent kinematic viscosity.	196
3.4.20	(a) Average temperature in the bath region as a function of arc current. (b) Maximum velocity in the bath region as a function of the arc current.	197
3.4.21	Mixing time maps for the bath regions under electric arcs with arc lengths of 25 cm and arc currents of (a) 36 KA. (b) 40 KA. (c) 44 KA. (d) 50 KA. Mixing times are expressed in seconds and 95% of uniformity is the criteria to define mixing.	197-198
3.4.22	Comparison of the heat balances in the bath region for the different arc currents tested (36, 40, 44, and 50 KA) keeping the same arc length of 25 cm. In the plot five elements contribute to the heat balance: (a) Heat from lateral wall, (b) Heat from bottom wall, (c) Heat from the arc, (d) Radiation losses and (e) Joule heat.	198
3.4.23	Effect of the wall function approach on the bath properties. (a) Axial profiles along the symmetry axis for potential, temperature, and axial velocity. (b) Temperature and radial velocity profiles along the radius at the bottom surface.	200
3.4.24	Comparison of the heat balances in the bath region for the different wall function approaches tested (equilibrium and non-equilibrium) keeping the same arc length of 25 cm and arc current of 40 KA. In the plot five elements contribute to the heat balance: (a) Heat from lateral wall, (b) Heat from bottom wall, (c) Heat from the arc, (d) Radiation losses and (e) Joule heat.	200
3.4.25	Effect of the turbulence model approach on the bath properties along the symmetry axis. (a) Axial velocity. (b) Temperature. Three different turbulence model are compared (standard k- $\epsilon$ , RNG, and the two-scale k- $\epsilon$ turbulence models).	201
3.4.26	Effect of the turbulence model approach on the bath properties along the bottom surface. (a) Radial velocity. (b) Temperature. Three different turbulence models are compared (standard k- $\epsilon$ , RNG, and the two-scale k- $\epsilon$ turbulence models).	202
3.4.27	Effect of the turbulence model approach on the bath turbulent properties along the radius at 0.25 m from top surface. (a) Turbulent kinetic energy. (b) Energy dissipation rate. (c) Turbulent kinematic viscosity.	202
3.4.28	Mixing time maps for the bath regions under electric arcs current of 40 KA and arc lengths of 25 cm for the three different turbulence models. (a) Standard k- $\epsilon$ . (b) RNG. (c) Two-scale k- $\epsilon$ . Mixing times are expressed in seconds and 95% of uniformity is the criteria to define mixing.	203

3.4.29	Comparison of the heat balances in the bath region for the different turbulence models tested (standard k- $\epsilon$ , RNG, and the two-scale k- $\epsilon$ ) keeping the same arc length of 25 cm and arc current of 40 KA. In the plot five elements contribute to the heat balance: (a) Heat from lateral wall, (b) Heat from bottom wall, (c) Heat from the arc, (d) Radiation losses and (e) Joule heat.	204
3.4.30	(a) Velocity, (b) temperature and (c) streamlines field in the bath region for a furnace radius of 1.5 m and bath depth of 0.35 m, keeping the same arc length of 25 cm and arc current of 40 KA.	205
3.4.31	(a) Velocity, (b) temperature and (c) streamlines field in the bath region for a furnace radius of 1.5 m and a bath depth of 0.7 m, keeping the same arc length of 25 cm and arc current of 40 KA.	206
3.4.32	Mixing time maps for the bath regions under electric arc currents of 40 KA and arc lengths of 25 cm for the different steel bath depths. (a) $H=0.35$ m. (b) $H=0.7$ m. Mixing times are expressed in seconds and 95% of uniformity is the criteria to define mixing.	207
3.4.33	Average temperature as a function of the bath volume keeping the arc length and current in their standard values of 40 KA and 25 cm respectively. Bath volume increments are due bath depth variations.	207
3.4.34	Comparison of the heat balances in the bath region for the different bath depths tested ( $H=0.35$ m, $H=0.5$ m, $H=0.7$ m) keeping the same arc length of 25 cm and arc current of 40 KA.	207
3.4.35	(a) Velocity, (b) temperature and (c) streamlines fields in the bath region for a furnace radius of 2.0 m and bath depth of 0.5 m, keeping the same arc length of 25 cm and arc current of 40 KA.	208-209
3.4.36	(a) Velocity, (b) temperature and (c) streamlines fields in the bath region for a furnace radius of 2.5 m and bath depth of 0.5 m, keeping the same arc length of 25 cm and arc current of 40 KA.	209-210
3.4.37	Mixing time maps for the bath regions under electric arc current of 40 KA and arc length of 25 cm for different furnace radii. (a) $R_{furnace}=2.0$ m. (b) $R_{furnace}=2.5$ m. Mixing times are expressed in seconds and 95% of uniformity is the criteria to define mixing.	210
3.4.38	Average temperature as a function of the bath volume keeping the arc length and current in their standard values of 40 KA and 25 cm respectively. Bath volume increments are due furnace radius variations.	211
3.4.39	Comparison of the heat balances in the bath region for the different furnace radii tested ( $R_{furnace}=1.5$ m, $R_{furnace}=2.0$ m, $R_{furnace}=2.5$ m) keeping the same arc length of 25 cm and arc current of 40 KA.	211
3.4.40	(a) Velocity, (b) temperature, (c) current density, (d) body force and (e) potential fields in the bath region for a furnace with a radius of 1.5 m and a bath depth of 0.5 m under the standard arc (25 cm and 40 KA) and using an anode ring as indicated in the figure (e).	212-213
3.4.41	a) Velocity, (b) temperature, (c) streamlines, (d) potential, (e) magnetic flux density, (f) current density, and (g) body force fields in the bath region for a furnace with a radius of 1.5 m and a bath depth of 0.5 m under the standard arc (25 cm and 40 KA)	214-215

and using a circular anode with a radius of 0.1 m.

3.4.42	(a) Velocity, (b) temperature, (c) streamlines, (d) potential, (e) magnetic flux density, (f) current density and (g) body force fields in the bath region for a furnace radius of 1.5 m and bath depth of 0.5 m, under the standard arc (25 cm and 40 KA) and using a circular anode with a radius of 0.05 m.	216-217
3.4.43	Effect of the anode configuration on the bath properties along the symmetry axis. (a) Temperature. (b) Axial velocity. (c) Potential.	218
3.4.44	Mixing time maps for the bath regions under the standard electric arc (40 KA and 25 cm) for the four different anode configurations. (a) Bottom anode (normal). (b) Anode ring. (c) Circular anode with radius of 0.1 m. (d) Circular anode with radius of 0.05 m.	218-219
3.4.45	Comparison of the heat balances in the bath region for the different anode configurations tested (bottom anode (normal), anode ring, circular anode with radius of 0.1 m, circular anode with radius of 0.05 m) keeping the same arc length of 25 cm and arc current of 40 KA.	219
3.4.46	Velocity and temperature fields in the bath region under the effect of bottom gas injection.	220
3.4.47	Figure 3.4.47 (a) Liquid velocity, (b) liquid temperature, (c) gas volume fraction, (d) magnetic flux density, (e) current density, and (f) body force fields in the bath region under the influence of the standard electric arc and the gas injection through 3 nozzles. Only 1/6th of the system is presented due symmetry.	221-222
3.4.48	Effect of varying the gas flow rate on the liquid velocity field. (a) $Q=1.6666 \times 10^{-4} \text{ m}^3/\text{s}$ . (b) $Q=5.0 \times 10^{-4} \text{ m}^3/\text{s}$ . (c) $Q=1. \times 10^{-3} \text{ m}^3/\text{s}$ . (d) $Q=1.5 \times 10^{-3} \text{ m}^3/\text{s}$ .	223
3.4.49	Effect of varying the gas flow rate on the liquid temperature field. (a) $Q=1.6666 \times 10^{-4} \text{ m}^3/\text{s}$ . (b) $Q=5.0 \times 10^{-4} \text{ m}^3/\text{s}$ . (c) $Q=1. \times 10^{-3} \text{ m}^3/\text{s}$ . (d) $Q=1.5 \times 10^{-3} \text{ m}^3/\text{s}$ .	224
3.4.50	Velocity and temperature fields in the bath region under the effect of a layer of slag.	226



## List of Tables

1.1.1	Summary of the main contrasts between steel production in the 70's and in the 90's [3].	20
1.1.2	Operational cost in the DC-EAF process [5].	22
2.1.1	Constant values for turbulence model and other constant parameters used in the calculations ( $\alpha_T$ is the turbulent Prandtl number for enthalpy).	43
2.1.2	Boundary conditions for the arc model. Variables solved are radial and axial velocities, pressure, enthalpy, and electric potential and turbulent parameters. Geometric arrangement is based on Figure 2.1.2.	44
2.2.1	Physical differences between welding arc process and DC-EAF process.	50
2.2.2	Boundary conditions for the arc model in welding processes. Geometric arrangement is based on symbols presented in Figure 2.1.2.	53
2.2.3	Mathematical representation of heat fluxes at the anode and bath surfaces for argon welding arc and their differences with respect to the expressions used in DC-EAF.	54
2.2.4	Argon welding arc numerical and experimental studies used to validate the two numerical approaches used in this thesis.	62
2.4.1	Computed electric arcs used in the parametric analysis for $B_\theta$ , $V_z$ and $T$ .	136
3.2.1	Boundary conditions in the bath region for a single steel phase model	156
3.2.2	Physical properties of steel and numerical values of some geometric parameters of the reactor	157
3.2.3	Interfacial source terms for the momentum and energy equations	158
3.2.4	Physical properties of argon and numerical values of some geometric parameters of the reactor	159
3.2.5	Physical properties of slag and some geometric parameters of the reactor	160
3.3.1	Physical properties of Woods metal	162
3.3.2	Geometric parameters of the simulated experimental systems	166
A.1	DC arc furnaces of the world (July 1998) [7]	241-243

## Acknowledgements

I wish to thank Professor Merton C. Flemings for kindly taking the responsibility of being my official advisor, for allowing me to develop my thesis project with entire freedom, and for his valuable suggestions to my thesis work.

I want to express my sincere gratitude to my thesis co-advisor, Dr. Gerardo Trapaga, whose role was fundamental during the development of all aspects of my work, throughout the entire process of my thesis. His academic contributions, his limitless knowledge of the literature, and his vigorous rate of work had an incalculable value, which made my doctoral experience a great event that I will always remember with affection. Nevertheless, of even greater value were his generous friendship and his great ability to make me motivated in my work. I consider Dr. Trapaga my best friend at MIT.

Thanks to Professor Scott and Professor Sadoway (members of my thesis committee) who made important suggestions to improve the final content of this work. Special thanks to Professor Sadoway for all the nice comments he had about my work, which gave me a great deal of motivation.

I also want to thank Professor John McKelliget for the important contributions he made to my work. I learned a great deal from his tremendous analytical skills and knowledge of this field, and in the discussions and personal communications we had during these years. I appreciate his reviews of my work and direct contributions to my thesis.

I also want to thank Mr. Mauro Kobrinsky for sharing with me his impressive academic skills, which I deeply admire, and for his valuable and special friendship. I also want to thank Dr. Patricio Mendez for the long and constructive conversations on plasma physics we had in the last years, but most importantly for his friendship.

Many thanks to my friends here at MIT: Sandra Rugonyi, Miguel Hurtado, Jorge and Gabriela Giampaolli, Miguel Marioni, Ante Salcedo, and Raymundo Arroyave for all the nice moments we shared together.

My family was a great source of motivation and encouragement. Thanks to my mother María Nelly, my father Aurelio, my brothers Gerardo and German, and my sister María Concepción, for the love I always received from them.

Thanks to my lovely wife Martha Carolina who was the source of inspiration, love, and compassion that every person needs to succeed in life. Her love constituted a daily driving force in the pursuit of my degree.

I want to express special thanks to my sponsor CONACyT (Mexican Government) for the financial support through a full scholarship given to this author during the entire duration of my doctoral studies.

Finally, I would like to dedicate this thesis to my lovely newborn baby Carmen Carolina, who was born two weeks before I presented my Final Exam. This great event provided me with extra motivation and increased my spirituality.

## Chapter 1: Introduction

### Section 1.1: Motivation

The steel-making industry has experienced dramatic changes over the last three decades. In the 1970's, the steel-making industry was producing over 600 million tons per year, primarily by the integrated plants following the route Blast Furnace (BF) - Basic Oxygen Furnace (BOF) [1]. However, several economic, environmental, and energy-conservation issues, as well as a decrease in the grades of the ores, began to change the relative importance of steel-making processes. From a technological point of view, the emergence of mini-mills, which recycle scrap in Electric Arc Furnaces (EAF), was perhaps the most interesting development.

Figure 1.1.1 shows how the EAF has gained acceptance at the expense of the integrated plants and has virtually displaced other steel-making alternatives, such as the old Open Hearth Process, in current world production. In the U.S, the production of steel in the EAF has reached about 40% in recent years.

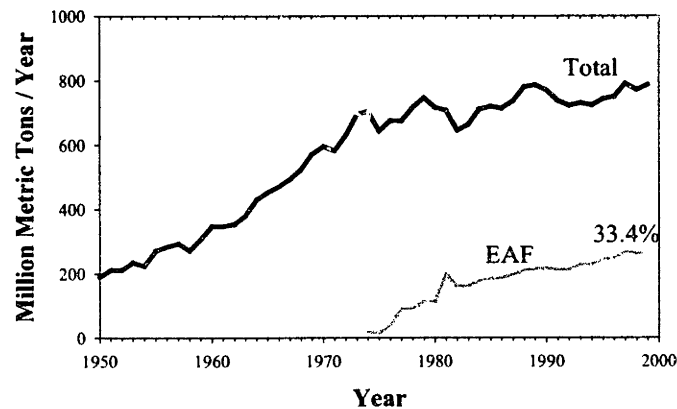


Figure 1.1.1 World crude steel production from all processes and EAF [1]

Table 1.1.1 summarizes the main contrasts between steel production in the 70's and the state in 1997. Significant differences in labor costs, total investment, productivity, environmental factors, etc., can be appreciated in the table. These changes illustrate the environment that led to the rapid growth of the EAF based mini-mills in the U.S.

The electric arc furnace is a batch reactor used in the steel-making industry to produce steel. Scrap, Direct-Reduced-Iron (DRI) and other raw materials are charged into the EAF along with lime and

other fluxes. Electric energy is applied to melt the solid charge and superheat the liquid for refining. The heat is produced as a consequence of current being transferred from carbon electrodes to the metal through an electric arc which forms a hot plasma that heats the melt by convection, radiation and electron drift. Other forms of energy can also be introduced in the EAF, such as oxy-fuel burners and cooled oxygen lances, which use chemical energy associated with combustion and oxidation reactions. The refining reactions, are different types of slag/metal exchanges, except for decarburization which mainly takes place in the melt. In order to accelerate refining reactions and melting rates, gas stirring is sometimes promoted using porous plugs and/or cooled lances.

Basically, there are two kinds of EAFs, categorized according to the type of current under which they operate [2]:

- AC Electric Arc Furnace. Alternating current passes from one electrode down through an arc and the metal charge, then from the charge up through an arc to the other electrode. Three phase currents with three electrodes are extensively used in industry (Figure 1.1.2).
- DC Electric Arc Furnace. Direct current passes from a single electrode (cathode) through an arc and the metal charge to an electrode in the bottom of the furnace (anode), as is shown in Figure 1.1.3.

	1970's	1990's
Steel Production (millions of tons/year)	600	780
Dominant technology	Integrated Plants	Mini-mills
Major Producers (emerging)	U.S., Europe, USSR, Japan	China, US, Japan, Germany, Russia, Korea
Environmental issues	Not important	Very important
Energy requirements (GJ/Ton)	35-40*	9-15**
Labor (man-hr/ton-steel)	6-12*	0.5-1.5**
Capital investment (\$/annual ton capacity)	1200-1500*	300-400**
Price of steel (\$/ton)	400	300-400

Table 1.1.1 Summary of the main contrasts between steel production in the 70's and in the 90's [3]

\*Integrated, \*\* Mini-mills

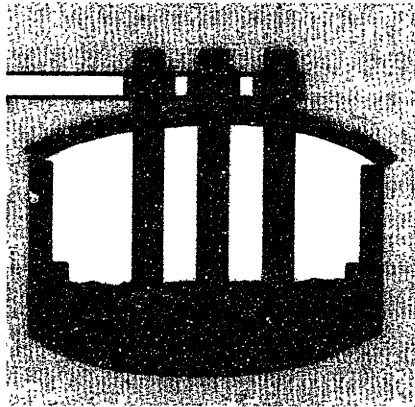


Figure 1.1.2 AC Electric Arc Furnace

It should be noted that EAF operations may also be classified as immersed or transferred, depending upon whether the arc is exposed to the gas atmosphere (transferred) or is submerged in the slag (submerged).

The EAF has undergone many technological improvements since this process first appeared in the late 1800's. The most important results of these improvements are shown in Figure 1.1.4 [4]. Additionally, cooling and protection of the furnace walls and ceiling with water-cooled panels, scrap preheating units and hot DRI charge have also enhanced furnace efficiency. Essentially, the main concerns for the steel-maker have been to reduce operational costs, including the electric energy consumption, and to increase the productivity of the operation [5] (see Table 1.1.2). Other important goals of each new technology or practice change in EAF are the reduction in labor cost, reduction in refractory consumption and reduction in environmental impact.

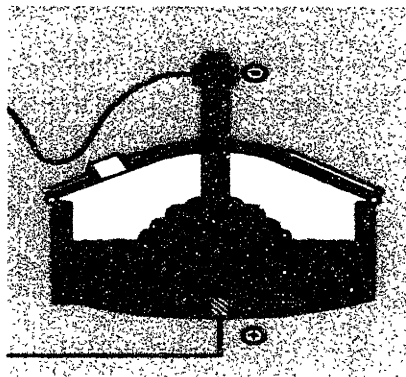


Figure 1.1.3 DC Electric Arc Furnace

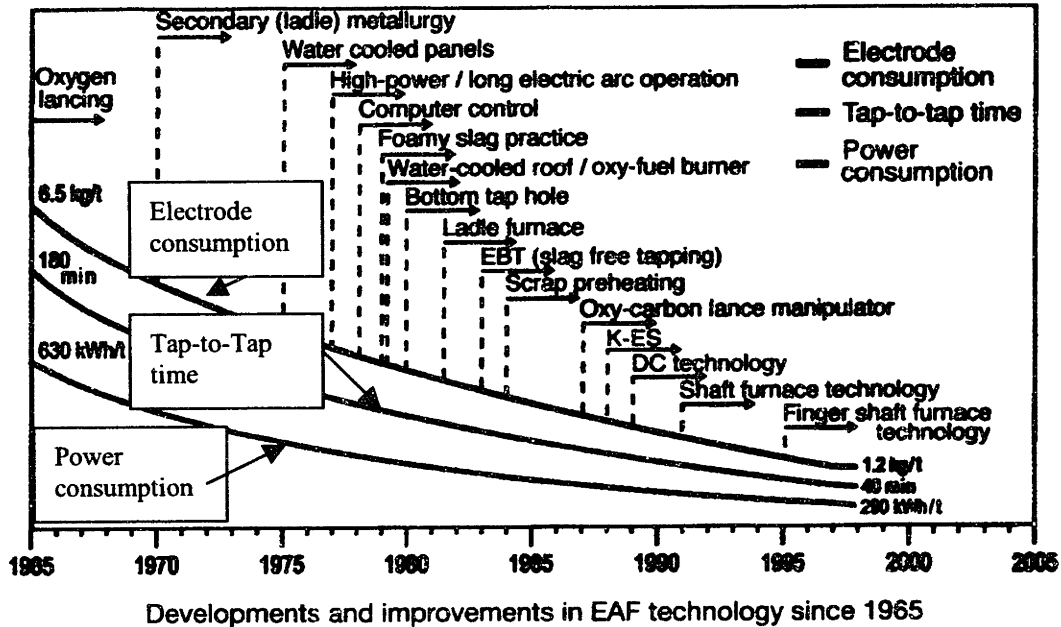


Figure 1.1.4 EAF evolution [4]. Operational cost expressed by power consumption (KWh per ton of steel) and electrode consumption (kg of carbon per ton of steel). Productivity is expressed by the tap-to-tap time in minutes.

Item	% of total operational cost
Electric Energy	64.8
Oxygen, Natural Gas	8.98
Coke	4.65
Electrode	7.92
Refractory & Lime	13.13
Other cost	0.48

Table 1.1.2. Operational cost in the DC-EAF process [5]

There is a decrease in electric energy input for a modern operation due to the implementation of the technological practices shown in Figure 1.1.4, as well as an increase in chemical energy input associated with the use of burners, post-combustion, etc.

At this point it should be mentioned that, in general, the changes in practice and design have come about by “trial and error”, and some of the advantages associated with these practices are far from being understood on physical grounds. These results varied from plant to plant, and in some cases from heat to heat [6].

In fact, one of the new technologies that enhanced the EAF efficiency was the adoption of DC systems in the late 1980's, as indicated in Figure 1.1.4. At that time, decreased electrode, energy, and refractory consumption, and a low noise level were claimed to be the most significant advantages of DC systems over traditional AC furnaces. However, it is known now that the most important benefit in the DC adoption was the reduction of the flicker effect in comparison with AC technology (the DC arc is more stable). When an AC furnace is operated the arc is cyclic, thus simultaneous contact between the three electrodes and the metal charge is inevitable. When this occurs the three-phase short circuit that results causes major increases in the power drawn from the supply network, inducing voltage fluctuation and potentially flicker. Another important characteristic in DC systems is that the arc voltage can be easily maintained without concernings on the current.

Nowadays, the DC technology covers approximately 70% of the new EAF being commissioned [7]. A list of the DC EAF systems around the world is presented in Appendix A (updated until 1998). In parallel with the worldwide spreading of the DC arc furnaces, the design of the electric arc furnaces in general has changed dramatically (see Figure 1.1.4). Special new features of the DC systems are the construction of taller and larger diameter shells, the implementation of two cathode furnaces, and the adoption of charge preheating systems.

## **Section 1.2: Scope**

In considering the EAF process, three different areas of interest can be defined [8]:

- electrical engineering problems associated with power delivery to the furnace,
- the mechanical features of furnace construction and supply of electrodes, and
- the metallurgical operations, that is, scrap melting rates, kinetics (slag/metal reactions) and transport phenomena.

The first two points involve areas where significant technological improvements have been implemented, but these are not necessarily due to a better understanding of the metallurgical aspects.

The following research efforts have been identified with regards to the understanding of metallurgical operations:

- The physical chemistry of high temperature reactions, studied extensively by Elliott and Chipman [8], greatly contributed to the thermodynamic understanding of the refining reactions in steel-making.

- Semi-empirical models, also called dynamic models [9], are based on overall mass and energy balances and implement thermochemical aspects of the reactions taking place in the furnace. These models are widely used in industry for control of the operation by predicting the operational behavior of the EAF. It should be stressed that these models do not provide basic insight into the complex phenomena taking place in EAF and are modified to represent a specific system based on plant experience.
- Stochastic (statistical) models that are based on recompilation of statistical data representing some specific aspects of the EAF in the form of correlations [6] or based on control algorithms such as “neural networks”.
- Transport phenomena in EAF. In contrast with the previous items, no significant research efforts have been done in this area.

Thus, the scope of this work involves addressing the mathematical modeling of transport phenomena in DC transferred EAFs for steel-making. The intention of this work is to provide insight into the fundamental behavior of this type of systems by defining the interrelationship among relevant process parameters and better understanding the physics of the system. Thus, an idealized 2D-axisymmetric geometry is employed, rather than a more complex particular furnace geometry. Also, since the cooling characteristics of the furnace vary according to particular designs, simplified boundary conditions are imposed to analyze heat transfer across the furnace walls in contact with the bath. These assumptions, however, can be readily relaxed to extend the model for the study of any particular industrial furnace.

### **Section 1.3: State of the Art in EAF Modeling**

Despite the fact that there have been no significant efforts in modeling EAF metallurgical operations, some individual areas related to EAF, and involving transport phenomena approaches, have been considered and are reviewed in this section. This includes a review of the state of the art in processes such as welding arc and ladle metallurgy.

#### **State of the Art in Electric Arc Modeling (EAF)**

The first attempt to address the mathematical representation of the EAF arc region based on magneto-hydrodynamics (MHD) equations and the turbulent convective heat transfer relations was made by Ushio et. al. [10]. The problem solved by Ushio required the electric characteristics of the arc to be known a priori and the assumption of constant values of some physical properties, which limited the



realistic representation of the arc. Szekely and McKelliget [11] presented a similar model, but they also investigated, for the first time, the effect of the arc on the steel bath temperature and fluid motion by coupling two models (one for the arc region and the other for the bath region). They were the first to formulate the different mechanisms of heat transfer from the arc. Also, McKelliget and Szekely studied in more detail the physics involved close to the graphite cathode electrode [12]. After these pioneering papers, some similar investigations have been reported in the literature, such as the work by Qian et. al. [13], by Seungho Paik et. al [14] and by Liping Gu et. al. [15]. The last two papers, however, presented models to represent other types of EAF systems (not for steel production), but followed the same formulation derived by McKelliget et. al.. In the work by Qian et. al., the electromagnetic problem was represented by the potential equation (Laplacian-formulation). However, they did not consider the effect of induced currents and also their results show physical inconsistencies at the bath surface, where inspection of their results shows that current density does not seem to be conserved. More recently, Larsen and Bakken [16] developed a simplified model to simulate high-current AC arcs using a magneto-fluid-dynamic model employing a magnetic formulation to represent the electromagnetic problem. A further intent to represent the arc region was presented by Hu et. al. [17] where the potential approach was employed to simulate the arc. However, laminar flow was assumed without the influence of induced currents. Their results show arcs without expansion and their only contribution was to suggest different ways to achieve converged numerical solutions.

In addition to the Magneto-fluid-dynamic approximation other approaches to represent the arc region are available, such as the Channel Arc Model [18,19,16]. The Channel Arc Model does not require the solution of a set of conservation equations (partial differential equations). The arc column is treated as a cylindrical conductor with uniform radius except for the short cathode contraction that generates the jet with uniform velocity and uniform temperature. In order to obtain the voltage and temperature of the arc, a simple heat balance is performed. However, the information obtained with this type of models is restricted to estimates of average values, which contrast with the detailed information about arc characteristics obtained with magneto-fluid-dynamic models.

Experimental studies in EAF are not commonly found in the literature. However, a few attempts to obtain experimental data in actual electric arcs have been made by Bowman [20] who reported velocity measurements for low-current electric arcs in air (arc current lower than 2160 A). Also, in another paper, Bowman [21] provided important order-of-magnitude information and a physical analysis that describes, in a rather simple way, the complex structure and physical characteristics of electric arcs. Jordan et. al. [22] measured some electrical properties of free-burning arcs between a graphite cathode electrode and molten steel at current levels up to 10 KA. From their measurements of cathode spot radii, cathode current densities of  $4.4 \times 10^7$  A/m<sup>2</sup> were reported, which are widely used to prescribe electromagnetic boundary conditions at the cathode

## **State of the Art in Bath Circulation Modeling (EAF)**

Kurimoto et. al. [23] presented a mathematical model to predict fluid flow patterns and temperature distributions in the bath region under the effect of electromagnetic body forces. However, the arc was not considered in their study and the boundary conditions at the top surface of the bath were too idealized for a realistic representation. Similarly, Bendzsak [24] studied the effect of electromagnetic forces on steel bath circulation in a High Powered EAF without considering a suitable representation of the arc-bath interactions. Recently, Liping Gu et. al. [25,26] published physical and mathematical representations of fluid flow in the steel bath considering specific operations in the EAF, such as gas bubbling injection, the use of oxy-fuel burners, and the effect of carbon boil on fluid flow. Experimentally, Deneys and Robertson [27,28] built a laboratory scale DC-EAF to study the effect of the arc in slag cleaning processes. In their system, Deneys et. al. studied the fluid flow phenomena on the surface of the molten slag using video photography while temperatures inside the slag were measured with thermocouples. Kang et. al. [29] and Murthy et. al. [30] built experimental setups to study the effect of electromagnetic body forces on fluid flow patterns and turbulence structure using a Woods metal system. They employed hot-wire anemometry in their unique measurements and were able to report useful data on velocity fields and turbulence characteristics, which are used in this thesis to validate certain aspects of the modeling work presented in a subsequent chapter.

It is clear that only a few attempts to model EAF operations have been reported in the past. However, some physical phenomena taking place in the EAF operation maintain some similarity with other metallurgical operations. These include slag-metal interaction, stirring with gas injection, stirring with electromagnetic forces, etc. These phenomena have been extensively studied in connection with ladle metallurgy, continuous casting, and furnace operations involving submerged electrodes, just to mention a few. By the same token, the electric arc has been studied in connection with welding and plasma systems.

The next section presents a review of the current state of the art in the mathematical modeling in Welding Arc processes (GTA), followed by a review of the relevant work involving melt stirring by gas injection in ladle metallurgy.

## **State of the Art in Welding Arc Modeling**

Welding arc presents electric arcs with fundamental similarities with the type of arcs found in EAFs. Then, due to the impossibility to obtain actual data from industrial DC-EAFs, the electric arc model can be tested with the welding process, since a lot of theoretical and experimental studies have been conducted in this area.

The first attempt to describe the physics involved in electric arcs was provided by Maecker [31], who first explained the generation of the high velocity jet produced by electromagnetic forces at high currents under an inviscid and isothermal flow. He derived expressions for maximum velocity and pressure through an asymptotic analysis from the momentum and Maxwell equations. Investigations by Lowke [32], Squire [33], Ramakrishnan [34,35], and Allum [36] provided analytical expressions to relate arc characteristics such as voltage, electric field, arc radius, and plasma velocity as a function of arc length, current, temperature and gas pressure. However, these analytical expressions were also obtained by neglecting viscous effects and assuming isothermal arcs, constant physical properties, and fixed shape of the arc.

As computational capabilities have increased over the past years, the numerical solutions representing electric arcs have become more realistic. In the welding area, some modelling efforts were reported by Hsu et. al. [37], by Mckelliget and Szekely [38], by Choo et al. [39] and by Kim et. al. [40] just to mention a few. In these papers, argon gas welding arcs were simulated using the current density at the cathode spot,  $J_c$ , as the only adjustable parameter. All these papers reproduced temperature fields, current, and heat flux densities at the anode surfaces, which were in excellent agreement with experimental measurements [41,37].

At this point it should be noted that welding modelling has experienced much greater advancements than EAF modelling. Mathematical models for welding are currently dealing with free surface problems (weld pool depressions), the influence of the geometry of the electrodes on the weld pool and arc characteristics [42,43], electrode sheath phenomena [44,45], and droplet formation [46], while in EAF, current models are limited to representing only isolated aspects of the operation. Part of the success achieved in welding modelling is due to the increasing amount of research done so far on both theoretical and experimental studies.

### **State of the Art in Ladle Metallurgy**

As indicated by the excellent review paper published by Mazumdar and Guthrie [47], the study of gas-stirred systems can be divided in three groups: physical modeling, mathematical modeling, and combined physical and mathematical modeling studies.

In most physical modeling studies, scale water-gas systems have been used mainly to measure velocities and gas holdup [48-51] to investigate different aspects such as gas-liquid interactions and turbulence structure [52-54], mixing phenomena [55-57], gas-liquid and liquid-liquid mass transfer [58-64], bubble behavior [65-66], and heat transfer aspects [67-68]. Also, the gas injection problem has been studied

for eccentric injection [69]. Physical models with melts have been reported, in both centric and eccentric configurations, but there are only few studies in this area in comparison to water systems [70,71].

With regard to mathematical modeling studies, two main approaches are reported in the literature. One involves “quasi-single-phase” models [49,72], that only consider a single liquid phase and in which the plume shape is imposed a-priori. The second approach involves two-phase models which, in turn, can be divided in Eulerian-Eulerian [73,74] and Lagrangian-Eulerian models [75-77]. The Eulerian-Eulerian type solves conservation equations for both gas and liquid phases on same computational domain. The Eulerian-Lagrangian approach solves the conservation equations for the liquid phase and the gas phase is handled by trajectory equations (in which bubbles behave as individual particles in a Lagrangian frame of reference). The two-fluid models do not require previous knowledge of plume shape, but still require some semi-empirical information to represent gas-fluid interactions (i.e., drag coefficients, bubble sizes, etc).

Other numerical models have been reported which address additional aspects important to ladle metallurgy, such as heat [78] and mass [79] transfer phenomena, representation of a top free surface [80,81], and the implementation of a third, slag, phase [82,83].

Experimental studies of mixing phenomena reported by Oeters et al. in centric (2D) and eccentric (3D) air-water systems [57,69,84] are also remarkable works.

Based on the above description of EAF modeling it is clear that no radically new contribution has been made to this field since the work of McKelliget and Szekely, more than 25 years ago. It is also apparent that the existing body of knowledge contains a number of simplifying assumptions that need to be further investigated and verified. In order to develop a more rigorous and comprehensive model the following aspects should be addressed in detail:

- The electromagnetic and hydrodynamic equations should be formulated and solved in a fully coupled manner. In particular, the role of induced currents, which have been neglected by all previous researchers, should be included in the model.
- The relative merits of formulating the electromagnetic field in terms of either the magnetic diffusion equation or the electric potential equation should be investigated. Special attention should be paid to the appropriate representation of electromagnetic boundary conditions in the vicinity of the electrodes.

- Comparison of the predictions of different turbulence models in the arc region should be performed. Previous investigators have assumed either a constant viscosity model or have adopted the k- $\epsilon$  model.
- Compressibility effects in the high velocity cathode jet should be investigated. These effects have not been addressed in any of the previous works.
- Much work needs to be performed on developing a realistic model of the coupling between the arc and the bath regions. Ideally, the two regions should be solved interactively; including the effects of surface depression and using accurate heat transfer correlations at the bath surface. Previous researchers arbitrarily assume a constant temperature on the bath surface, with little justification.
- Submerged gas injection, slag-metal interactions, and electromagnetic forces in the bath are other important effects that have not, so far, been incorporated into existing models.
- Mixing phenomena, such as turbulence characteristics, mixing times, and temperature stratification in the bath region should be included. These effects are not included in previous models.
- Finally, a detailed analysis of the effect of process parameters (e.g., current, arc length, bath dimensions, anode arrangements, etc) on the behavior of the furnace (i.e., heat transfer to the bath, heating efficiency, mixing times in the bath, etc) has yet to be reported in the literature.

#### **Section 1.4: Objectives**

Increases in energy efficiency and productivity in EAF operations seem to have leveled off during the past two decades. Simple technological innovations and changes in operational practice are unlikely to result in significant improvements. Significant further optimization of EAF practice is probably only possible by obtaining a fundamental understanding of the chemical and physical processes that occur. This fundamental understanding is best obtained through a program of experimental research planned and augmented with accurate mathematical models of the system. For these reasons, the present work is focused on a basic study of DC EAF operations from a transport phenomena point of view, taking into account the physical principles that govern the process.

The work has the following specific objectives:

1) Develop a fundamental mathematical model to represent the arc region and to establish the relationship between the electric operational parameters and the heat transfer efficiency into the bath. This involves the calculation of heat fluxes and shear stresses at the arc/bath interface.

2) Develop a fundamental mathematical model to represent the bath region using results from the arc model as boundary conditions. The model should be capable of predicting velocities and temperatures in the bath as well as turbulence parameters and bath homogenization times.

3) The model should include as many real effects as possible, e.g. non-symmetric geometries, submerged gas injection, and the presence of a slag layer.

The ultimate goal is to develop a comprehensive tool to perform process analysis, evaluate the current state of EAF operations, and to delineate conditions under which EAF practice can be optimized. Although such a comprehensive model does not currently exist in the literature, it is envisioned that it would be very useful for addressing issues such as temperature stratification in the bath, electric arc heating efficiency, optimal location of lances and/or injection nozzles to promote better homogenized melts, definition of conditions for better dissolution of DRI (Direct Reduced Iron) and other additions, understanding of the exchange of species from the arc gases to the melt (as for example the problem of N<sub>2</sub> pickup), and understanding of chemical reactions in the system.

## **Section 1.5 Approach**

The operation of a typical EAF heat can be summarized in the following steps [2]:

- Charging: the EAF is charged with raw materials (scrap, DRI, pig iron, hot metal, lime, fluxes, etc.).
- Melting: the roof is closed and the electrodes are lowered to create the arc that will melt the solid charge and will superheat it for the refining step.
- Refining: once the charge is melted, required compositions and temperatures are targeted.
- Deslagging/Tapping: the EAF is deslagged and then tapped.

The melting and refining periods are the logical choices for analysis. However, due to the erratic and unpredictable operation in the melting stage, the refining period will be the more tractable step. In this stage, the arc can be considered to be stable and a bath analysis can be performed.

Transport phenomena problems associated with the EAF metallurgical operations can be divided in three groups:

- Heat transfer, fluid flow and electromagnetic phenomena in the arc region, and behavior of the electromagnetically driven plasma jet, in which thermal energy is generated by Joule heating and a local “equilibrium” of multiple gas species is established.
- Bath circulation: the actual fluid flow in the slag/metal system driven by electromagnetic forces, buoyancy forces, and the interaction between the plasma jet and the bath, as well as the evolution, or auxiliary injection, of gases.
- Arc-Bath heat and momentum transfer: this interaction links the arc with the bath region.

If the mechanisms controlling the rate of refining reactions are to be understood, transport phenomena aspects associated with the operation, should be studied and understood. In order to understand these phenomena, the heart of the operation must be addressed: the electric arc.

It is suggested that an appropriate representation of the system would involve modeling the arc region and then linking it to the liquid system (slag/molten steel). This approach is shown schematically in Figure 1.5.1. This figure is a schematic representation of Figure 1.1.3 (DC-EAF) representing a simplified view of a DC-EAF system in the refining stage, where all scrap is already melted. The idealization of the reactor consists in considering the system to be divided in two main regions. The first region is located between the graphite cathode electrode and the bath surface, i.e. the electric arc region. The second region is the bath by itself where slag, steel and gases coming from injection or carbon boil are present, i.e. the bath is a three phase region. Both regions are coupled through the interface where the arc provides the necessary heat to melt the scrap first and then keep the melt in a liquid state. The electron flow passes from the cathode through the arc and then enters and travels through the bath until it reaches the anode closing the electric circuit. Finally, the last arc-bath interaction comes from mechanical interaction due to the arc jet impinging the free surface. The high velocity jet directed vertically from the cathode region to the bath surface impinges on the bath surface and the jet is deflected in radial direction. The impingement produces a high pressure at the arc-bath surface that deforms the free surface forming a depression in the liquid melt, while the deflection of the jet produces a shear stress that acts on the liquid steel. The arc pressure, the shear stress, the heat flux and the current at the bath surface are the coupling elements that make possible to

describe the effect of the arc on the bath of a DC-EAF. It is important to note that the model does not account for the deformation of the free surface, so the bath region depends on the arc, but the arc calculation is independent of the bath calculation.

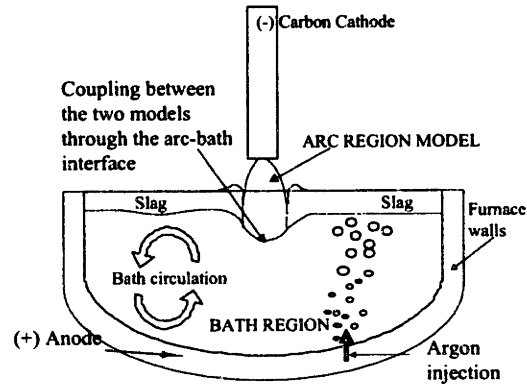


Figure 1.5.1 The DC-EAF system. Schematic representation of the approach followed in this work.

## Section 1.6: Layout of the thesis

After the introduction presented in this chapter, the following chapters discuss the mathematical modeling formulation, validation, and results for both regions modeled in the DC-EAF, i.e. the arc and the bath regions.

Chapter 2 contains a detailed description of the mathematical formulation of the arc region followed in this thesis. Partial validations of the models are presented by comparing predictions with experimental measurements reported in the literature for related systems such as Welding arcs and other measurements found in the literature for higher current arcs stroke between graphite electrodes in air atmospheres. Two alternative approaches to represent the magnetic problem are briefly presented and compared for the welding arc simulations. The results of the arc region, along with a sensitivity study of some of the unknown parameters in the model (some assumptions such as compressibility, turbulence model, current density at the cathode spot, etc.) are also addressed and discussed in this chapter. Finally, a parametric study including the main process variables of the arc (arc current and arc length) is performed, followed by a description of a general dimensionless representation of the electric arc in DC-EAF found in this research.

Chapter 3 presents the mathematical representation of the bath region, where three different systems were formulated: single steel model, gas-steel model, and slag-steel model systems. The validation of the bath models is also presented in this chapter using physically similar systems (Kang's experiments and ladle physical models). Results of the bath region under the effect of the arc for the three models



considered (single steel, gas-liquid, and steel-slag) are presented along with a parametric study of some process parameters such as the arc conditions, gas flow rate, anode configuration, and aspect ratio of the furnace. The analysis is based on calculations of mixing times, heat balances (heat flows through refractory walls, top surface, etc.), temperature distributions in the bath, and arc heating efficiencies.

Finally, the conclusions obtained in this thesis are presented in Chapter 4, and recommendations for future work are presented in Chapter 5.

## Chapter 2: Arc Modeling

### Section 2.1: Mathematical Model of the Arc Region

#### Section 2.1.1: Description of the Arc Physics

The most important aspect to be considered in typical industrial Direct-Current Electric Arc Furnaces (DC-EAF) is the arc region. The arc provides the required power to melt and transform solid scrap into liquid steel. Therefore, due to its importance, this work focuses on a detailed study of the arc region. Describing the arc accurately has enormous practical importance because it allows prescription of arc-bath interactions at the bath surface (heat flux, current density, shear stress), and hence, an accurate quantitative description of the effect of the arc on the bath.

Specifically, this section presents a detailed physical description of the arc region, which is then used to formulate a mathematical representation of the arc.

A typical representation of the arc is shown schematically in Figure 2.1.1, where a summary of the critical physical phenomena is presented. Electric current flow through the arc is driven by a potential difference between the graphite cathode and the anode located at the bottom of the furnace. However, since steel is a much better electric conductor than plasma in the arc, the potential difference between the two electrodes is considered to be practically the same as the potential between the graphite cathode and the bath surface.

The furnace atmosphere predominantly consisting of air fills the gap between the graphite cathode and the bath surface. Air under standard thermodynamic conditions is not a conductor of electricity. Then, the following question arises: How current flows between the air gap to close the electric circuit? The answer is that graphite cathodes start emitting electrons at temperatures around 4000 K [12] (thermionic emission) and these high-energy electrons collide with gas molecules. Resulting from the collision process is the ionization of gas and its enhancement of electric conductivity. Collisions also help to equilibrate temperatures of all species present in the gap (molecules, ions, electrons, etc). This equilibrium is promoted by increasing the number of collisions, i.e. increasing the number of gas molecules or increasing pressure, and by avoiding high voltage differences, since this represents a higher difference between electron and ion temperatures. The arc operates at atmospheric pressure with high enough molecule density to be considered an arc in equilibrium, condition that is known as Local Thermodynamic Equilibrium (LTE) [85].

Current at the cathode is concentrated in a tiny spot with an extremely high current density ( $\sim 4.4 \times 10^7 \text{ A/m}^2$  [22]). When current leaves the cathode surface the conduction zone expands from this tiny cathode spot to a much wider area, i.e. the arc becomes wider along the axial direction and current density vectors decrease in magnitude to meet the charge conservation requirement. The result is lower current densities found in the arc column than in the cathode spot and also some radial components of current densities arise as the current spreads.

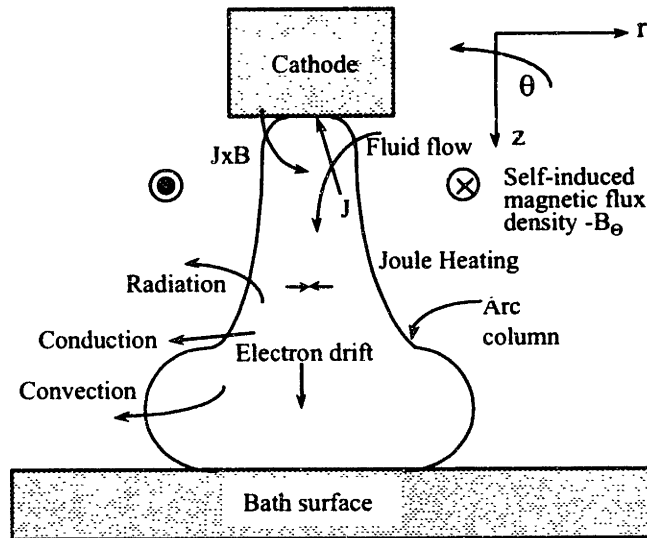


Figure 2.1.1 Schematic representation of the arc region in a DC-EAF. The main phenomena are depicted in the figure.

As current flows through the arc, a self-induced magnetic field in the azimuthal direction is generated. Current density interacts with its self-induced magnetic field to produce electromagnetic body forces, expressed in terms of the vectorial cross product of these two electric quantities. The current has two vector components but it can be considered to be predominantly in the axial direction, and consequently the electromagnetic forces are mainly aligned in the radial direction and they decrease as current densities decrease, i.e. as the distance from the cathode increases. Pressure counterbalances the body forces in such a way that a high-pressure zone is created below the cathode that forces gas to flow towards the bath surface resulting in a high velocity plasma jet. The velocities inside the jet can be of the order of several thousand meters per second. Finally, the jet reaches the bath where it is deflected and a further expansion of the arc region is experienced due to the radial flow parallel to the bath. Impingement of the jet generates another high-pressure zone (this time just above the bath) and this pressure is apparently capable of significantly deform the bath surface [21]. The jet flow defines the arc shape shown in Figure

2.1.1. However, the arc region is strictly defined as the zone where current conduction takes places. It has been suggested that this region is bounded along the positions where the 10,000 K isotherm is located [22,86].

There are other important phenomena that need to be considered to understand the behavior of the arc. The passage of current heats the plasma by ohmic resistance (Joule heat) resulting in temperatures even much higher than 10,000 K and with high temperature gradients (since current density magnitudes are expected to vary significantly through the arc). Energy transported by electron flow and radiation from the arc are mechanisms that must be considered in the energy balance. Thus, the complex structure of the arc makes it a very interesting but, at the same time, a very difficult process to model. Therefore before giving a statement of the model equations representing the physics, it is necessary to introduce some simplifying assumptions.

### **Section 2.1.2: Assumptions**

The main assumption involved in the present model is to consider the plasma in Local Thermodynamic Equilibrium (LTE), implying that all species present in the arc column have the same temperature. This assumption is known to be valid almost through the entire arc column in DC-EAF arcs (also called high-intensity free burning arcs), but this assumption is not strictly valid in the vicinity of the cathode and bath surfaces where departure from equilibrium is a very well known issue [87]. The LTE assumption is fundamental for the mathematical formulation since it allows a development of a single or one-temperature plasma model, instead of a more complex two-temperature plasma model.

Another key assumption is the a-priori prescription of the current density value at the cathode spot,  $J_c$ , which is considered to be constant and with a value of  $4.4 \times 10^7$  A/m<sup>2</sup> for graphite electrodes, according to experimental data of spot diameters measured by Jordan et. al. [22]. These measurements were performed for arc currents up to 10 KA and  $J_c$  was found to be independent of the arc current and arc length. If the current density at the cathode would not be available, the inclusion of the graphite electrode would be required in the modeling work. However, the certainty of the value of  $J_c$  is only for a limited range of arc currents (up to 10 KA) and does not cover all ranges of industrial DC-EAF currents ( $\gg 10$  KA). Besides, some other estimations for values of  $J_c$  have been found in the literature [16,21]. For this reason a sensitivity of the effect of  $J_c$  on the arc model results is performed in subsequent sections in this thesis.

A list of these and other important assumptions is given below:

- Plasma is in Local Thermodynamic Equilibrium (LTE).

- 2-D cylindrical coordinates are used to model this system
- Electrode and wall furnaces are excluded from the calculation domain since they have no critical effect on the arc region.
- Steady state solution.
- Bath surface is considered flat.
- Turbulence flow regime exists and can be represented by the standard k-ε turbulence models.
- Compressibility effects are neglected.
- At the colder electrodes, the conductivity is considered to correspond to the hotter electrons (departure from LTE), and this is approximated by assuming that the electric conductivity there, can be associated with the nearest nodal position located in the plasma.
- Physical properties are considered to depend on temperature.
- The plasma is considered optically thin, i.e. no absorption is taking place inside the arc.
- Air is the only gas present in the furnace.
- The arc region calculation is independent from the bath surface temperature.

A further discussion of some of these assumptions is necessary. Exclusion of furnace walls is possible since the plasma is considered to be optically thin to radiation. Exclusion obeys the need to solve numerically in detail a small region occupied by the plasma with the minimum of grid points. The exclusion of graphite is valid since the current density is known a priori and the temperature of the cathode surface can be expressed by the Richardson-Dushman expression (equation 2.1.1) for thermionic emission, which relates the cathode temperature to its current density

$$J_c = AT_c \exp\left(-\frac{e\phi_c}{k_B T_c}\right) \quad (\text{eq. 2.1.1})$$

where,  $e$  is electronic charge,  $k_B$  is the Boltzman constant,  $A=60 \times 10^4 \text{ A}^{-1} \text{ m}^{-2} \text{ K}^{-2}$ , and for carbon, the work function of cathode material  $\phi_c \sim 4.75 \text{ eV}$ . A current density of  $4.4 \times 10^7 \text{ Am}^{-2}$  requires a cathode temperature,  $T_c$ , of about 4130 K, which is below the boiling point of carbon, ( $\sim 4700 \text{ K}$ ).

Steady state is a valid assumption for DC furnaces, but it should be mentioned that this assumption is not valid for AC furnaces. The solution can be 2D due to symmetry of the problem and the geometric arrangement of the electrode and bath surfaces in the furnace. Some arc instabilities due to external magnetic fields and motion of the bath surface are known to be present [26,21], which introduce swirl components for velocities and arc deflections, but they can be neglected to simplify the problem.

Considering a bath flat surface constitutes the weakest simplification of the model, since it is known that the jet pressure has an important effect on the bath surface depression [21]. However, including this effect would significantly increase the complexity of the problem.

Fluid flow is considered to be in turbulent regime. Taking characteristic values of the arc parameters, it is possible to estimate the Reynolds number with values of the order of  $\sim 2.5 \times 10^5$  (density and viscosity at 20,000 K:  $\rho \sim 0.00456 \text{ kg/m}^3$ ,  $\mu \sim 1.7638 \times 10^{-5} \text{ kg/ms}$ , velocity  $V \sim 5000 \text{ m/s}$ , and arc length  $L \sim 0.2 \text{ m}$ ). In a free jet, transition from laminar to turbulent flow is found to take place at Reynolds numbers around  $1.0 \times 10^5$ . Therefore, a turbulent flow regime is expected in the arc. However, it is not known if the standard k- $\epsilon$  model provides a good description of turbulence in the arc. In order to test the effect of turbulence representation, a sensitivity of several turbulence models is also addressed in this study.

Compressibility effects are expected in the arc due to the high velocities estimated, and significant temperature variation in the system. An estimation of maximum velocities in the arc can be obtained by using the well known Maecker equation (equation 2.1.2 [31]), which is derived assuming inviscid flow in an isothermal plasma

$$V_{\max} = \left( \frac{\mu_o J_c I}{2\pi\rho} \right)^{0.5} \quad (\text{eq. 2.1.2})$$

where,  $I$  is the arc current and  $\mu_o$  is the magnetic permeability with a value of  $4\pi \times 10^{-7}$  henry/m. Assuming a temperature of 20,000 K and a current of 50,000 A, a maximum velocity of 9000 m/s is obtained and a maximum Mach number of  $\sim 1.6$  is expected (sonic velocity for air at 20,000 K is 5520 m/s). Under this supersonic flow regime the effect of compressibility is expected to play an important role. This means that neglecting compressibility effects is an oversimplification. However, the effect of compressibility is also examined in this study.

The assumption of optically thin plasma is required to avoid a complex computation of radiation inside the arc where absorption and scattering of radiative energy is expected. However, this assumption is valid in some cases with small arc sizes.

Assuming that air is the only gas involves another simplification to the problem since the furnace atmosphere is also composed by vapors coming from steel and slag, CO from carbon boil, and other gases. However it is difficult to determine the composition of the mixture of gases. Then, assuming that air is the only gas present in the arc, makes the simulation of the system possible at this stage.

The arc effectively can be treated as independent from the bath, since a flat surface is considered and the bath surface temperature does not affect the arc computations as will be shown in a subsequent section, i.e., sensitivity of the anode temperature.

Finally, considering that the physical properties are exclusively a function of temperature is a reasonable assumption. The properties for air are calculated at a pressure of one atmosphere [88].

### Section 2.1.3: Governing Equations

Based on the assumptions presented above, the mathematical representation can be stated based on the computational domain shown in Figure 2.1.2.

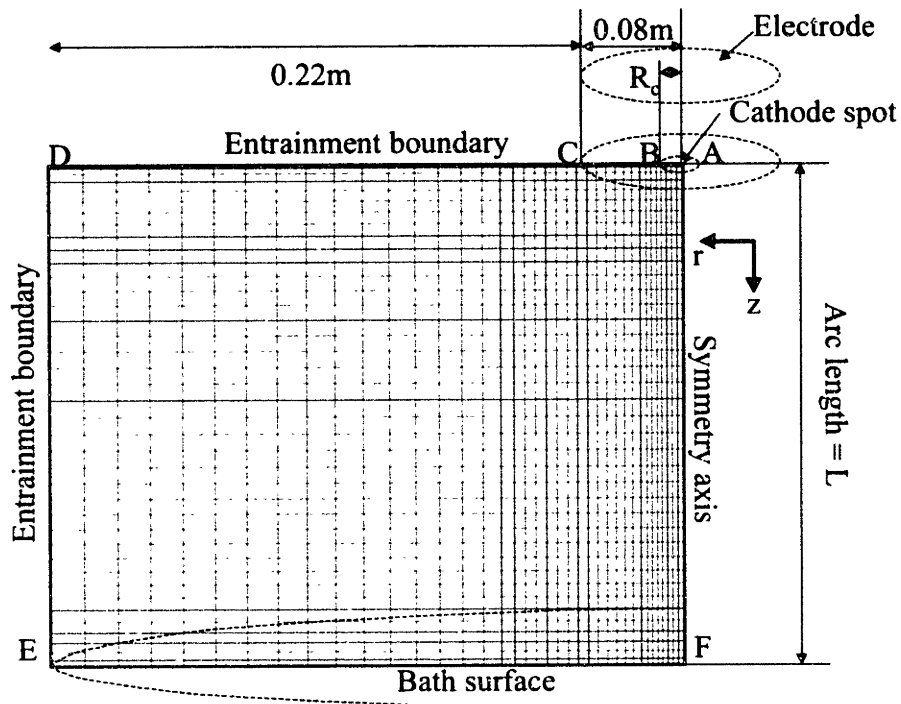


Figure 2.1.2 2D cylindrical polar coordinate representation of the computation domain in the arc region. The figure shows the non-uniform grid employed and all boundaries. The boundaries are: symmetry axis (AF), cathode surface (AC) which contains the cathode spot (AB), bath surface boundary (EF) and the entrainment (fixed pressure) boundaries (CD) and (DE).

The governing equations are:

Continuity equation:

$$\frac{\partial}{\partial z}(\rho v_z) + \frac{1}{r}(\rho r v_r) = 0 \quad (\text{eq. 2.1.3})$$

Conservation of axial momentum:

$$\begin{aligned} \frac{\partial}{\partial z}(\rho v_z^2) + \frac{1}{r} \frac{\partial}{\partial r}(\rho r v_r v_z) = & -\frac{\partial P}{\partial z} + \frac{2\partial}{\partial z} \left( \mu_{eff} \frac{\partial v_z}{\partial z} \right) \\ & + \frac{1}{r} \frac{\partial}{\partial r} \left( r \mu_{eff} \left( \frac{\partial v_z}{\partial r} + \frac{\partial v_r}{\partial z} \right) \right) - B_\theta J_r \end{aligned} \quad (\text{eq. 2.1.4})$$

Conservation of radial momentum:

$$\begin{aligned} \frac{\partial}{\partial z}(\rho v_r v_z) + \frac{1}{r} \frac{\partial}{\partial r}(\rho r v_r^2) = & -\frac{\partial P}{\partial r} + \frac{2}{r} \frac{\partial}{\partial r} \left( \mu_{eff} r \frac{\partial v_r}{\partial r} \right) - \frac{2v_r}{r^2} \mu_{eff} \\ & + \frac{\partial}{\partial z} \left( \mu_{eff} \left( \frac{\partial v_r}{\partial z} + \frac{\partial v_z}{\partial r} \right) \right) + B_\theta J_z \end{aligned} \quad (\text{eq. 2.1.5})$$

where  $v_r$  and  $v_z$  are the radial and axial components of velocity respectively,  $P$  is the pressure,  $\rho$  is the density,  $J_z$  and  $J_r$  are the axial and radial components of current density,  $B_\theta$  is the azimuthal magnetic flux density, and  $\mu_{eff}$  is the effective viscosity. The left hand side of equations 2.1.4 and 2.1.5 represents convective terms, while the right hand sides represent the pressure gradient, the viscous and electromagnetic body force (or Lorentz forces) terms, respectively. Body forces are the result of the cross product  $J \times B$ , which can be expressed by the components  $-J_r B_\theta$  in the axial and  $J_z B_\theta$  in the radial directions, respectively.

Conservation of energy:

$$\frac{\partial}{\partial z}(\rho v_z h) + \frac{1}{r} \frac{\partial}{\partial r}(\rho r v_r h) = \frac{\partial}{\partial z} \left( \frac{k_t}{C_p} \frac{\partial h}{\partial z} \right) + \frac{1}{r} \frac{\partial}{\partial r} \left( \frac{k_t r}{C_p} \frac{\partial h}{\partial r} \right) + S_r \quad (\text{eq. 2.1.6})$$

where the source term  $S_r$ , is described as:



$$S_i = \left( \frac{J_z^2 + J_r^2}{\sigma} \right) - S_r + \frac{5 k_B}{2 e} \left( \frac{J_z}{C_p} \frac{\partial h}{\partial z} + \frac{J_r}{C_p} \frac{\partial h}{\partial r} \right) \quad (\text{eq. 2.1.7})$$

where,  $h$  is the enthalpy,  $C_p$  is the specific heat,  $k$  is the thermal conductivity and  $\sigma$  is the electric conductivity. The first term in right hand side of equation 2.1.7 is the Joule heat,  $S_r$  represent the radiation losses per unit volume and the last term is the heat transported by the electrons flow, known as Thompson effect.

Maxwell equations:

$$\nabla \times \bar{E} = 0 \quad (\text{eq. 2.1.8})$$

$$\nabla \times \bar{H} = \bar{J} \quad (\text{eq. 2.1.9})$$

$$\nabla \cdot \bar{B} = 0 \quad (\text{eq. 2.1.10})$$

$E$  is the electric field and  $H$  is the magnetic field.

Charge conservation equation

$$\nabla \cdot \bar{J} = 0 \quad (\text{eq. 2.1.11})$$

Additionally, Ohm's law is used:

$$\bar{J} = \sigma (\bar{E} + \bar{V} \times \bar{B}) \quad (\text{eq. 2.1.12})$$

Ohm's law has two terms, the first term represents the current driven by the potential gradients and the second term represents the induced current produced due to the motion of the electric conductor (i.e., the plasma).

The Maxwell equations, the charge conservation equation and Ohm's law, are needed to determine the electric characteristics of the arc. However, it may be convenient to express the electric problem in terms of the electric potential by combining equations 2.1.11 and 2.1.12

$$\frac{1}{r} \frac{\partial}{\partial r} \left( \sigma r \frac{\partial \phi}{\partial r} \right) + \frac{\partial}{\partial z} \left( \sigma \frac{\partial \phi}{\partial z} \right) = \frac{\partial}{\partial z} (\sigma v_r B_\theta) - \frac{1}{r} \frac{\partial}{\partial r} (r \sigma v_z B_\theta) \quad (\text{eq. 2.1.13})$$

where  $\phi$  is the electric potential related to the electric field through the following equation:

$$\bar{E} = -\nabla\phi \quad (\text{eq. 2.1.14})$$

By solving equation 2.1.13 it is possible to obtain the current density components with the help of Ohm's law:

$$J_r = -\sigma \left( \frac{\partial\phi}{\partial r} - v_z B_\theta \right) \quad (\text{eq. 2.1.15a})$$

$$J_z = -\sigma \left( \frac{\partial\phi}{\partial z} + v_r B_\theta \right) \quad (\text{eq. 2.1.15b})$$

Finally, due to the fact that most of the current is axially directed, the magnetic flux density field can be derived from the integration of Ampere's law (eq. 2.1.9):

$$B_\theta = \frac{\mu_o}{r} \int_0^r J_z r dr \quad (\text{eq. 2.1.16})$$

Then, equations 2.1.13 to 2.1.16 define entirely the electromagnetic problem, and are derived from combining the Maxwell's, Ohm's and the charge conservation equations.

The standard k- $\epsilon$  turbulence model is used to represent turbulence in the plasma. In this formulation, additional transport equations for turbulent kinetic energy,  $k$ , and energy dissipation rate,  $\epsilon$ , are solved:

$$\frac{\partial}{\partial z} (\rho v_z k) + \frac{1}{r} \frac{\partial}{\partial r} (\rho r v_r k) = \frac{\partial}{\partial z} \left( \frac{\mu_t}{\sigma_k} \frac{\partial k}{\partial z} \right) + \frac{1}{r} \left( \frac{r \mu_t}{\sigma_k} \frac{\partial k}{\partial r} \right) + S_k - \rho \epsilon \quad (\text{eq. 2.1.17})$$

$$\frac{\partial}{\partial z} (\rho v_z \epsilon) + \frac{1}{r} \frac{\partial}{\partial r} (\rho r v_r \epsilon) = \frac{\partial}{\partial z} \left( \frac{\mu_t}{\sigma_\epsilon} \frac{\partial \epsilon}{\partial z} \right) + \frac{1}{r} \left( \frac{r \mu_t}{\sigma_\epsilon} \frac{\partial \epsilon}{\partial r} \right) + S_\epsilon \quad (\text{eq. 2.1.18})$$

where  $S_k$  and  $S_\epsilon$  are defined as:

$$S_k = \mu_t \left[ 2 \left\{ \left( \frac{\partial v_z}{\partial z} \right)^2 + \left( \frac{\partial v_r}{\partial r} \right)^2 + \left( \frac{v_r}{r} \right)^2 \right\} + \left( \frac{\partial v_z}{\partial r} + \frac{\partial v_r}{\partial z} \right)^2 \right] \quad (\text{eq. 2.1.19})$$

and:

$$S_\varepsilon = C_1 \varepsilon \frac{S_k}{k} - C_2 \rho \frac{\varepsilon^2}{k} \quad (\text{eq. 2.1.21})$$

$C_1$  and  $C_2$  are constants of the k- $\varepsilon$  model, while  $\alpha_k$  and  $\alpha_\varepsilon$  are the Prandtl numbers for  $k$  and  $\varepsilon$  respectively. These constants are defined in Table 2.1.1 with other constant parameters used in this formulation.

The turbulent nature of the flow is describe using the effective viscosity:

$$\mu_{\text{eff}} = \mu + \mu_t \quad (\text{eq. 2.1.22})$$

where the turbulent viscosity,  $\mu_t$ , is calculated directly from the solution of the standard k- $\varepsilon$  turbulence model:

$$\mu_t = C_D \rho \frac{k^2}{\varepsilon} \quad (\text{eq. 2.1.23})$$

Complete set of equations (2.1.3 - 2.1.23) define the mathematical statement for the arc problem. It can be noted the high degree of coupling between the equations and the strongly non-linear nature of the problem. The electromagnetic variables are calculated to define sources in the momentum and energy conservation equations, and velocities are employed in Ohm's law to obtain the electric potential and current densities. Also, all physical properties are function of temperature (or enthalpy), which further couples the set of transport equations. Closure of the mathematical statement is provided by appropriate boundary conditions presented in the following section.

$C_D$	$C_1$	$C_2$	$\alpha_H$	$\alpha_k$	$\alpha_\varepsilon$	$T_c$	$J_c$
0.09	1.44	1.92	0.9	1.0	1.3	4000 K	$4.4 \times 10^7 \text{ Am}^{-2}$

Table 2.1.1 Constant values for turbulence model and other constant parameters used in the calculations ( $\alpha_H$  is the turbulent Prandtl number for enthalpy)

## Section 2.1.4: Boundary Conditions

A complete list of boundary conditions employed in the arc model is given in Table 2.1.2. The geometric arrangement is expressed in terms of the symbols used in Figure 2.1.2.

These boundary conditions express zero velocities at bath and cathode surfaces, while logarithmic wall functions are employed for turbulence variables [89]. At the entrainment boundaries, a fixed pressure condition is employed (atmospheric pressure) to allow gas inflow or outflow to meet the conservation of mass and these boundaries are assumed to be free of turbulence. At the symmetry axis all variables have a zero flux condition.

	$v_r$	$v_z$	$P$	$h$	$\phi$	$k$	$\varepsilon$
AB	0	0		$7.4 \times 10^6 \text{ J/kg}$ ( $T_c=4000 \text{ K}$ ) and (eq. 2.1.25)	$\left(\frac{\partial \phi}{\partial z}\right) = -\frac{J_c}{\sigma}$	0 (wall function)	$\frac{\partial \varepsilon}{\partial z} = 0$ (wall function)
BC	0	0		$7.4 \times 10^6 \text{ J/kg}$ ( $T_c=4000 \text{ K}$ )	$\left(\frac{\partial \phi}{\partial z}\right) = 0$	0 (wall function)	$\frac{\partial \varepsilon}{\partial z} = 0$ (wall function)
CD	Fixed atmospheric pressure (entrainment boundary)			$\frac{\partial h}{\partial z} = 0$	$\left(\frac{\partial \phi}{\partial z}\right) = 0$	$\frac{\partial k}{\partial z} = 0$	$\frac{\partial \varepsilon}{\partial z} = 0$
DE	Fixed atmospheric pressure (entrainment boundary)			$\frac{\partial h}{\partial r} = 0$	$\left(\frac{\partial \phi}{\partial r}\right) = 0$	$\frac{\partial k}{\partial r} = 0$	$\frac{\partial \varepsilon}{\partial r} = 0$
EF	0	0		$1.71 \times 10^6 \text{ J/kg}$ ( $T_b=1800 \text{ K}$ ) and (eq. 2.1.31)	$\phi = 0$	0 (wall function)	0 (wall function)
AF	0	$\frac{\partial v_z}{\partial r} = 0$		$\frac{\partial h}{\partial r} = 0$	$\left(\frac{\partial \phi}{\partial r}\right) = 0$	$\frac{\partial k}{\partial r} = 0$	$\frac{\partial \varepsilon}{\partial r} = 0$

Table 2.1.2 Boundary conditions for the arc model. Variables solved are radial and axial velocities, pressure, enthalpy, electric potential and turbulent parameters. Geometric arrangement is based on Figure 2.1.2.

Enthalpy values at the cathode (graphite) and bath surfaces are set (4000 K at the cathode and 1800 K at the bath). Additional details are involved to model heat fluxes at the cathode and bath surfaces, which will be described in detail in a subsequent section. At entrainment boundaries, zero diffusion fluxes for all variables are set and energy transported by inflow or outflow is considered in the energy balance.

Electric potential values are imposed at the bath (zero value) and cathode surfaces. Allowance is made for the potential to vary at the cathode to ensure that the desired current,  $I$ , passes through the spot of known radius, which depends exclusively on the current of the arc ( $J_c$  is constant). The relation between spot radius,  $R_c$ , and arc current,  $I$ , is expressed by equation 2.1.24. The rest of the boundaries are treated as zero flux conditions for the electric potential.

$$R_c = \left( \frac{I}{\pi J_c} \right)^{0.5} \quad (\text{eq. 2.1.24})$$

## Section 2.1.5: Cathode and Bath Representations

### Cathode region

At the cathode, presence of a voltage drop (known as cathode fall) can be associated with a heat flux given by the following equation

$$Q_{c\text{fall}} = J_c V_c \quad (\text{eq. 2.1.25})$$

This heat flux is denominated  $Q_{c\text{fall}}$  and  $V_c$  denotes the voltage drop at the cathode in volts. This flux is positive because it heats the arc. The cathode fall represents a much steeper potential gradient (several volts in a small region close to the cathode) than normal potential gradients found in the arc column, which is not possible to resolve by numerical models due to its microscopic nature. This voltage drop is a consequence of departure from equilibrium at cathode. Estimated value of the potential drop,  $V_c$ , is about 4 V for graphite cathodes in normal industrial furnaces [11].

### Bath region

Effect of the arc on the bath surface is the key aspect that allows coupling between the arc model and the bath representation. The important arc-bath interactions that have to be considered are:

- Heat transfer (heat flux from the arc to the bath surface)
- Shear stress and pressure at the bath surface due to gas jet impinging on the bath surface
- Current density at the arc-bath interface

Several heat transfer mechanisms are important to represent realistically the total heat transfer boundary condition from the arc at the bath surface. The mechanisms considered are:

- Anode fall
- Condensation of electrons
- Convective heat transfer
- Radiation heat transfer
- Energy transported by electrons

**Anode fall.** Despite the fact that the bath surface is not the actual anode, this flux is named anode fall due to physical similarities between this voltage drop and the cathode fall. Then, the anode fall can be expressed similarly to cathode fall (equation 2.1.25).

$$Q_{afall} = J_a V_a \quad (\text{eq. 2.1.26})$$

where  $J_a$  is the current density at the anode, which depends on arc conditions given by the solution of the arc model.  $V_a$  is the anode fall, representing a steep potential gradient close to the bath surface as a consequence of departure from equilibrium.

**Condensation of electrons.** This heating mechanism results from condensation of electrons that move from the arc to the liquid (steel) phase. The condensation process generates a heat flux proportional to the work function of liquid steel.

$$Q_{conden} = J_a V_\Phi \quad (\text{eq. 2.1.27})$$

where  $V_\Phi$  is the work function of steel. For steel, the sum of work function and anode fall is equal to 8 V [90].

**Convection.** The high velocity jet impinging on the anode surface heats the bath by convection and this heat is calculated assuming that the rate of heat transfer is governed by an empirical correlation obtained from the results of re-entry studies [91].

$$Q_{conv} = \frac{0.915}{\sigma_{Hw}} \left( \frac{\rho_b \mu_b}{\rho_w \mu_w} \right)^{0.43} \left( \rho_w \mu_w \frac{v_r}{r} \right)^{0.5} (h_b - h_w) \quad (\text{eq. 2.1.28})$$

where  $\sigma_{Hw}$  is the enthalpy Prandtl number and the subscript  $b$  denotes positions at the edge of the boundary layer while  $w$  represents surface bath positions.

**Radiation heat transfer.** Radiation coming from the arc to the bath surface is calculated by means of approximate view factors described by the following equation [11].

$$Q_{rad,i} = \int_{V_j} \frac{S_r}{4\pi r_{i,j}^2} \cos \Psi dV_j \quad (\text{eq. 2.1.29})$$

where  $r_{i,j}$  is the vector joining each surface element at the bath surface with each volume element in the arc,  $V_j$ ,  $\Psi$  is the angle formed between  $r_{i,j}$  and the vector normal to the bath surface. The subscript  $i$  represents a bath surface element, while the subscript  $j$  denotes a volume element in the arc. The heat flux received at a specific bath surface element,  $i$ , is the integral that includes all the individual contributions to radiation into the bath surface element, from each volume element in the domain.

**Thompson effect.** Transport of thermal energy by hot electrons is called Thompson effect, which can be described by the equation

$$Q_{Tho} = \frac{5J_a}{2e} k_B (\alpha T_b - T_w) \quad (\text{eq. 2.1.30})$$

where the parameter  $\alpha$  represents the ratio between electron temperature to plasma temperature at the anode fall (departure from LTE). In the calculations a value of 1.2 is set for  $\alpha$  [10].

The total heat flux is then given by the arithmetic sum of all the contributions given by the following equation:

$$Q_{Total} = Q_{Tho} + Q_{afall} + Q_{conden} + Q_{conv} + Q_{rad} \quad (\text{eq. 2.1.31})$$

**Shear stress at the bath surface.** The shear stress may be assumed to follow a Newtonian representation defined by

$$\tau_a = -\mu_w \left. \frac{dv_r}{dz} \right|_w \quad (\text{eq. 2.1.32})$$

here,  $\tau_a$  is the shear stress at the bath surface.

### Section 2.1.6: Physical Properties

The physical properties are taken from calculations reported by Murphy et al. [88], which are presented in Figure 2.1.3 together with values obtained from other sources [85,92]. There are some

differences in computed properties, but they follow the same trends with temperature. The shape of some of these curves, such as those for specific heat and thermal conductivity (Figures 2.1.3 (d) and 2.1.3 (c)), shows some peaks at specific temperatures, which are associated with ionization processes for air. As mentioned above, it is interesting to note the strong non-linearity dependence shown in all the curves.

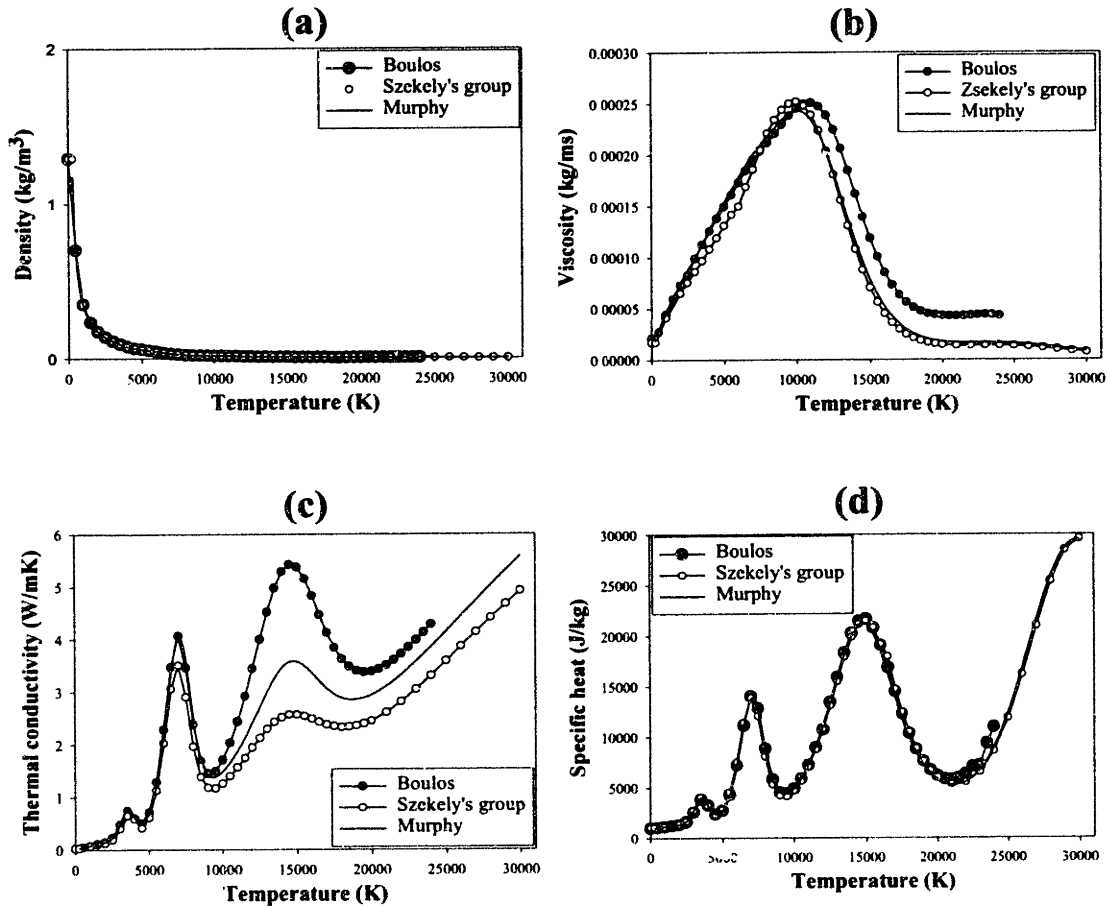


Figure 2.1.3 Physical properties of air at 1 atm as a function of temperature. (a) density, (b) viscosity, (c) thermal conductivity, (d) specific heat. Line represents calculations done by Murphy [88], filled dots are computations reported by Boulos [85] and unfilled dots are data used by Szekely et al. [92]. Radiation losses are taken from Morris et al. [93]



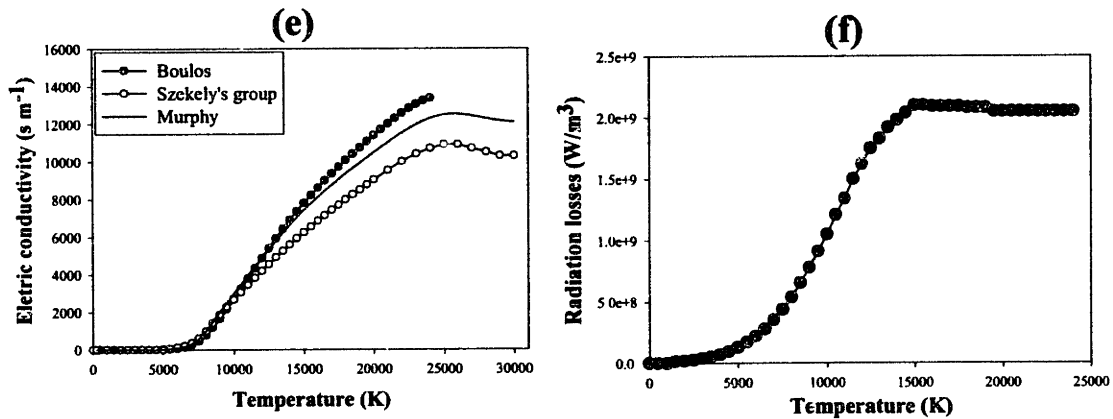


Figure 2.1.3 (cont.) Physical properties of air at 1 atm as a function of temperature. (e) electric conductivity, (f) radiation losses. Line represents calculations done by Murphy [88], filled dots are computations reported by Boulos [85] and unfilled dots are data used by Szekely et al. [92]. Radiation losses are taken from Morris et al. [93]

## Section 2.2: Arc Model Validation

One of the most imperative needs of this work was to obtain reliable data from experimental or industrial DC-EAF. Unfortunately, to the knowledge of the author, acquisition of experimental information from actual process has not been done yet. Some reasons for this lack of experimental information include the aggressive nature of EAF operations and the significant difficulty in obtaining measurements without affecting production. For example, fumes generated in the furnaces prevent visualization of the arc and therefore temperature fields measurements are impossible.

On the other hand, there is no useful model if validation against real conditions is missing. Therefore, the approach followed in this thesis is to validate, at least partially, the DC-EAF models by describing and simulating processes or systems for which the physics involved resembles that in DC-EAF operations. These systems must have the advantage of being studied extensively both theoretically and experimentally. Specifically in representing the arc model, similar systems found in the literature are:

- Welding arc processes (GTAW)
- Low current arc experimental setup reported by Bowman [20]

These two systems present arcs with fundamental similarities with the type of arcs found in EAFs. In fact, the last system listed above was built (physical model) specifically to study the behavior of industrial arc furnaces. With regard to the welding process, the main advantage is that extensive studies have been published in the literature [37,41,38,42,94] and the state-of-the-art in modeling these systems is quite sophisticated when compared with modeling of EAFs. Besides, experimental information is detailed

and even temperature maps have been reported. Then, the welding arc is an excellent preliminary testing case to validate the arc model. However, big differences exist between both arc systems that prevent from fully extrapolating the model from a small welding arc directly to a big EAF.

## Section 2.2.1: Welding Arc Process

### Section 2.2.1.1: Physical Description of the Welding Process (Differences with EAF)

The typical representation of the arc shown in Figure 2.1.1 also applies to the arc found in welding. However, there are big differences between arcs found in welding and those found in EAF systems which are presented in Table 2.2.1. The physics is very similar, but the main difference involves the order of magnitude of characteristic quantities. For example, currents in EAF are at least one order of magnitude higher than those in welding. As a consequence of this current difference, velocities (resulting from Lorentz forces, which are dependent on current) are much higher in EAF systems. The same can be said about the size of the arc, which again is at least one order of magnitude bigger in EAF than in welding. The combination of these order of magnitude differences produce a turbulence regime in EAF and a laminar one in welding, sonic or supersonic regimes in EAF and subsonic regimes in welding, and the relevance of induced currents in EAFs which are not present in welding. Therefore, it is obvious that mathematical formulations for welding differ somehow from the formulation presented in section 2.1.

Difference	EAF	Welding Arc
Gas atmosphere	Composed by several gases (predominantly air, CO <sub>2</sub> , CO, H <sub>2</sub> , H <sub>2</sub> O, metal vapors, etc.) without defined composition	Well-controlled Ar atmosphere.
Anode	Anode is located at bottom of the furnace (for model representation, anode is located at bath surface)	Work piece plays the role of anode.
Arc length and size scales	Arc lengths of the order of ~0.1 to ~0.5 m.	Arc lengths of the order of 1 to ~10 mm.
Cathode materials and sizes	Graphite cathode of ~10 cm to 64 cm in diameter with flat surface.	Tungsten (sometimes small amounts of Th). Cathode of small diameter with sharp edges.
$J_c$	$4.4 \times 10^7 \text{ Am}^{-2}$	$6.5 \times 10^7 \text{ Am}^{-2}$
Current, $I$	Between 10,000 A up to 100,000 A	Between 50 A to 500 A
Voltage drops, $V$	60-800 V	5-20 V
Velocities	~ 1000 m/s to 10,000 m/s	50 m/s to 500 m/s
Flow regime	Turbulent	Laminar
Flow regime	Probably sonic or supersonic	Subsonic

Table 2.2.1 Physical differences between welding arc process and DC-EAF process

## Section 2.2.1.2: Mathematical Representation of the Welding Arc: Potential and Magnetic Approaches

In view of the different operating conditions for welding and EAF processes, which are discussed in the previous sections, some simplifications on the previously described mathematical representation are possible. First, welding arcs operate on a laminar regime and hence, a turbulent model is not required to solve the problem. Secondly, values for the magnetic Reynolds number are very low:

$$Re_m = V_o L_o \sigma \mu_o = \frac{\text{magnetic convection}}{\text{magnetic diffusion}} \quad (\text{eq. 2.2.1})$$

where  $V_o$  is a characteristic velocity,  $L_o$  is a characteristic length,  $\sigma$  is the electric conductivity and  $\mu_o$  is the magnetic permeability. Taking characteristic values for welding ( $L_o=0.01$  m,  $V_o=300$  m/s,  $\mu_o=4\pi \times 10^{-7}$  henry/m,  $\sigma=12000$  sm<sup>-1</sup>) gives a value magnetic Reynolds number of ~0.04, i.e. under welding conditions magnetic Reynolds number values are much less than one indicating that magnetic diffusion dominates over magnetic convection. Thus, there is no need to include induced currents in the representation and Ohm's law can be simplified as:

$$J = \sigma E \quad (\text{eq. 2.2.2})$$

Therefore, Ohm's law in equation 2.2.2 will lead to a different electric formulation than the one presented in equations 2.1.13-2.1.16 for EAF in section 2.1.3. As part of this work, two alternative approaches were tested to mathematically represent the welding arc process.

**Electric Potential Approach.** Absence of induced currents in the Ohm's law leads to a different potential equation without the convective terms present in equation 2.1.13, i.e.,

$$\frac{1}{r} \frac{\partial}{\partial r} \left( \sigma r \frac{\partial \phi}{\partial r} \right) + \frac{\partial}{\partial z} \left( \sigma \frac{\partial \phi}{\partial z} \right) = 0 \quad (\text{eq. 2.2.3})$$

while current densities are now obtained with equation 2.2.2 that can be expressed for the radial and axial components as:

$$J_r = -\sigma \left( \frac{\partial \phi}{\partial r} \right) \quad (\text{eq. 2.2.4a})$$

$$J_z = -\sigma \left( \frac{\partial \phi}{\partial z} \right) \quad (\text{eq. 2.2.4b})$$

Finally, the magnetic flux density field can be derived from the integration of Ampere's law.

$$B_\theta = \frac{\mu_o}{r} \int_0^r J_z r dr \quad (\text{eq. 2.2.5})$$

Note that equation 2.2.5 is the same as 2.1.16. With this approach equations 2.2.2 to 2.2.5 describe the electromagnetic problem.

**Magnetic Approach.** The potential equation is derived (combining Ohm's law and the charge conservation equation) and is solved to obtain current and magnetic flux density fields using Ampere's law. An alternative formulation can be derived if a different set of equations is employed. Specifically, in the magnetic approach, two Maxwell equations, i.e. Faraday's law (equation 2.1.8) and Ampere's law (equation 2.1.9), are combined with Ohm's law (equation 2.2.2) to derive the so-called magnetic diffusion equation,

$$\frac{\partial}{\partial r} \left( \frac{1}{\sigma r} \frac{\partial r B_\theta}{\partial r} \right) + \frac{\partial}{\partial z} \left( \frac{1}{\sigma} \frac{\partial B_\theta}{\partial z} \right) = 0 \quad (\text{eq. 2.2.6})$$

Once the magnetic flux density field is obtained, the current density components can be derived using Ampere's law.

$$J_r = -\frac{1}{\mu_o} \frac{\partial B_\theta}{\partial z} \quad (\text{eq. 2.2.7})$$

$$J_z = \frac{1}{r \mu_o} \frac{\partial r B_\theta}{\partial r} \quad (\text{eq. 2.2.8})$$

In this formulation there is no need to solve the electric potential  $\phi$  or electric field  $E$ , since the coupling with energy and momentum conservation equations is completely fulfilled with the magnetic flux density  $B_\theta$  and the current densities  $J_r$  and  $J_z$ . However, it is possible to obtain the potential using appropriate relations (i.e., equations 2.2.2 and 2.1.14).

Both formulations should give the same arc representation for welding because they represent the same physical phenomena, but mathematically and numerically they present differences and the intrinsic advantages and disadvantages associated with each formulation are studied in this work.

**Boundary conditions.** Table 2.2.2 (based on the same Figure 2.1.2) lists the boundary conditions required to specify the problem using both formulations, i.e. magnetic and potential approaches. Boundary conditions for the magnetic flux density field needs a further explanation since this variable was not considered in the formulation of the mathematical problem for DC-EAF. At the cathode (inside and outside the cathode spot) the magnetic flux density field,  $B_\theta$ , is calculated from knowledge of the current at the cathode spot and assuming that this surface behaves as a long perfect conductor:

$$B_\theta = \frac{\mu_o I r}{2\pi R_c^2} \quad \text{for } r \leq R_c \quad (\text{eq. 2.2.9})$$

$$B_\theta = \frac{\mu_o I}{2\pi r} \quad \text{for } r > R_c \quad (\text{eq. 2.2.10})$$

	$v_r$	$v_z$	$P$	$h$	$\phi$	$B_\theta$
AB	0	0		$7.2 \times 10^6 \text{ J/Kg}$ ( $T_c=4000 \text{ K}$ ) and eq. 2.1.25	$\left(\frac{\partial \phi}{\partial z}\right) = -\frac{J_c}{\sigma}$	eq. 2.2.9
BC	0	0		$7.2 \times 10^6 \text{ J/Kg}$ ( $T_c=4000 \text{ K}$ )	$\left(\frac{\partial \phi}{\partial z}\right) = 0$	eq. 2.2.10
CD	Fixed atmospheric pressure			$\frac{\partial h}{\partial z} = 0$	$\left(\frac{\partial \phi}{\partial z}\right) = 0$	eq. 2.2.10
DE	Fixed atmospheric pressure			$\frac{\partial h}{\partial r} = 0$	$\left(\frac{\partial \phi}{\partial r}\right) = 0$	eq. 2.2.10
EF	0	0		$5.2 \times 10^5 \text{ J/Kg}$ ( $T_a=1000 \text{ K}$ ) and eq. 2.1.31	$\phi = 0$	$\frac{\partial B_\theta}{\partial z} = 0$
AF	0	$\frac{\partial v_z}{\partial r} = 0$		$\frac{\partial h}{\partial r} = 0$	$\left(\frac{\partial \phi}{\partial r}\right) = 0$	$B_\theta = 0$

Table 2.2.2 Boundary conditions for the arc model in welding processes. Geometric arrangement is based on symbols presented in Figure 2.1.2.

**Anode and cathode representations.** In analogy to the model for EAF (section 2.1.5), Table 2.2.3 presents heat fluxes at the anode and cathode surfaces and the shear stress at the anode. The mathematical representation is in some cases identical to previous equations applied for EAF

representation, but it is noted that since the cathode and the gases are different from those in EAF, some values and constants used in the model are different.

Effect	Expression	Difference with DC-EAF model
Cathode fall	$Q_{c\text{fall}} = J_c V_c$	$J_c = 6.5 \times 10^7 \text{ Am}^{-2}$ $V_c = 4 \text{ V}$ [38]
Anode fall and work function	$Q_{a\text{fall}} = J_a (V_a + V_\phi)$	$V_a + V_\phi = 6.76 \text{ V}$
Convective heat	$Q_{\text{conv}} = \frac{0.515}{\sigma_w} \left( \frac{\rho_b \mu_b}{\rho_w \mu_w} \right)^{0.11} \left( \rho_w \mu_w \frac{dv_r}{dr} \right)^{0.5} (h_b - h_w)$	Different correlation [38] Gas properties (Argon) Anode temperature of 1000 K
Radiation from arc	$Q_{\text{rad},j} = \int_{V_j} \frac{S_r}{4\pi r_{i,j}^2} \cos \Psi dV_j$	Identical
Thompson effect	$Q_{\text{Tho}} = \frac{5J_a}{2e} k_B (\alpha T_b - T_w)$	Anode temperature at 1000 K
Total heat flux at anode surface	$Q_{\text{Total}} = Q_{\text{Tho}} + Q_{a\text{fall}} + Q_{\text{conden}} + Q_{\text{conv}} + Q_{\text{rad}}$	Identical
Shear stress	$\tau_a = -\mu_w \frac{dv_r}{dz} \Big _w$	Identical!

Table 2.2.3 Mathematical representation of heat fluxes at the anode and bath surfaces for argon welding arc and their differences with respect to the expressions used in DC-EAF.

**Physical properties.** In welding, an argon atmosphere is typically used. The physical properties for this gas were obtained from Boulos et. al [85], who reported an extensive list of properties calculated as a function of temperature at atmospheric pressure. However, physical properties are reported only for a limited range of temperatures (up to 25,000 K). Figures 2.2.1 (a) - (e) present density, specific heat, thermal conductivity, electric conductivity, and viscosity. Figure 2.2.1 (f) shows radiation losses per unit volume  $S_r$ , as a function of temperature computed under the assumption of optically thin radiation plasma by Tampkin and Evans [95].

Comparing Figures 2.1.3 and 2.2.1, it can be seen that, due to different ionization processes, air presents more drastic changes in properties than argon, such as in the case of the specific heat. This difference plays a significant role in the complexity to obtain a converged numerical solution, when comparing argon and air simulations.

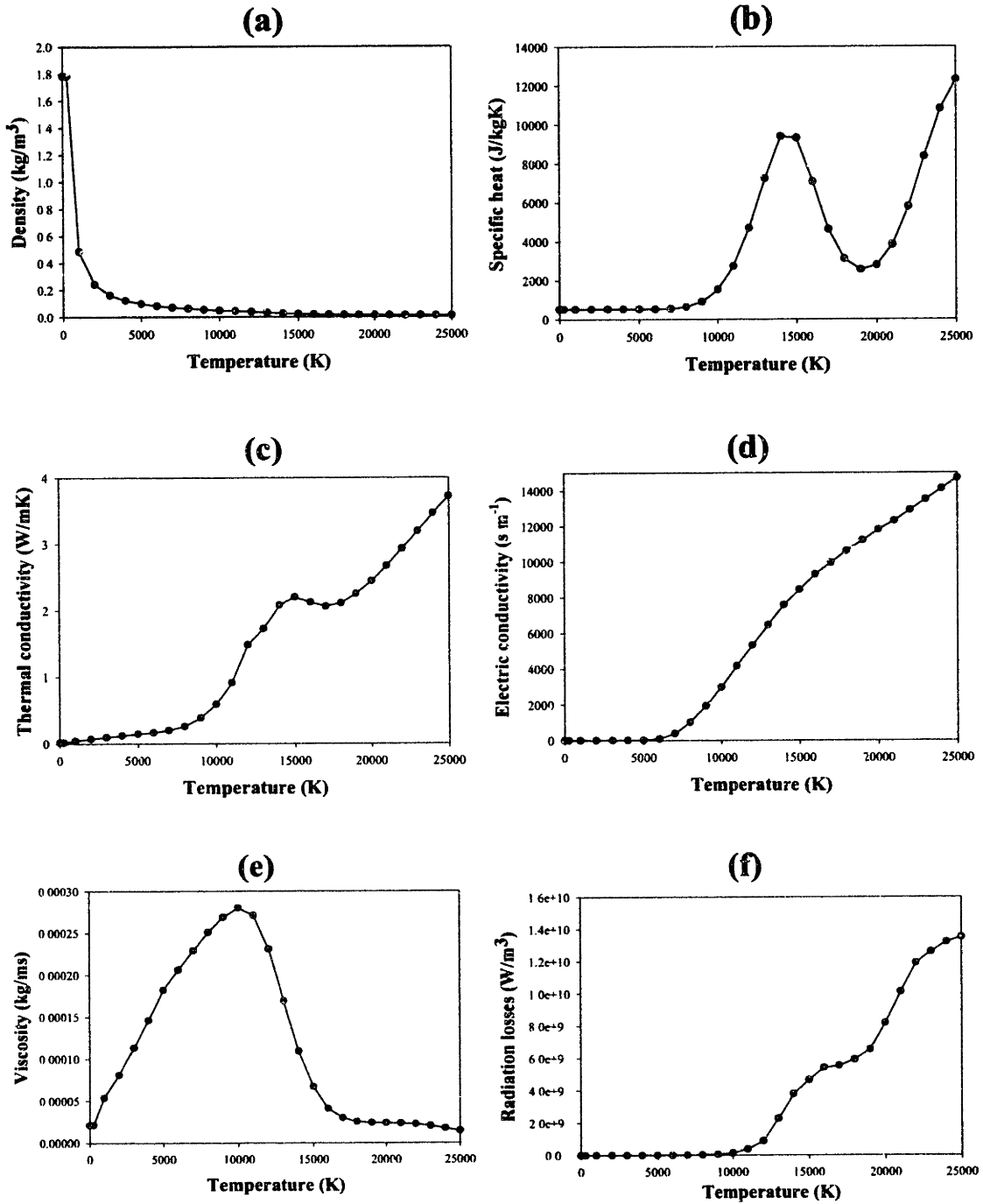


Figure 2.2.1 Argon physical properties as a function of temperature at 1 atm (Boulos et. al [85]) (a) density, (b) specific heat, (c) thermal conductivity, (d) electric conductivity, (e) viscosity, (f) radiation losses (Radiation losses are taken from Tampkin and Evans [95]).

### Section 2.2.1.3: Comparison between the Two Formulations

**Solution technique.** The two numerical representations were cast into numerical models to solve simultaneously all governing equations together with their respective boundary conditions, as described in Table 2.2.2 and using physical properties from Figure 2.2.1. The numerical method consists in transform all partial differential equations (transport equations) to algebraic equations by applying the technique called “control volume control integration” proposed by Patankar [96]. The problem was implemented in the commercial CFD code “PHOENICS version 3.2”. PHOENICS handles fluid flow and heat transfer problems and separate FORTRAN subroutines were written to describe the electromagnetic problem. Numerical domain of 60x60 grids were used and calculations took about 3000 iterations to converge the set of equations into a solution, which was considered when all imbalances of the transport equations were lower than 1%. CPU times were about 2 hours for simulation on a 233MHz Pentium II processor.

**Comparison between the two electromagnetic approaches: Potential versus Magnetic.** The comparison explores the behavior of the main characteristics of the arc such as temperatures, velocities, current densities, magnetic flux densities, arc pressure, heat fluxes and shear stresses at the anode. The electromagnetic quantities are the most important variables to be compared, since the objective of this comparison involves the differences regarding the solution techniques.

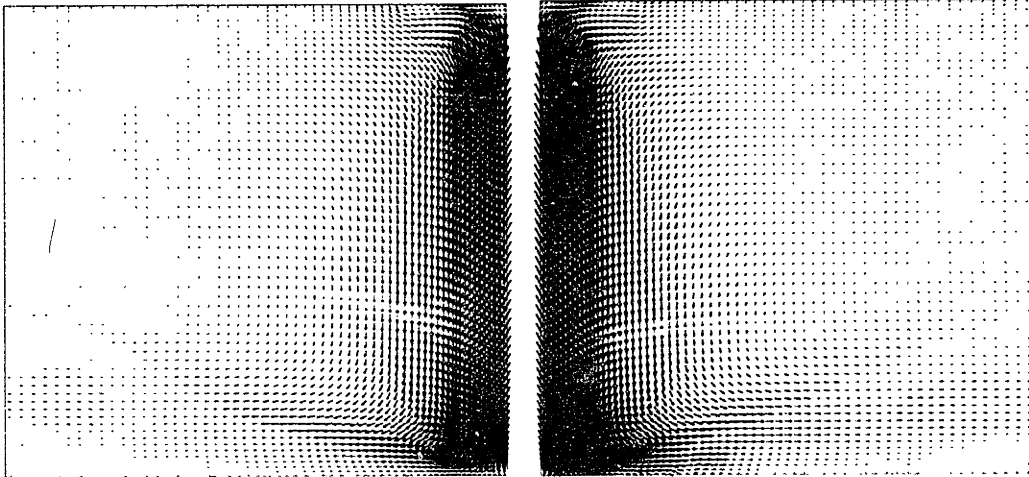
Figure 2.2.2 shows velocity, arc pressure, temperature, current density, magnetic flux density and electromagnetic body force fields for an argon welding arc with 200 A and 10 mm calculated using the two approaches. In general, both approaches show similar results. In the velocity field plot (Figure 2.2.2 (a)), it is seen that the arc jet is directed from the cathode to the anode along the symmetry axis as a result of fluid being sucked from the entrainment boundary close to the cathode. The arc pressure field (Figure 2.2.2 (b)) explains this velocity field. The arc pressure has a maximum value just below the cathode where electromagnetic forces show their maximum values. This high-pressure zone and the steep pressure gradients there, make argon gas to flow towards the anode. When the jet reaches the anode it is deflected in the radial direction, but the impingement zone is associated with a second high-pressure zone. The temperature field (Figure 2.2.2 (c)) shows maximum values of ~21,000 K just below the cathode where the highest Joule heat is generated due to the highest current densities being concentrated in the vicinity of the cathode, as can be seen in Figure 2.2.2 (d). The Joule heat in the arc decreases as the distance from the cathode increases since current densities decrease as the arc expands. In the anode region, the temperature field follows the convective nature of the jet, expanding in the radial direction as the jet is deflected upon impingement with the anode surface. Finally, the magnetic flux density fields (Figure 2.2.2 (e)) present some differences in shape, but they reflect the same patterns in both approaches. Figure 2.2.2 (f) indicates how body forces show their preferential alignment in the radial direction close to the symmetry axis and predominantly close to the cathode.



(a)

**Magnetic approach**

**Potential approach**



(b)

**Magnetic approach**

**Potential approach**

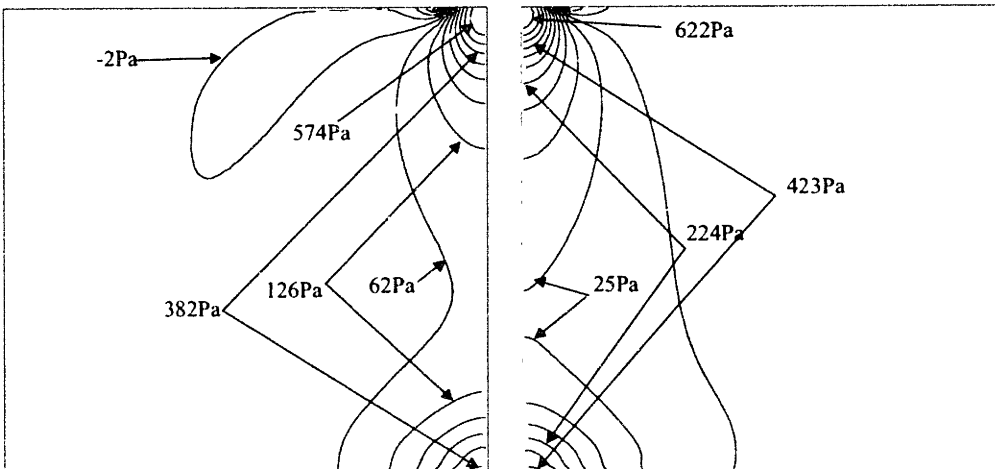
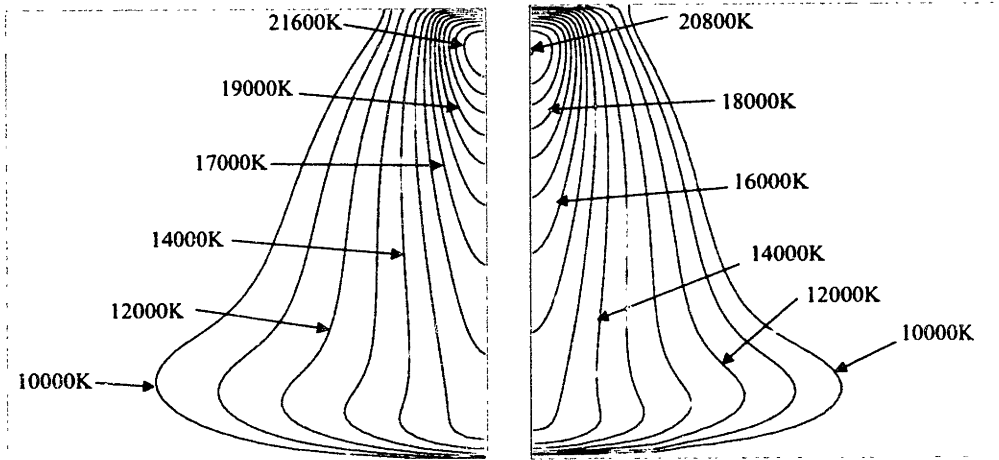


Figure 2.2.2 Comparison of computed results for an argon welding arc with 200 A and 10 mm using two approaches: Potential approach (PA) and magnetic approach (MA). a) Velocity field. b) Pressure field.

(c)

**Magnetic approach**

**Potential approach**



(d)

**Magnetic approach**

**Potential approach**

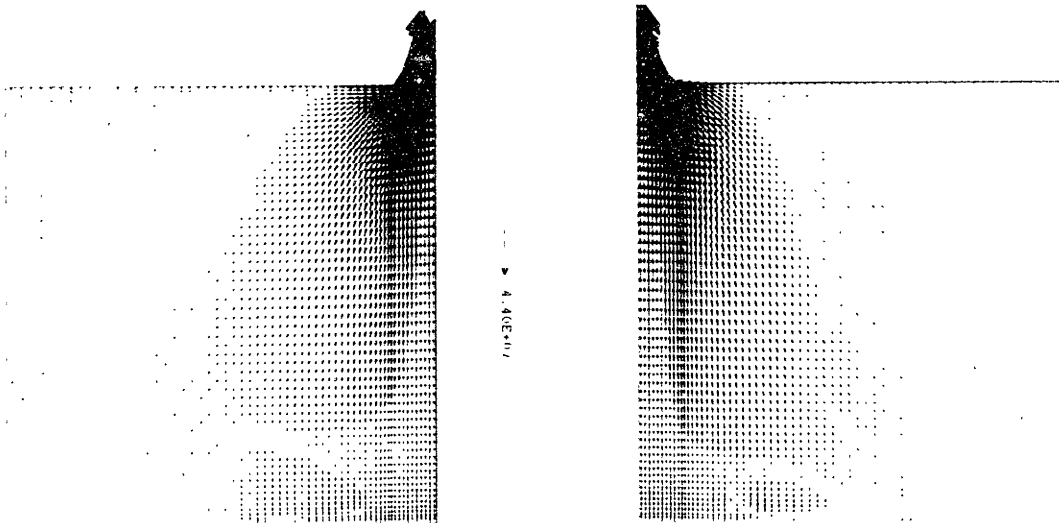
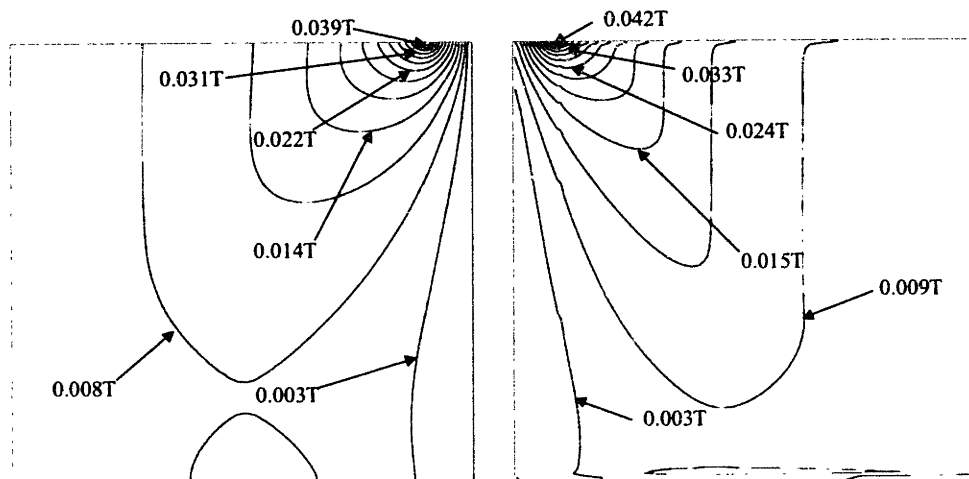


Figure 2.2.2 (cont.) Comparison of computed results for an argon welding arc with 200 A and 10 mm using two approaches: Potential approach (PA) and magnetic approach (MA). c) Temperature field. d) Current density field.

(e)

**Magnetic approach**

**Potential approach**



(f)

**Magnetic approach**

**Potential approach**

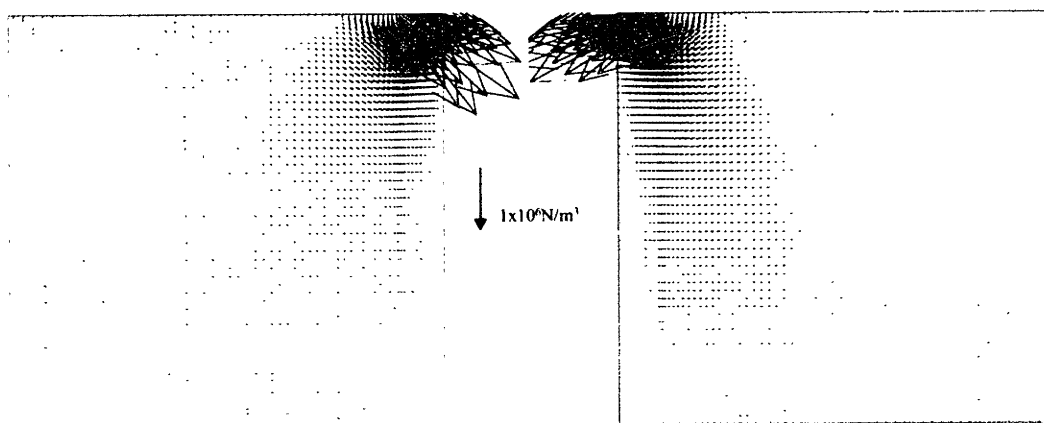


Figure 2.2.2 (cont.) Comparison of computed results for an argon welding arc with 200 A and 10 mm using two approaches: Potential approach (PA) and magnetic approach (MA). e) Magnetic flux density field. f) Electromagnetic body force field.

A more detailed comparison can be appreciated if characteristic variables are presented for specific locations using x-y plots. Figure 2.2.3 (a) shows the comparison between radial profiles of the magnetic flux densities at five different axial positions for the same argon arc with 200 A and 10 mm. Axial positions are expressed in dimensionless form,  $Z/L$ , where  $Z$  is axial distance from the cathode and  $L$  is the arc length. Both approaches behave similarly close to the cathode but the agreement between the two approaches starts departing from each other close to the anode. The same can be said when radial current densities are plotted for the same axial positions, as shown in Figure 2.2.3 (b). Close to the cathode, a better agreement is found between the two approaches. In this plot it can be appreciated the spreading of current taking place at the arc boundary, where the radial current components increase rapidly until reaching maximum values close to the symmetry line. The maximum radial current density decreases with an increase in the axial distance from the cathode since the arc expands and current densities decrease, but maximum values are located at higher radial distances. The same behavior is observed in the magnetic flux density field, since both variables ( $J$  and  $B_{\theta}$ ) define the conduction region within the arc. The axial component of current gives also an indication of the arc expansion as shown in Figure 2.2.3 (c), where the maxima are located at the symmetry axis, and the arc expansion is observed by the wider distribution and lower maximum values of axial current density,  $J_z$ .

Figures 2.2.3 (a) -2.2.3 (c) represent the electromagnetic characteristics of the arc given by the two approaches where it is clear that despite the fact that both approaches must represent the same physical problem, some differences are observed, specially close to the anode.

Figure 2.2.3 (d) presents results for some other important arc characteristics (arc pressure, arc velocity, and arc temperature) plotted along the symmetry line. Both approaches give similar predictions, but the potential approach predicts slightly higher velocities and pressures but lower temperatures values than the magnetic approach.

Figure 2.2.3 (e) presents shear stress and arc pressure at the anode for another case of argon welding arc with 200 A but 6.3 mm arc length. Evidently there are differences between predicted profiles given by the two approaches. This same lack of agreement is found for heat flux at the anode, which is plotted in Figure 2.2.3 (f).

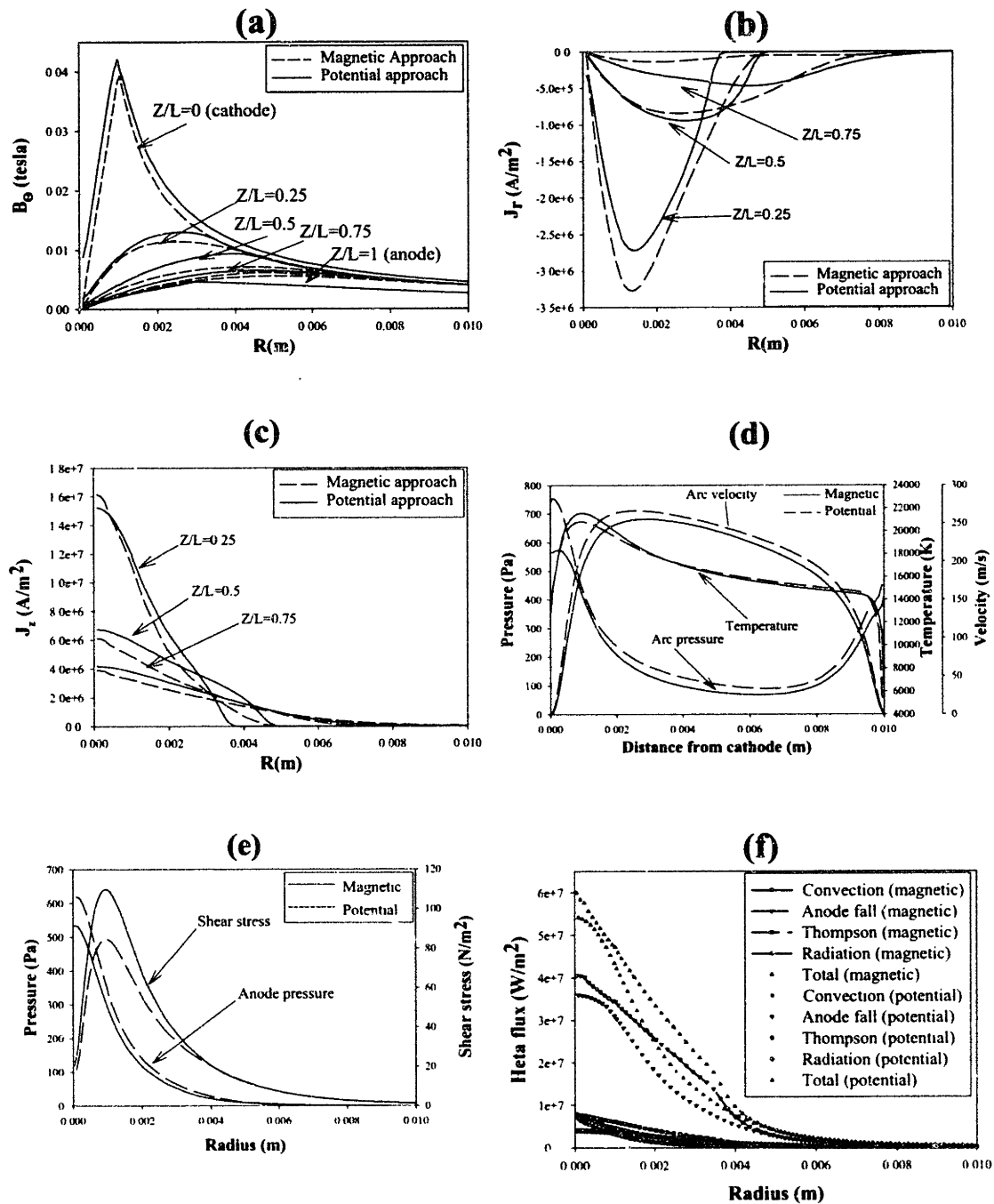


Figure 2.2.3 Comparison between potential and magnetic approaches for an argon welding arc of 200 A current and 10 mm arc length. (a) Magnetic flux density radial profiles at  $Z/L=0$ ,  $Z/L=0.25$ ,  $Z/L=0.5$ ,  $Z/L=0.75$  and  $Z/L=1$ . (b) Radial current density profiles at  $Z/L=0.25$ ,  $Z/L=0.5$  and  $Z/L=0.75$ . (c) Axial current density profiles at  $Z/L=0.25$ ,  $Z/L=0.5$  and  $Z/L=0.75$  axial positions. (d) Arc velocity, arc pressure and arc temperature along the symmetry axis. (e) Shear stress and arc pressure at the anode. (f) Heat fluxes at the anode.

### Section 2.2.1.4: Comparison against Experimental Data and other Numerical Studies

In order to partially validate the arc model, relevant measurements and results from experimental and numerical works reported in the literature were used to compare with predictions of the mathematical model. The conditions for the different systems used in the comparison, which are summarized in Table 2.2.4, range from typical currents used in welding operations to higher current experimental systems.

Case	Arc length, $L$ (mm)	Arc current, $I$ (A)	Gas	Type of investigation (reference)
Case A	10	200	Argon	Experimental and Numerical by Hsu et. al [37]
Case B	20	200	Argon	Experimental and Numerical by Hsu et. al [37]
Case C	10	300	Argon	Experimental and Numerical by Hsu et. al [37]
Case D	10	200	Argon	Numerical by Lee and Na [42]
Case E	6.3	200	Argon	Numerical by Lee and Na [42]
Case F	6.3	200	Argon	Experimental by Olsen [41]
Case H	6.3	200	Argon	Experimental by Nestor [41]

Table 2.2.4 Argon welding arc numerical and experimental studies used to validate the two numerical approaches used in this thesis.

**Temperature maps.** Figure 2.2.4 shows a comparison between predicted for both potential and magnetic approach and experimental temperature fields for welding argon arcs cases A, B and C in Table 2.2.4. It can be said that agreement between experiments and computations is quite good in both approaches and for all arcs, reflecting not only an agreement in the shape but also a quantitative agreement. Examination of the contour plots in Figure 2.2.4 shows that the maximum temperatures in all the cases are located just below the cathode. It is also noted that the maximum temperatures increase as the arc currents increase.

Figure 2.2.5 (a) shows a comparison between predicted temperature axial profiles along the symmetry axis in this study and results reported by Hsu et. al for case A in Table 2.2.4. The agreement between both numerical approaches and Hsu's results is very good. However, Hsu predicts slightly lower overall temperatures. In this plot, the temperature rises suddenly from the cold cathode temperature to a maximum value in less than 1mm and then decreases steadily as the distance from cathode increases up to reaching the cold anode surface.

**Velocity at the symmetry axis.** Figure 2.2.5 (b) shows the predicted axial velocity profile at the symmetry line for the argon arc case A in Table 2.2.4 calculated by the two approaches analyzed in this

work and the model developed by Hsu et. al. The agreement is again very good but Hsu's model gives a higher estimation of the axial velocity. The velocity increases rapidly from a zero value at the cathode due to high pressure produced by electromagnetic forces and reaches maximum values at 2mm from the cathode, then decreases slowly until reaching the anode surface.

**Pressure distributions.** Figure 2.2.5 (c) presents the pressure profile at the symmetry line computed by the two approaches together with computations done by Hsu (case A in Table 2.2.4) and additional simulations performed by Lee and Na (case D in Table 2.2.4). Here, a good general agreement is observed, except for the magnetic approach used in this work, where a big difference is obtained near the cathode. In contrast the agreement is very good between the simulation reported by Lee and Na (case D) and the potential approach as can be seen by the radial pressure distributions at the anode surface shown in Figure 2.2.5 (d). Again, the magnetic approach does not agree that well. In the plot, the two high-pressure zones are clearly seen, i.e. one high-pressure close to cathode due to electromagnetic body forces (Maecker effect) and the second at the anode surface in the jet impingement zone.

**Current densities.** Additional experimental results have been reported by Nestor and Olsen (cases F and H in Table 2.2.4). Figure 2.2.5 (e) shows the comparison between experimental results (cases F and H) and simulations done using the two approaches. The agreement is very good, although it can be noted that the magnetic approach seems to over predict current densities, when comparing with the other curves. As seen in the figure, a Gaussian-like shape current distribution is obtained at the anode.

**Heat flux at the anode.** Figure 2.2.5 (f) shows a comparison between experimental results reported by Nestor and Olsen and numerical simulations done in this work with the two approaches for an arc of 200 A and 6.3 mm arc length. This comparison shows that again the potential approach seems to represent better experimental results. It should be mentioned that the total heat flux plotted in the figure represents the sum of the four heat transfer mechanisms explained previously. Again, a Gaussian-like curve for the heat flux distribution is obtained at the anode.

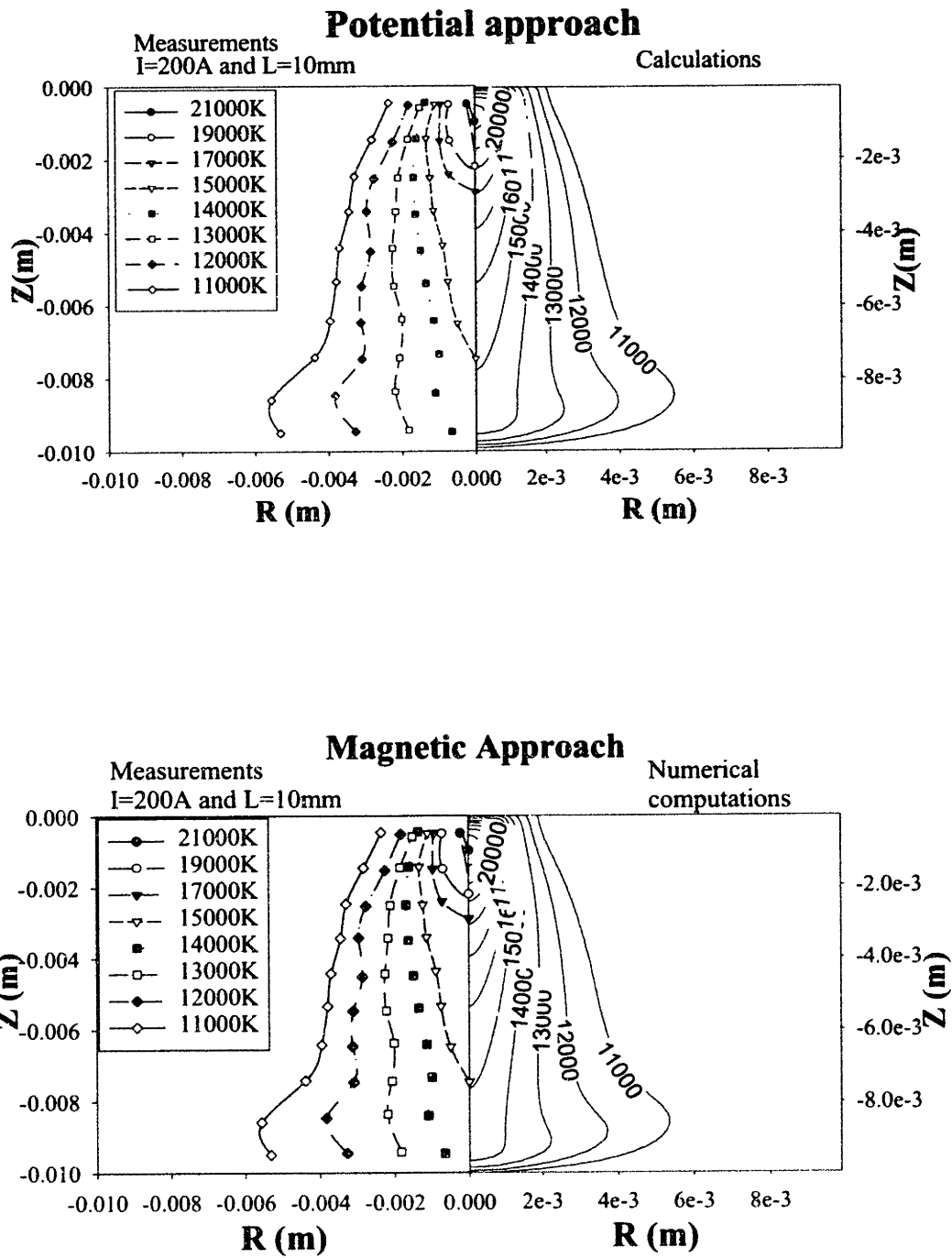


Figure 2.2.4 Comparison between experimental temperature maps by Hsu et. al. (case A in Table 2.2.4) and computations. Upper plots present the Potential approach while lower plots present the Magnetic approach.



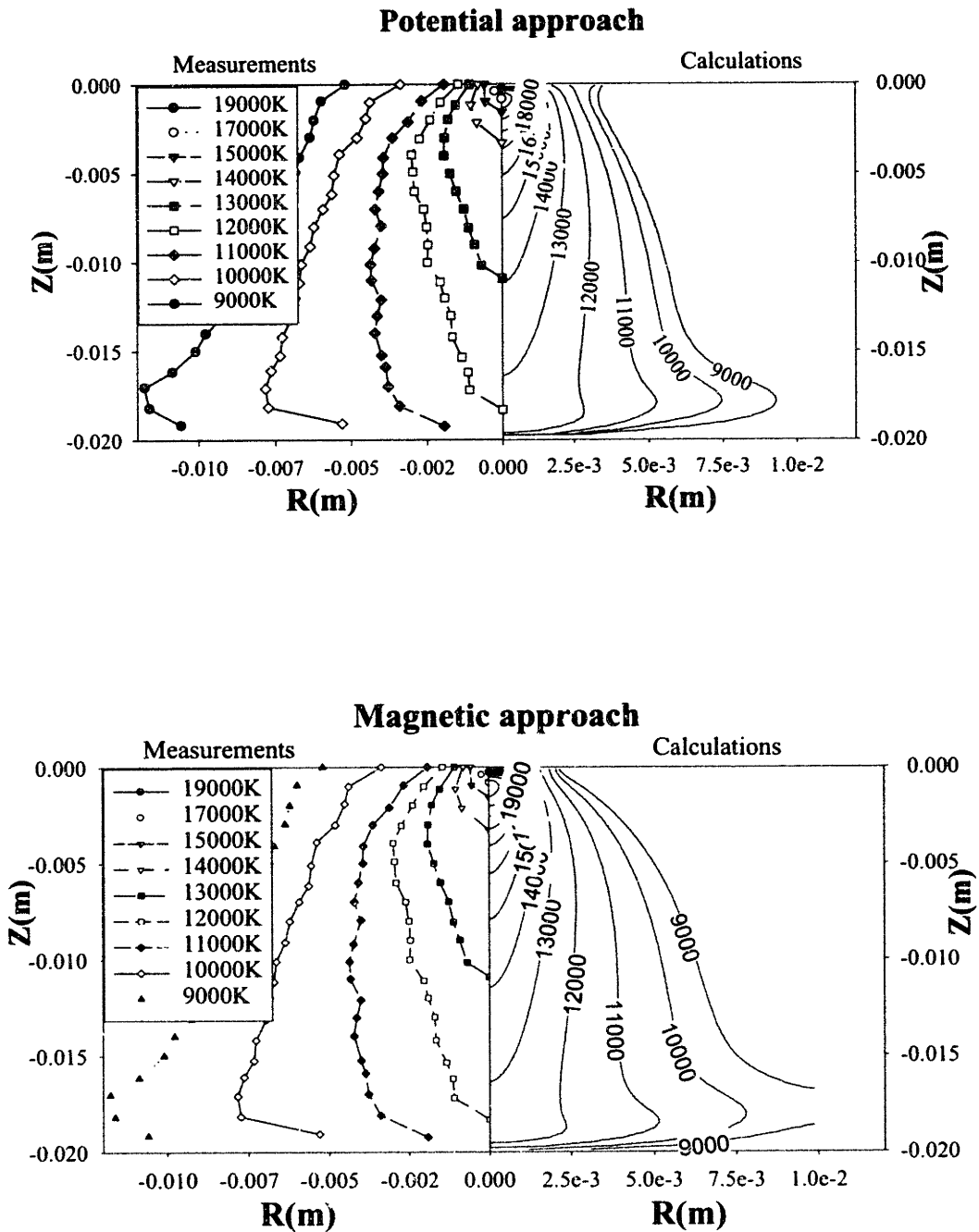


Figure 2.2.4 (cont.) Comparison between experimental temperature maps by Hsu et. al. (case B in Table 2.2.4) and computations. Upper plots present the Potential approach while lower plots present the Magnetic approach.

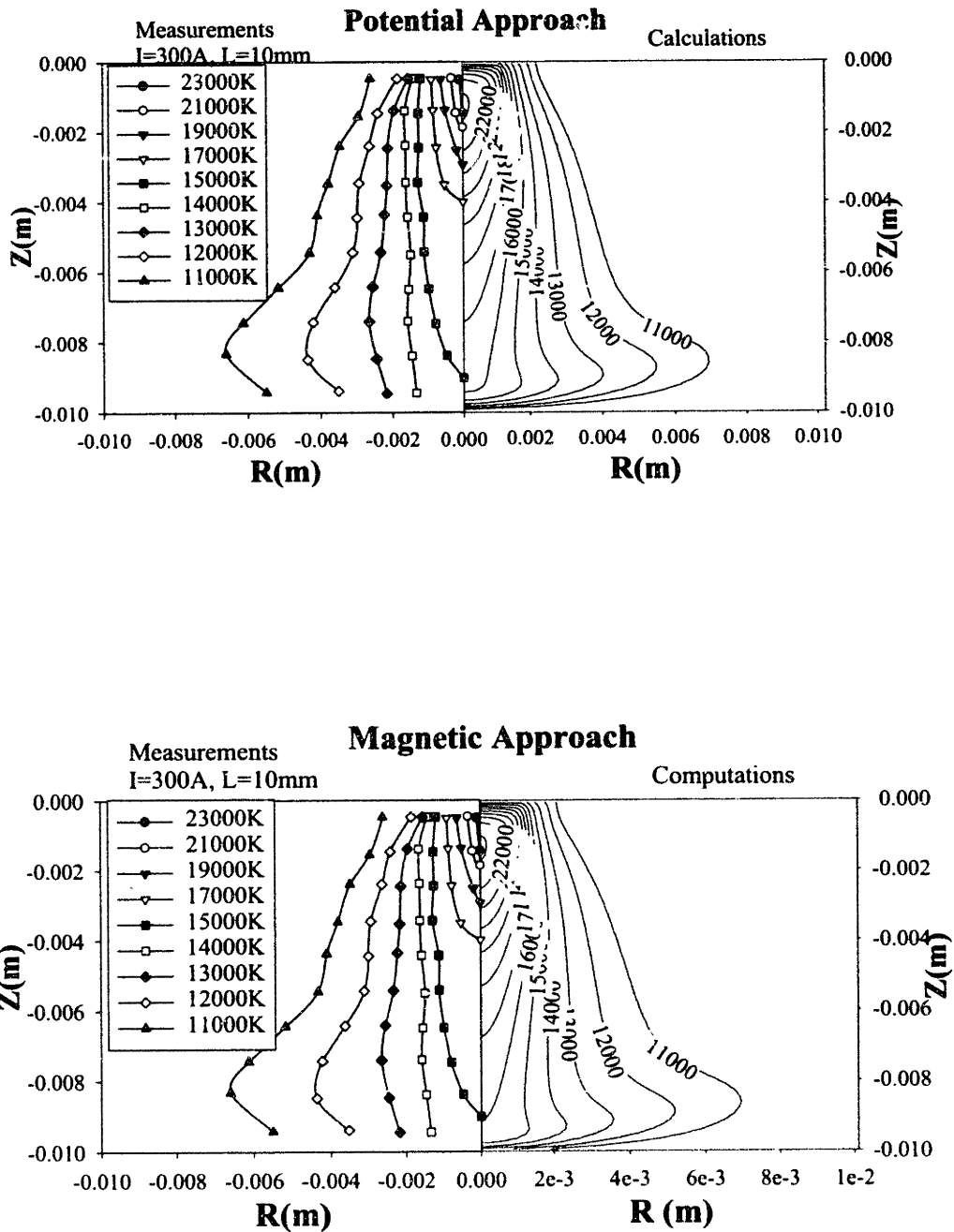


Figure 2.2.4 (cont.) Comparison between experimental temperature maps by Hsu et. al. (case C in Table 2.2.4) and computations. Upper plots present the Potential approach while lower plots present the Magnetic approach.

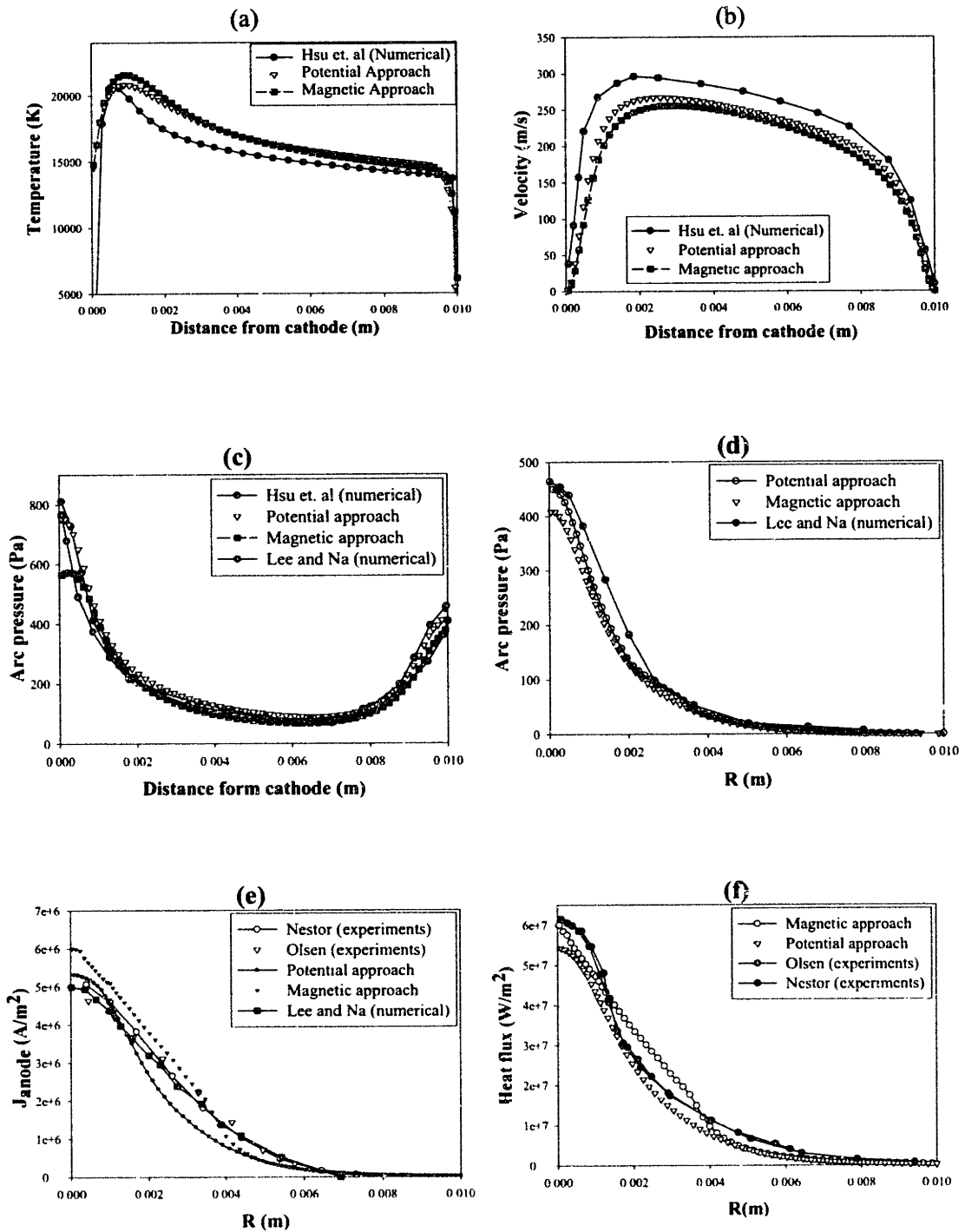


Figure 2.2.5 Comparison between results from the potential and magnetic approaches against experimental and other numerical simulations reported in the welding literature. (a) Temperature along the symmetry axis (case A in Table 2.2.4). (b) Velocity profile along the symmetry axis (case A in Table 2.2.4). (c) Arc pressure along the axis (case A and D in Table 2.2.4). (d) Arc pressure at the anode surface (case D in Table 2.2.4). (e) Current distribution at the anode (case F and H in Table 2.2.4). (f) Heat flux distribution at the anode (case F and H in Table 2.2.4).

In summary, it can be said that the potential and magnetic approaches provide good enough representation of the main arc characteristics. However, the potential approach gives a better representation of the arc, particularly in the region close to the cathode. Another advantage associated with the potential approach includes its better convergence behavior than for the case of the magnetic approach.

## **Section 2.2.2: Bowman Experimental Information**

Despite the fact that welding arcs represent good testing cases, for the arc model, the process does not meet some basic aspects of real DC-EAF arcs. The main differences include the gas atmosphere and the order of magnitude of the process parameters, such as the arc currents and arc lengths.

The work reported by Bowman [20] represents the only experimental study that describes the jet structure of free-burning arcs in air under relatively high currents and arc lengths, in comparison to those used in welding. In his paper, Bowman employed the called “ball-bearing deflection technique” in which a box with holes stands above an air free-burning arc horizontally positioned. The arc runs from a 5 cm graphite cathode electrode to a 15 cm graphite anode plate. Balls (3, 4 or 5 mm in diameter) are dropped through the horizontal arc and the horizontal deflections of the balls are recorded by allowing them to strike a carbon paper. From the deflection distributions, drag coefficients were determined and radial plasma velocity profiles were calculated using iterative techniques.

### **Section 2.2.2.1: Comparison of Model Predictions with Experimental Measurements by Bowman**

Bowman reported three experimental cases: The arc length was set to 7 cm and three different arc currents were employed: 520 A, 1150 A and 2160 A. The currents and arc lengths are much higher than those used in the welding cases previously presented. Therefore, turbulence effects are expected to be present in these measurements, and thus, the model presented in section 2.1 applies to this situation.

Figure 2.2.6 (a) shows contour plots for velocity and temperature, while Figure 2.2.6 (b) presents turbulent viscosity and magnetic flux density fields for an arc of 2160 A and 7 cm of arc length. The interesting point to be stressed here, is the effect that turbulence has on the velocity and temperature fields. Turbulence enhances mixing between the hot gases inside the arc and the cold gases outside the arc. Mixing phenomena expands the jet and this explains why velocities near the anode are much slower due to this jet expansion. Mixing is enhanced at the impingement zone where maximum turbulent viscosity is found.

Figures 2.2.7(a) to 2.2.7(c) show measured and predicted axial velocity profiles in the radial direction at three different distances from the cathode (2 cm, 3.8 cm and 5.5 cm), for a 520 A arc current, while Figure 2.2.7 (d) shows the axial velocity along the symmetry axis. In general, a good agreement is observed between experiments and predictions, although the model predicts slightly higher values of axial velocities, particularly in the center of the jet.

Figures 2.2.8 (a) -2.2.8 (c) present experimental and predicted radial profiles of axial velocities predicted at 2, 3.8 and 5.5 cm from the cathode for an arc with a current of 1150 A. The agreement between measurements and predictions is even better than in the previous case. Figure 2.2.8 (d) shows the corresponding axial velocity profile along the symmetry axis for the same arc together with the experimental data. As seen in the figure, the agreement between experimental data and the predictions is very good.

Finally, the same plots are shown in Figures 2.2.9 (a) - 2.2.9 (d) for a 2160 A arc. Here, the radial profiles are well predicted close to the cathode but significant departure is observed at larger distances. A closer inspection of the axial velocity profile at the symmetry axis, indicates that the model over predicts the measured velocity values. Probably, the less accurate predictions in this case are due to higher turbulence effects in comparison with cases with lower arc currents. Turbulence may become important at 2160 A of current. In fact, transition between laminar to turbulent regime is expected to occur at this arc current according to the Reynolds criteria for free jets. Then, below 2160 A, a laminar flow regime may be expected. The over prediction close to the anode in the velocity profile shown in Figure 2.2.9 (d) can be explained due to the very well known complexity in representing any laminar to turbulent transitional flows. However, it should be noted that the experimental data may have significant error due to the unsophisticated measuring technique employed in the experimental work. Another source of error is the drag correlation employed to estimate velocities both, experimental and predicted.

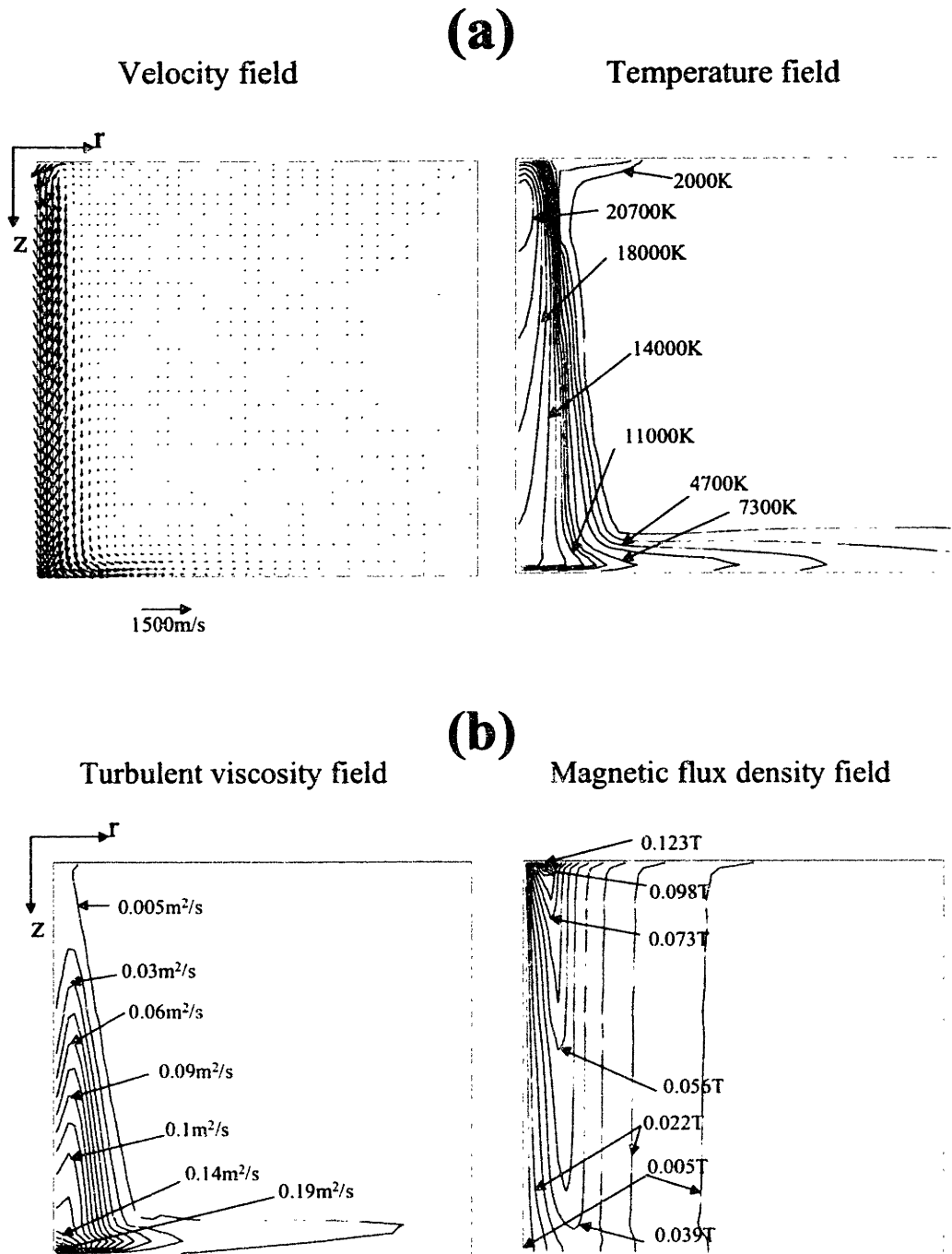


Figure 2.2.6 Computed fields for an electric arc with 2160 A and 7 cm arc length as in Bowman experiments. (a) Velocity and Temperature fields. (b) Turbulent kinematic viscosity and magnetic flux density fields.

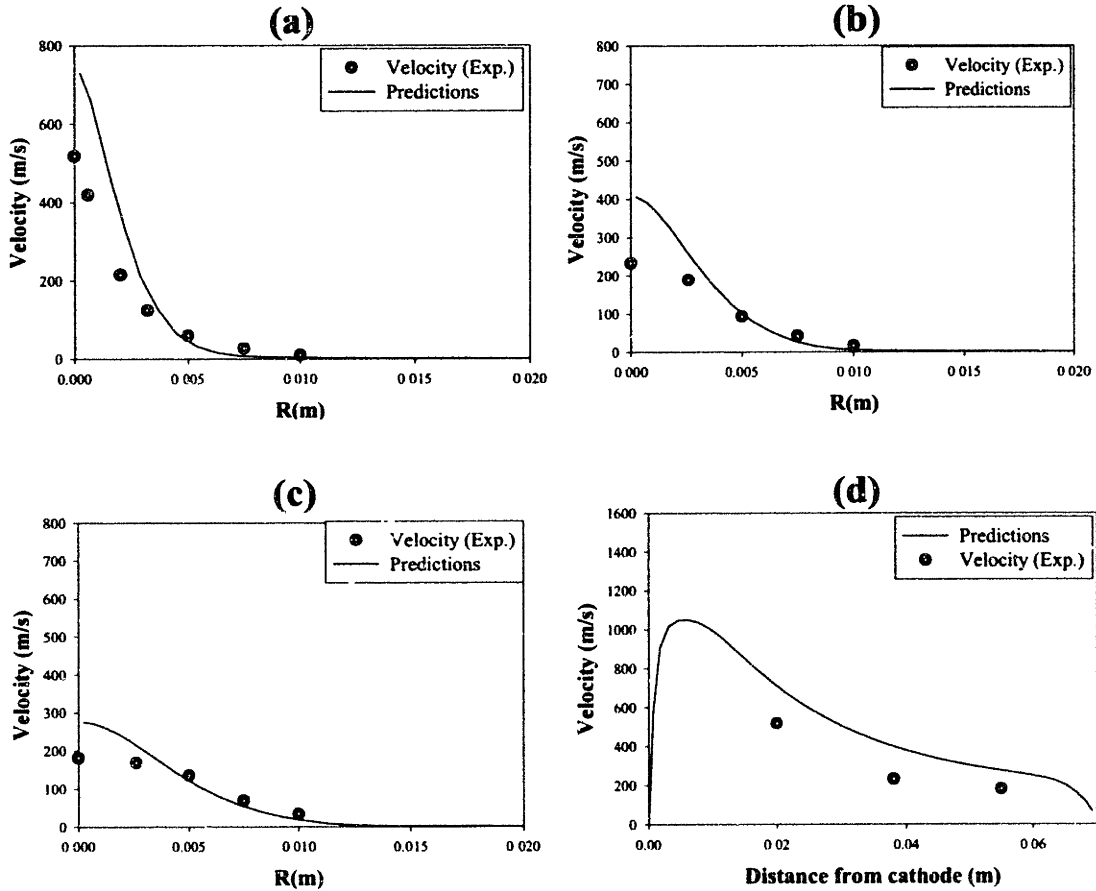


Figure 2.2.7 Comparison between simulations and experimental measurements by Bowman for a 520 A and 7 cm electric arc in air. Radial profiles of axial velocity at (a) 2 cm, (b) 3.8 cm and (c) 5.5 cm from cathode. (d) Axial velocity profile along the symmetry axis.

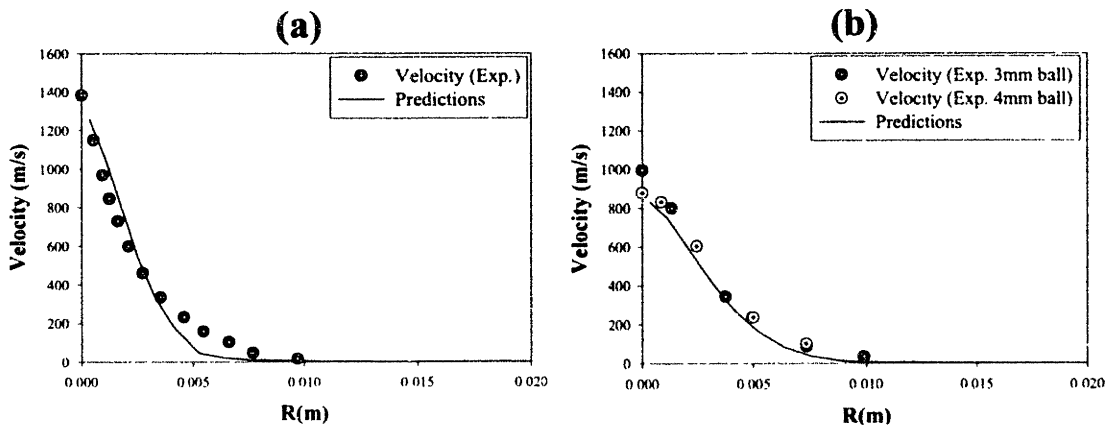


Figure 2.2.8 Comparison between simulations and experimental measurements by Bowman for a 1150 A and 7 cm electric arc in air. Radial profiles of axial velocity at (a) 2 cm, and (b) 3.8 cm from cathode.

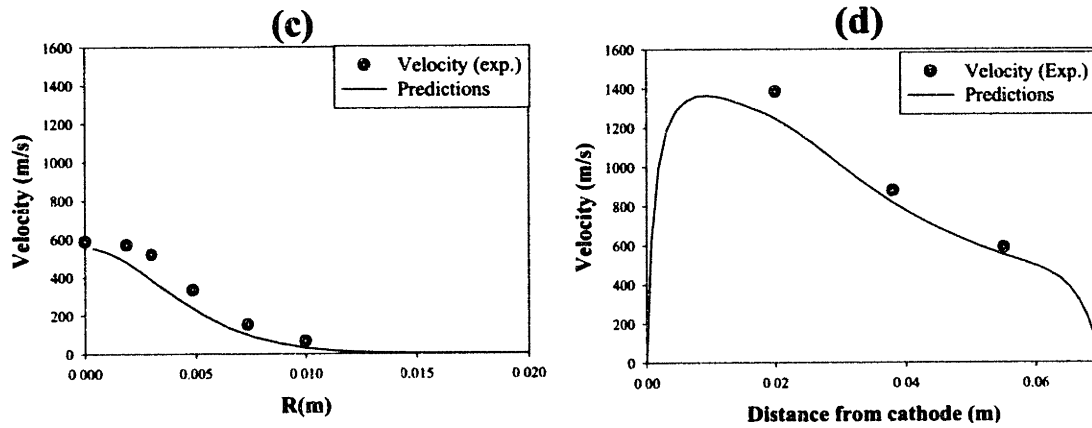


Figure 2.2.8 (cont.) Comparison between simulations and experimental measurements by Bowman for a 1150 A and 7 cm electric arc. (c) Radial profile of axial velocity at 5.5cm from cathode. (d) Axial velocity profile along the symmetry axis.

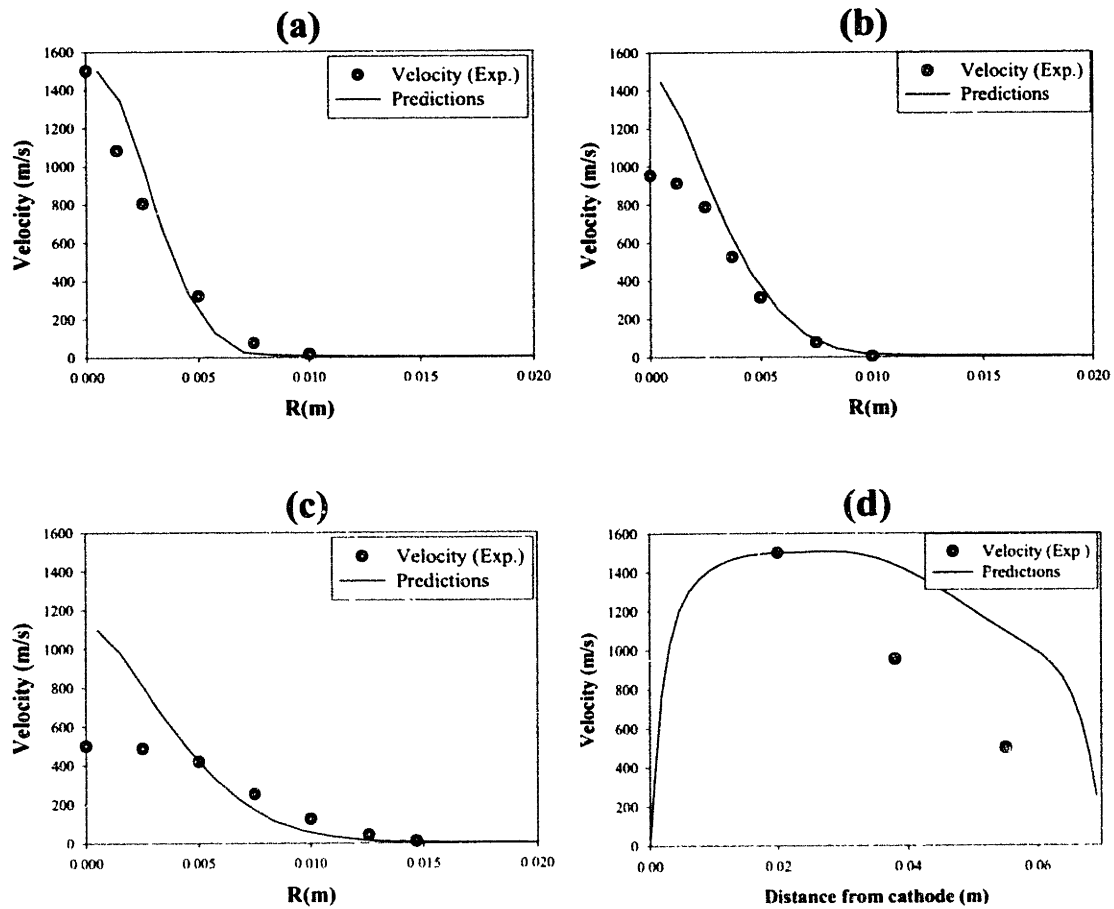


Figure 2.2.9 Comparison between simulations and experimental measurements by Bowman for a 2160 A and 7 cm electric arc. Radial profiles of axial velocity at (a) 2 cm, (b) 5.5 cm, and (c) 3.8 cm from cathode. (d) Axial velocity profile along the symmetry axis.



## Section 2.3: Arc Results

Arc results are presented in this section based on the mathematical representation of the arc region described in section 2.1. A numerical study should explore the effect of resolution grid on computation results, then, the first part of this section is devoted to present a grid sensitivity study. Following the grid sensitivity, the arc characteristics and extensive discussion on the physics of the arc region is presented for a standard case of an electric arc with 40 KA of current and 25 cm arc length. This arc represents an intermediate condition between low and high values of current and arc lengths considered in this study. Individual effects are subsequently analyzed, including the sensitivity of some of the most important simplifying assumptions used in the arc model on the arc characteristics, i.e. compressibility effects, effect of bath temperature, effect of induced currents, effect of cathode current density and turbulent effects. Finally, the process is analyzed based on a parametric study of the two main parameters of the process: arc length,  $L$ , and arc current,  $I$ . This analysis summarizes the main findings obtained in the arc modeling work.

### Section 2.3.1: Grid Sensitivity

In order to test the effect of the grid size on the arc results, three different non-uniform 2-D grids in cylindrical coordinates were compared, 30x30, 34x34, and 38x38 in the r-z plane for a system with 40 KA arc current and 0.25 m arc length.

The critical region in the computational domain is the cathode spot where most of the convergence problems were detected. In this region, a good grid resolution is required to describe properly the different phenomena occurring in the vicinity of the cathode, which determine the behavior in the rest of the arc column. However, using too many cell points has a negative effect because it makes the problem very difficult to converge and substantially increases the CPU time requirements. Figure 2.3.1 shows results of radial profiles of magnetic flux density along the cathode spot for the grids tested. The arc conditions for these calculations correspond to the standard case ( $I = 40$  KA and  $L = 0.25$  m). At the cathode spot, 5, 6, and 7 cells are accommodated for the 30x30, 34x34 and 38x38 grids, respectively. As seen in the figure, the magnetic flux density field increases with radial distance until reaching a maximum at the spot radius. Similar trends can be seen for all grids. A coarser grid (30x30) is unable to define the boundary conditions for the magnetic flux density,  $B_{\theta}$ , especially close to the symmetry axis where  $B_{\theta}$  should be zero. In contrast, grids with 34x34 and 38x38 nodes define the cathode spot regions with good accuracy (i.e., extrapolation to the origin).

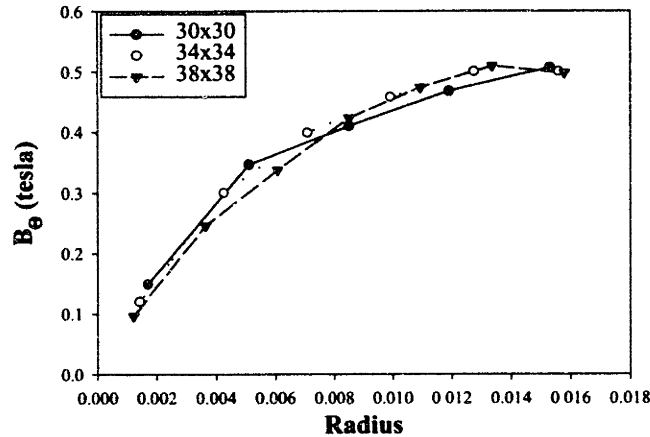


Figure 2.3.1 Computed magnetic flux density profile along the cathode spot for three different grids.

In order to describe the effect of the grid on some arc characteristics in the arc column, Figure 2.3.2 shows comparisons of velocity (a), temperature (b), pressure (c) and current density (d) profiles along the symmetry axis for all grids used. Velocities (Figure 2.3.2 (a)) are similar in all cases, but it can be seen that with a coarser grid the vicinity of the cathode and bath regions are not sufficiently resolved. Also coarser grids predict a slightly lower maximum velocity but higher overall axial velocities along the axis. Finer grids present a similar trend for velocity along the axis. Temperature profiles along the axis are shown in Figure 2.3.2 (b) where significant differences in the predictions near the cathode are found for the three grids. Coarser grids present colder cathode surfaces, which changes as the grid resolution increases. Pressure and Current density fields at the symmetry axis (Figures 2.3.2 (c) and 2.3.2 (d)) present similar trends in the grid sensitivity study. Coarser grids predict low pressures and current densities along the axis and close to the cathode where the strongest differences are appreciated while close to the bath surface all grids predict the same values.

Other important issues deserving closer inspection regarding grid sensitivity involve the accuracy in the prediction of the arc-bath interactions at the bath surface. Figure 2.3.3 presents a comparison of predictions for arc pressure, current density, and shear stress for all grids examined, considering the same standard arc. The predicted current density at the bath surface presents similar behavior for the three grids and no major differences are observed. Pressure plots at the bath surface also present similar trends, except at the symmetry, where differences in the maximum values are appreciable at center. Finally, the maximum values of the shear stress decrease, as the grid becomes finer. This trend can be explained since a better resolution of the velocity field in the vicinity of the bath surface is obtained with finer grids. This resolution allows a better representation of the fluid flow adjacent to the bath. This final plot clearly illustrates how the lack of grid resolution can introduce significant errors in the calculations.

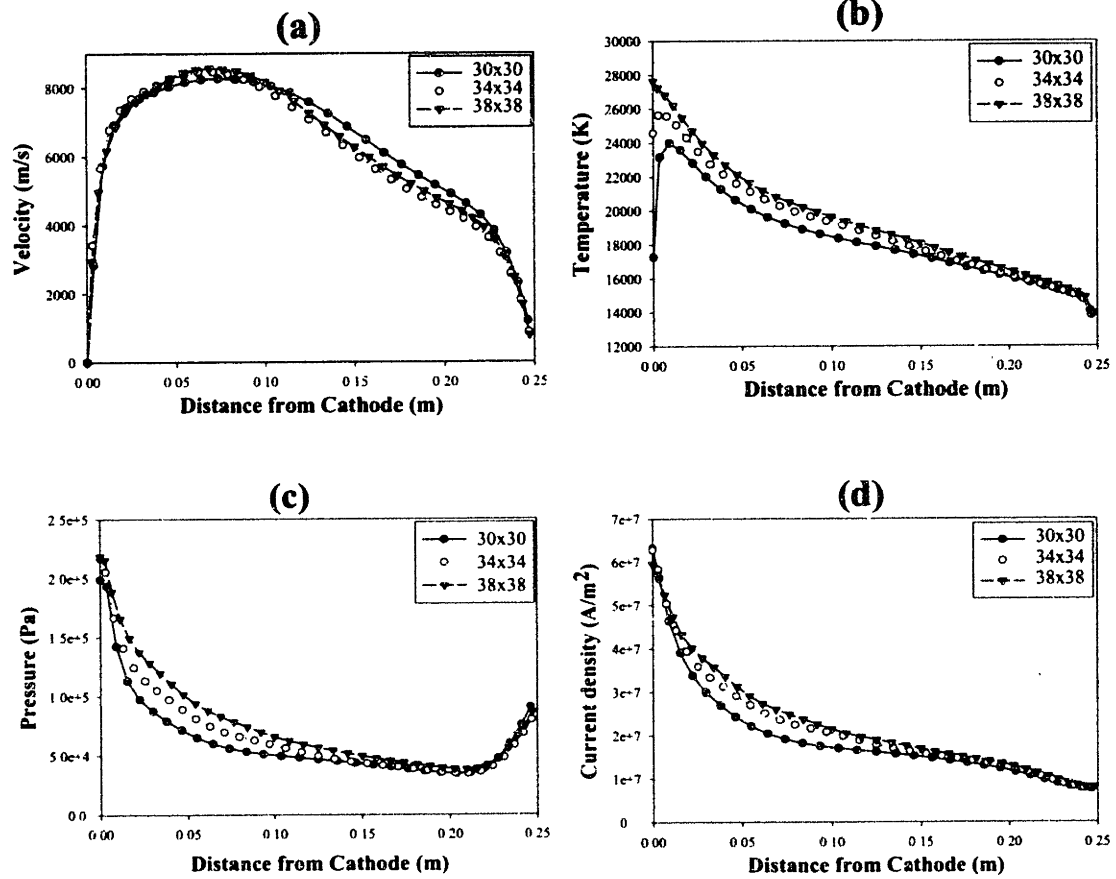


Figure 2.3.2 Grid sensitivity: (a) axial velocity along the axis; (b) temperature along the axis; (c) arc pressure along the axis; and (d) current density along the axis.

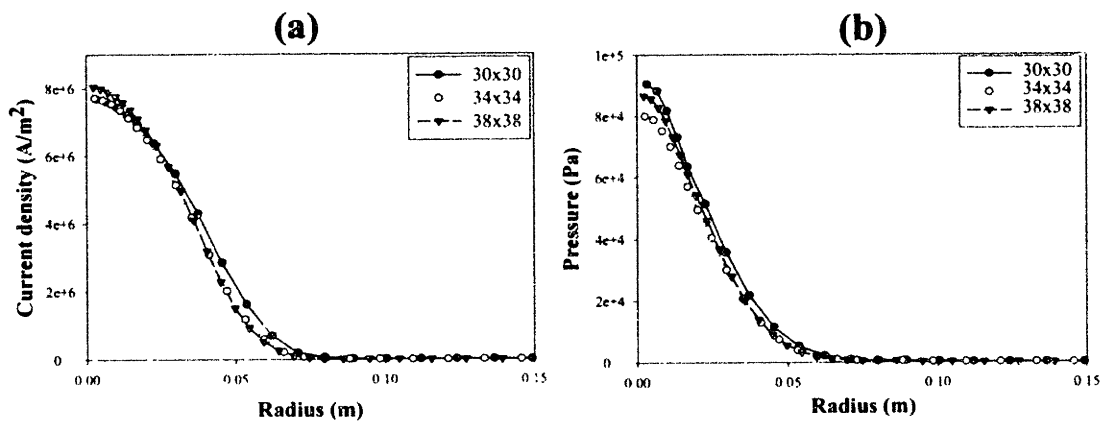


Figure 2.3.3 Grid sensitivity: (a) current density at the bath surface; (b) pressure profile at the bath surface.

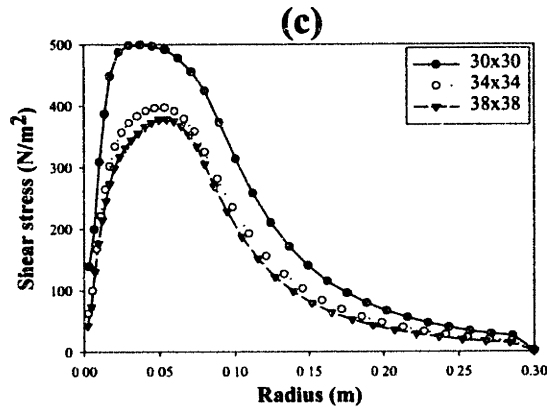


Figure 2.3.3 (cont.) Grid sensitivity: (c) shear stress at the bath surface.

### Section 2.3.2: Physics Involved in the Arc Process Based on the Standard Case (40 KA Arc Current and 0.25 m Arc Length)

In this section, a detailed description of an electric arc will be presented based on results from the model. Physics of the arc can be fully described by analyzing each variable field, individually, and connecting them through their coupling in the governing equations that describe the system. In this way, the field for a single variable is a consequence of the rest of the variables due to the high coupling between them. Then, all fields are necessary for a coherent description of the arc.

Figure 2.3.4 shows computed velocity (a) and pressure (b) fields for the standard case. The jet formed in the cathode region and directed towards the bath can be explained by observing the pressure field shown in the same figure. Close to the cathode region a high-pressure zone is developed to counterbalance high electromagnetic body forces acting in that region and, as a consequence, a high velocity jet is developed and directed towards the bath. The jet expands due to turbulent mixing with entrained fluid along the edge of the jet. The jet travels from a high-pressure zone at the cathode to a low-pressure zone in the arc column, but when it reaches the bath, a second high-pressure zone is generated as jet impinges onto the bath surface. The impingement effect forces gas to flow in the radial direction, parallel to the bath surface. Figure 2.3.4 (c) shows the velocity profile along the symmetry axis. The velocities rapidly rise from zero at the cathode to a maximum of approximately 8500 m/s, 10 cm from the cathode. Then, velocity decreases due to the jet expansion until it reaches a zero value at the bath surface. The pressure profile along the symmetry axis is shown in Figure 2.3.4 (d), where the two high-pressure zones developed at the cathode and anode regions are clearly seen. A pressure value at the cathode is of the order of  $2.2 \times 10^5$  Pa (~ 2 atmospheres) and at the bath is about  $1.2 \times 10^5$  Pa (~ 1 atmosphere).

Figure 2.3.5 shows the potential (a) and current density (b) fields for the same standard case. The electric potential is derived from the charge conservation requirement, i.e. directly from the current density components. The potential depends on the electric conductivity of the gas, which in turn is affected by the temperature, velocity, and magnetic flux density fields. Furthermore, the current density depends on the applied potential and also on the induced currents generated as the gas flows:

$$\vec{J} = -\sigma(\underbrace{\nabla^{app} \varphi}_{\text{applied}} + \underbrace{\nabla^{ind} \varphi}_{\text{induced}} - \vec{V} \times \vec{B}) \quad (\text{eq. 2.3.1})$$

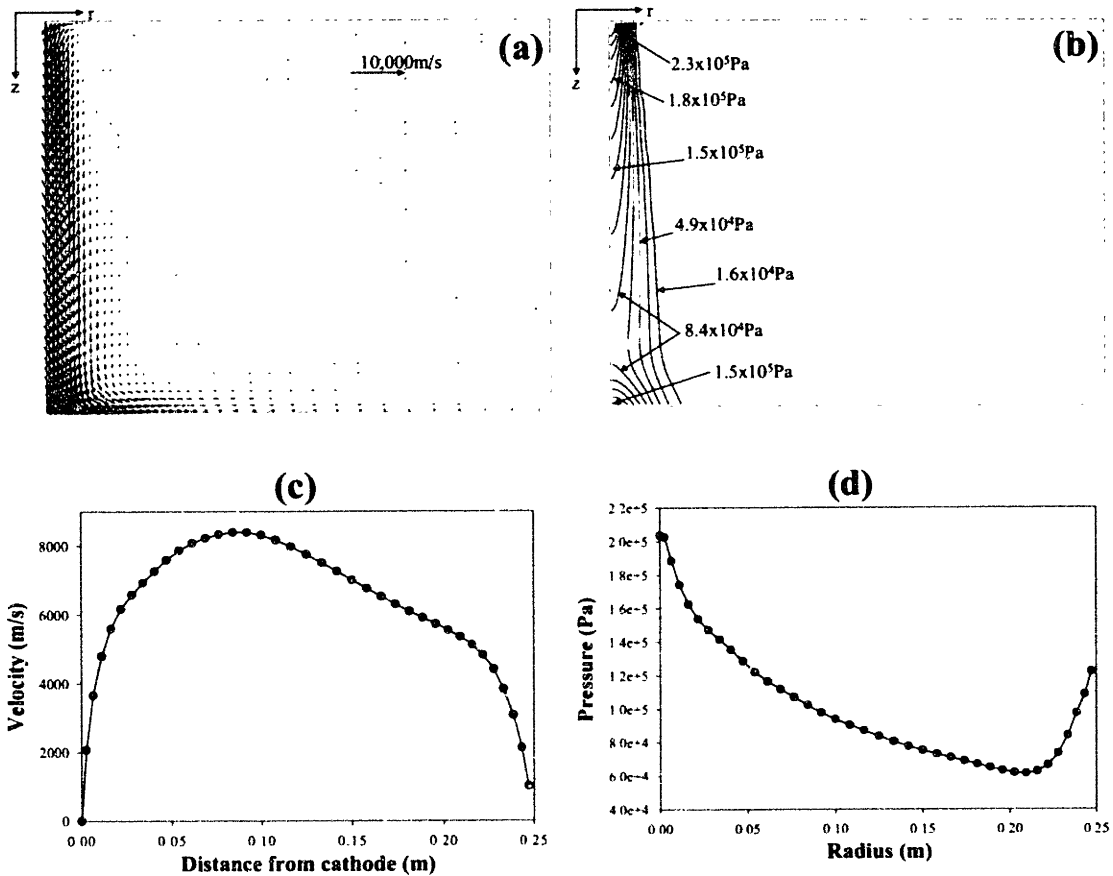


Figure 2.3.4 Computed results for the standard electric arc (40 KA arc current and 0.25 m of arc length). (a) Arc velocity field; (b) Arc pressure field; (c) Axial velocity along the symmetry axis; (d) Pressure distribution along the symmetry axis.

In our calculations, one of the two components of current comes from the total gradient and was obtained as:

$$\vec{J} = -\sigma(\nabla^{app} \varphi + \nabla^{ind} \varphi) \quad (\text{eq. 2.3.2})$$

this contribution to the current can be expressed physically as vectors always pointing normal to the potential lines illustrated by the vector field presented in Figure 2.3.5 (c). In contrast, the current density term, due to the cross product  $\nabla \times B$ , can be observed in Figure 2.3.5 (d). It can be appreciated that, close to the bath and cathode surfaces, induced currents are predominant in the axial direction, while in the arc column and close to the symmetry line these induced currents are predominantly aligned in the radial direction. The reason for the form of this induced current field can be explained by analyzing each component of the induced currents:

$$J_r = \sigma v_z B_\theta \quad (\text{eq. 2.3.3a})$$

$$J_z = -\sigma v_r B_\theta \quad (\text{eq. 2.3.3b})$$

As indicated by equation 2.3.3b, the axial component of induced current is proportional to  $v_r$  and then, close to the bath and cathode surface, the velocity is preferentially directed in the radial direction. However, close to the cathode, the radial velocity is negative (see Figure 2.3.4 (a)) and hence induced currents point towards the bath. In contrast, in the vicinity of the bath, the radial velocity is positive (see Figure 2.3.4 (a)), which explains the axial induced current densities pointing towards the cathode, as shown in Figure 2.3.5 (d). Employing the same reasoning, the radial vector of the induced currents found in the arc column are a consequence of the high axial velocities found close to the symmetry axis. The radial induced current densities are proportional to the axial velocity,  $v_z$ , as indicated by equation 2.3.3a.

The sum of the two components of current density shown in Figures 2.3.5 (c) and 2.3.5 (d), respectively, results in the total current density field shown in Figure 2.3.5 (b).

Another important characteristic of the potential field is that it can be used to define the arc shape. The arc region can be defined as the region where conduction of current takes place. As seen in Figure 2.3.5 (a), the shape of the electric potential field shows a region of nearly horizontal iso-potential lines close to the symmetry axis, which change slope and become nearly vertical lines. The extension of the horizontal lines increases as the distance from the cathode increases due to expansion of the arc. Since the current density vectors are normal to the potential lines, the axial components of current are located along these horizontal lines. By inspection of the potential values, it is clear that potential gradients decrease with distance from the cathode (leading also to an axial current density decrease). Vertical iso-potential lines indicate that no axial components are present. Moreover, due to lower temperature values in those regions (as will be shown in Figure 2.3.7 (a)) and consequently low electric conductivities, radial components of current density are also expected to be small. Vertical iso-potential lines are more evident close to the cathode, where the arc region is better defined. As the distance from the cathode increases, verticality of the potential lines changes due to arc expansion. Close to the anode, however, the lines become almost horizontal. The region with horizontal lines can be considered as the conductive region of the arc.

Therefore, if the ends of the horizontal iso-potential lines in Figure 2.3.5 (a) are connected, the shape of the arc can be defined, which is the same shown in Figure 2.3.5 (b) for the arc current density field. Figure 2.3.5 (e) shows radial profiles of axial current density at four different axial positions (5, 12.5, 20 cm from the cathode and at the bath surface). The arc expansion is evident from this figure, where a narrow distribution of axial current density is defined close to the cathode, and wider distributions are observed as the distance from the cathode increases. Consequently, arc current densities are higher close to the cathode and decrease as the distance from the cathode increases.

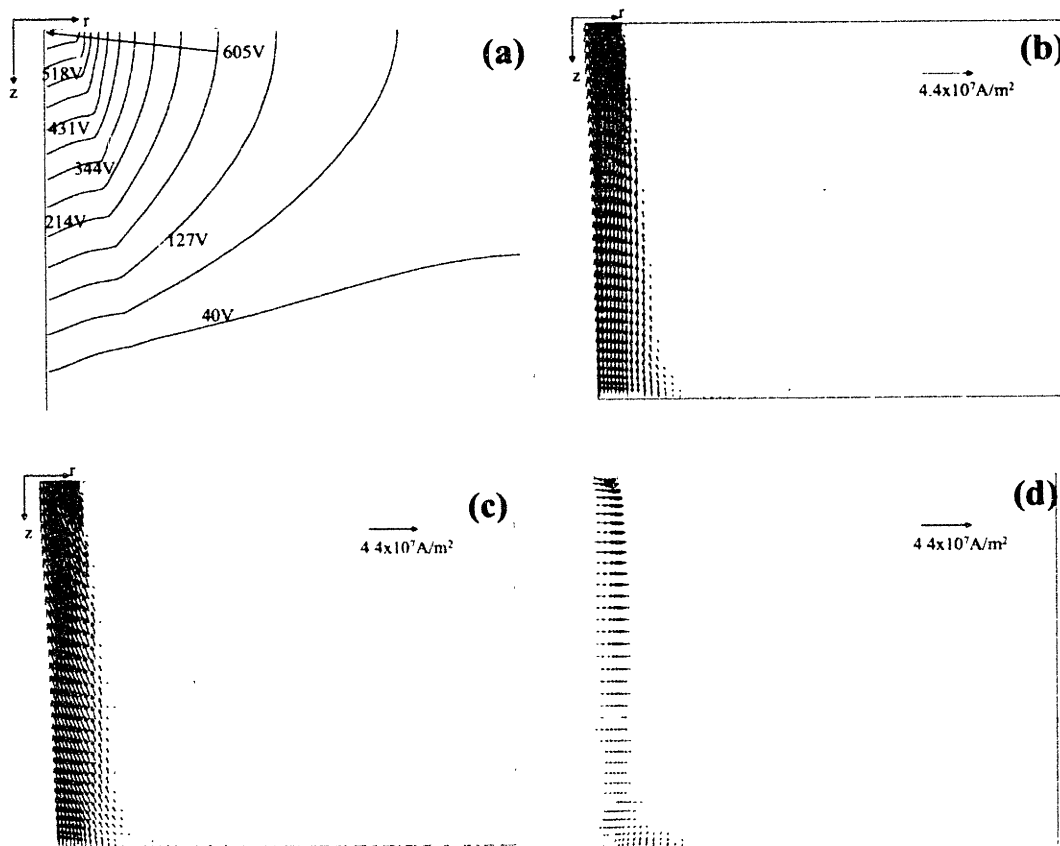


Figure 2.3.5 Computed results for the standard electric arc (40 KA arc current and 0.25 m arc length). (a) Potential field. (b) Total current density field. (c) Potential derived current density field. (d) Induced current density field.

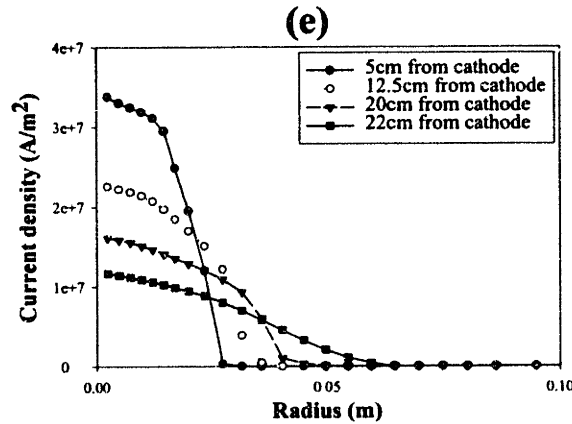


Figure 2.3.5 (cont.) Computed results for the standard electric arc (40 KA arc current and 0.25 m arc length). (e) Axial current density profiles along the radius at 5, 12.5 20 and 22 cm from cathode.

Figure 2.3.6 shows predictions of the magnetic flux density (a) and electromagnetic body force (b) fields. The magnetic flux density is an important electric quantity because it is required to compute the body force field (by the cross product  $J \times B$ ), which drives the jet flow. The magnetic flux density field is derived from integration of Ampere's law, assuming that the current density is predominantly directed in the axial direction (equation 2.1.16). Examining Ampere's law, two terms can be recognized in that equation: The radial integral, which is proportional to the total arc current, and the factor  $1/r$  outside the integral. Maximum values of the magnetic flux density are calculated close to the cathode (0.53 tesla), and they decrease as the distance from the cathode increases. The reason for the decrease in these values is due to the expansion of the arc radius. Although the total current is conserved and therefore the integral has the same value, the factor  $1/r$  in Ampere's law gives a smaller magnetic flux density value as the arc radius increases with increasing distances from the cathode. The magnetic flux density field gives also an indication of the arc shape. Figure 2.3.6 (c) shows radial magnetic flux density profiles at 5, 12.5, 20 cm from the cathode and at the bath surface. The magnetic flux density values start from zero at the symmetry axis, reach a maximum, and then decrease rapidly with increasing radial distances. The maximum is located at the edge of the conduction region (i.e., the arc radius position). Farther from the maximum, the radial profiles decrease because the integral has reached the same maximum value (total arc current value), but the factor  $1/r$  decreases with radial distance. Therefore, the rate of decrease for the magnetic flux density field in such region is proportional to  $1/r$ . Since the location of the maximum magnetic flux density defines the arc radius, a line can be drawn connecting the maximum points in the  $B_\theta$  field (Figure 2.3.6 (a)) to determine the shape of the arc. In this way, the magnetic flux density field also gives a physical representation of the arc shape, similar to the potential and current density fields (based on the electric conduction zone).



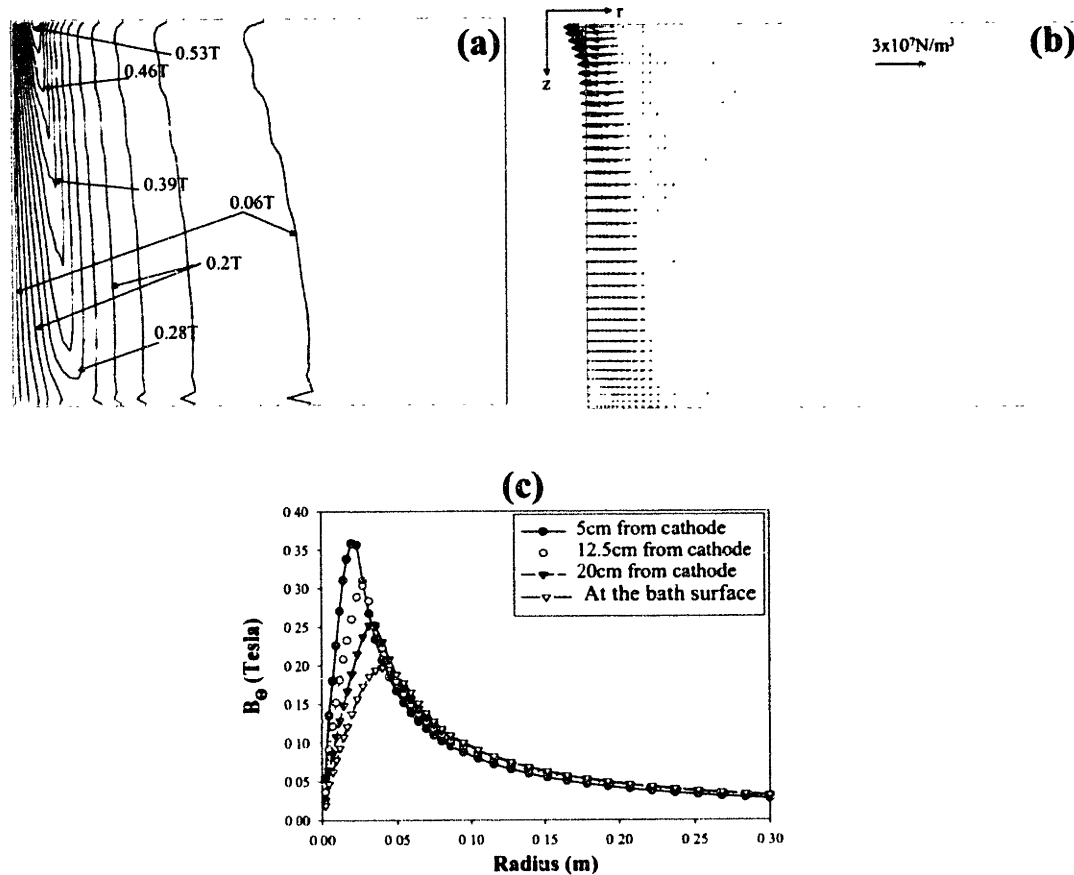


Figure 2.3.6 Computed results for the standard electric arc (40 kA arc current and 0.25 m arc length). (a) Magnetic flux density field,  $B_\theta$ ; (b) Electromagnetic body force vector field; (c)  $B_\theta$  radial profiles at 5, 12.5, 20 cm from cathode and at the bath surface.

As seen in Figure 2.3.6 (b), the body forces are predominantly aligned in the radial direction due to a predominantly axial current density flow. Values of electromagnetic body forces are maximum close to the cathode due to maximum current and magnetic flux density values (see Figure 2.3.6 (a) and 2.3.5 (b)). As the distance from the cathode increases, current density vectors and magnetic flux density values decrease and therefore electromagnetic body forces also decrease. However, despite the fact that the maximum current densities are at the symmetry axis, maximum forces are not since the magnetic flux density is zero at the symmetry. Thus, maximum forces are located between the symmetry axis and the arc radius. The large electromagnetic force vectors found close to the cathode are responsible for the high-pressure zone developed there as shown in Figure 2.3.4 (b). However, expansion of the electric arc is important in developing the jet flow. If the arc would not expand, no radial currents would appear, and iso-cylindrical magnetic flux density and current density fields would be obtained. Consequently, the pressure field would also be composed of iso-pressure cylinders that would not be able to generate the jet. In other words, the jet forms due to arc expansion. This arc expansion decreases axial current densities, magnetic flux density and even more important, decrease the body forces. Then, pressure decreases as the distance

form the cathode increases, so the jet flow is possible since a low pressure zone is formed just below the cathode generating the pressure gradients to drive the flow.

Figure 2.3.7 (a) shows the predicted temperature field for the standard case. Close to the cathode, maximum temperatures around 27000 K are present, but as distance from the cathode increases temperatures decrease as shown in Figure 2.3.7 (b). Therefore, Joule heating effects associated with the large current densities close to the cathode are responsible for these high temperatures. Shape of the temperature contours shows that convection plays a key role as a heat transfer mechanism. Close to the symmetry axis and also close to the bath surface, the isotherms follow the fluid flow patterns of the gas. However, convection is not enough to dissipate the large amount of Joule heat generated in the arc column, and radiation has to be taken into account as a heat releasing mechanism. In terms of an overall energy balance, the arc power (considered to be equal to the product  $I \times V$ ) is balanced by all mechanisms of heat dissipation described in the model formulation.

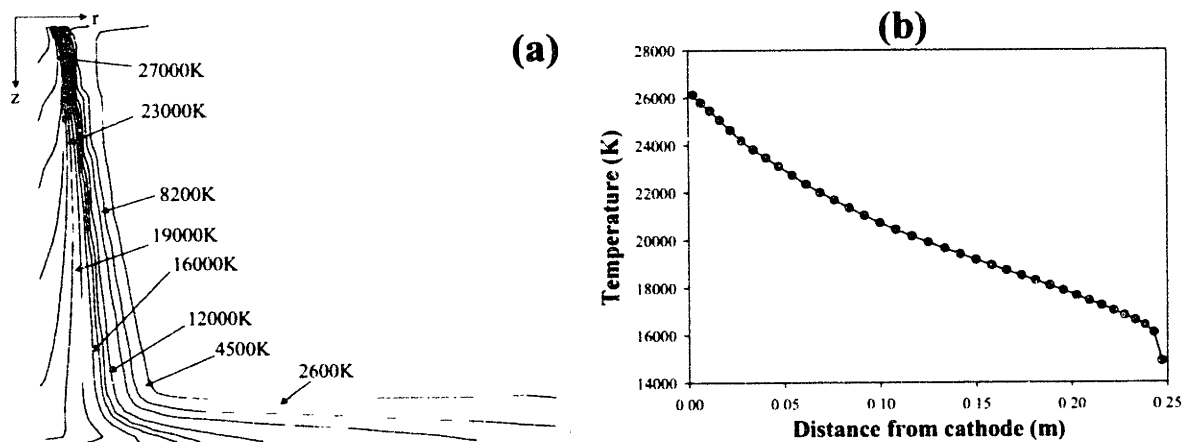


Figure 2.3.7 Computed results for the standard electric arc (40 KA arc current and 0.25 m arc length). (a) Temperature field; (b) Temperature distribution along the symmetry axis.

Figure 2.3.8 shows predicted fields of various physical properties of the arc, such as kinematic viscosity 2.3.8 (a), density 2.3.8 (b), and electric conductivity 2.3.8 (c) for air gas. These properties are exclusively function of temperature. Examining Figures 2.3.7 (temperature field) and 2.3.8 it is evident the similarity between the contours of the properties and the temperature contours. The contours of physical properties follow the temperature distributions and its specific relation with temperature is indicated by their temperature dependence reported in Figure 2.1.3. The kinematic viscosity is defined as the ratio of laminar viscosity over density. Viscosities are low at low temperatures and increase until reaching a maximum at 10000 K and then decreases with increasing temperature. The maximum kinematic viscosities are found along the 10000 K isotherm, which is also considered as the limit to the visible arc radius. Then, inside and outside the arc region, smaller viscosities are found. Densities are extremely low inside the arc

(regions where temperatures are above 10,000 K) but, outside the arc, the density can be at least two order of magnitude higher than in the arc column. The electric conductivity is an important physical property since its values define the conduction zone. At approximately 8000 K the electric conductivity has values close to zero and increases rapidly with temperature; however, at about 10,000 K or 11,000 K the conductivity are high enough to allow conduction of electric current. The electric conductivity increases with temperature until it reaches a plateau at 25,000 K where it remains constant at approximately  $12500 \Omega^{-1} \text{m}^{-1}$ . Close to the cathode, the highest electrical conductivities are found due to the region of maximum temperatures in the arc. As the temperature of the gas decreases towards the bath, the electric conductivity decreases. This effect of having a worst conductor as the distance from the cathode increases, is a further indication of the arc expansion leading to smaller current density vectors.

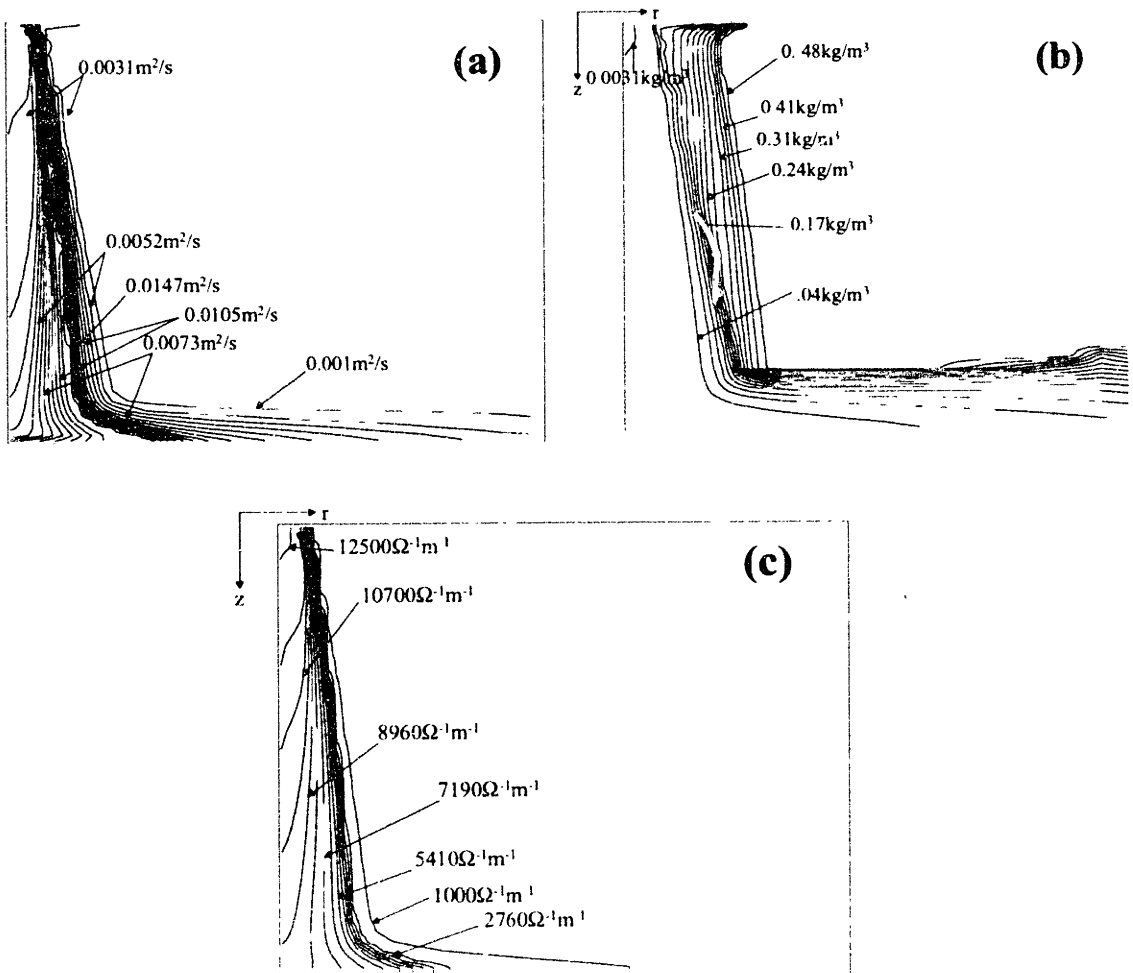


Figure 2.3.8 Computed results for the standard electric arc (40 kA arc current and 0.25 m arc length). (a) Kinematic viscosity; (b) Density; (c) Electric conductivity.

Finally, Figure 2.3.9 shows contour fields of turbulent parameters predicted for the standard conditions. The turbulent kinetic energy,  $k$ , the energy dissipation rate,  $\varepsilon$ , and the turbulent kinematic viscosity,  $\nu_t$ , are shown in Figure 2.3.9 (a), (b) and (c) respectively. The turbulent kinetic energy and the energy dissipation rate show two regions of interest regarding turbulence characteristics. The first region is in the well-developed arc jet far from the cathode while the second region is along the bath surface associated with the jet impingement. The shape of the contours for these two turbulent parameters also reflect the arc expansion. In fact, turbulence promotes mixing between cold gas outside the arc and hot gases inside the arc resulting in gas entrainment that expands the jet. The turbulent kinematic viscosity, being a function of  $k$  and  $\varepsilon$ , shows similar trends as these two variables. It is noted that viscosity values in some zones in the arc are about three orders of magnitude greater than laminar viscosities. Thus, mixing promoted by turbulence is significantly enhanced inside the arc and close to the impingement zone.

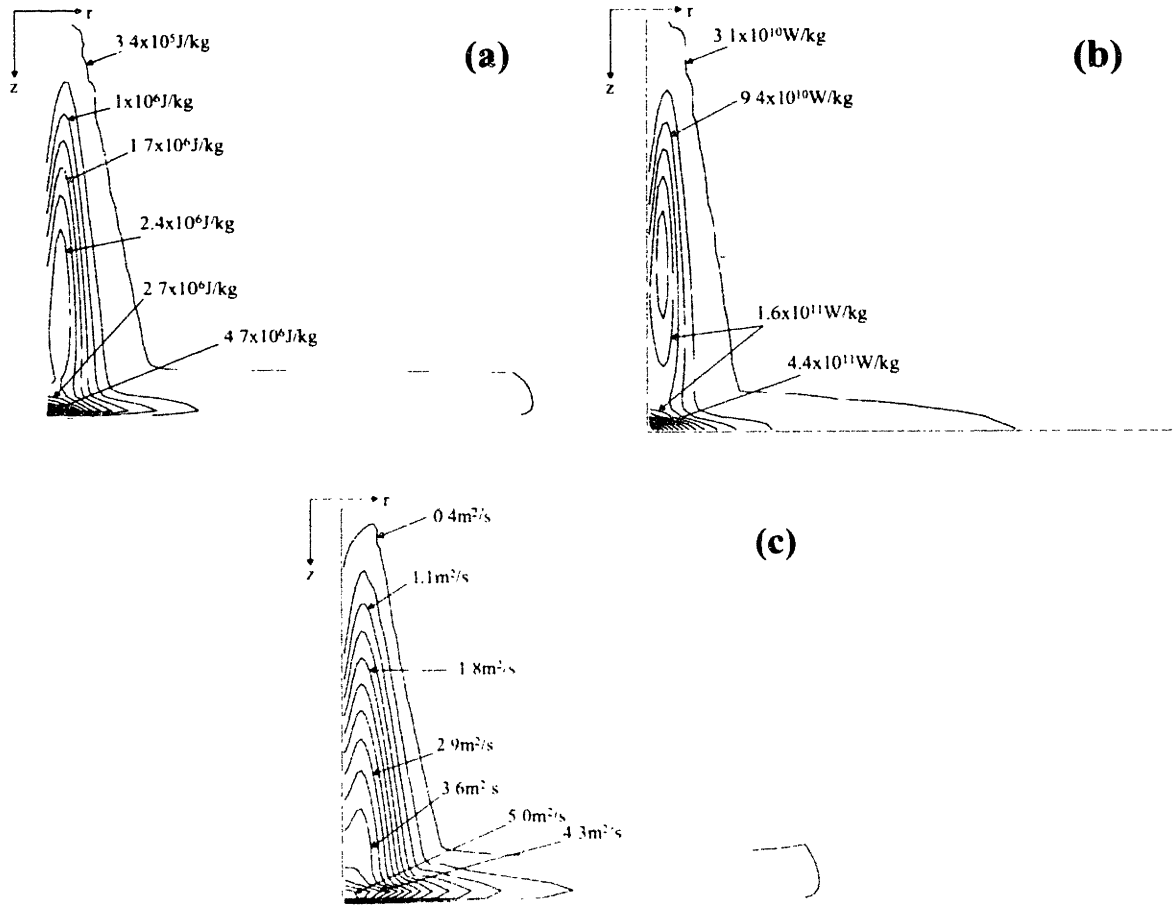


Fig 2.3.9 Computed results for the standard conditions (40 KA arc current and 0.25 m arc length) (a) Turbulent kinetic energy; (b) Turbulent energy dissipation rate; (c) Turbulent kinematic viscosity

The main objective in representing the arc characteristics is to be able to estimate arc-bath interactions, which allow the bath region to be represented under the influence of the arc. Arc-bath interactions represent the arc influence on the bath region at the arc-bath interface.

Computed arc-bath interactions for the bath representations are shown in Figure 2.3.10, where current density (a), heat fluxes (b), cumulative heat flow (c), shear stress (d), arc pressure (e) and temperature (f) at the bath surfaces are presented.

The current density at the bath shows a Gaussian like distribution with a maximum value of  $\sim 8.0 \times 10^6 \text{ A/m}^2$  for the standard case. The current distribution extends up to  $\sim 8 \text{ cm}$  in the radial direction. It is noted that at the cathode the spot radius (with a  $J_c$  of  $4.4 \times 10^7 \text{ A/m}^2$  and arc current of 40 KA) is around 1.7 cm. This means that arc expands almost 5 times from cathode.

Heat flux from the arc to the bath (Figure 2.3.10 (b)) is composed by different contributing mechanisms, as was explained in section 2.1.5. These mechanisms, expressed by equations 2.1.26 to 2.1.30, are convection, anode fall and condensation of electrons, Thompson effect, and radiation. From the figure it is seen that electronic mechanisms have a significant contribution to the heat transfer to the bath close to the symmetry axis, but they are unimportant beyond 10 cm from the center. In contrast, convection and radiation are the most widely distributed mechanisms for the whole radial distance, but convection is always higher than radiation along the entire radius of the bath, at least for the standard arc case. The total heat flux at the anode resulting from the additive effects of all mechanism considered has also a Gaussian-like shape (as in the current distribution) presenting maximum values at the axis. The heat transfer from the arc can be better understood by integrating the heat flux over the entire bath area. This integration constitutes the cumulative heat flow representation presented in Figure 2.3.10 (c) along the radius. In this plot, convection, electronic (anode fall, condensation of electrons and Thompson effect) and radiation contributions, as well as the total heat flow, are shown in cumulative form. From this plot, convection is the major heat transfer mechanism, followed by radiation and then the electronic with the smallest heat contribution. As mentioned above, electronic is the biggest contribution near the center but, since the current is concentrated in a small circle, the other two mechanisms (radiation and convection) end up as major contributors to heat flow. In a circle bath area with 0.3 m in diameter, almost 3 MW are transferred from the arc to the bath for heating purposes.

The shear stress at the anode presented in Figure 2.3.10 (d) has a zero value at the center but increases rapidly until it reaches a maximum value of  $\sim 450 \text{ N/m}^2$  at  $\sim 7 \text{ cm}$  from the center. Following the maximum, a continuous decrease in the shear stress is observed. The shape of the shear stress curve is related to the radial gas velocity, which is zero at the center and increases as the jet is deflected at the impingement point (see Figure 2.3.4 (a))

The pressure profile at the anode also shows a Gaussian distribution along the radius as seen in Figure 2.3.10 (e). More than 1 atmosphere is predicted at the center. This value is extremely high and would create a big surface depression on the steel bath, which is not considered in the model. It has been documented that arc instabilities are present in the actual process that have the effect of dispersing the arc thrust and this high pressure should actually be much lower because of the dispersion.

Finally, the temperature profile at the bath is presented in Figure 2.3.10 (f). As seen in the figure, the temperature decreases from its maximum value in the center (~15000 K) to the outer radial position where a minimum temperature of ~5000 K is observed.

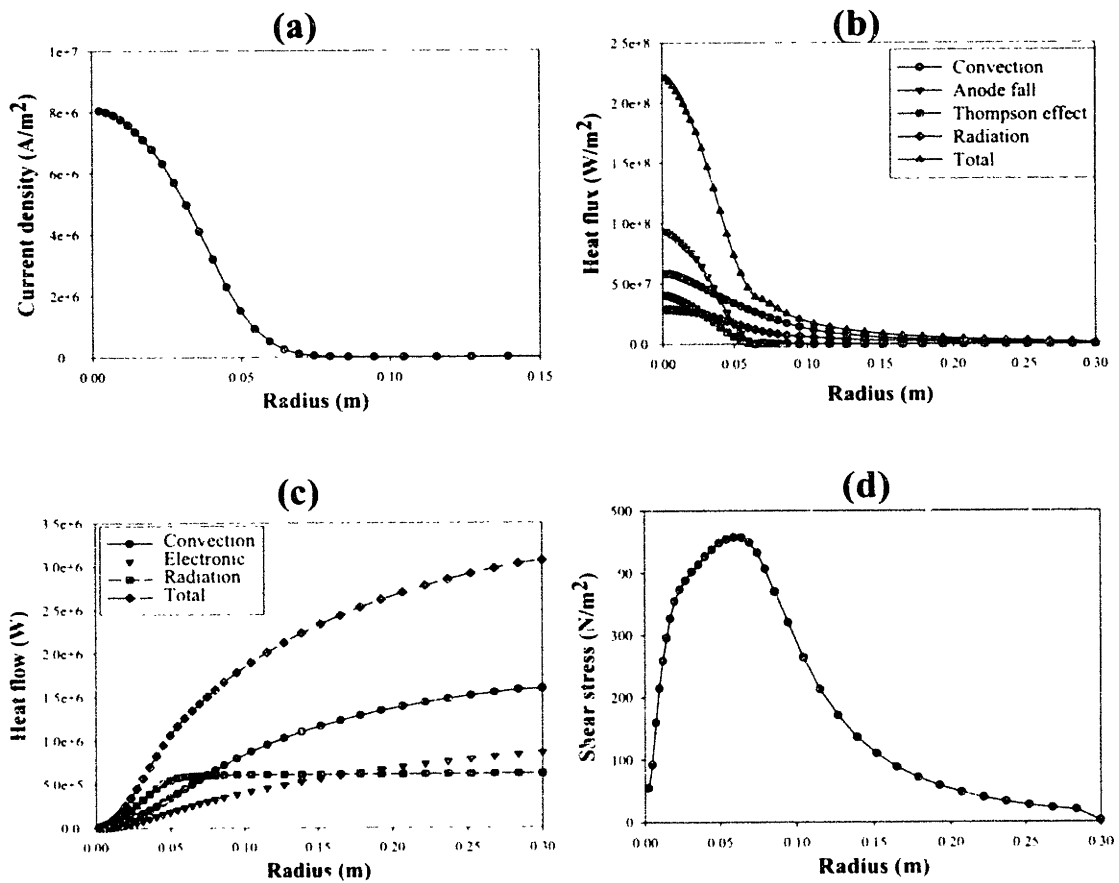


Figure 2.3.10 Arc-bath interactions at the bath surface. (a) Current density and (b) Heat flux distribution. (c) Cumulative heat flux. (d) Shear stress.

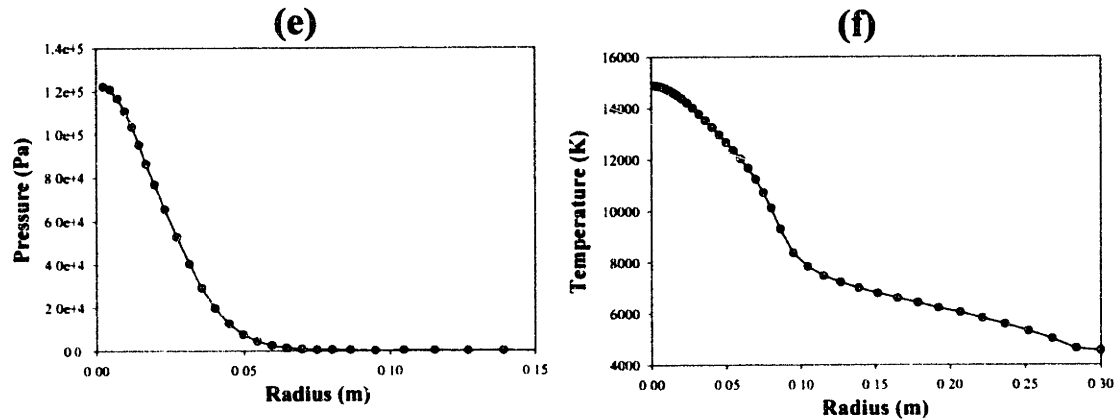


Figure 2.3.10 (cont.) Arc-bath interactions at the bath surface. (e) Arc pressure. (f) Arc temperature.

### Section 2.3.3: Sensitivity Analysis: Effect of Model Parameters and Assumptions

In this section, the effects of some assumptions and model parameters on the representation of the arc characteristics are examined in detail. The effects addressed in this section are (a) current density at the cathode,  $J_c$ , (b) turbulent model, (c) bath temperature, (d) compressibility, and (e) induced currents. These effects are brought into this discussion since they can be used to support, or in some cases explore the consequences, of some of the physical assumptions used to formulate the arc model. All effects discussed in the following sections are explored using as a case study the standard electric arc conditions (40 KA and 0.25 m).

#### Section 2.3.3.1: Effect of Current Density at the Cathode ( $J_c$ )

The current density at the cathode was considered to have a value of  $4.4 \times 10^7 \text{ A/m}^2$  measured by Jordan et. al. [22] for graphite electrodes. However, currents used to measure the current density at the cathode were up to 10 KA. Therefore, it may not be possible to extrapolate this  $J_c$  to a high current arc as those used in industrial DC-EAF. Also, some other investigations [16,21,97] have reported different values for  $J_c$ , and in all cases these values are smaller than  $4.4 \times 10^7 \text{ A/m}^2$ . For the above reasons, a  $J_c$  value of  $1.0 \times 10^7 \text{ A/m}^2$  was used to run a simulation for the standard electric arc case (40 KA and 0.25 m) in order to compare the results with those obtained with a  $J_c$  of  $4.4 \times 10^7 \text{ A/m}^2$ . In this way, it is possible to examine the effect that  $J_c$  has on important arc characteristics such as temperature, velocity, current density, electric potential and arc-bath interactions.

Figure 2.3.11 shows a comparison of the current density fields obtained with a large  $J_c$  of  $4.4 \times 10^7 \text{ A/m}^2$  (a) and with a small  $J_c$  of  $1.0 \times 10^7 \text{ A/m}^2$  (b). The first distinguishable element between the two cases is

the higher cathode spot radius,  $R_c$ , of 3.5 cm for the small  $J_c$  compared to a  $R_c$  of 1.7 cm obtained with a larger  $J_c$  (equation 2.1.24). In general, big differences are observed close to the cathode with smaller current densities obtained in the small  $J_c$  case. However, close to the bath, similar values of current density vectors can be appreciated for both fields. A clearer representation of the previous statement is presented in Figure 2.3.11 (c) where axial current density distributions along the radius are plotted at three different axial positions (5, 12.5 and 20 cm from the cathode). Close to the cathode the curves representing axial current density profiles for the small  $J_c$  are much lower than those for the large  $J_c$ , but both representations ( $J_c$  small and large) are similar close to the bath surface. As explained in the previous section, a close relationship exists between axial current densities and magnetic flux densities. Therefore, Figure 2.3.11 (d) presents radial profiles for the magnetic flux density at the same three axial positions for both small and large  $J_c$ 's. Of course, the same trends as in the previous figure are observed in this plot. Close to the cathode lower magnetic flux density profiles are obtained for the small than for large  $J_c$ .

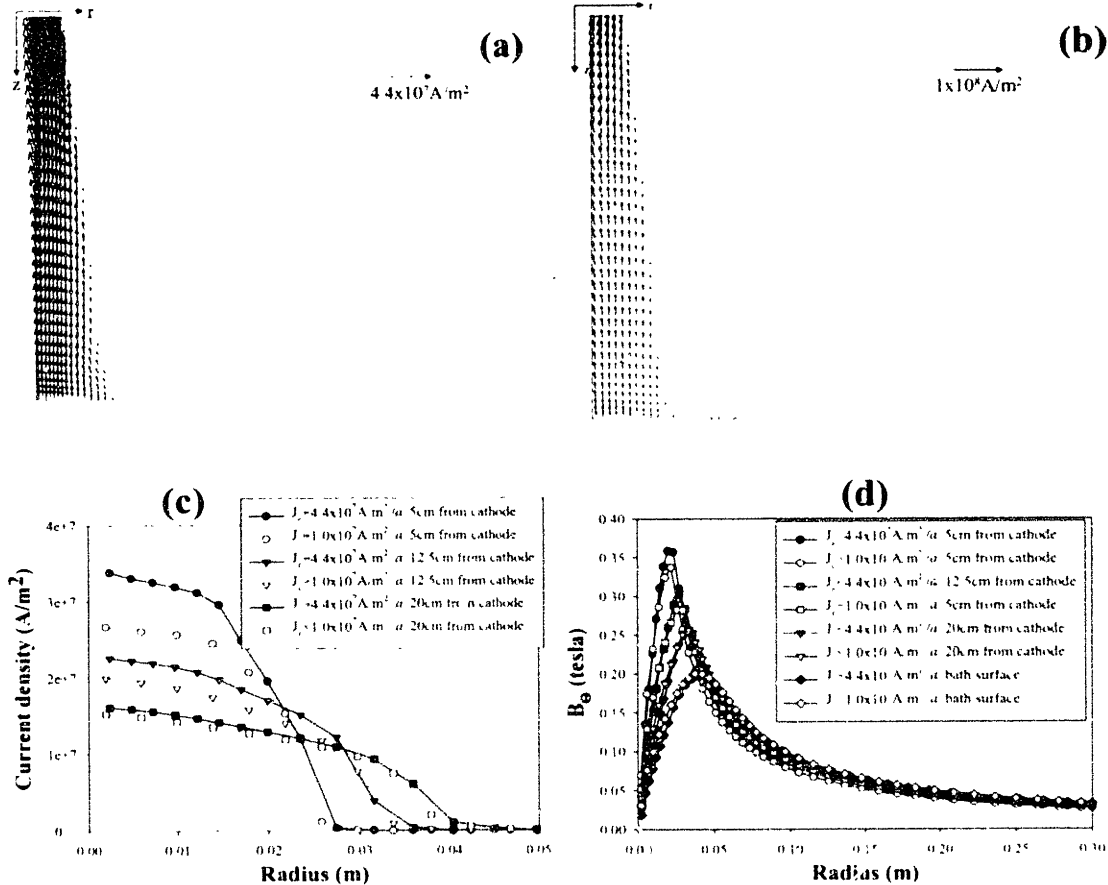


Figure 2.3.11 Computed electric quantities with two different  $J_c$ 's (a) Computed current density fields for a  $J_c$  of  $4.4 \times 10^7 \text{ A/m}^2$ . (b) Computed current density fields for a  $J_c$  of  $1.0 \times 10^7 \text{ A/m}^2$ . (c) Axial current density profiles along the radius at distances from the cathode of 5, 12.5 and 20 cm. (d) Magnetic flux density radial profiles at 5, 12.5 and 20 cm from cathode.



The consequences of lower current densities obtained from smaller  $J_c$  values are: a) lower Joule heat dissipation leading to lower temperatures (maximum temperature of 23500 K with small  $J_c$  compared with 27000 K with a large  $J_c$ ). b) Lower electromagnetic body forces; which are also responsible for lower pressure values at the cathode ( $1.44 \times 10^5$  Pa with small  $J_c$  compared with  $2.3 \times 10^5$  Pa for a large  $J_c$ ). c) Lower pressures produce a lower velocity in the jet (maximum velocities of 6356 m/s with small  $J_c$  against more than 8000 m/s with large  $J_c$ ). Figure 2.3.12 shows temperature, pressure and velocity profiles along the symmetry axis for both large and small  $J_c$ 's. From the plot it is clear the big effect that  $J_c$  has on the arc characteristics close to the cathode, where big departures between lines representing temperature and pressure are obtained. However, as the distance from cathode increases and approaches the bath, both computations converge to almost the same values.

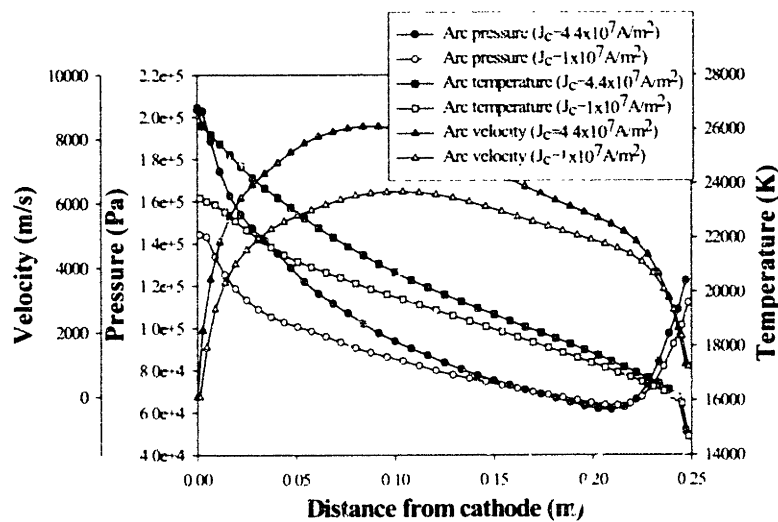


Figure 2.3.12 Effect of  $J_c$  on arc characteristics. Temperature, pressure and velocity fields are plotted along the axis for two different cathode spot current densities ( $4.4 \times 10^7$  A/m<sup>2</sup> and  $1.0 \times 10^7$  A/m<sup>2</sup>).

The arc-bath interactions are expected to be similar since the arc characteristics are not influenced close to the bath by changing  $J_c$ . However, since the velocities are quite different between the two cases, estimation of some arc-bath interactions such as shear stress and heat flux by convection are expected to be different. Figure 2.3.13 shows predicted arc-bath interactions for both small and large  $J_c$ 's. Heat fluxes are presented in Figure 2.3.13 (a) where very similar behavior is found in both cases. The different heat flux components, such as electronic contributions (anode fall and Thompson effect) are exactly the same. Convection is lower for small  $J_c$  than for large  $J_c$  due to the lower velocities found with small  $J_c$  and radiation is slightly higher for small  $J_c$ , probably due to a wider arc column generated by a larger  $R_c$  value at the cathode that radiates more heat per unit volume. The shear stress, which is function of the arc

velocities, is probably the more sensible arc-bath interactions to  $J_c$  variations, as shown in Figure 2.3.13 (b). Smaller velocities associated with smaller  $J_c$  lead to lower shear stresses at the bath.

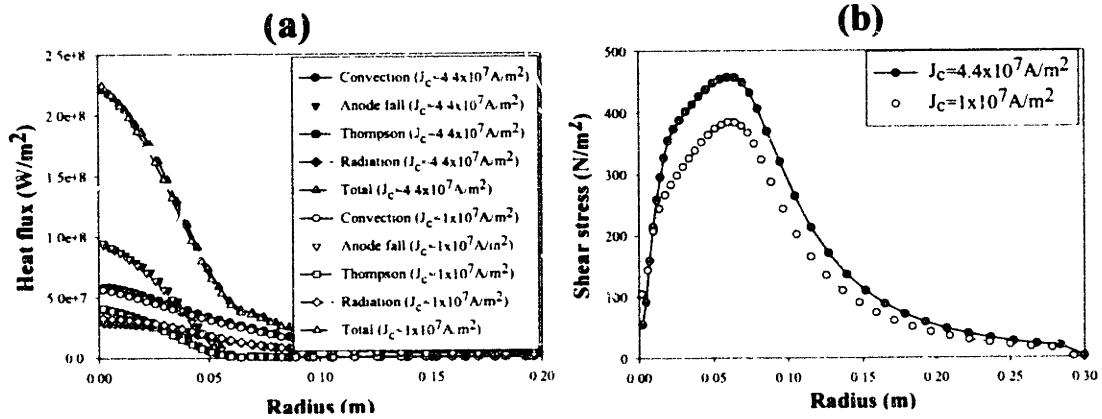


Figure 2.3.13 Effect of  $J_c$  on arc-bath interactions. (a) Heat fluxes for  $J_c$  of  $4.4 \times 10^7 \text{ A/m}^2$  and  $J_c$  of  $1.0 \times 10^7 \text{ A/m}^2$ . (b) Shear stress distribution at the bath for  $J_c$  of  $4.4 \times 10^7 \text{ A/m}^2$  and  $J_c$  of  $1.0 \times 10^7 \text{ A/m}^2$ .

### Section 2.3.3.2: Effect of the Turbulence Model

Although turbulence is known to be present inside the arc, it is quite complex to provide a rigorous representation for it. As a first approximation, the standard k- $\epsilon$  model was used to account for turbulence in the arc. However, it is accepted that the k- $\epsilon$  model has limitations because it is unable to represent turbulent flows subjected to strongly directed body forces (as in this case). It is also important to stress that the k- $\epsilon$  model is a high Re number model implying that it is only applicable to those cases where fully developed turbulent regime is expected. But the weakest restriction of the k- $\epsilon$  model is that only applies to isotropic turbulence flows [89].

For these reasons, other turbulent models were employed to examine the effects of turbulence representation predictions on turbulent parameters and arc characteristics. Selecting a turbulence model is a difficult task since no experimental information is available for the real process to be able to make comparisons. The additional models employed were a) The RNG turbulence model and b) The two scale k- $\epsilon$  turbulence model. Both models are derived from the Bussinesq approximation [98] as in the k- $\epsilon$  model; however, their formulations involved different assumptions.

In the case of RNG, the same equations as in the k- $\epsilon$  model are employed (equations 2.1.17-2.1.23), but different model constants are determined from a re-evaluation of parameters controlling the production of  $\epsilon$ . Additionally, an extra source term for the energy dissipation rate is derived from Renormalization Group (RNG) methods (for details see [89]).

The two-scale  $k-\epsilon$  model differs from the standard  $k-\epsilon$  model in the assumption that a spectral equilibrium exists between the largest and the smallest eddies. Spectral equilibrium means that once turbulence is generated in the largest eddy, it is dissipated immediately at the same point in the smallest eddy. In general, this is not the real case, because there is a vast size of eddies where production and dissipation take place. In the two-scale model, the turbulence-energy spectrum is divided in two parts, roughly at the wave number above which no mean-strain production occurs. The first part is the 'production' region and the second is the 'transfer' region. The total turbulent energy is assumed to be divided between the production region,  $K_p$ , and the transfer region,  $K_t$ . The rate of energy transferred out of the production rate,  $E_p$ , is a sink of  $K_p$  but at the same time a source of  $K_t$ , while  $E_t$  is a sink of  $K_t$ . Hence, four turbulence parameters are used to characterize the production and dissipation processes,  $K_t$ ,  $K_p$ ,  $E_t$  and  $E_p$ . Each parameter is associated with its own transport equation, then the two-scale  $k-\epsilon$  model solves four transport equations instead of two equations solved for the standard  $k-\epsilon$  model (for details see [89]).

### RNG Turbulence model

Figure 2.3.14 shows contour plots for the main turbulent parameters (turbulent kinetic energy,  $k$ , energy dissipation rate,  $\epsilon$ , and kinematic turbulent viscosity,  $\nu_t$ ) computed for the standard  $k-\epsilon$  and the RNG model.

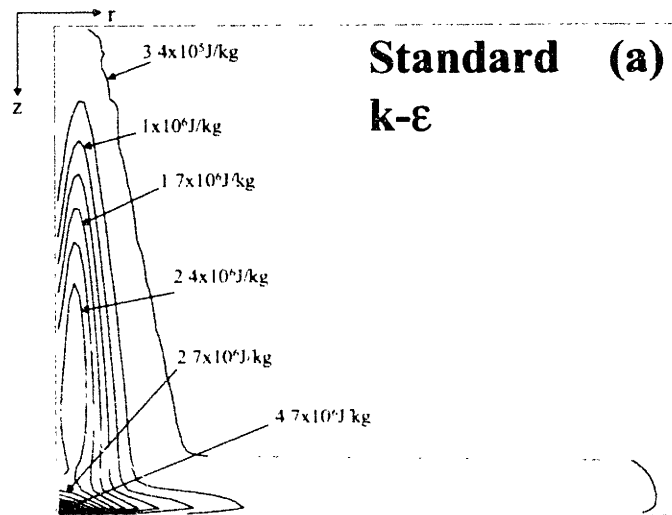


Figure 2.3.14 Comparison between standard  $k-\epsilon$  and RNG turbulence models. (a) Computed turbulent kinematic energy,  $k$ .

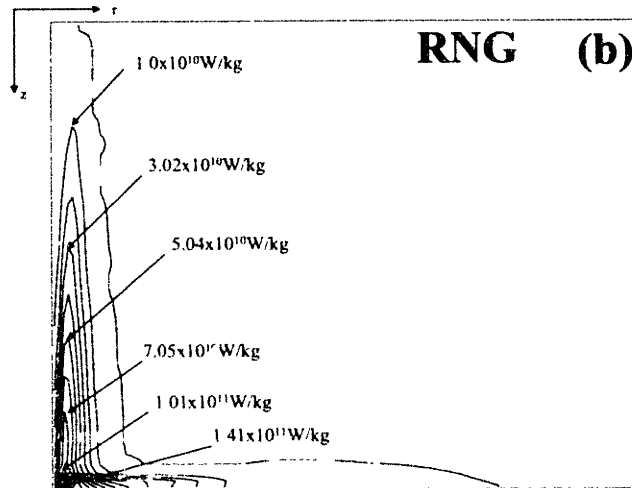
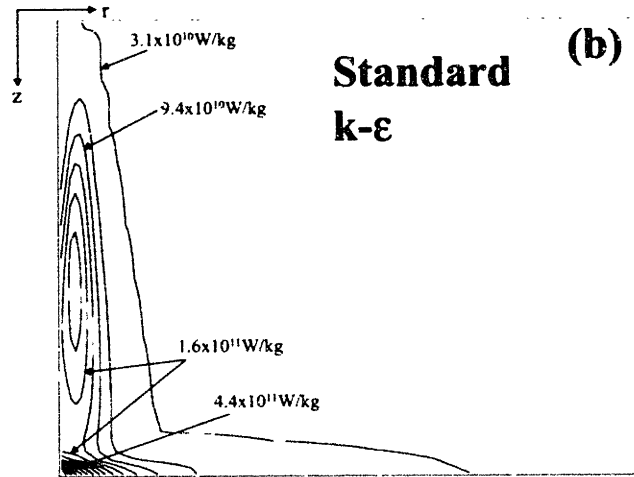
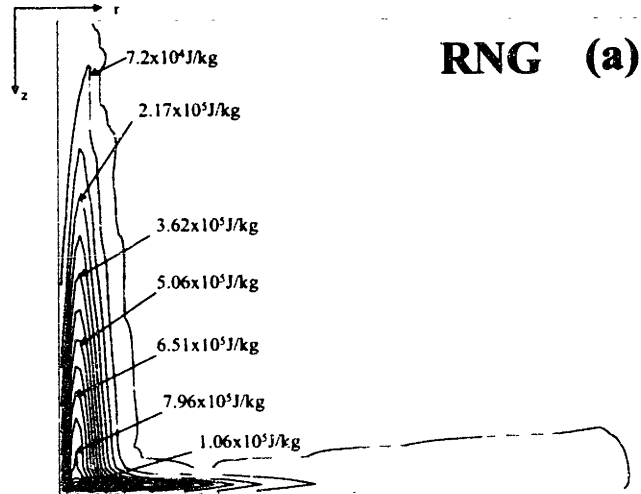


Figure 2.3.14 (cont.) Comparison between standard k-ε and RNG turbulence models. (a) Computed turbulent kinematic energy,  $k$ . (b) Energy dissipation rate,  $\epsilon$ .

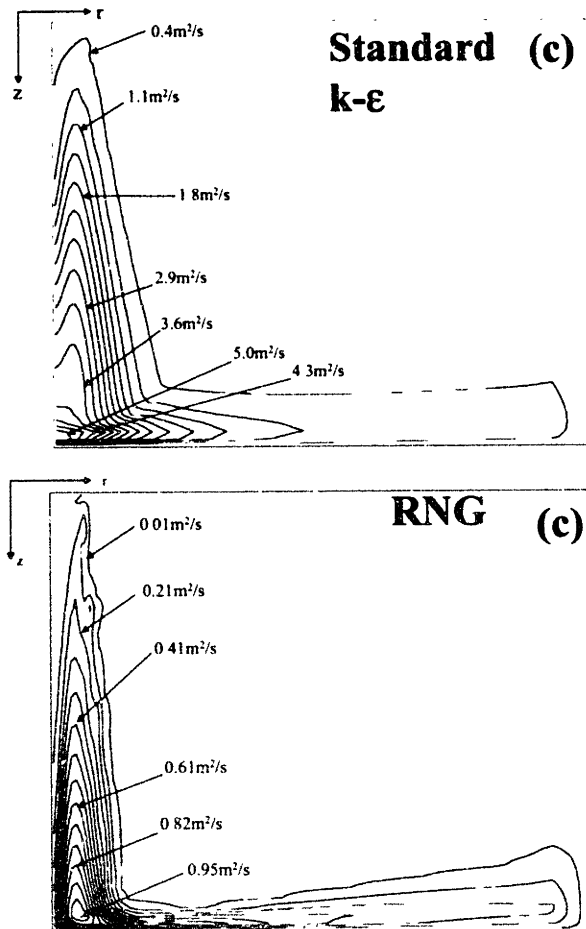


Figure 2.3.14 (cont.) Comparison between standard k-ε and RNG turbulence models. (c) Turbulent kinematic viscosity,  $\nu_t$ .

Similar trends are obtained with the two models for the main turbulence parameters showing two developed regions of turbulence: one along the axis in the axial direction (following the arc jet) and the second along the bath surface in the radial direction (following the gas impingement region). Outer line contours represent lower turbulent values for all parameters, and the maximum turbulence is found at the center close to the bath (impingement point). However, it can be noted that the k-ε model predicts five times larger turbulent kinetic energies, energy dissipation rates and turbulent viscosities than the RNG model ( $k$ , maximum of  $4.6 \times 10^6$  J/kg with k-ε and  $1.01 \times 10^6$  J/kg with RNG;  $\epsilon$  maximum of  $4.4 \times 10^{11}$  W/kg with k-ε while  $1.41 \times 10^{11}$  W/kg with RNG; and  $\nu_t$  maximum of  $5 \text{ m}^2/\text{s}$  with k-ε while  $0.95 \text{ m}^2/\text{s}$  with RNG). Also, wider contour distributions are obtained with the k-ε model compared to RNG. Then, it can be said that mixing is notoriously enhanced when using the k-ε model compared with the RNG representation.

### Two-scale k-ε Turbulence model

Figure 2.3.15 shows contour plots for the main turbulent parameters computed from the two-scale k- $\epsilon$  model. These parameters are: turbulent kinetic energy in the production region,  $K_p$  (a), and in the transfer region,  $K_t$  (b), energy dissipation rate in the production region,  $E_p$  (c), and in the transfer region  $E_t$  (d), and the kinematic turbulent viscosity,  $\nu_t$  (e). The turbulent kinematic viscosity,  $\nu_t$ , obtained from the standard k- $\epsilon$  model is presented for comparison in Figure 2.3.15 (f). Again, similar trends are obtained for all turbulence parameters obtained from the two-scale model. Two regions are clearly appreciated in the plots: the jet and bath boundary regions. Turbulence increases from the external boundary to the symmetry axis and the maximum value is observed at the bath surface in the jet impingement zone.

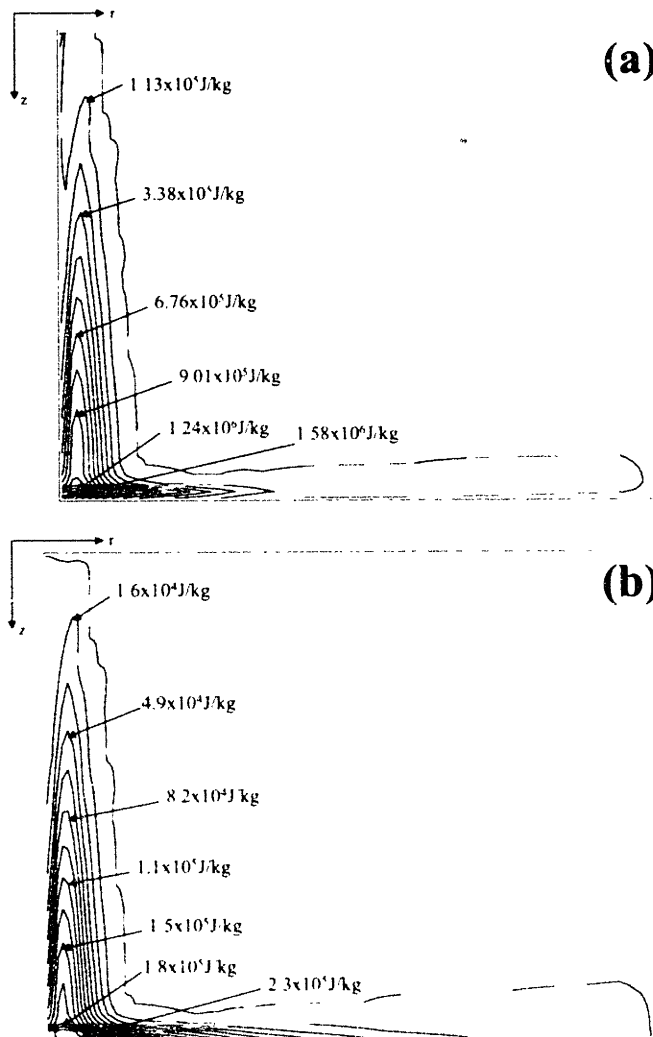


Figure 2.3.15 Turbulence parameters computed from the two-scale k- $\epsilon$  model (a) Turbulent kinetic energy in the production region,  $K_p$ . (b) Turbulent kinetic energy in the transfer region,  $K_t$ .

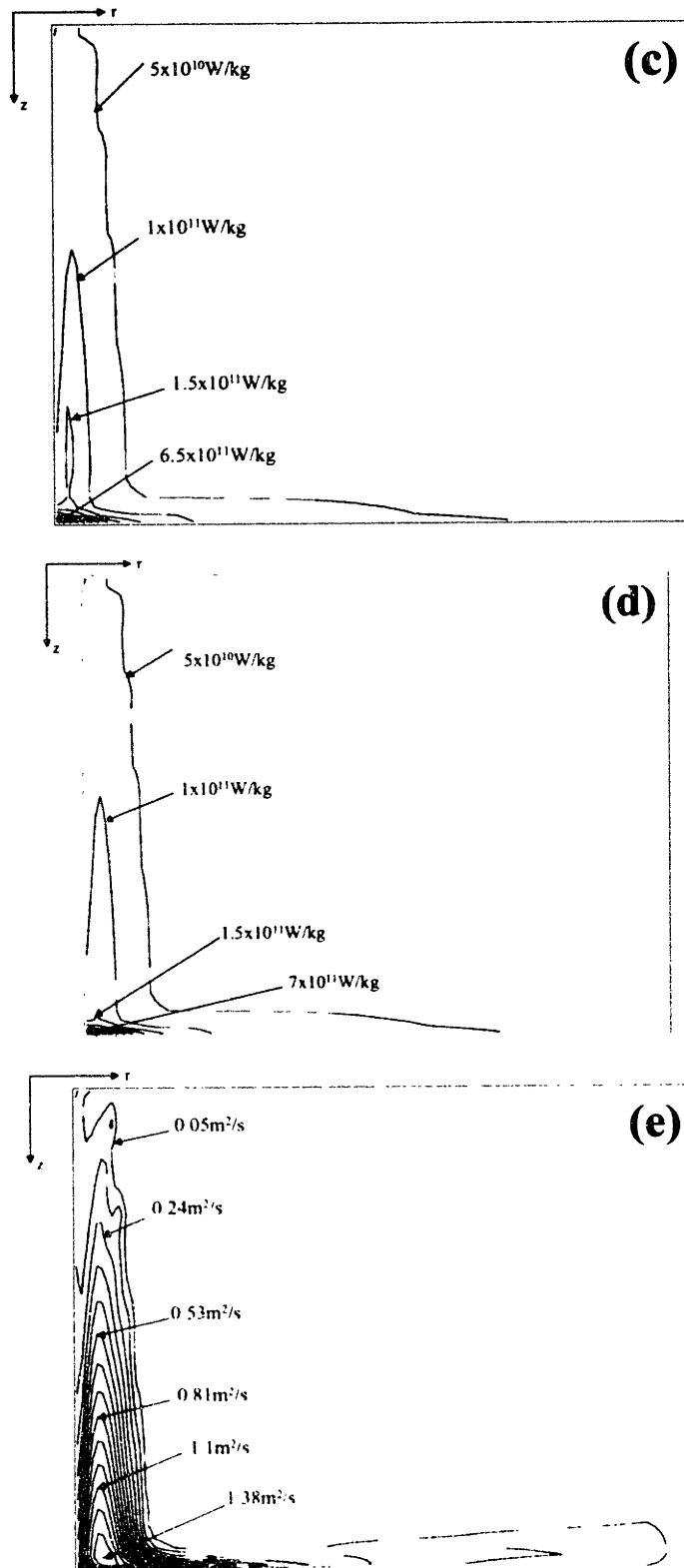


Figure 2.3.15 (cont.) Turbulence parameters computed from the two-scale k-ε model (c) Energy dissipation rate in the production region,  $E_p$ . (d) Energy dissipation rate in the transfer region,  $E_t$ . (e) Turbulent kinematic viscosity,  $\nu_t$ .

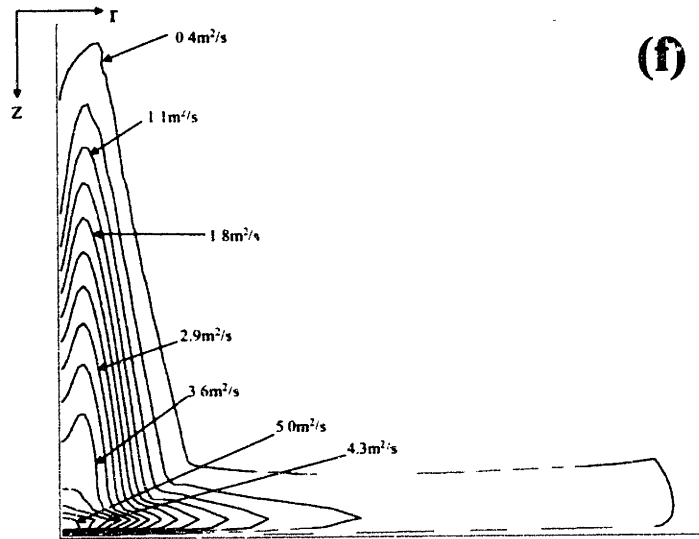


Figure 2.3.15 (cont.) Turbulence parameters computed from the two-scale k-ε model (f) Turbulent kinematic viscosity,  $\nu_t$  obtained from the standard k-ε model.

The two-scale model computes the turbulent kinematic viscosity as:

$$\nu_t = 0.09 \left( \frac{(K_p + K_t)^2}{E_p} \right) \quad (\text{eq. 2.3.4})$$

and as with the RNG model, the two-scale model predicts much lower turbulent viscosities than the standard k-ε model and, therefore the predicted mixing is less intensive with the two-scale model (Figures 2.3.15 (e) and (f)). However, the two-scale model predicts a higher turbulent viscosity than the RNG model (maximum of 1.38 m<sup>2</sup>/s with the two-scale against 0.95 m<sup>2</sup>/s with the RNG).

### Effect of turbulence models on arc characteristics and arc-bath interactions

Computed pressure, temperature and velocity profiles along the axis are presented in Figure 2.3.16 (a), (b) and (c), respectively. Under prediction of mixing by the two-scale and RNG models is evident in all plots presented in Figure 2.3.16. Temperatures along the axis are similar for all cases close to the cathode (Figure 2.3.16 (a)), but as the distance from the cathode increases, temperatures predicted by the two-scale and RNG models are much higher than those predicted by the standard k-ε model. Temperatures are much higher with the two-scale and RNG models because the arc does not expand due to poor mixing, as predicted by the models. Velocities at the axis also indicate that mixing of gas is reduced with the two-scale and the RNG models (Figure 2.3.16 (b)). This explains why the velocities predicted by the two-scale and RNG models do not decrease as distance from the cathode increases as actually happens with the standard k-ε model, where the axial velocity reaches a maximum 10cm from cathode and then decreases due to



intense mixing produced at the boundary of the jet. Since jet does not experience enough mixing with the two-scale and RNG models, this jet reaches the bath with a higher momentum and, consequently, predicted arc pressures at the bath (Figure 2.3.16 (c)) are much higher by these two models. Similarly, lower arc expansion promoted under the two-scale and RNG models can be appreciated in Figure 2.3.16 (d), where heat fluxes at the bath are compared for the three turbulence models. Heat fluxes depicting higher and narrower distributions are predicted by the two-scale and RNG models. Finally, the shear stresses shown in figure 2.3.16 (e) indicate the same behavior, predicting much higher shear stresses with the lower mixed jet predicted by both RNG and two-scale  $k-\epsilon$  models (almost three times bigger maximum shear stresses predicted by RNG and two-scale  $k-\epsilon$ ).

It is important to stress the significant differences in results when selecting alternative turbulence formulations to represent arc characteristics and arc-bath interactions. This issue, however, can not be resolved in this work because of the lack of experimental information. In order to simplify the problem and facility the study, the standard  $k-\epsilon$  model was selected for the calculations.

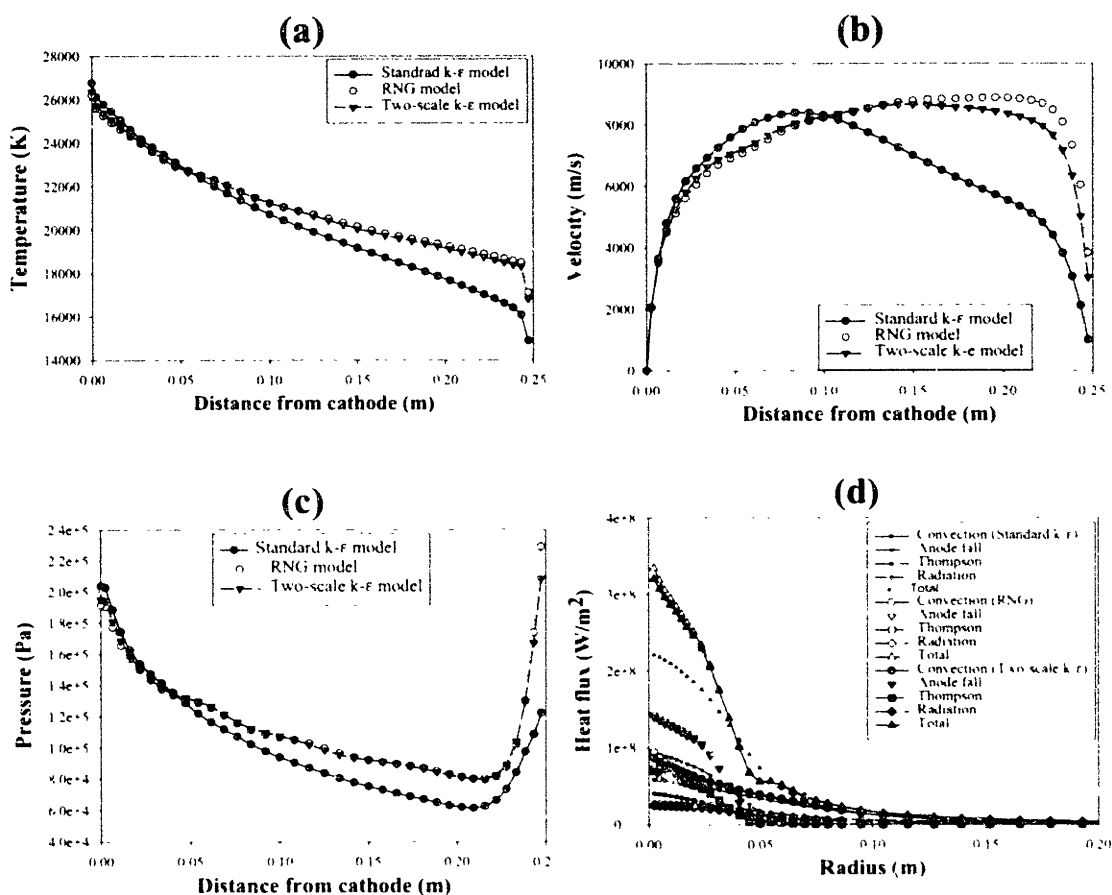


Figure 2.3.16 Effect of the turbulence model on arc characteristics and arc-bath interactions. (a) Temperature along the axis. (b) Axial velocity along the arc axis. (c) Pressure along the axis. (d) Heat fluxes at the bath.

(e)

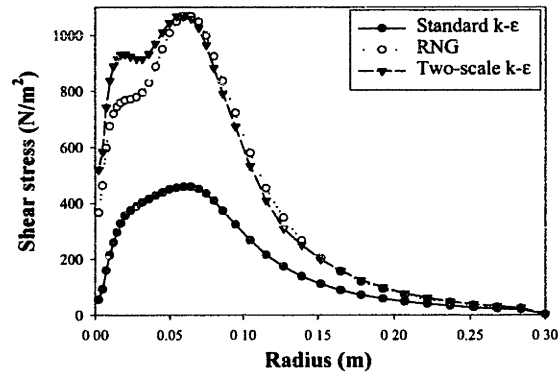


Figure 2.3.16 (cont.) Effect of the turbulence model on arc characteristics and arc-bath interactions. (e) Shear stress at the bath surface.

### Section 2.3.3.3: Effect of the Anode Temperature

One of the main assumptions used in the approach to represent the DC-EAF system is the recognition of two regions that can be treated separately: the arc and bath regions. However, this extremely important assumption is physically expressed by two additional simplifications: a) the surface depression on the molten bath has to be neglected and b) a constant bath temperature condition. These two assumptions make possible decoupling the bath from the arc for numerical purposes allowing us to compute first the arc and use these arc results as boundary conditions for the bath region, instead of solving both regions simultaneously. Bath depression is important but would complicate the model in such a way that it would make this computation extremely complex. However, the bath temperature assumption was not explained in the model description section and therefore requires further discussion.

In this section, the effect that the bath temperature has on the representation of the arc-bath interactions is analyzed. The model assumption previously stated (see section 2.1.2) implies that the bath temperature is not a critical parameter affecting the bath results. However, if the bath temperature would affect arc-bath interactions, then coupling between bath and arc regions would be necessary, either by an iterative procedure or by a single simulation comprising the bath and arc regions together.

Figure 2.3.17 presents predicted arc-bath interactions computed with two different bath temperatures of 1800 K and 3500 K. A temperature of 1800 K was originally chosen as the bath temperature boundary condition for the standard case, while 3500 K constitutes a value near the boiling point of pure iron, which is considered to be the highest possible temperature at the bath surface. The arc current, shear stress, heat flux and gas temperature at the anode are presented as a function of the radius for the two bath temperatures considered in Figures 2.3.17 (a), (b), (c) and (d) respectively.

All plots in Figure 2.3.17 show that the bath temperature does not affect arc-bath interactions. The arc current (Figure 2.3.17 (a)) and shear stress (Figure 2.3.17 (b)) curves are identical. Heat flux is almost the same not only for the total heat flux but also regarding heat mechanisms. Only convection and Thompson effect present small difference (almost undistinguishable). This small difference is due to the fact that both convection and Thompson effects are directly proportional to the temperature difference between the bath and gas at the bath surface as indicated by equations 2.1.28 and 2.1.30. But, as can be seen in Figure 2.3.17 (d), gas temperatures are exactly the same for both bath temperatures, so even the physical properties are the same at the bath surface.

Then, it is concluded that the bath temperature does not play an important role and, therefore, 1800 K represents a good approximation for practical purposes allowing the decoupling between the arc and the bath regions.

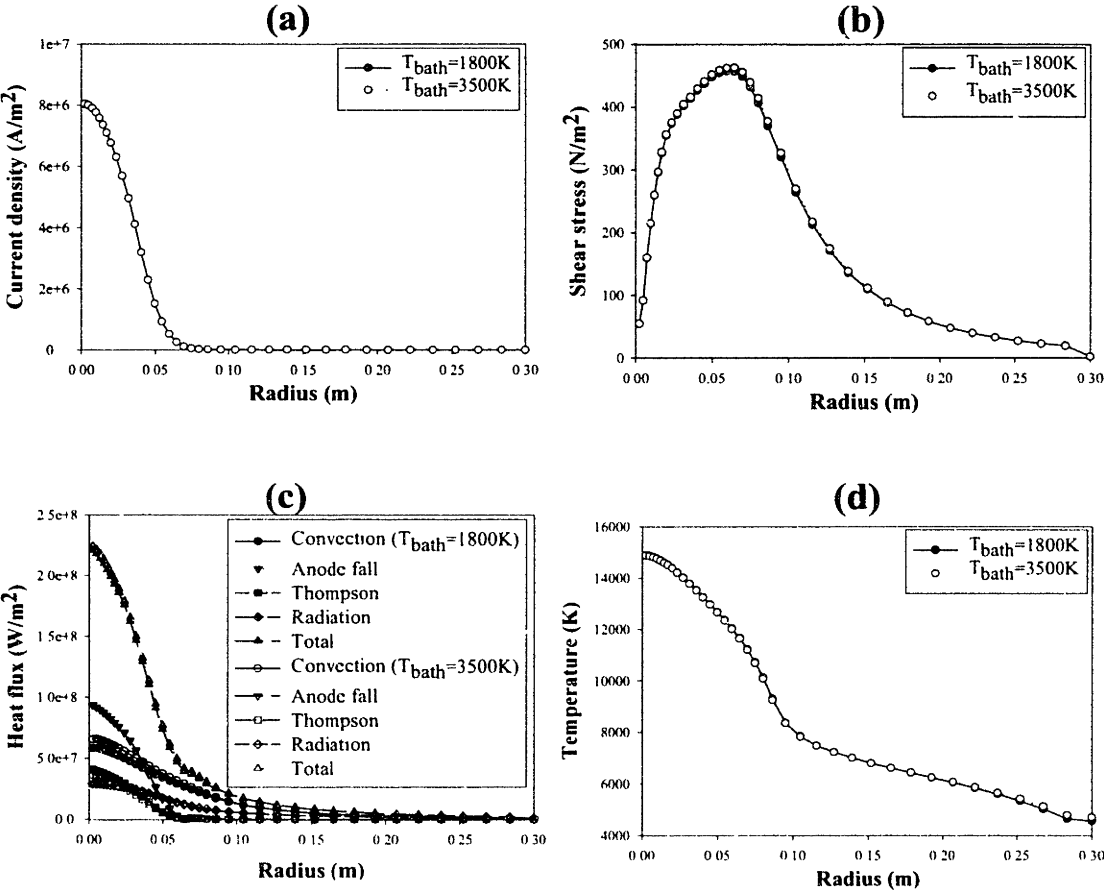


Figure 2.3.17 Effect of bath temperature on arc-bath interactions. (a) Arc current. (b) Shear stress. (c) Heat flux. (d) Gas temperature at the bath.

### Section 2.3.3.4: Effect of Compressibility

A key assumption of this model is the representation of fluid flow phenomena in the arc without considering compressibility effects. However, after computing the arc region under normal conditions for the standard case (40 KA and 0.25 m), the results are such that the Mach number field shows that inside the arc column some portion of the domain is under supersonic flow regime (Mach numbers above one in Figure 2.3.18). Therefore, compressibility effects must be somehow considered if more accurate representation is expected from the arc model.

In order to account for compressible effects, the stagnation enthalpy,  $H$ , needs to be invoked as a function of the static (normal) enthalpy,  $h$ , through the following relation:

$$H = h + 0.5\bar{V} \cdot \bar{V} \quad (\text{eq. 2.3.5})$$

where  $V$  is the gas velocity.

Compressibility affects some physical properties, but its most important effect is on density, whose variation with pressure can be expressed by the isentropic approximation [99] as:

$$\rho = \rho_o \left( \frac{P}{P_o} \right)^{\left( \frac{1}{\gamma} \right)} \quad (\text{eq. 2.3.6})$$

where  $\rho$  is density, which depends on temperature and pressure,  $\rho_o$  and  $P_o$  refer to pressure and density at normal pressure or stagnant conditions,  $P$  is pressure and  $\gamma$  is the ratio of specific heats ( $C_p/C_v$ ).

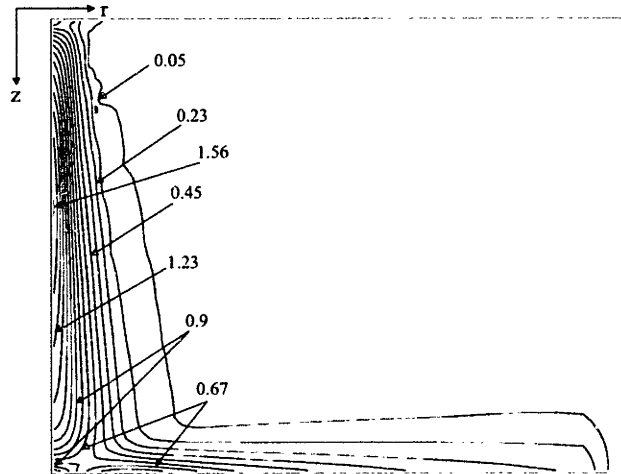


Figure 2.3.18 Computed Mach number field for the standard arc case (40 KA and 0.25 m) without considering compressibility effects.

Figure 2.3.19 shows velocity and temperature fields calculated for the standard arc case with and without considering compressibility effects. Maximum temperatures with compressibility effects are lower (24000 K) than without compressibility (27000 K). Another important difference is that the region of maximum temperature, close to the cathode, is larger when compressibility is accounted for than when it is not considered. Velocities under compressible flow regime are much lower (maximum velocity 4495 m/s) than without compressibility effects (maximum velocity of  $\sim 85000$  m/s). It is clear that this huge difference in the velocity fields is related to density changes as can be appreciated in Figures 2.3.20 (a) and 2.3.20 (b) where a comparison of density fields under normal and compressible flow regimes are presented, respectively. As seen in this figure, lower densities are found inside the arc region but minimum values of  $0.003 \text{ kg/m}^3$  are predicted under no compressible effects, while a minimum of  $0.01 \text{ kg/m}^3$  (three times larger) is found under compressible flow regime. Therefore, density increases almost three times with compressible flow regime, which in turns allows continuity requirements to be met with lower velocities. Having much lower velocities and temperatures also means that other arc characteristics are greatly affected. For example, the potential field varies considerably when compressibility effects are considered as shown in Figure 2.3.21 (a) and (b). A voltage drop of 552 V is obtained with compressibility while without compressibility 605 V voltage is obtained. Moreover, the potential contour field is less affected by convective terms (less inclined potential lines close to the symmetry axis). Current densities with compressibility effects (Figure 2.3.21 (d)) show vectors that are not radially deflected at the symmetry axis as happens without considering compressible flow (Figure 2.3.21 (c)). Flow deflection close to the symmetry is a consequence of the convective terms that decrease when compressible flow is considered. Another variable related to the effect of the velocity field is the turbulent kinematic viscosity,  $\nu_t$ , presented in Figure 2.3.22 with compressible flow (a) and without compressible flow (b). This figure shows that turbulent viscosity decreases a factor of two from no compressible to compressible flow calculations (from a maximum of  $5 \text{ m}^2/\text{s}$  to a maximum of  $2.5 \text{ m}^2/\text{s}$ ).

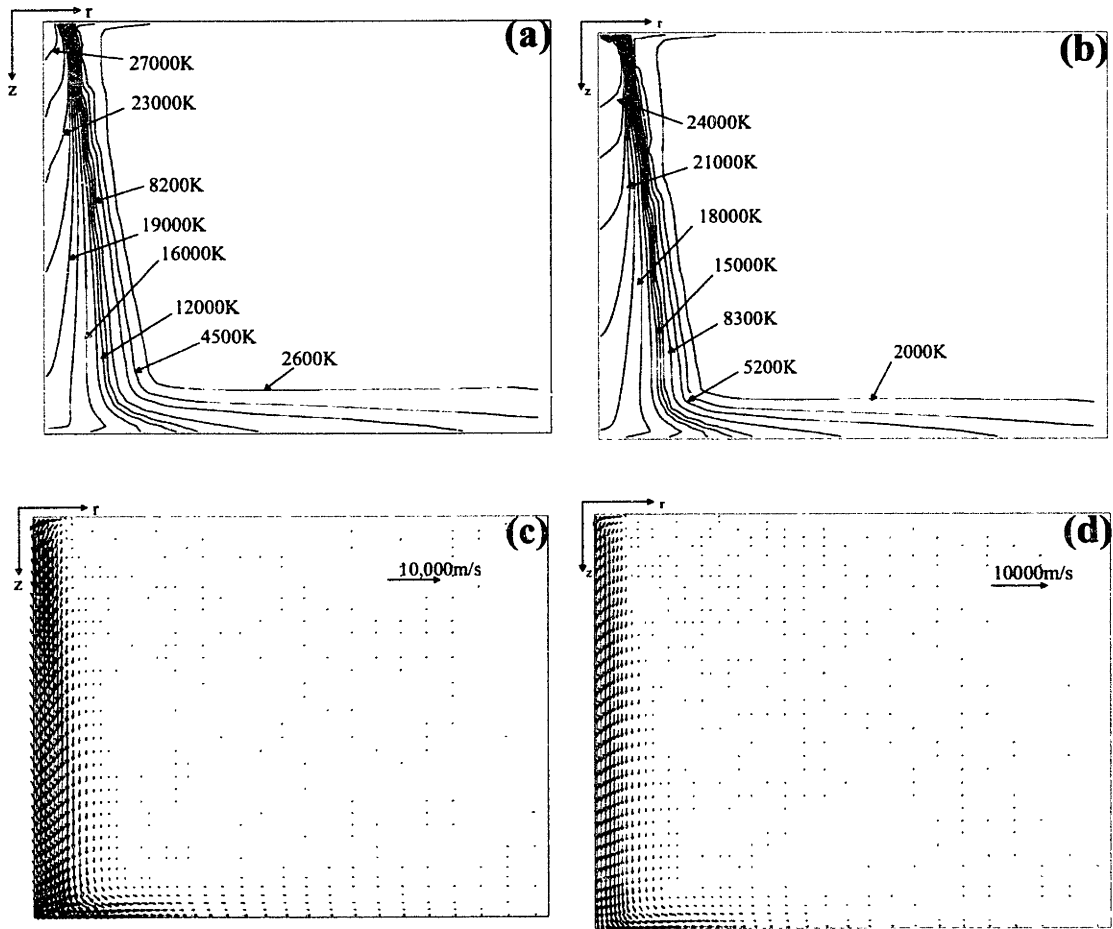


Figure 2.3.19 Effect of compressibility on velocity and temperature in the arc. (a) Arc Temperature without compressibility. (b) Arc Temperature with compressibility. (c) Arc velocity without compressibility. (d) Arc velocity with compressibility.

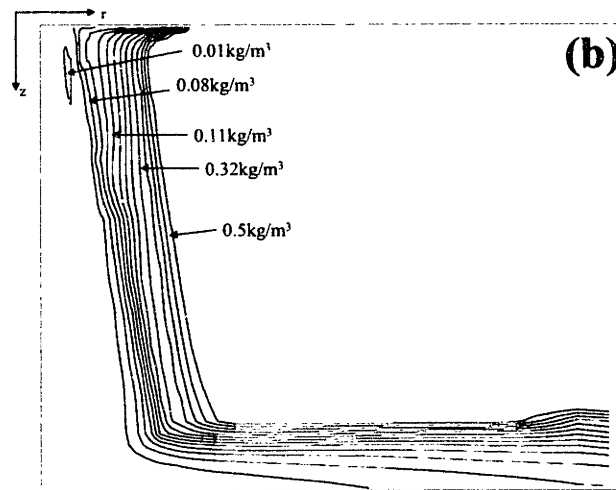
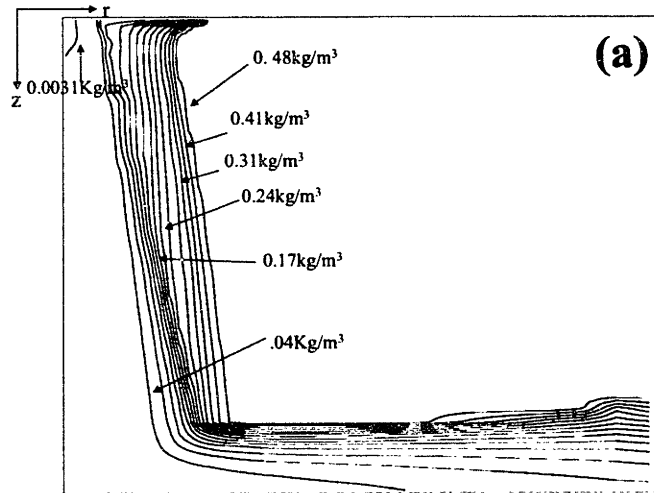


Figure 2.3.20 Effect of compressibility on density fields. (a) Density without compressibility. (b) Density with compressibility.

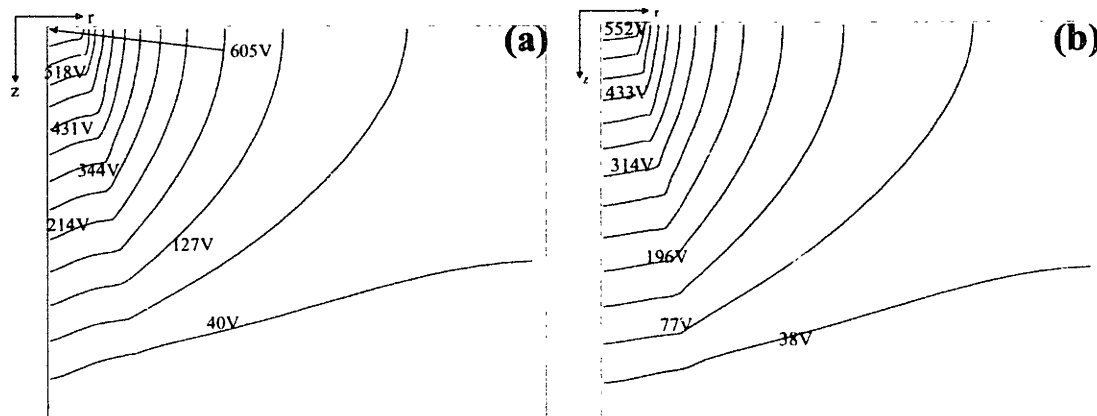


Figure 2.3.21 Effect of compressibility on electric parameters. (a) Potential without compressibility. (b) Potential with compressibility

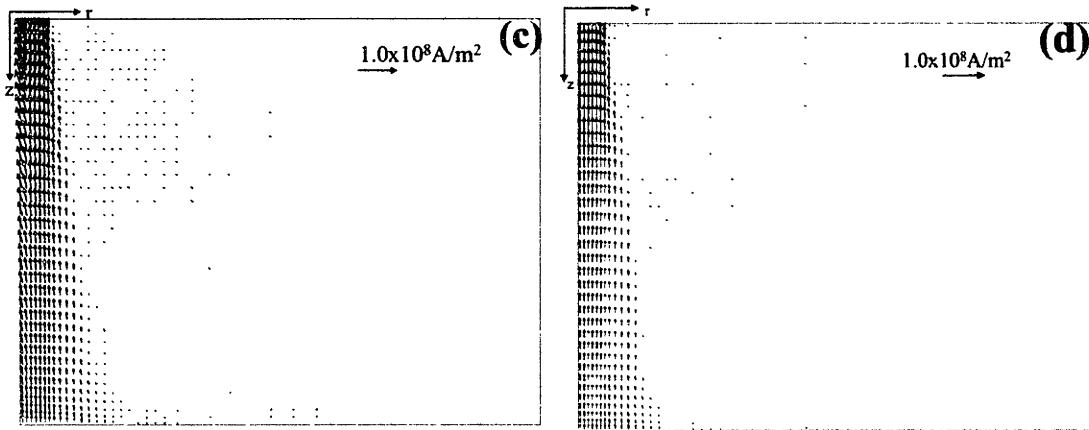


Figure 2.3.21 (cont.) Effect of compressibility on electric parameters. (c) Current density without compressibility. (d) Current density with compressibility.

Arc-bath interactions are also affected by compressible flow consideration. Figure 2.3.23 shows the predicted heat flux, pressure, and shear stress at the bath surface. Heat fluxes are not affected greatly; however, heat fluxes are lower when compressible flow is implemented in the model (Figure 2.3.23 (a)). The arc pressure also shows a decrease when compressibility effects are used (Figure 2.3.23 (b)). A more interesting result is found for the comparison of shear stresses presented in Figure 2.3.23 (c). A rare double peak in the shear stress curve under compressibility effects contrasts with the single peak obtained without compressibility effects.

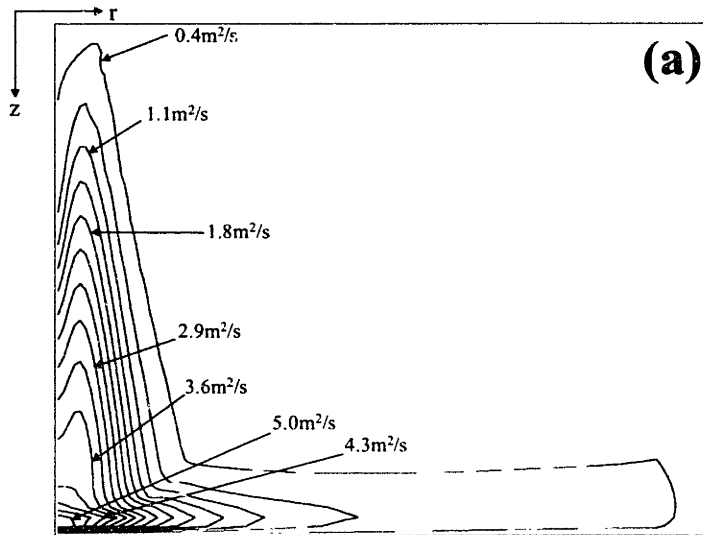


Figure 2.3.22 Effect of compressibility on turbulent kinematic viscosity,  $\nu_t$ . (a) Without compressibility.



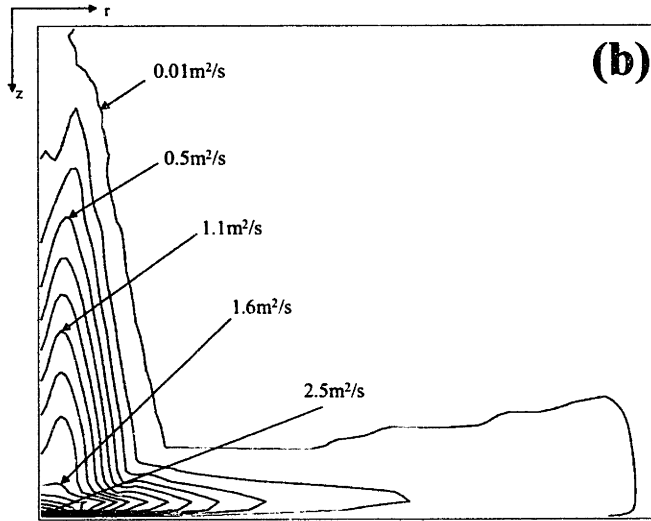


Figure 2.3.22 (cont.) Effect of compressibility on turbulent kinematic viscosity,  $\nu_t$ . (b) With compressibility.

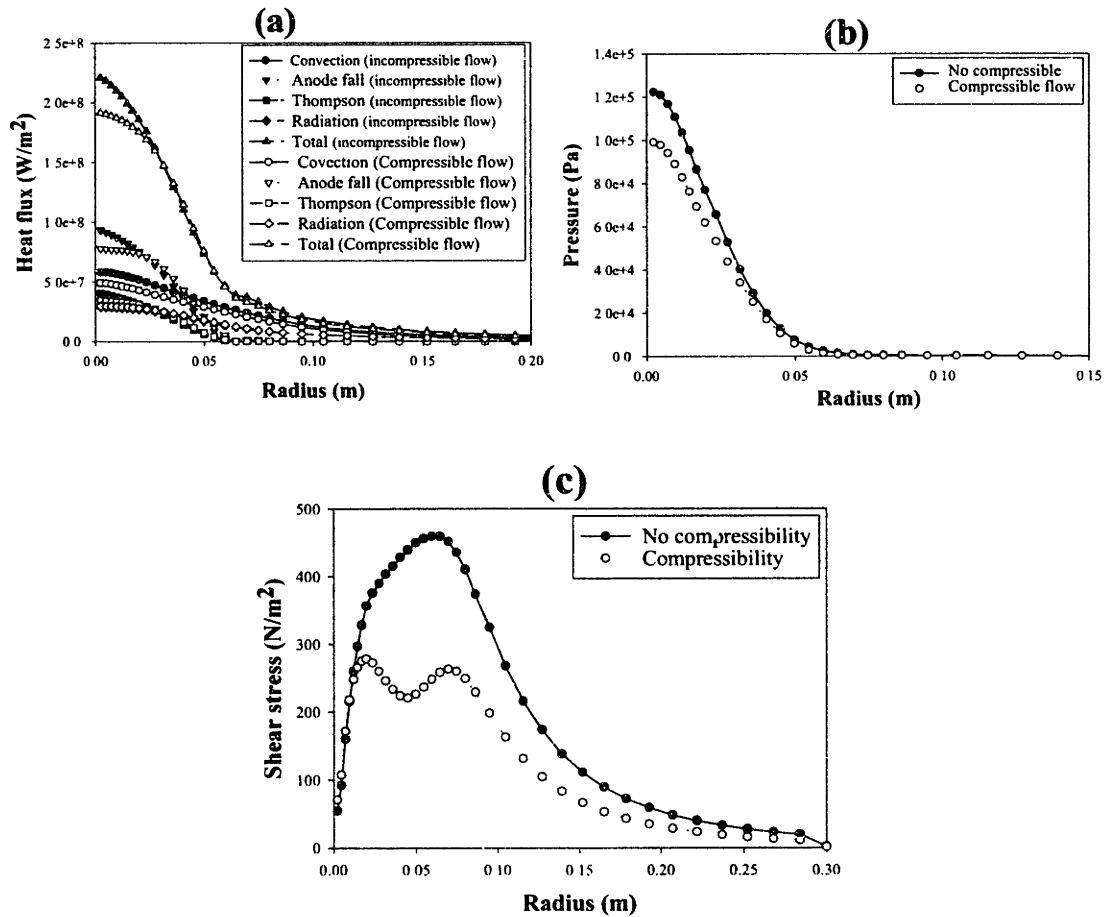


Fig 2.3.23 Effect of compressibility on arc-bath interactions. (a) Heat fluxes. (b) Pressure. (c) Shear stresses.

It seems that compressibility effects are very important and it was demonstrated that their inclusion leads to somewhat different arc results. However, since there are not any experimental measurements from actual EAFs, no conclusive evidence exists indicating that calculations including compressibility represent the most realistic approach. Inclusion of compressibility effects in our model is limited to this section, meaning that the remaining of results and analysis presentation will continue without considering compressibility. The main reason for not including compressible flow in subsequent results is because the convergence behavior of the arc model is significantly affected when compressibility is considered. And in fact, under certain conditions it is practically impossible to obtain converged solutions.

### **Section 2.3.3.5: Effect of Neglecting Induced Currents**

Induced currents are expected to appear in the arc region, under conditions prevailing inside the arc. Therefore, in this section, instead of justifying the adoption of induced currents, an examination of their effect on arc characteristics is conducted by including a calculation of the standard arc (40 KA and 0.25 m) without considering induced current and then contrasting it with the same representation but including induced components of current.

If induced currents are not included in the formulation, the electromagnetic problem significantly simplifies and the couplings between electromagnetic and fluid flow phenomena becomes simpler. The potential conservation equation is reduced from the Poisson representation (equation 2.1.13) to a Laplacian representation (equation 2.2.3). Ohm's law changes from equation 2.1.12 to a simpler form expressed as:

$$J = \sigma E \quad (\text{eq. 2.3.7})$$

Figure 2.3.24 compares arc temperature and velocity fields for case considering ((a) and (c)) and not considering ((b) and (d)) induced currents. Regarding temperature fields, a maximum temperature of 28000 K is obtained without induced currents, instead of 27000 K when they are considered. However, similar profiles are obtained all over the domain, except close to the cathode and at the symmetry axis, where induced currents force the isotherms to align almost parallel to the axis, situation that does not occur when induced components of current are taken into account. In contrast, similar maximum velocities are obtained (8395 m/s and 8553 m/s) whether induced currents are considered or not. Also, the jet profiles shown in Figures 2.3.24 (c) and 2.3.24 (d) appear to be very similar, except that the arc expansion is larger when induced currents are included.

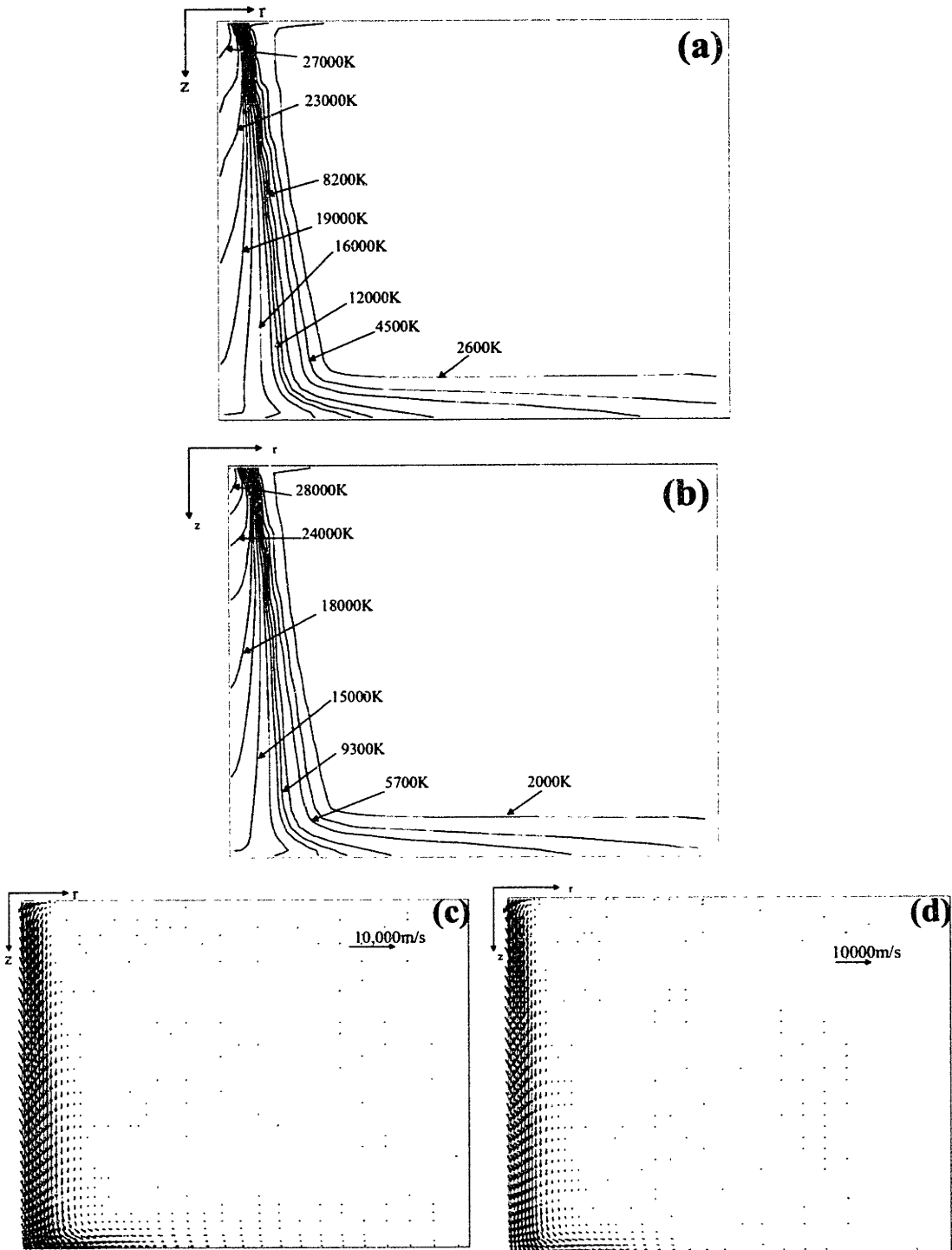


Figure 2.3.24 Effect of induced currents on arc properties. (a) Arc temperature field with induced currents. (b) Arc temperature field without induced currents. (c) Arc velocity field with induced currents. (d) Arc velocity field without induced currents.

The computed electric quantities reflect clearly the effect of the induced currents as illustrated in Figure 2.3.25 (a) to 2.3.25 (f), which shows electric potential, electric current distribution and magnetic flux density fields with and without the influence of induced currents. In Figures 2.3.25 (a) and (b) it is clearly seen that induced currents play an important role in the electric potential overall balance. The effect is evident when a total voltage drop of 534 V (without induced currents) is compared against 605 V (with induced currents), implying that Poisson representation of electric potential conservation equation (equation 2.1.13) increases the voltage drop due to the extra convective source terms. Also, close to the symmetry axis the effect of induced currents deflects potential lines, which in turn generates a significant increase of the radial current density components that do not appear when induced currents are neglected. Without induced effects, the potential lines are both more horizontal in the arc region (conduction zone) and more vertically oriented outside the conduction region. On the contrary, the induced currents deflect potential lines as can be appreciated by inspection of the fields shown in Figures 2.3.25 (a) and (b).

Similarly, the current density fields reflect their respective potential fields from which they are calculated (Figure 2.3.25 (c) and (d)). As stated before, the effect of including induced effects on the current calculations is the generation of radial current density vectors close to the symmetry axis and axial current density vectors close to both anode and cathode surfaces. Radial components from induced effects are mainly present in the arc column close to the symmetry axis, where maximum velocities are predicted. However, induced radial currents have two components and these arise from different opposing contributions: one calculated from the derivative of the potential field components with respect to radial distance (radial component of current density), which points in the radial negative direction. This first term does not appear when induced effects are not considered since the potential lines are horizontal. The second contribution of the radial induced current density comes from the cross product  $V \times B$  that points in the radial positive direction. It is evident from the induced current density field shown in Figure 2.3.25 (c) that the first term dominates. Finally, magnetic flux density fields, which are intimately related to the axial component of the current density, are presented in Figure 2.3.25 (e) and (f) including and not including induced effects, respectively. Induced effects deflect iso-lines of magnetic flux density which otherwise would be straight vertical lines outside the conduction zone. Vertical lines indicate that the arc boundary is better defined without induced effects. Potential, magnetic flux density, and current density fields show a longer arc expansion (wider arc radius) when induced currents are considered.

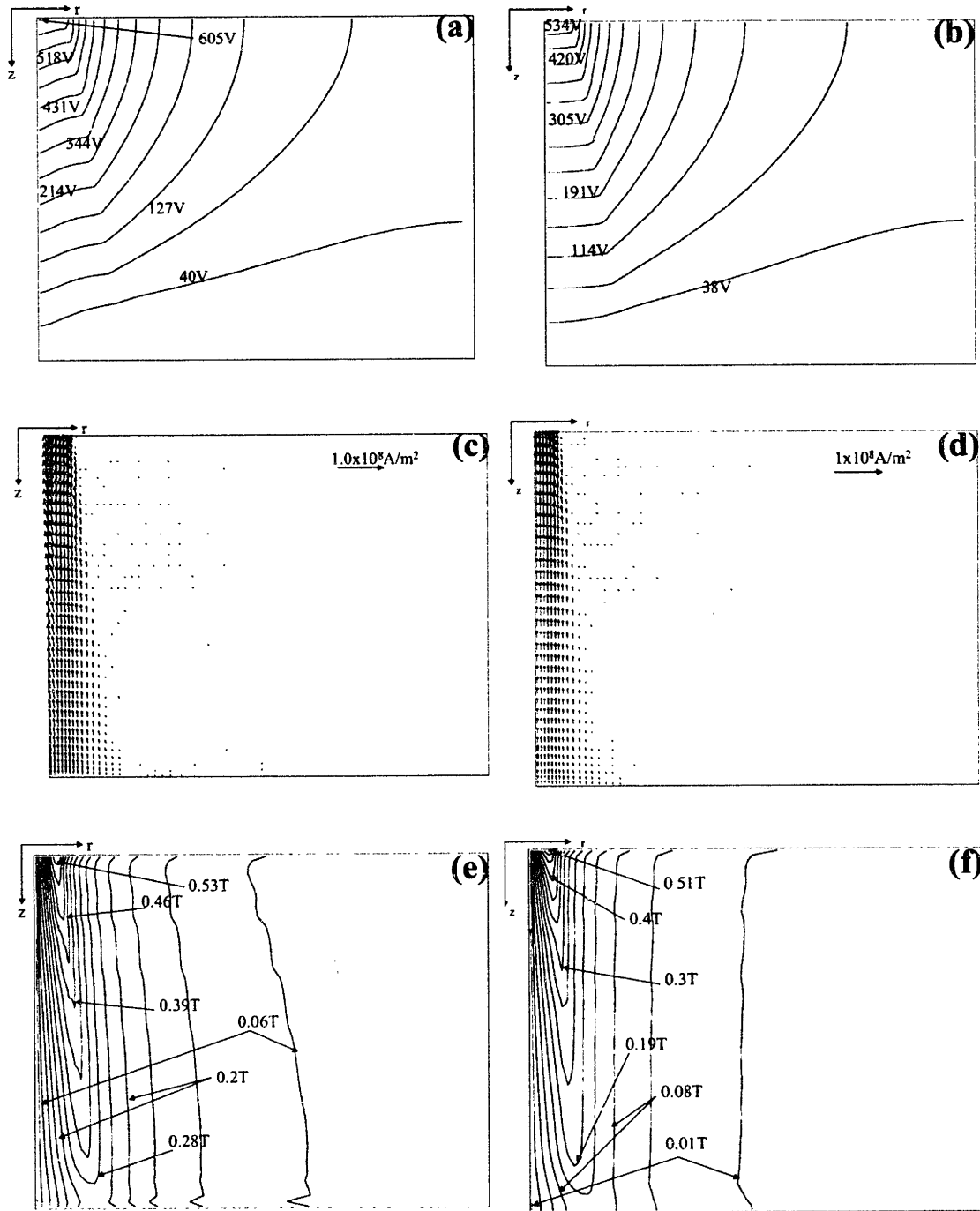


Figure 2.3.25 Effect of induced currents on arc properties. (a) Electric potential with induced currents. (b) Electric potential without induced currents. (c) Current density field with induced currents. (d) Current density field without induced currents. (e) Magnetic flux density field with induced currents. (f) Magnetic flux density field without induced currents.

Computed arc-bath interactions are presented in Figure 2.3.26 where heat flux and shear stress profiles are plotted along the bath surface. Heat fluxes are very similar including or not including induced

effects. Perhaps only convection slightly varies in Figure 2.3.26 (a). The effect of the jet velocity is illustrated in Figure 2.3.26 (b) showing that shear stresses increase when induced effects are considered.

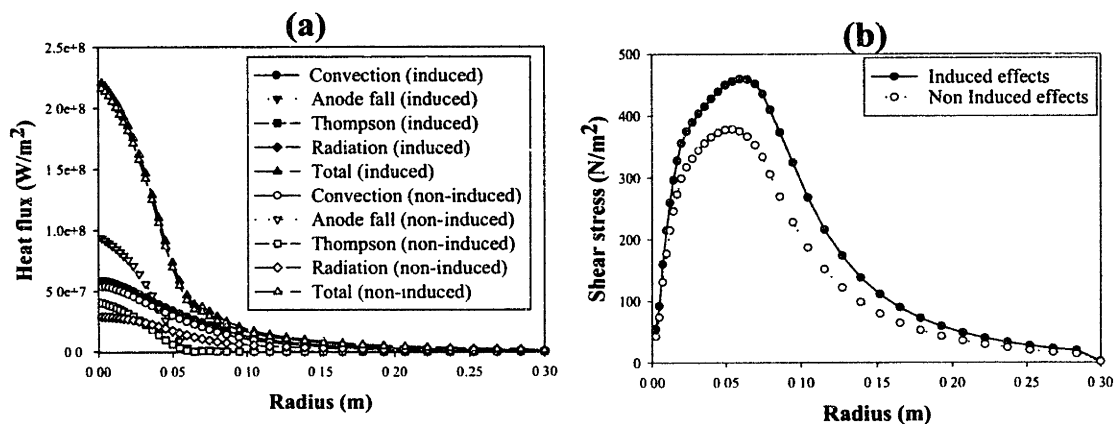


Figure 2.3.26 Effect of induced currents on arc-bath interactions. (a) Heat fluxes at the anode. (b) Shear stresses at the anode.

## **Section 2.3.4: Process Analysis: Effect of the Process Variables on the Arc Behavior**

The previous two sections of this chapter were devoted to give an extensive description of the physics present in air electric arcs and to study specific effects of particular issues and simplifying assumptions involved in the mathematical formulation. In this section, a detailed study is presented on the effect that important process parameters have on the main arc characteristics. Two main process parameters are selected to characterize electric arc operations: arc current and arc length. In actual furnace operations, the variables that are actually controlled are the arc voltage and arc power, rather than the arc current and arc length. However, the operational variables are intimately related to our selected process variables. Arc power depends on arc voltage and arc resistance or arc current. But the arc resistance is definitely a function of arc length. What happens in real operations is that the operator selects a voltage (voltage tap) and, the arc current and arc length are adjusted automatically by the system to meet the furnace arc power and voltage. In our computations, an opposite sequence is used. Arc length and current are selected first and the voltage (and consequently the arc power) is obtained from the computation. This approach may lead to arc powers that are beyond real arc powers used in commercial furnaces. However, this approach allows us to gain physical understanding of the system, as will be shown in the following sections.

In order to test the effect of these two main process parameters, a set of computations were run varying both arc length and arc current. Five different arc lengths and four different arc currents were employed trying to cover a wide range of practical conditions. Values used for current are 36 KA, 40 KA, 44 KA, and 50 KA; while arc lengths employed are 0.15 m, 0.2 m, 0.25 m, 0.3 m, and 0.35 m.

### **Section 2.3.4.1: Effect of Arc Current on Arc Characteristics and Arc-Bath Interactions**

#### **Arc Characteristics**

The first arc parameter to be analyzed is the arc current. The first variable considered is the velocity along the symmetry axis, presented in Figures 2.3.27 where the effect of varying arc current (from 36 KA to 50 KA) is analyzed for a constant arc length of 25 cm. As seen in the plot, as the current increases the velocity increases. However, differences are more evident in the arc column rather than close to the cathode and bath surfaces.

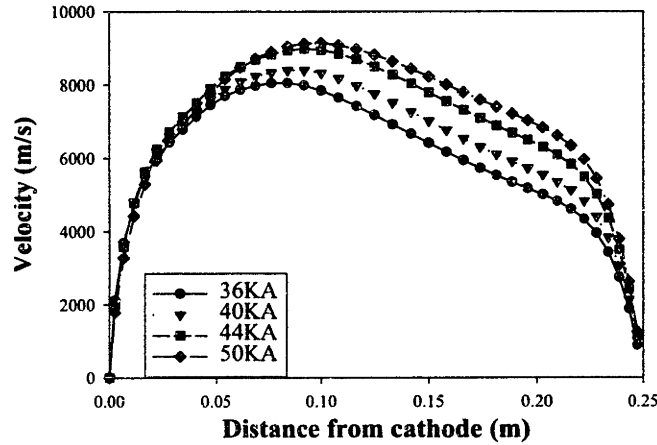


Figure 2.3.27 Effect of the arc current on axial velocity profile along the axis for constant arc length of 25 cm.

Temperature profiles along the symmetry axis are presented in Figure 2.3.28 as a function of arc current for an arc length of 25 cm. As the arc current increases, the energy dissipated by Joule heating effect also increases, and, consequently, the temperature in the arc increases as seen in the profiles shown in the figure. However, temperature differences are small and only apparent in the arc column.

The corresponding arc pressure variations with arc current along the symmetry axis are presented in Figure 2.3.29. As seen in the plots, increasing arc current produces an arc pressure increase. At the cathode, this increase should be associated with an increase in body forces, while, at the bath, the increase in pressure is due to a greater thrust of the impinging arc jet.

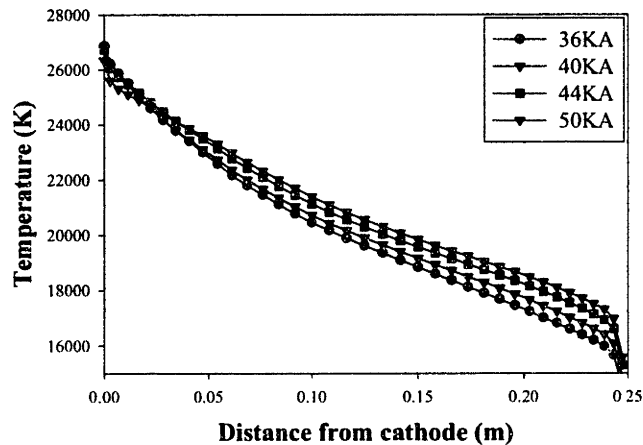


Figure 2.3.28 Effect of the arc current on temperature profile along the axis for an arc length of 25 cm.



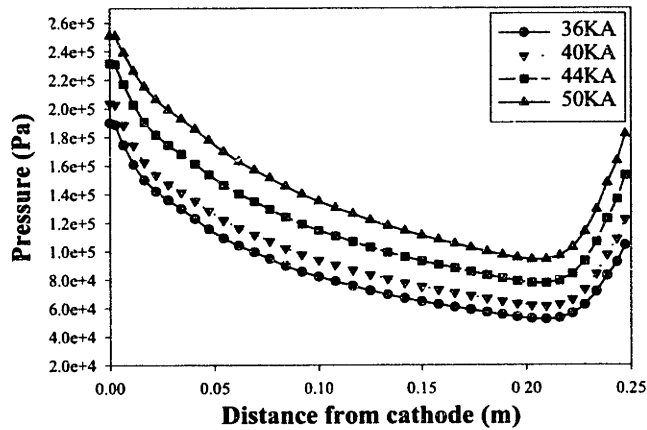


Figure 2.3.29 Effect of the arc current on arc pressure for a constant arc length of 25 cm.

As expected, the arc current density is greatly affected by the arc current used. Figure 2.3.30 shows radial profiles of axial current density at three different axial locations from the cathode (4.5, 14.5 and 23.1 cm) for an arc length of 0.25 m and different arc currents. This figure shows that the farther the location from the cathode, the wider are the current density distribution and, consequently, the lower the current densities. It is also appreciated that the current density increases as the arc current increase, for the same axial position. It is also noticed that wider distributions are obtained with higher currents at the same axial position.

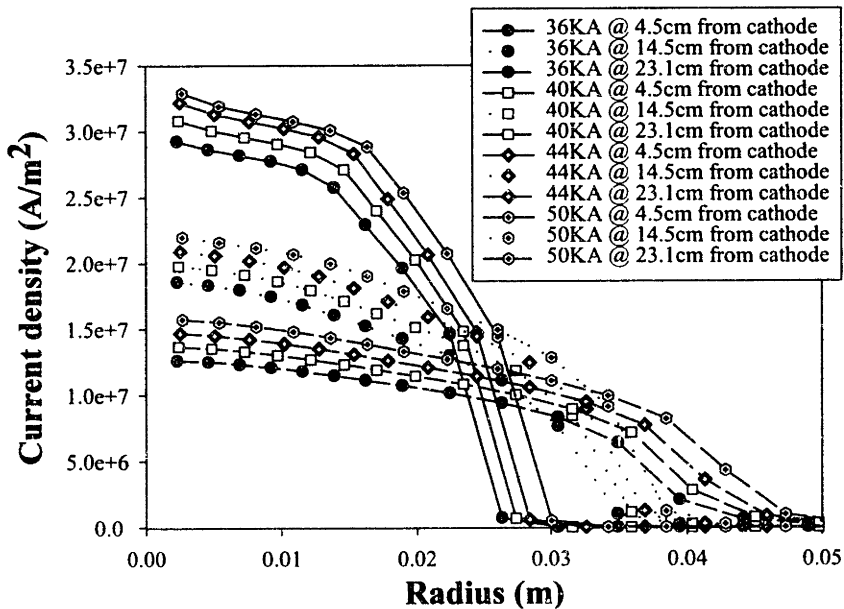


Figure 2.3.30 Effect of the arc current on axial current density for arc length of 25 cm. In the plots axial current density at three different positions is presented for each current: (a) 4.5 cm, (b) 14.5 cm, (c) 23.1 cm.

The effect of arc currents on the magnetic flux density for an arc length of 25 cm is shown in Figure 2.3.31, at four different axial positions of 5 cm, 12.5 cm and 20 cm from the cathode, as well as at the bath surface. The general trends observed for the magnetic flux density show how increases as the arc current increase. As explained in previous sections, the magnetic flux densities increases in the arc region until it reaches a maximum value at the arc radius and then decrease at a rate proportional of  $1/r$  as the radius increases. Maximum magnetic flux density values increase as the arc current increases and the radial position where this maximum is located also increases as the arc current increases. This last point can be better appreciated by the curves for the locations 20 cm from the cathode and the bath surface (Figures 2.3.31 (c) and (d), respectively). Of course, a higher current in the arc results in a wider arc region and higher values of the magnetic flux density, as previously shown. Also, as the distance from the cathode increases, the magnetic flux density values in the fields decrease due to arc expansion (the curves become less steep.)

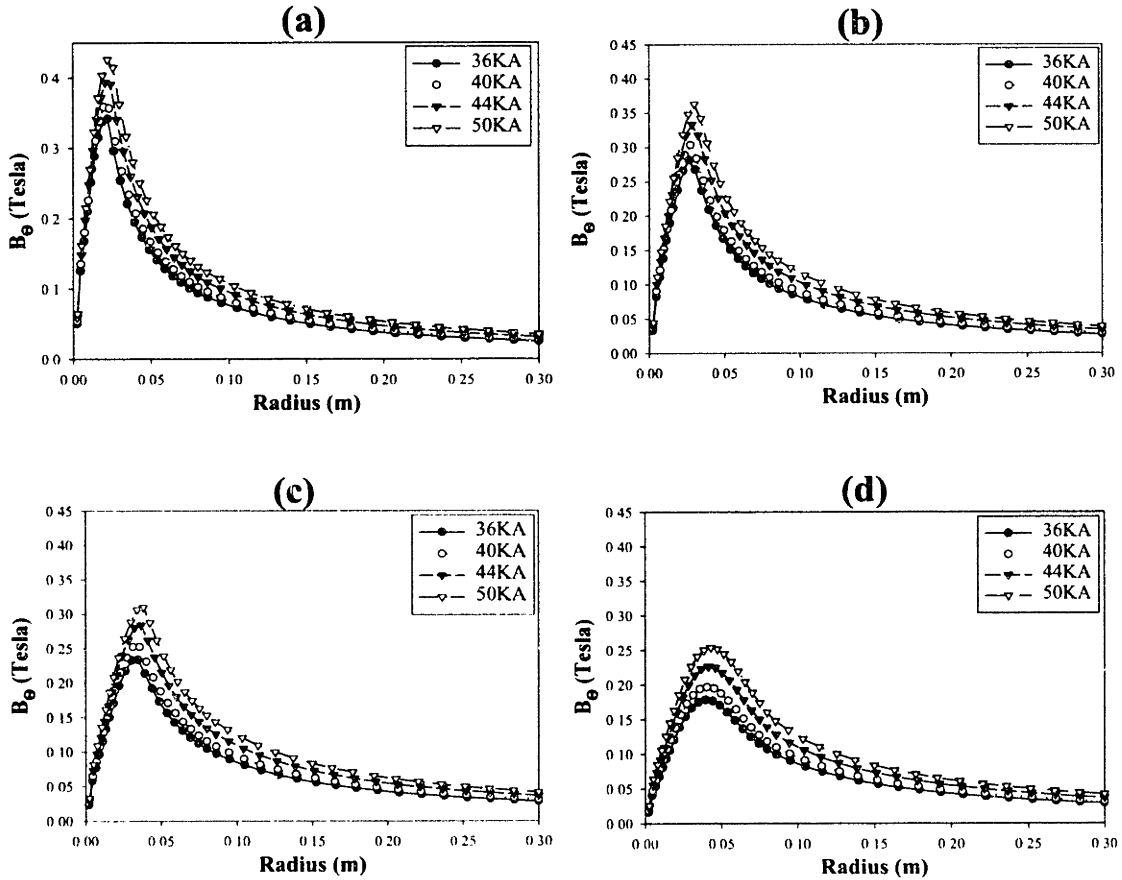


Figure 2.3.31 Effect of the arc current on  $B_\theta$  radial profiles for an arc length of 0.25 m at four different axial positions: (a) 5 cm, (b) 12.5 cm, (c) 20 cm, (d) at bath surface.

## Arc-Bath Interactions

Arc-bath interactions are also very sensitive to variations of arc current. Intuitively, the arc current density at the bath is expected to have a linear relationship with arc current. Figure 2.3.32 shows predicted arc current density profiles at the bath surface for a constant arc length of 25 cm and the various currents employed in the study. As expected, the arc current density at the bath increases as arc current increases for a given arc length. However, it is interesting to note that the current density distributions at the bath have the same radial extent for a given arc length regardless of the arc current (~8 cm for a 25 cm arc length).

Figure 2.3.33 shows predicted heat fluxes at the bath surface for an electric arc of 25 cm and all the currents: (a) 36 KA, (b) 40 KA, (c) 44 KA, and (c) 50 KA.

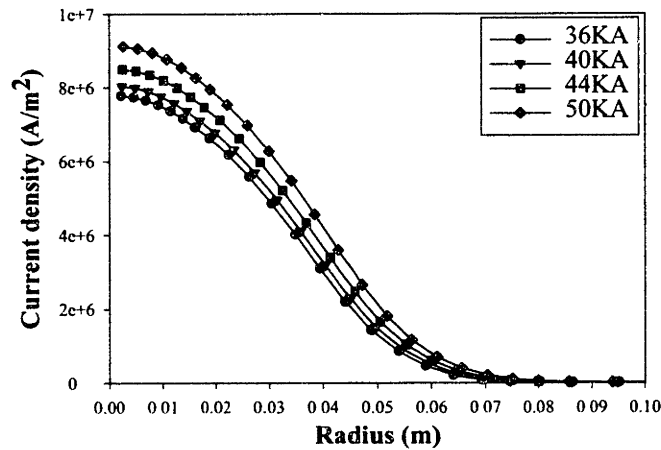


Figure 2.3.32 Effect of the arc current on current density at the bath surface for the four arc currents employed and an arc length of 25 cm.

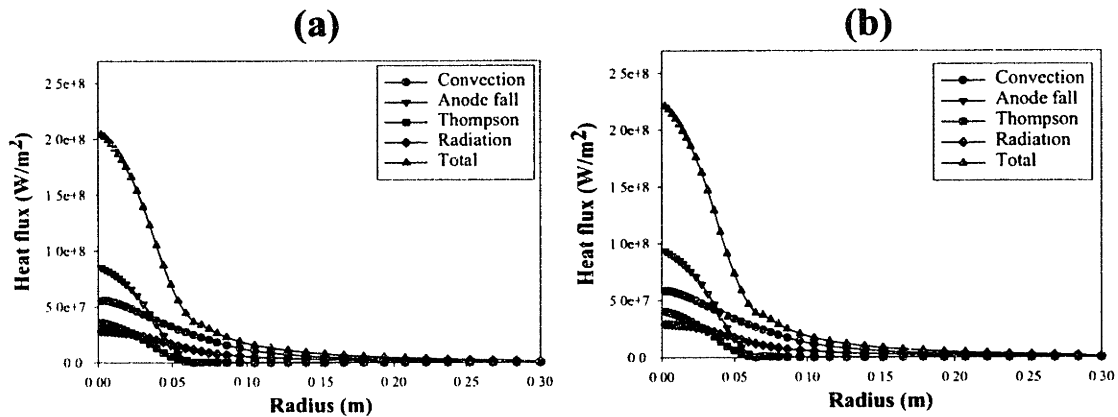


Figure 2.3.33 Effect of the arc current on heat flux at the bath surface for the different arc currents employed in this study and an arc length of 25 cm. (a) 36 KA. (b) 40 KA.

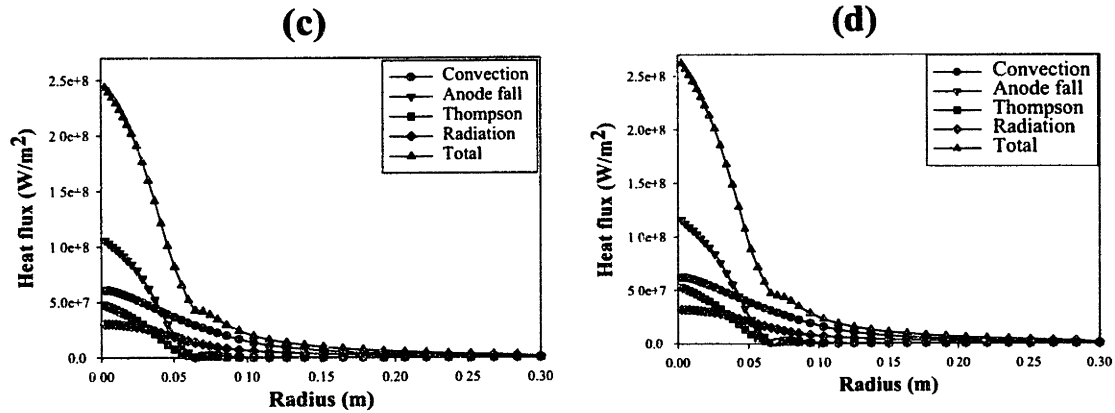


Figure 2.3.33 (cont.) Effect of the arc current on heat flux at the bath surface for the different arc currents employed in this study and an arc length of 25 cm. (c) 44 KA. (d) 50 KA.

From the plots presented in Figure 2.3.33, it is concluded that an increase in the arc current results in an increase of the maximum total heat flux at the bath for a constant arc length. However, when the different contributions to heat transfer are closely inspected, the electronic and convective contributions seem to be affected by arc current while radiation is unaltered by arc current. It should be mentioned that due to the cylindrical nature of the system, the fact that the electronic contribution exceeds by far the other mechanisms at the center does not mean that this is the most important contribution. The last statement can be illustrated more evidently if the cumulative heat flow contributing mechanisms are plotted as a function of radius as shown in Figure 2.3.34 (a) to (d) for all currents tested in this study and with the same arc length of 25 cm. The total heat flow transferred to a of 0.3 m of radius circular area increases with of arc current (from 2 MW at 36 KA to almost 3 MW for a 50 KA arc current), keeping the arc length constant at 0.25 m. Inspection of the different heat transfer contributions indicates that radiation remains basically constant and independent of the arc current. On the contrary, convection and electronic contributions increase as the arc current increases. The electronic contribution definitely depends on the arc current since this heat is proportional to the arc current. But convection increases with arc current due to the higher plasma velocities as the current increases.

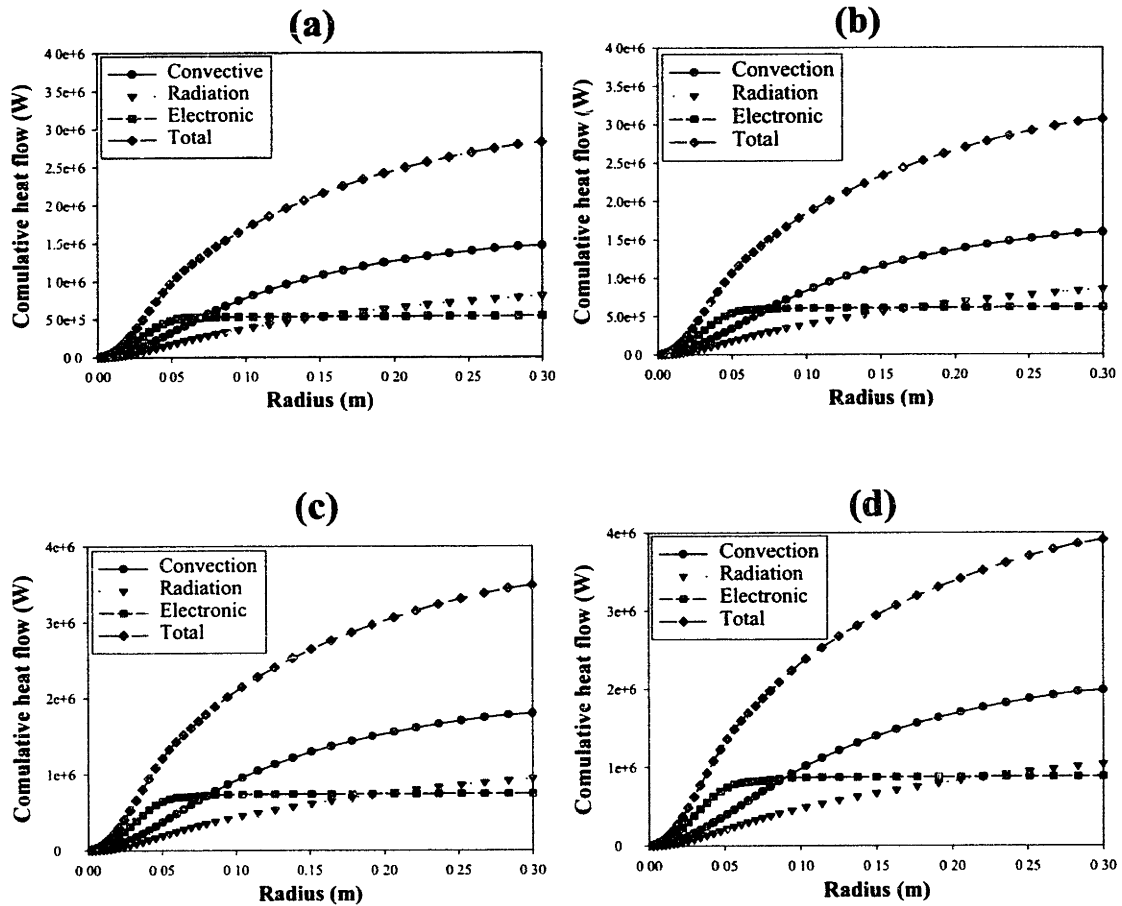


Figure 2.3.34 Effect of the arc current on cumulative heat flow at the bath surface for all the currents employed in this study and an arc length of 25 cm. (a) 36 KA. (b) 40 KA. (c) 44 KA. (d) 50 KA.

Predicted shear stresses at the bath surface for all arc currents employed in the analysis and an arc length of 25 cm are presented in Figure 2.3.35. An increase in the arc current induces an increase in shear stress. All the curves in Figure 2.3.35 start from zero at the axis but increase rapidly until reaching a maximum. This maximum depends on the arc current ( $\sim 280 \text{ N/m}^2$  for 36 KA to  $\sim 470 \text{ N/m}^2$  for 50 KA) and the radial position of the maximum is almost the same for all cases ( $\sim 7 \text{ cm}$ ) but a slight displacement to the right is observed as the arc current increases. Finally, the shear stresses rapidly decrease after the maximum is reached and approach asymptotically to zero at longer distances.

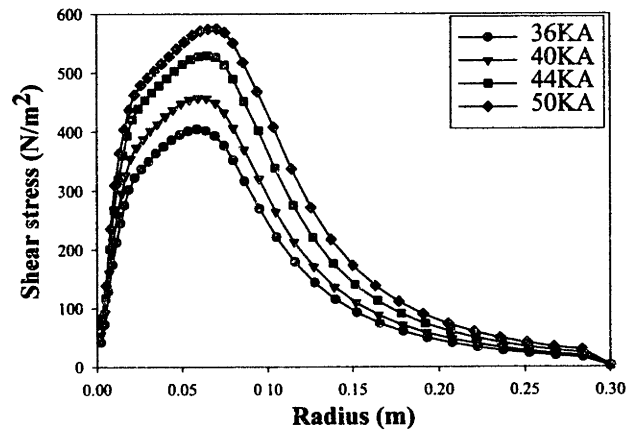


Figure 2.3.35 Effect of the arc current on shear stress at the bath surface for the four arc currents employed in this study and a constant arc length of 25 cm.

Figure 2.3.36 shows predicted anode temperatures as a function of radius for different arc currents and arc length of 25 cm. The temperature profiles at the anode show similar trends with slightly higher values as the arc current increases.

Predicted arc pressures at the bath surface are presented in Figure 2.3.37 for the different currents and the arc length of 25 cm. Again, as in almost all variables analyzed so far, arc pressure at the bath increases with an increase in arc current. A similar trend as that followed by arc current density (Figure 2.3.32) is obtained for arc pressure, as expected. Increasing arc current increases arc pressure due to the effect that arc current has on arc velocity.

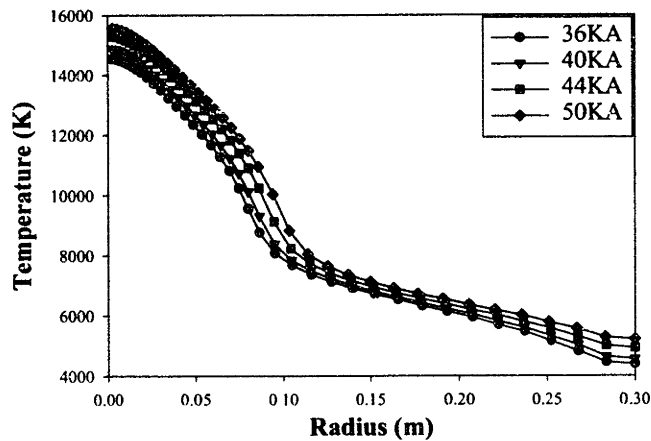


Figure 2.3.36 Effect of the arc current on temperature at the bath surface for the four arc currents employed in this study and a constant arc length of 25 cm.

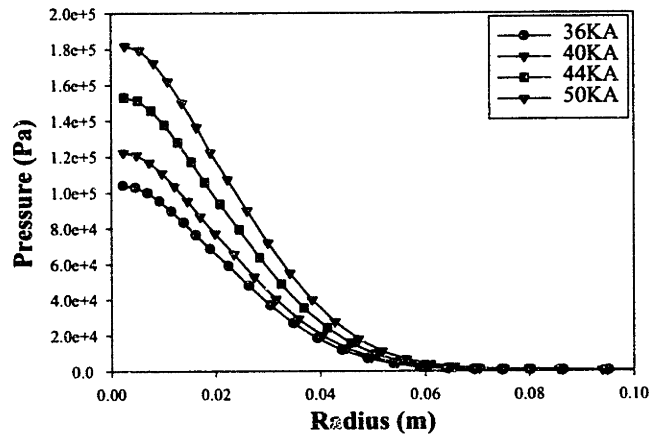


Figure 2.3.37 Effect of the arc current on arc pressure at the bath surface for the four arc currents employed in this study and a constant arc length of 25 cm.

### Section 2.3.4.2: Effect of Arc Length on Arc Characteristics and Arc-Bath Interactions

The previous section studied the effect of arc current on arc characteristics and arc-bath interactions. In that analysis, a constant arc current was used, so variations were considered due to arc length a not arc current. In this section, the arc length is the variable under which the arc characteristics and arc-bath interactions are analyzed.

#### Arc Characteristics

Arc jet velocities along the symmetry axis are plotted for different arc lengths (15, 20, 25, 30 and 35 cm) maintaining a constant arc current of 40 KA (Figure 2.3.38). In contrast to the sensitivity of the arc current, the arc length does not affect too much the maximum velocities and maximum positions, although the maximum velocity values increases just a little by increasing arc lengths. What is more affected in these velocity profiles is the velocity at the bath surface that decreases as the arc length increases. In fact, it can be appreciated that the longer the arc is the lower the velocity is due to mixing and expansion of the jet, which results in lower velocities as the distances from the cathode increases. Therefore, increasing arc length helps to further expand the jet by mixing. As stated before, arc currents generate body forces and arc pressure at the cathode, so at the same current no major changes are expected in the arc velocity. However, when the arc length is short (below 15 cm) the arc jet does not have enough space to fully develop when it reaches the bath surface. This is probably why arc velocities are lower for very short arc lengths (15 cm).

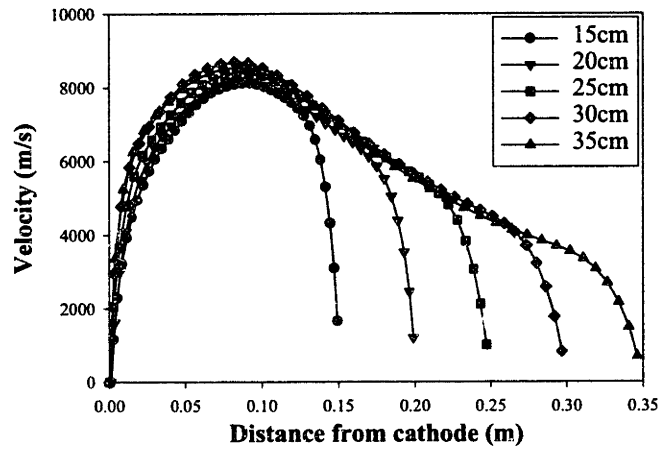


Figure 2.3.38 Effect of the arc length on the axial velocity profile along the symmetry axis with a constant arc current of 40 KA.

Predicted temperature profiles along the symmetry axis are presented as a function of arc length for an arc current of 40 KA in Figure 2.3.39. Practically the same temperature is obtained for all arc lengths. The temperature decreases steadily with distance from the cathode from a maximum value at the cathode to the lowest values at the bath surface as a consequence of arc expansion and the associated decrease in arc current density. Then, the only effect that arc length has on arc temperature, along the symmetry axis, is that, by increasing the arc length, allows further decrease in the arc temperature due to a further arc expansion. Thus, the temperature at the bath decreases as the arc length increases.

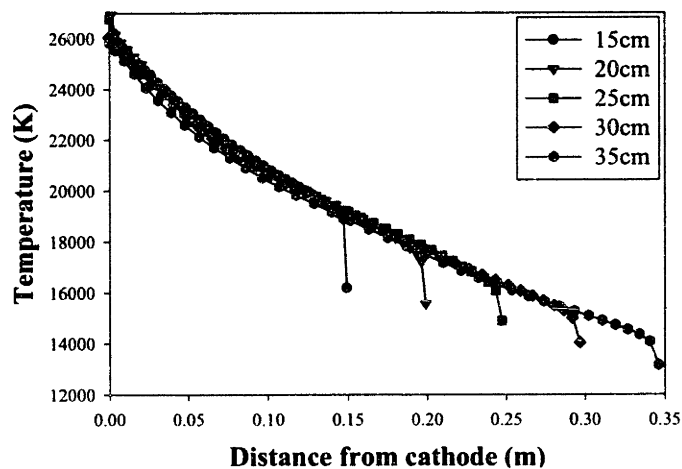


Figure 2.3.39 Effect of the arc length on the temperature profile along the symmetry axis with a constant arc current of 40 KA.



Predicted arc pressure variations with arc length along the symmetry axis for a constant arc current of 40 KA are presented in Figure 2.3.40. As seen in the plots, an increase in arc does not have almost any effect on arc pressure along the axis. But again, due to a greater arc expansion of the arc jet, increasing arc length affects the resulting pressure at the bath. Increasing arc length decreases bath pressure due to the attenuated arc jet. In contrast, the arc pressure at the cathode is not sensitive to the arc length variations and depends exclusively on arc current.

Predicted arc current density profiles along the symmetry axis are presented in Figure 2.3.41. Plots for all arc lengths with 40 KA of arc current are presented in this figure. Similar behavior to the previous variables is found for arc current density along the axis. No major effect is seen as the arc length increases. Larger arc lengths lead to lower current densities at the anode which is consistent with the behavior presented for the other arc variables.

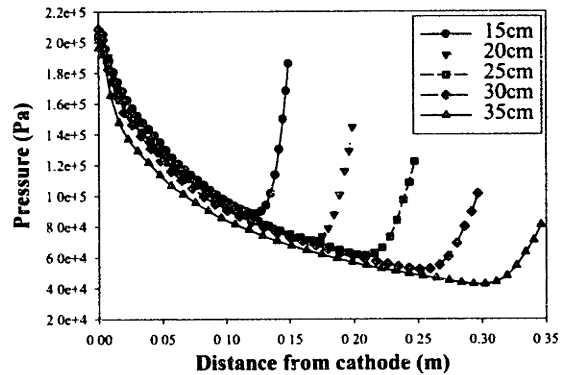


Figure 2.3.40 Effect of the arc length on the pressure profile along the axis with a constant arc current of 40 KA.

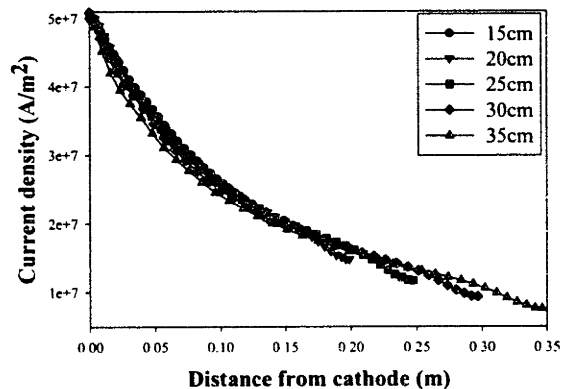


Figure 2.3.41 Effect of the arc length on the current density profile along the axis with a constant arc current of 40 KA.

## Arc-Bath Interactions

Arc-bath interactions are greatly affected by arc length as anticipated by the arc characteristics presented above.

Predicted arc current densities at the anode are plotted in Figure 2.3.42 for different arc lengths (15, 20, 25, 30 and 35 cm) and for a constant arc current of 40 KA. As stated before, longer arc lengths lead to lower current density distributions at the bath. But, since the arc current is the same, the current density distributions are wider as the arc length increases. In this way, the integral of the current density over the circular bath surface area corresponds to 40 KA. Therefore, larger arc lengths give lower maximum current densities at the center, but with wider distributions.

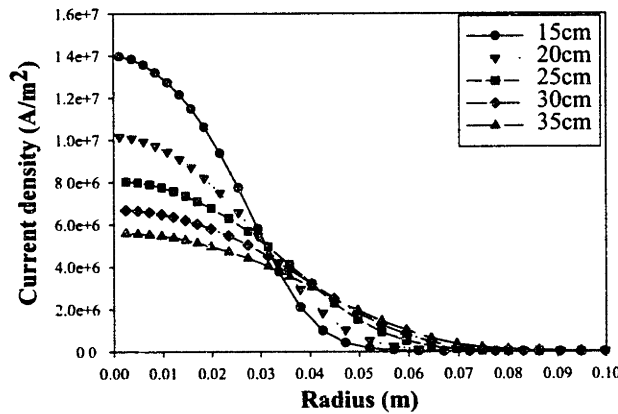


Figure 2.3.42 Effect of the arc length on the current density profile at the bath surface with a constant arc current of 40 KA.

Predicted heat fluxes at the bath are presented in Figure 2.3.43 for an electric arc of 40 KA and for different arc lengths of 15 (a), 20 (b), 25 (c), 30 (d), and 35 cm (e). It can be appreciated that as in the case of current densities at the bath, maximum total heat fluxes at the center strongly decrease with increasing the arc length (from 350 MW/m<sup>2</sup> to ~150 MW/m<sup>2</sup>). But, similarly, the distributions are wider as the arc length increases. Convective, radiation and electronic contributions (anode fall and Thompson effect) all have lower maxima at the center as the arc length increases, but, at the same time, show wider distributions in the radial direction. Cumulative heat flows from the arc to the bath surface are presented in Figure 2.3.44 for the corresponding heat fluxes presented in Figure 2.3.43 (arc of 40 KA and arc lengths of 15, 20, 25, 30 and 35 cm). From these plots can be appreciated how the total heat contribution from each mechanism is affected by arc length variations. It is not surprising that despite the fact that the maximum heat fluxes are predicted for shorter arcs, the total heat flow (integral over the bath area) increases as the arc length increases (from ~2 MW with an arc length of 15 cm to ~3.5 MW with 35 cm arc length). This is expected

since an increase in the arc length for a constant current leads to an increase in the arc resistance and, consequently, the arc power increases. Convection is the main heat transfer mechanism for all arc length cases. The second most important contribution changes from electronic at short arc lengths to radiation for large arc lengths. What happens is that the total electronic contributions to heat flow are the same regardless the arc length, since only an arc current of 40 KA is considered. In contrast, radiation increases significantly from short to long arcs, being very low for a 15 cm arc length (slightly lower than electronic contribution), but changes to very high values at large arc lengths (twice the electronic contribution at 35 cm arc length).

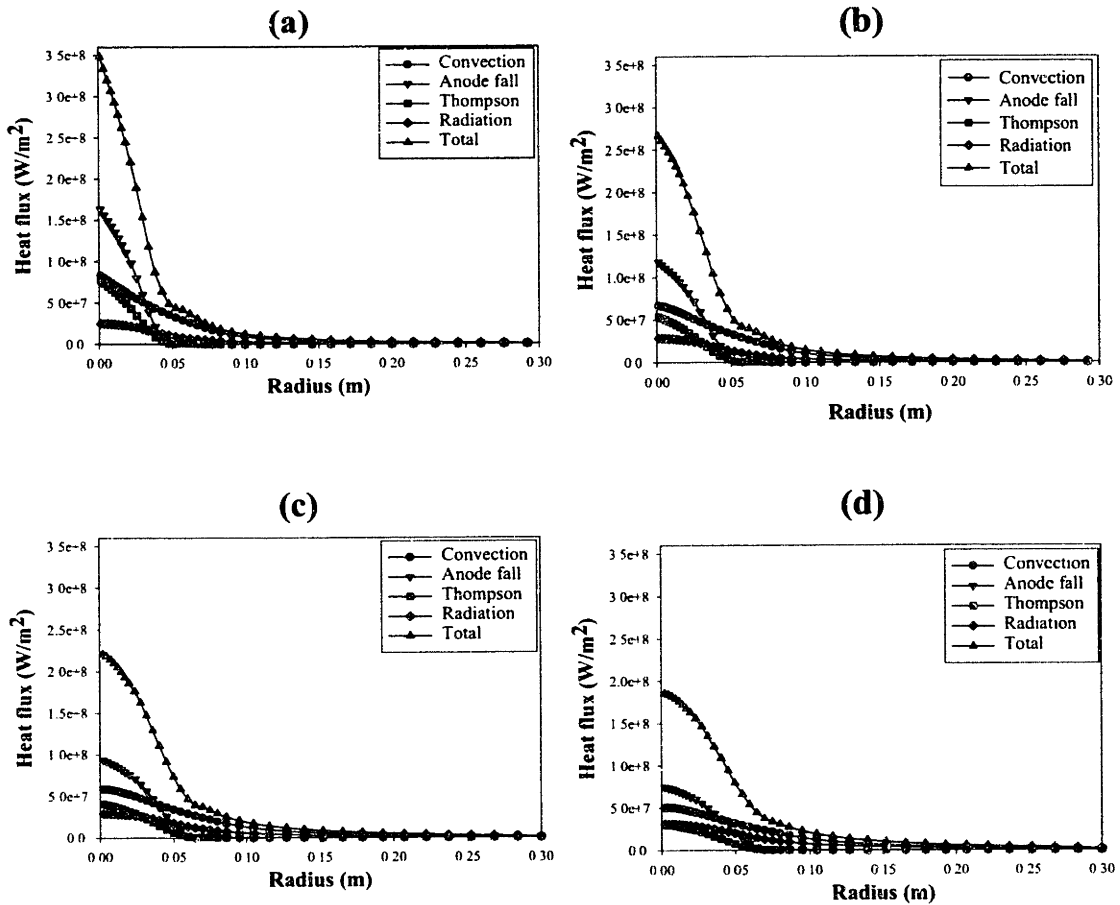


Figure 2.3.43 Effect of the arc length on the heat flux at the bath surface for an arc current of 40 KA and different arc lengths: (a) 15 cm, (b) 20 cm, (c) 25 cm, (d) 30 cm.

(e)

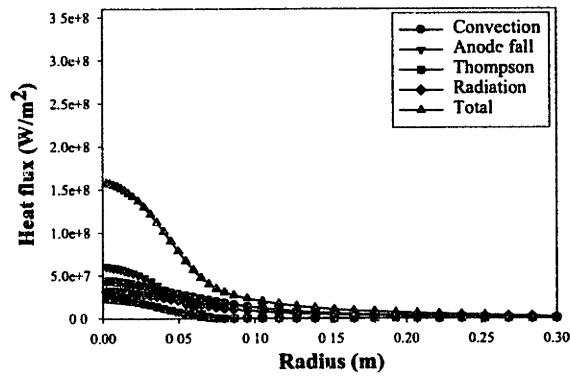
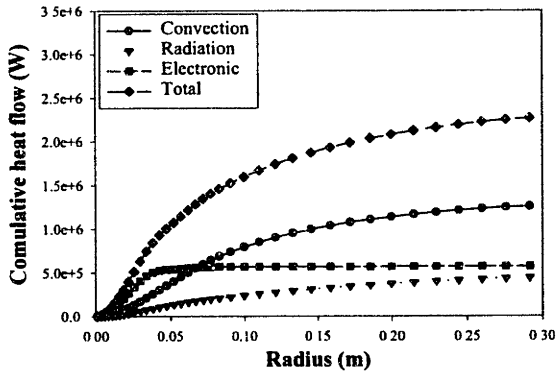
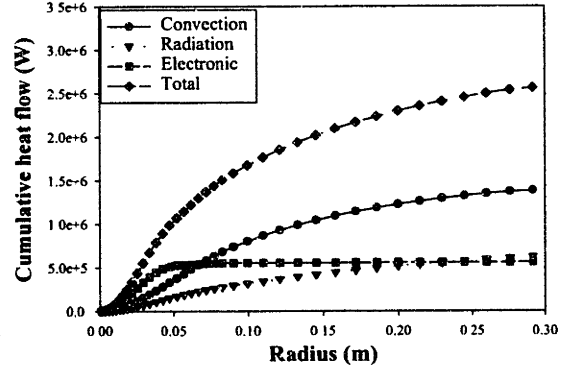


Figure 2.3.43 (cont.) Effect of the arc length on the heat flux at the bath surface for an arc current of 40 KA and different arc lengths: (e) 35 cm.

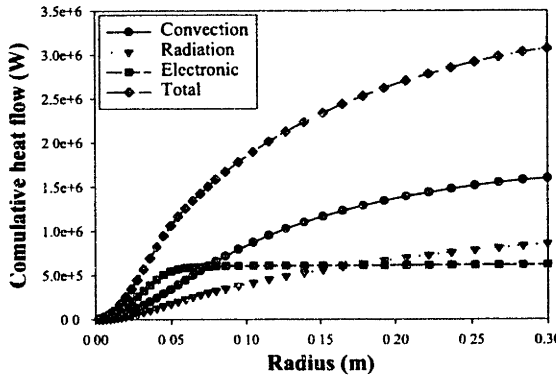
(a)



(b)



(c)



(d)

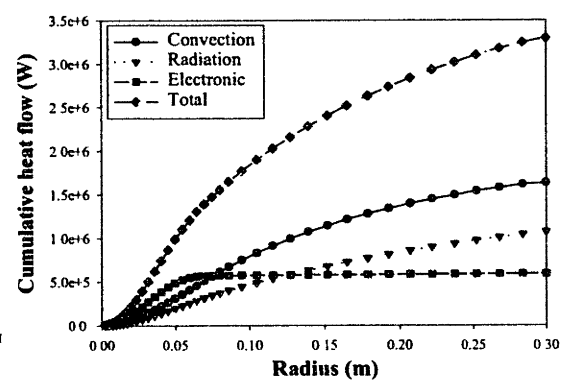


Figure 2.3.44 Effect of the arc length on the heat flow at the bath surface for an arc current of 40 KA and different arc lengths: (a) 15 cm, (b) 20 cm, (c) 25 cm, (d) 30 cm

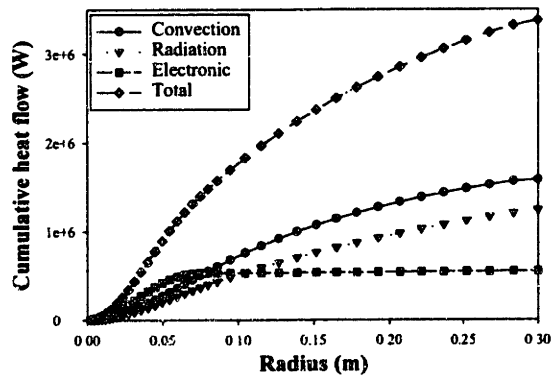


Figure 2.3.44 (cont.) Effect of arc length on the heat flow at the bath surface for an arc current of 40 KA and different arc lengths: (e) 35 cm.

Predicted shear stresses at the bath surface are presented in Figure 2.3.45 for different arc lengths under an arc current of 40 KA. Maximum shear stresses decrease with increasing arc length. But the radial position at which this maximum appears is displaced to the right with an increase in the arc length. Then, for an arc length of 15 cm, a high maximum value of  $\sim 530 \text{ N/m}^2$  with a very narrow distribution is obtained, while for 35 cm of arc length, a maximum of  $320 \text{ N/m}^2$  but with a much wider distribution is predicted.

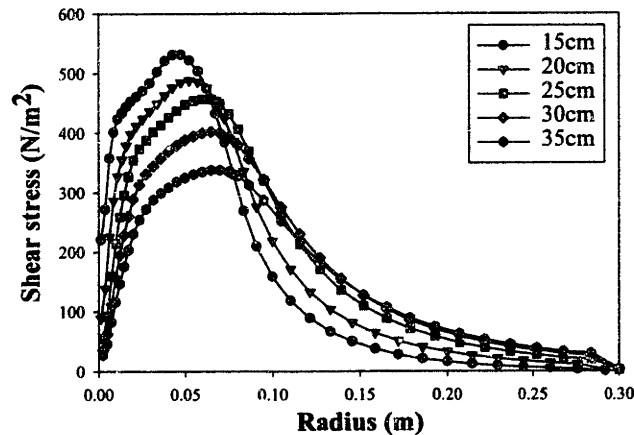


Figure 2.3.45 Effect of the arc length on the shear stress at the bath surface with a constant arc current of 40 KA.

Figure 2.3.46 shows predicted radial profiles of gas temperature at the bath surface for different arc lengths and for a constant arc current of 40 KA. At the symmetry axis and up to a radial distance of  $\sim 8$  cm, the gas temperature at the bath increases as the arc lengths decreases. For a 15 cm arc length, a maximum temperature above  $16000 \text{ K}$  is obtained at the center, while for an arc length of 35 cm,  $\sim 13000 \text{ K}$

at the center is predicted, i.e. more than 2000 K of difference between maximum temperatures corresponding to 15 and 35 cm arc lengths, respectively.

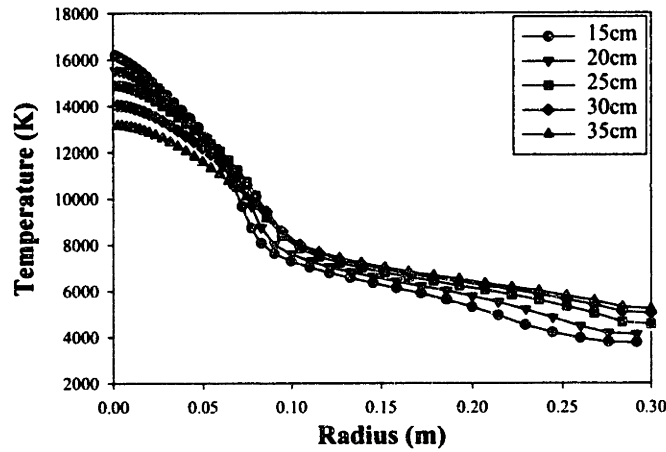


Figure 2.3.46 Effect of the arc length on the arc temperature at the bath surface with a constant arc current of 40 KA.

The opposite behavior is observed for longer radial distances, approximately 8 cm from the center, i.e. the gas temperature increases with an increase in arc length. This change in behavior after 10 cm is explained in terms of mixing and the effect of arc length on arc current and arc temperature along the axis. Temperatures at the axis decrease with arc length due to arc expansion, which leads to lower current densities. Then it is consistent to find higher temperatures at the center for shorter arcs. But larger arcs are better mixed than shorter arcs since hot gases are contained in larger arc regions (bigger volume). Therefore, hot gases are extended to larger radius for larger arc lengths. This explains why the temperatures beyond ~10 cm increase with an increase in arc length.

Finally, the predicted arc pressure at the bath surface as a function of radial position is presented in Figure 2.3.47 for electric arcs with different arc lengths and arc current of 40 KA. A similar behavior to the current density profiles is observed in this plot. Maximum arc pressures at the center increase as the arc length decreases, but, at the same time, the arc pressure profiles become wider as the arc length increases.

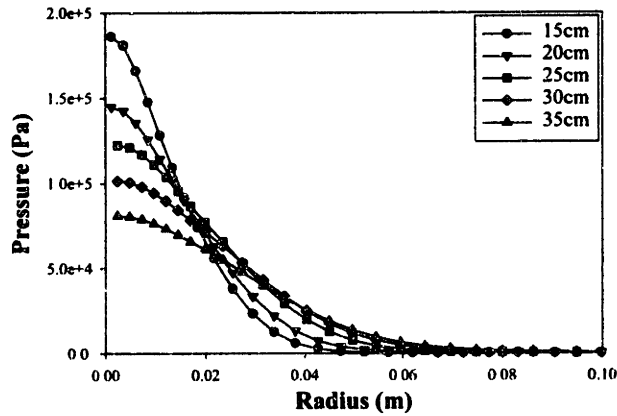


Figure 2.3.47 Effect of the arc length on the pressure at the bath surface with a constant arc current of 40 KA.

## Section 2.4: Discussion and Summary of the Arc Process

The last two sections studied the effects of arc current and arc length on arc characteristics and arc-bath interactions. However, the analysis presented in the previous sections was more qualitative than quantitative. Then, some of the trends in the arc characteristics, that are now apparent and well identified, can be better represented by isolating key characteristics and properties in simpler x-y plots.

### Arc-Bath interactions

Dependencies with arc current and arc length of current density, heat flux, arc pressure, and shear stress at the bath surface as well as voltage drop through the arc column are presented in this section.

Figure 2.4.1 shows the maximum total heat fluxes at the bath surface as a function of arc current (a) and arc length (b). Each line in Figure 2.4.1 (a) represents a different arc length and, by analogy, each line in Figure 2.4.1 (b) represents a different arc current. A linear dependency is observed between the maximum heat flux and the current for any arc length. Increasing the arc current increases the maximum heat flux at the bath. Regarding the arc length dependency, the maximum heat flux at the bath decreases with increasing arc lengths, but the dependency is not linear. It can be concluded that the arc length has a greater effect on the maximum heat flux at the bath than the arc current.

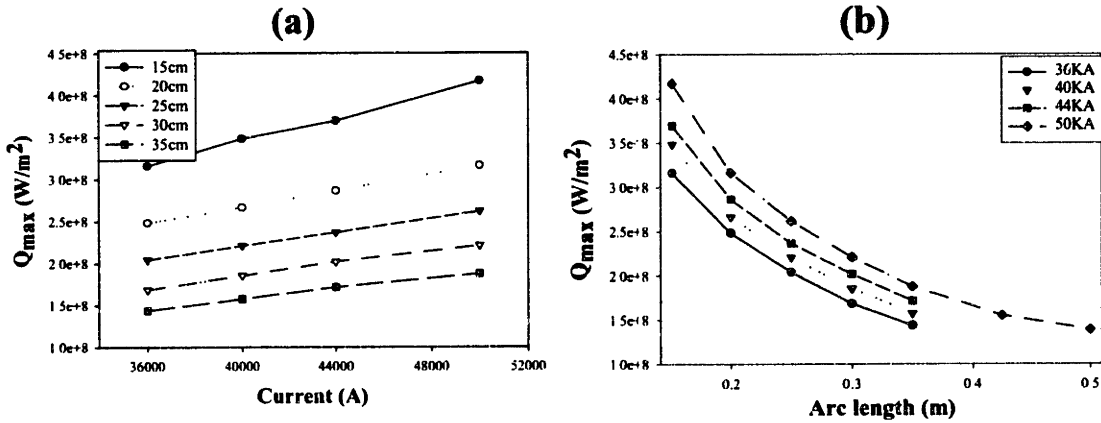


Figure 2.4.1 Maximum heat fluxes at the bath as a function of the two main process parameters: (a) Arc current. (b) Arc length.

Figure 2.4.2 presents the total heat input to the bath surface as a function of current (Figure 2.4.2 (a)) and arc length (Figure 2.4.2 (b)). The total heat flow increases linearly as the current increases as shown in Figure 2.4.2 (a). The lines in that figure represent constant arc lengths and lower lines correspond to shorter arcs. Then, increasing arc length has the effect of increasing the amount of heat to the bath, but this increase is not linear as can be seen by the separation between the parallel lines. This same behavior can be seen in Figure 2.4.2 (b), where the total heat flow is plotted as a function of the arc length and shows that increasing the arc length increases the total heat, but the curves become asymptotic increase for large arc lengths. For short arcs, an increase in the arc length produces a bigger increase in the heat flow, as compared to that for large arc lengths. Each line represents a different arc current and higher current lines represent higher total heat flows transferred to the bath.

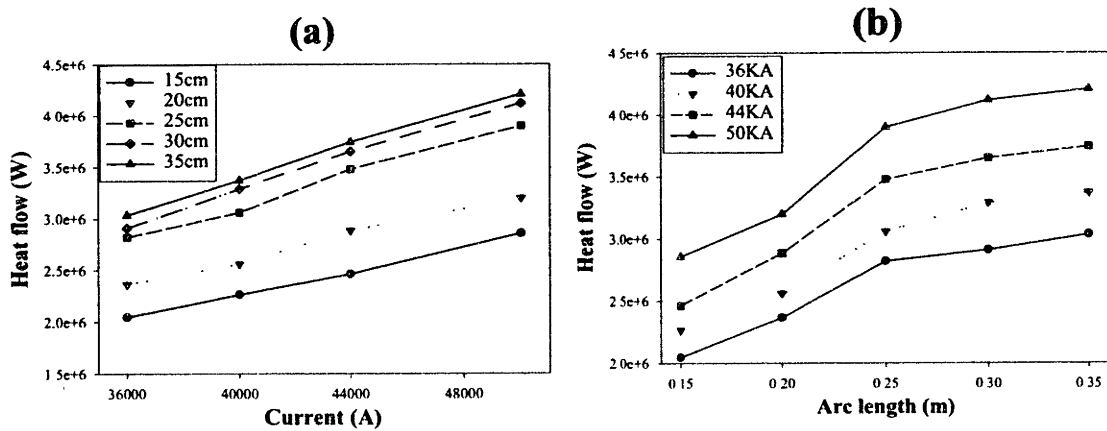


Figure 2.4.2 Total heat flow from the arc to the bath as a function of the two main process parameters: (a) Arc current. (b) Arc length.



Figure 2.4.3 presents the total voltage drop through the electric arc as a function of current (Figure 2.4.3 (a)) and arc length (Figure 2.4.3 (b)). The voltage drop increases slightly with arc current as described by the small slopes of the linear relationships presented in Figure 2.4.3 (a). The lines represent different arc lengths. Increasing the arc length increases the voltage drop for the same current, which can be interpreted as an increase in the arc power (Arc power =  $V \times I$ ). Figure 2.4.3 (b) shows the voltage dependence with arc length, where it is clear the linear dependence between the voltage drop and arc length. Increasing the arc length leads to an increase in the voltage drop for a constant current. However, the slope in the lines presented in Figure 2.4.3 (b) is much steeper than the slopes in Figure 2.4.3 (a). Then, these results show that the arc length has a greater influence on the arc power than the arc current. However, the arc power is not an indication of how much heat is transferred to the bath as shown in Figures 2.4.2. This can be appreciated if a careful comparison between Figures 2.4.2 (b) and 2.4.3 (b) is conducted. Arc power increases linearly with arc length for a constant arc current, but heat flow does not increase at the same rate but rather increases asymptotically with arc length (especially for long arc lengths), which indicates a lost in heat transfer efficiency for higher arc powers.

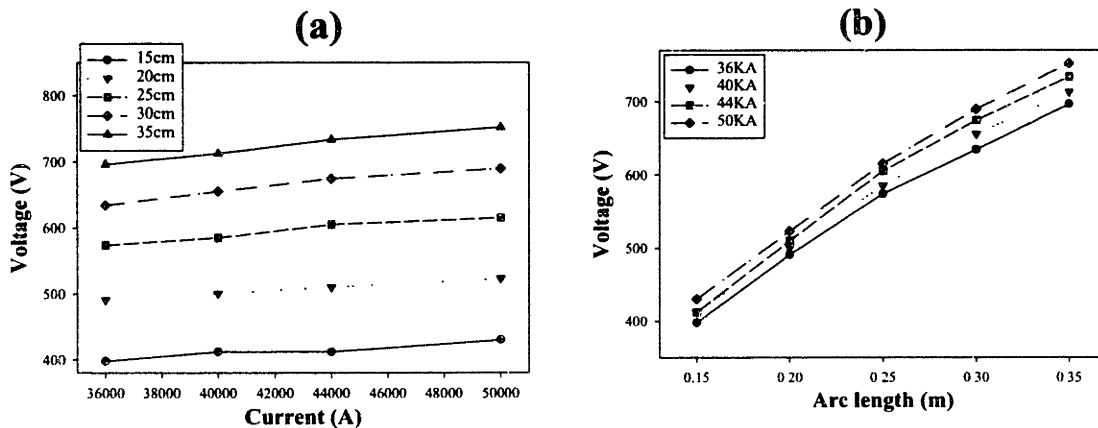


Figure 2.4.3 Total voltage drop in the electric arc as a function of the two main process parameters: (a) Arc current. (b) Arc length.

Figure 2.4.4 presents the maximum arc pressure at the bath surface as a function of current (Figure 2.4.4 (a)) and arc length (Figure 2.4.4 (b)). The maximum pressure at the bath surface increases linearly with arc current and decreases strongly (inversely proportional) with arc length.

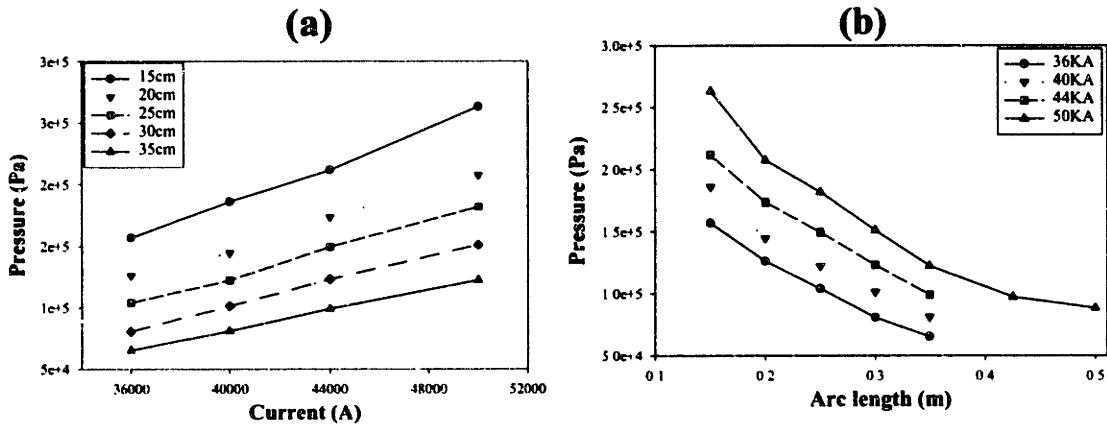


Figure 2.4.4 Maximum arc pressure at the bath as a function of the two main process parameters: (a) Arc current. (b) Arc length.

Figure 2.4.5 presents the relation between the maximum arc current density at the bath surface as a function of arc current (a), and as function of arc length (b). The maximum arc current density at the bath surface increases linearly with arc current and decreases strongly (inversely proportional) with arc length. This behavior indicates that arc pressure and arc current density are intimately related.

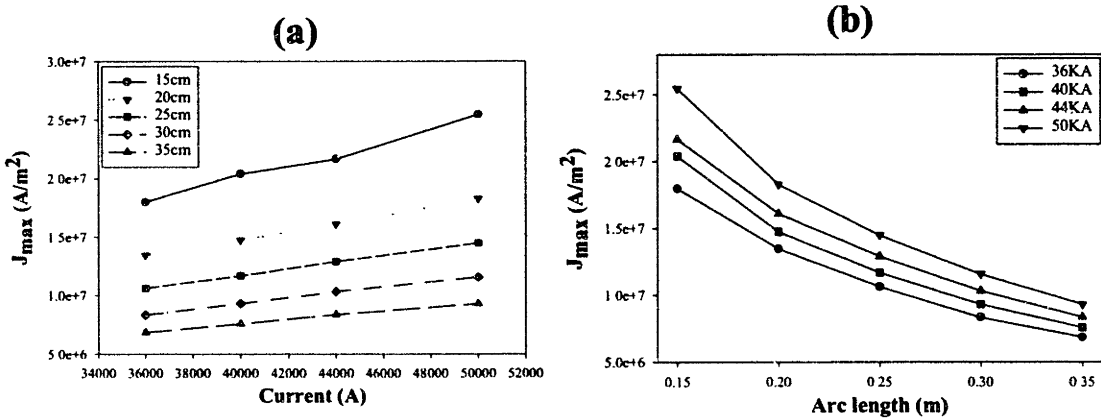


Figure 2.4.5 Maximum arc current density at the bath as a function of the two main process parameters: (a) Arc current. (b) Arc length.

Figure 2.4.6 shows the maximum shear stresses at the bath surface as a function of arc current (Figure 2.4.6 (a)) and arc length (Figure 2.4.6 (b)). The maximum shear stress increases linearly with arc current but the slope depends on the arc length, the shorter the arc length the steeper the slope, as shown in Figure 2.4.6 (a). In contrast, an increase in the arc length leads to a decrease in the maximum shear stress at the bath (Figure 2.4.6 (b)).

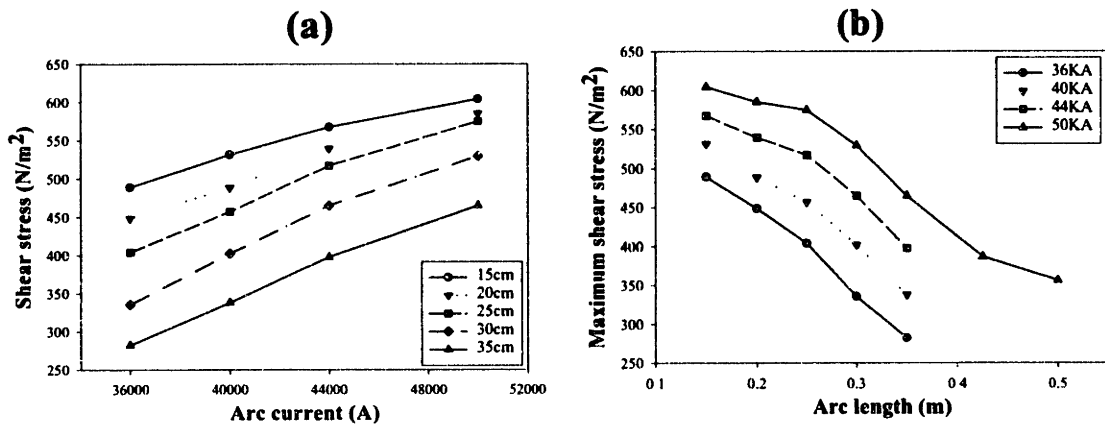


Figure 2.4.6 Maximum shear stress at the bath surface as a function of the two main process parameters: (a) Arc current. (b) Arc length.

### Parametric Study and Summary

It is clear from the previous sections that arc parameters, such as arc length and arc current, greatly affect arc properties and arc-bath interactions. This section has the intention to present summary of the process by correlating some important arc characteristics with the main arc variables, i.e. arc current,  $I$ , and arc length,  $L$ . The summary is expected to have a rather general or universal validity and whenever possible presented using dimensionless groups. Generalization of the knowledge gained with the model is, at the end, one of the important objectives of the modeling work.

Figure 2.4.7 shows the relationship between the maximum jet velocity (along the symmetry axis) and the arc current. The line in the plot corresponds to the well-known Maecker equation (equation 2.1.2), analytically derived under the assumption of inviscid flow and isothermal arc conditions.

The maximum velocities are expected to appear close to the cathode, where the Maecker equation applies. Temperatures of the order of 19000 K are predicted around the cathode region and this corresponds to a plasma density of about  $4.9 \times 10^{-3} \text{ kg/m}^3$ .

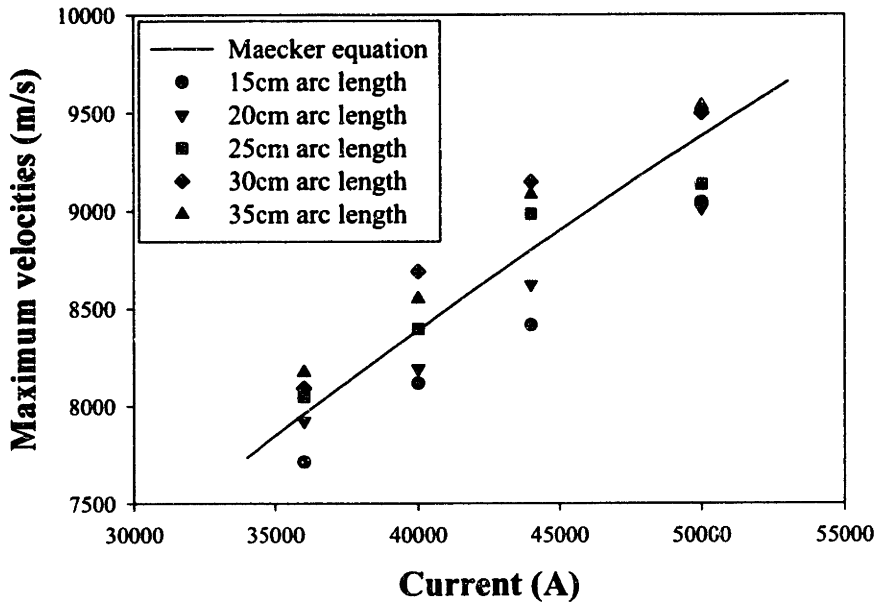


Figure 2.4.7 Maximum plasma velocities as function of arc current. Line represents Maecker equation and symbols are maximum velocities predicted in this study for all arc lengths.

Maecker equation is important because it is an analytical expression derived from the conservation equations and is widely used to provide estimated values. However it is known that Maecker equation overestimates maximum velocities [38]. Also, this expression is an oversimplification because it assumes a constant radial current density distribution, isothermal plasma and neglects the effect of the cathode surface.

The results in Figure 2.4.7 show that the maximum arc velocity follows a functionality with the arc current ( $V_{\max} \propto I^{0.5}$ ) dictated by Maecker equation. However, as shown in the figure the maximum velocity is also a function of the arc length.

Maecker derived another relation that correlates the arc pressure below the cathode (due electromagnetic body forces) and the arc current.

$$P_{\max} = \frac{\mu_o I J_c}{4\pi} \quad (\text{eq. 2.4.1})$$

From the above equations, the pressure is expected to scale linearly with arc current. For a given  $J_c$  value of  $4.4 \times 10^7 \text{ A/m}^2$ , a 4.4 slope value is expected which is presented in Figure 2.4.8 together with

predicted arc pressures. Fitting the data of 15 cm arc length and 36, 40, 44 and 50 KA to a linear equation gives a 4.98 slope, i.e. a 13.2% higher slope than that predicted by Maecker. This means that if equation 2.4.1 is multiply by a factor of 1.132 a better fitting of the data is obtained, as shown by the dashed line in Figure 2.4.8. In this figure it is also appreciated that the arc length does not significantly affect the arc pressure. Therefore, the pressure below the cathode is proportional to arc current and is practically independent of arc length.

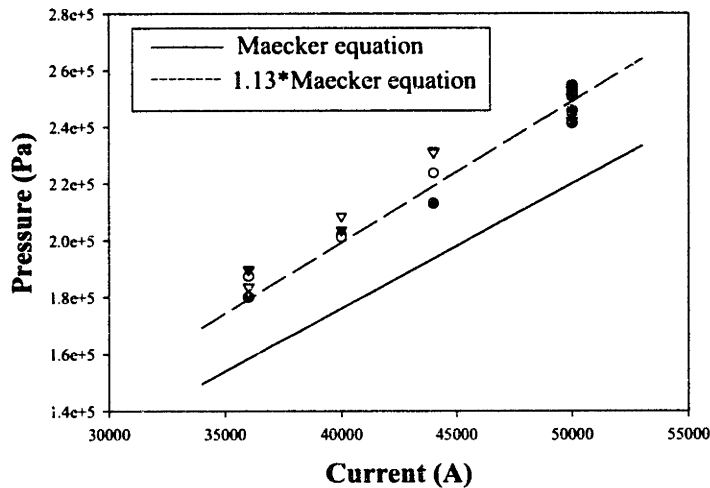


Figure 2.4.8 Maximum pressure below cathode as function of arc current. Solid line represents Maecker equation and dots are maximum arc pressures predicted in this study for all arc lengths. Dashed line is Maecker equation augmented 13.2% (equation 2.4.1 multiplied by 1.132).

Figure 2.4.9 shows the relation between the maximum bath current density, in dimensionless form ( $J_{max}/J_c$ ), and dimensionless arc length  $L/R_c$  for all currents and arc lengths employed in this study. In fact, this dimensionless arc length ( $L/R_c$ ) involves the two main process parameters, i. e. the arc length and the arc current, which is related to the arc spot radius,  $R_c$ , through the equation 2.1.24.

Since the spot current density is constant, the spot radius is only a function of the arc current,  $I$  ( $R_c \propto I^{0.5}$ ). The figure shows that for small values of  $L/R_c$ ; i.e. for short arc lengths and high currents, high values of current density at the bath are obtained. In contrast, for large  $L/R_c$  values (high arc lengths and small currents) small currents densities are obtained. The functionality is expressed by the following fitting equation (also presented in Figure 2.4.9):

$$\frac{J_{\max}}{J_c} = \frac{2.855}{(L/R_c)} \quad (\text{eq. 2.4.3})$$

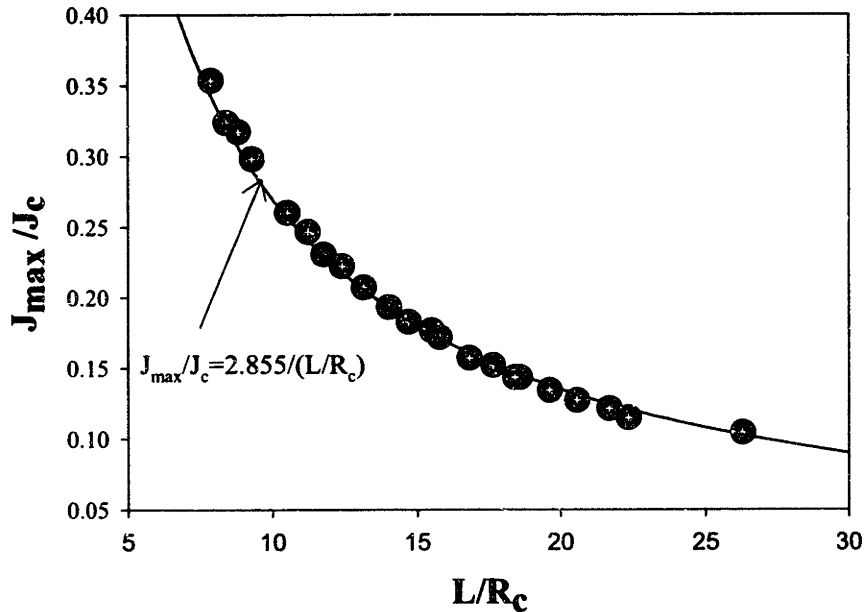


Figure 2.4.9 Computed maximum dimensionless current densities at the bath surface as function of dimensionless arc length. Variables in dimensionless form are:  $J_{\max}/J_c$  and  $L/R_c$ .

A very interesting finding in this work is presented in Figure 2.4.10. In this plot, the dimensionless arc radius ( $R_a/R_c$ ) is plotted as a function of the dimensionless axial position  $Z/R_c$ , for a large number of predicted conditions. The arc radius,  $R_a$ , is determined by the 10000 K isotherm, which according to Jordan [22] is coincident with the visible arc radius and can be used to define the conduction zone. The dots are experimental points reported by Bowman [21] and the lines are the predicted dimensionless arc radius as a function of dimensionless axial distance for all cases considered in this study. An excellent agreement between predictions and experiments is observed in the plot. It is a very helpful to recognize that all arc shapes lie on the same line when plotted in dimensionless form. It is noted that departure from the fitted line occurs in the vicinity of the bath, where the arc undergoes some additional expansion due to the impingement of the jet on the bath. But the main contribution reported in Figure 2.4.10 is that the arc shape can be represented conveniently by single universal curve for a wide range of arc currents and arc lengths (arc powers). Of course, the universal shape is restricted to electric arcs under air atmosphere and stroke between graphite cathode electrodes. The shape of the arc presents a quadratic relationship with the axial distance from cathode:

$$\frac{R_a}{R_c} = \left( 0.863747 - 0.2527 \frac{Z}{R_c} \right)^{0.5} \quad (\text{eq. 2.4.4})$$

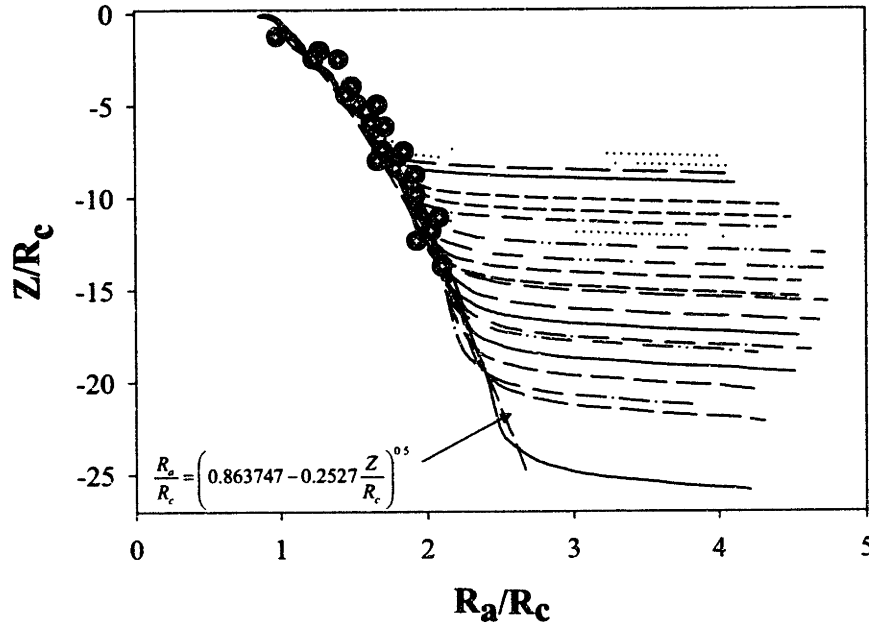


Figure 2.4.10 Arc shape expressed in dimensionless form. Dimensionless arc radius ( $R_a/R_c$ ) position along dimensionless axial distance ( $Z/R_c$ ) is reported for the complete set of arcs computed in this study. Dots are experimental data reported by Jordan [21]. The arc radius was determined to correspond to the 10,000 K isotherm.

The importance of Figure 2.4.10 is that since the arc region can be expressed in a unique fashion, at least ignoring the immediate region close to the bath, it is possible to express the arc characteristics in an analog universal way. To probe the last statement, magnetic flux density radial profiles are plotted in Figures 2.4.11 (a) to (d) for three different arc conditions, presented in Table 2.4.1, at the same dimensionless axial distances,  $Z/R_c$ , of 0, 2, 5 and 7. The figure shows similar functionalities in the profiles but the magnitudes in the values of the magnetic flux densities are not the same. If the magnetic flux density radial profiles presented in Figure 2.4.11 are now plotted in the correct dimensionless forms, a single profile can be obtained as indicated in Figures 2.4.12. Magnetic flux density values were normalized by dividing them over the maximum value at the specific  $Z/R_c$  position,  $B_{max}^0$ , while the radius was normalized with the arc radius,  $R_a$ . The arc radius is a function of the axial dimensionless distance  $Z/R_c$  as indicated in equation 2.4.4 and Figure 2.4.10.  $B_{max}^0$  is the maximum magnetic flux density value at each axial distance. Therefore, this variable is a function of both the arc current and the dimensionless axial distance  $Z/R_c$ . As can be seen in Figure 2.4.12(e), all profiles lie on the same line regardless the axial

position and arc current. Then it is possible to give simple expressions for each part of the magnetic flux density profiles. In this way, the region inside the arc can be expressed as a cubic function of the radius (implying a parabolic profile for  $J_z$ , since  $B_\theta$  is obtained by integration of the axial current density):

$$\frac{B_\theta}{B_{\max}^0} = 1.8632 \left( \frac{R}{R_a} \right) - 0.5874 \left( \frac{R}{R_a} \right)^2 - 0.19117 \left( \frac{R}{R_a} \right)^3 \quad \text{for } R \leq R_a \quad (\text{eq. 2.4.5})$$

Outside the arc, the profile is inversely proportional to the dimensionless radius:

$$\frac{B_\theta}{B_{\max}^0} = \frac{1}{\left( \frac{R}{R_a} \right)} \quad \text{for } R > R_a \quad (\text{eq. 2.4.6})$$

In order to obtain the  $B_\theta$  field, equations 2.4.5 and 2.4.6 can be employed but  $R_a$  and  $B_{\max}^0$  values must be first obtained. The arc radius,  $R_a$ , can be easily obtained from Figure 2.4.10 or from equation 2.4.4.

However,  $B_{\max}^0$  can be expressed as a function of the dimensionless distance,  $Z/R_c$ , regardless the arc current, if it is expressed in dimensionless form by dividing over the maximum value of  $B_\theta$  in the entire domain,  $B_{MAX}$ .  $B_{MAX}$  is always located at the cathode and can be expressed analytically as:

$$B_{MAX} = \frac{\mu_0 I}{2\pi R_c} \quad (\text{eq. 2.4.7})$$

Figure 2.4.13 shows a plot of  $B_{\max}^0/B_{MAX}$  against  $Z/R_c$  for the three arcs considered. Similar trends are observed for all three arcs considered. The functionality between  $B_{\max}^0/B_{MAX}$  and  $Z/R_c$  can be expressed by:

$$\frac{B_{\max}^0}{B_{MAX}} = \exp \left( 0.0363 - 0.1959 \left( \frac{Z}{R_c} \right)^{0.5} \right) \quad (\text{eq. 2.4.8})$$

Arc current (KA)	Arc length (m)	$R_c$ (m)	$B_{MAX}$ (Tesla)	$T_{MAX}$ (K)	$V_{MAX}$ (m/s)
36	0.35	0.016138	0.4674	25954	8186.88
40	0.25	0.017011	0.4942	26751	8415.437
50	0.15	0.019019	0.5673	26896	9103.81

Table 2.4.1 Computed electric arcs used in the parametric analysis for  $B_\theta$ ,  $V_z$  and  $T$



This means that before the impingement zone is reached, a unique or universal  $B_\theta$  field expressed in dimensionless form can be obtained using equations 2.4.5 and 2.4.6 since  $B_{max}^0$  and  $R_a$  are available through equations 2.4.8 and 2.4.4, due to the universal arc shape behavior for the range of conditions explored in this study.

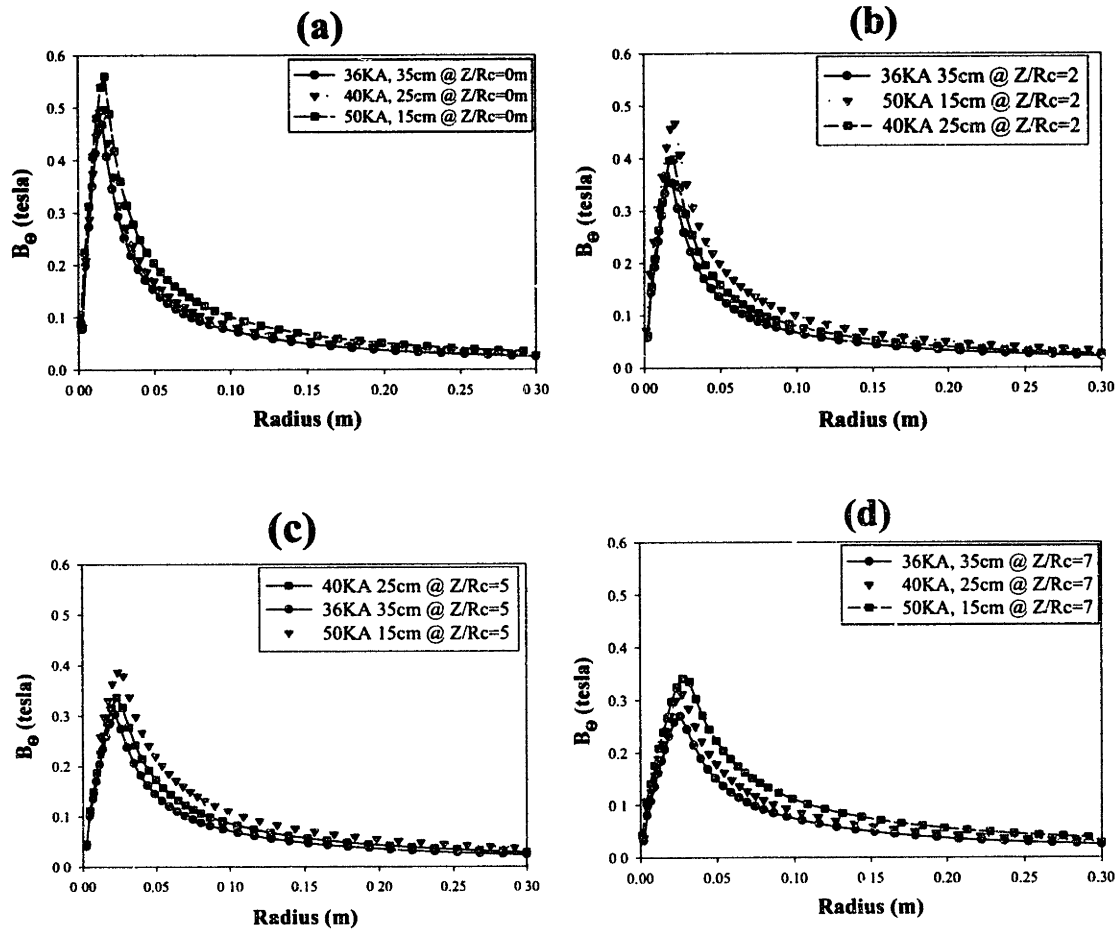


Figure 2.4.11  $B_\theta$  radial profiles at the same dimensionless axial distances for the three arcs presented in Table 2.4.1. The profiles correspond to the dimensionless axial distances of (a)  $Z/R_c=0$ . (b)  $Z/R_c=2$ . (c)  $Z/R_c=5$ . (d)  $Z/R_c=7$ .

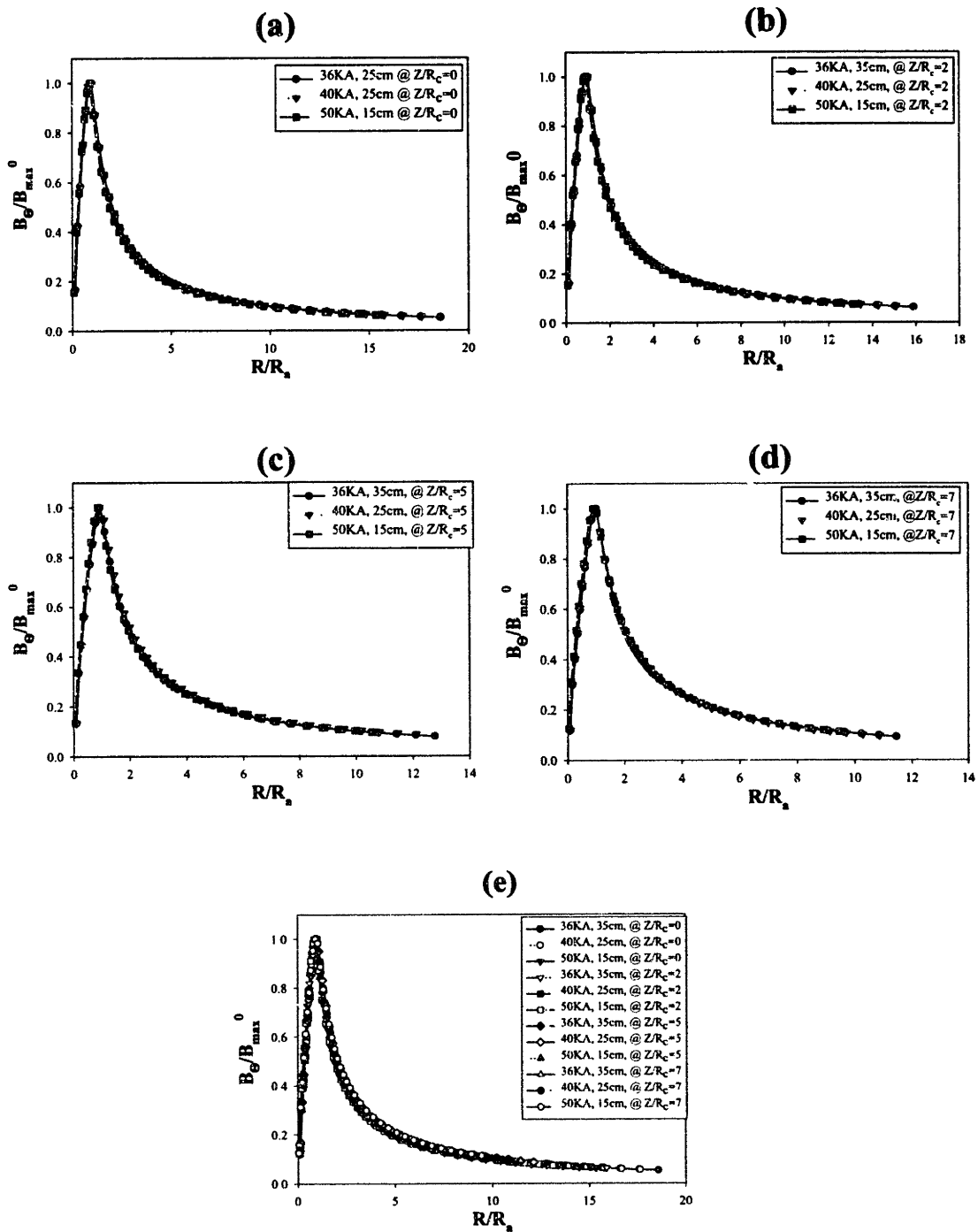


Figure 2.4.12 Dimensionless magnetic flux density radial profiles ( $B_\theta/B_{max}^0$  against  $R/R_a$ ) for the three arcs presented in Table 2.4.1. The profiles correspond to the same dimensionless axial distances of (a)  $Z/R_c=0$ , (b)  $Z/R_c=2$ , (c)  $Z/R_c=5$ , (d)  $Z/R_c=7$ , (e) All distances plotted together to show the universal nature of the radial profile.

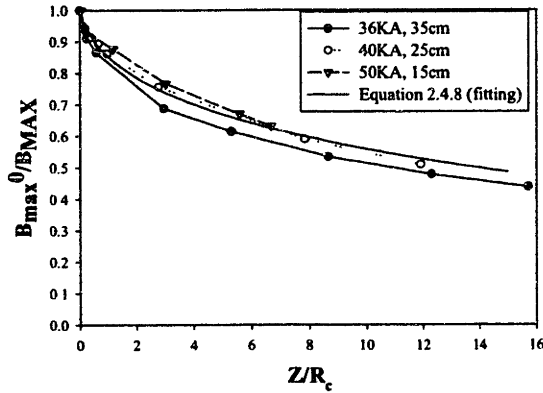


Figure 2.4.13 The  $B_{max}^0/B_{MAX}$  profile along the dimensionless distance of  $Z/R_c$  for the arcs presented in Table 2.4.1.

Temperature fields can also be presented in the same universal dimensionless way just as the  $B_\theta$  field described above. Again, considering the same arc cases included in Table 2.4.1, temperature radial profiles are plotted in Figure 2.4.14 (a) to (c) at three different dimensionless axial distances of 2, 5, and 7. However, not big differences are observed in the plots for the different arcs. Then, Figure 2.4.14 (d) shows the radial temperature profiles for the 36 KA and 35 cm arc at six axial distances ( $Z/R_c=1.43, 4.1, 6.62, 9.38, 12.3, 15.067$ ), and as seen in the figure, arc temperatures decrease as distance from the cathode increases and the profiles become wider as the arc expands.

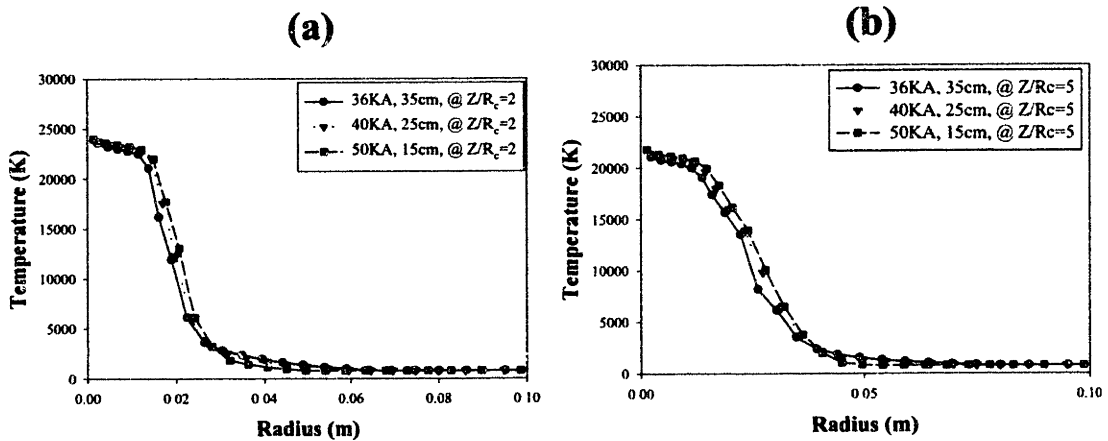


Figure 2.4.14 Temperature radial profiles for the arcs presented in Table 2.4.1. The profiles correspond to the same dimensionless distances of (a)  $Z/R_c=2$ . (b)  $Z/R_c=5$ .

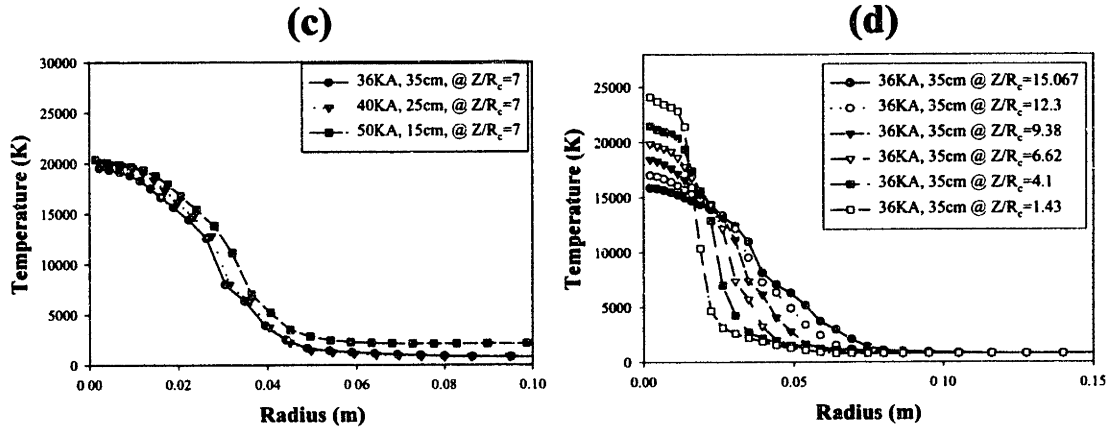


Figure 2.4.14 (cont.) Temperature radial profiles for the arcs presented in Table 2.4.1. The profiles correspond to the same dimensionless distances of (c)  $Z/R_c=7$ . (d) Temperature radial profiles are plotted at six different axial distances from cathode for an arc of 36 KA and 35 cm.

Figure 2.4.15 presents the same temperature radial profiles as in Figure 2.4.14 but this time in dimensionless form. The temperature has been normalized by dividing over its maximum value at each axial position,  $T_{max}^0$ , which it is always located at the symmetry axis. The radial distance can be normalized exactly as the previous case, by dividing it over the arc radius,  $R_a$ , which in turns can be obtained via equation 2.4.4. It can be appreciated that the temperature radial profiles are similar in dimensional form but they become even more when these profiles are plotted in dimensionless form. When all arc cases and axial distances are plotted together (Figure 2.4.15 (e)), it is interesting to note that a single line can be observed inside the arc ( $R_a < 1$ ) but outside the arc differences are more evident. However, since the arc region is the most important region in our calculation domain, a simple expression can be given for radial temperature profiles regardless the arc current and axial distance (but only valid in the arc region outside the impingement zone):

$$\frac{T}{T_{max}^0} = 0.0425 + \frac{0.9744}{\left(1 + \exp\left(-\frac{(R/R_a) - 1.079}{0.2647}\right)\right)} \quad (\text{eq. 2.4.9})$$

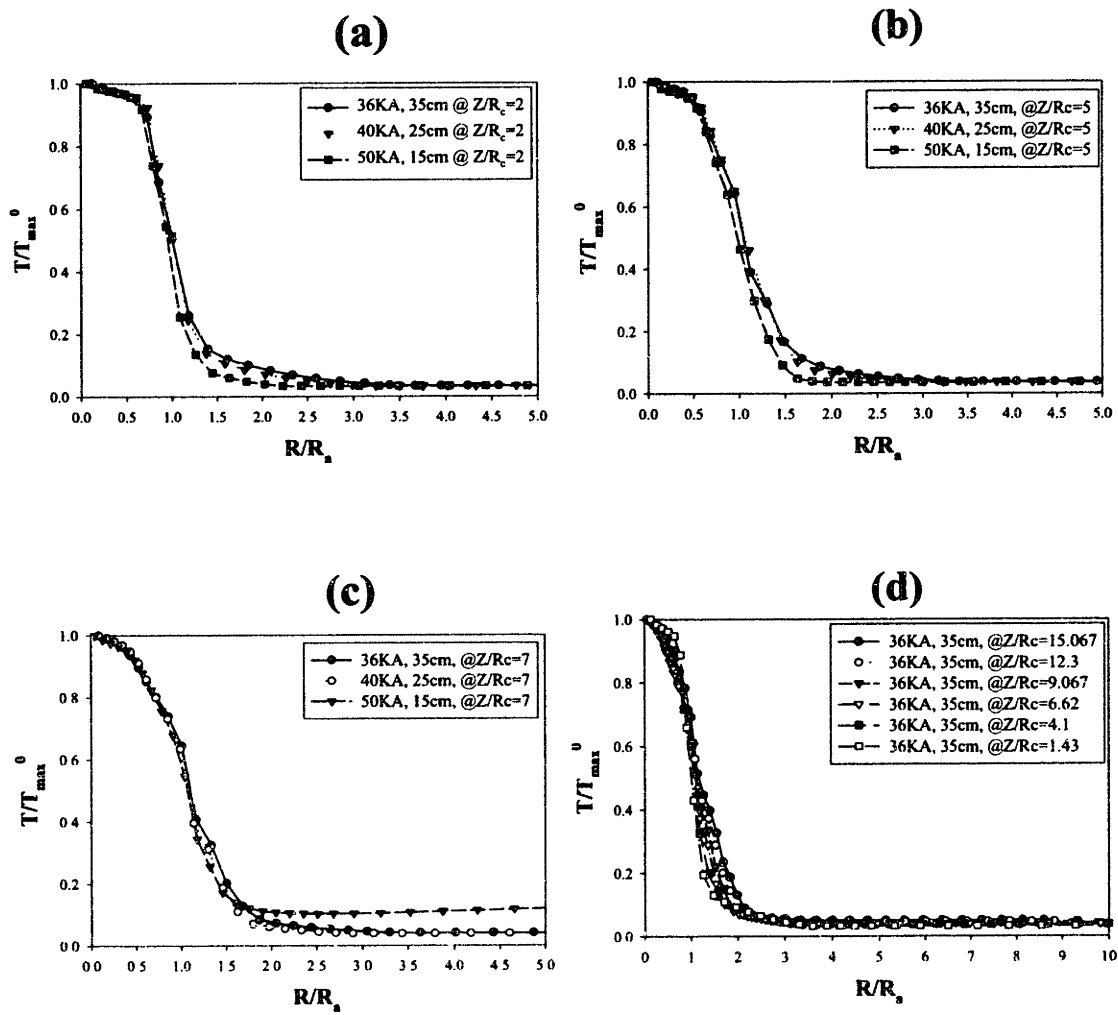


Figure 2.4.15 Dimensionless temperature radial profiles for the arcs presented in Table 2.4.1. The profiles correspond to those in Figure 2.4.14: (a)  $Z/R_c=2$ . (b)  $Z/R_c=5$ . (c)  $Z/R_c=7$ . (d) Dimensionless temperature radial profiles are plotted at six different axial distances from cathode for the arc of 36 KA and 35 cm.

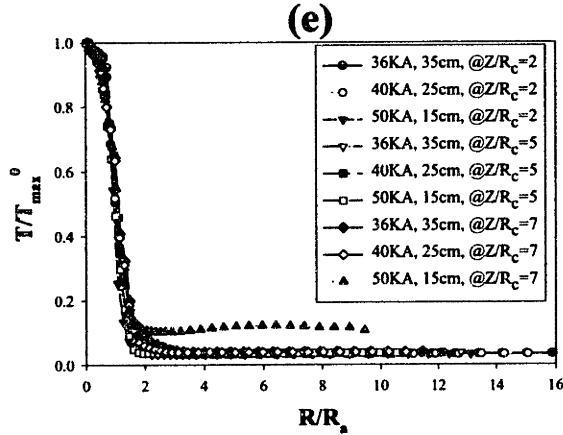


Figure 2.4.15 (cont.) Dimensionless temperature radial profiles for the arcs presented in Table 2.4.1. The profiles correspond to those in Figure 2.4.14: (e) Lines from Figures (a), (b), (c) and (d) are plotted together.

In order to obtain the entire temperature field inside the arc region, it is necessary to obtain the axial temperature profiles at the symmetry axis,  $T_{max}^0$ , and at the arc radius,  $R_a$ . Equation 2.4.4 expresses the universal relation between the arc radius and the axial distance. To obtain a unique expression for the temperature at the axis,  $T_{max}^0$ , the three arc cases in Table 2.4.1 were used to obtain a dimensionless plot for the dimensionless temperature,  $T_{max}^0/T_{MAX}$ , along the dimensionless axial distance,  $Z/R_c$ .  $T_{MAX}$  is the maximum temperature obtained in the domain, which is always located in the vicinity of the cathode. This value must be obtained from the computation, but does not vary too much in the range of conditions analyzed in this thesis due to the constant value of  $J_c$  employed in the simulations (25954 K-26896 K). Figure 2.4.16(a) shows the axial profile of temperature as a function of axial distance for the three arcs in dimensional form. Figure 2.4.16(b) presents the dimensionless version of Figure 2.4.16(a). It is easily seen that all axial temperature lines converge into a single line. The importance of this finding is that is possible to generate a complete temperature field inside the arc region, just before the impingement point, if  $T_{MAX}$  is available. Consequently, fields of all physical properties can be estimated since they depend exclusively on temperature as was originally stated in this model, under the assumptions considered.

The expression for  $T_{max}^0/T_{MAX}$  versus  $Z/R_c$  is given as:

$$\frac{T_{max}^0}{T_{MAX}} = 0.4352 + 0.55366 \exp\left(\frac{-(Z/R_c)}{12.9745}\right) \quad (\text{eq. 2.4.10})$$

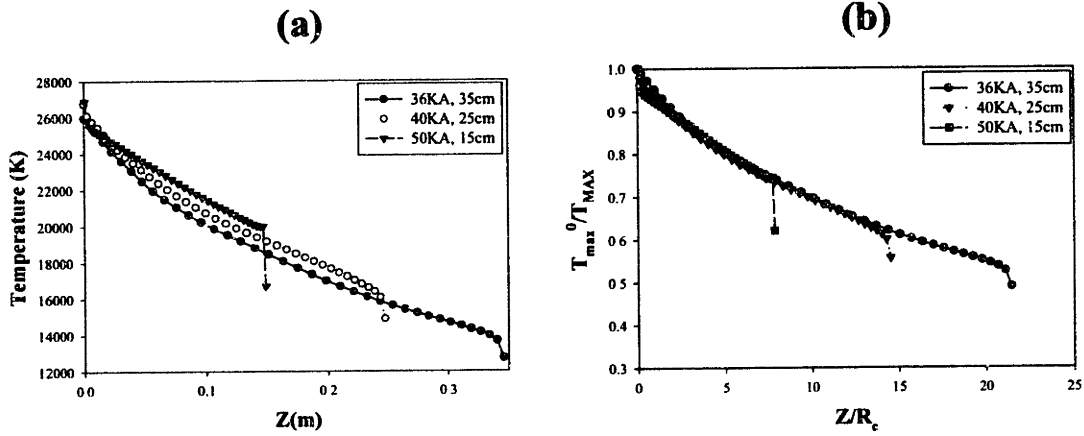


Figure 2.4.16 Temperature axial profiles along the symmetry axis for the arcs in Table 2.4.1. (a) Dimensional axial profiles. (b) Dimensionless profiles obtained when  $T_{max}^0$  is divided by the maximum temperature in the domain,  $T_{MAX}$ , while  $Z$  is divided by  $R_c$ .

Axial velocity fields are also treated under the same methodology to obtain a unique velocity field. The axial velocity is predominant inside the arc but away from the cathode and bath surfaces where the radial velocities dominate the flow motion. Figure 2.4.17 shows radial profiles of axial velocities for the three arcs considered in Table 2.4.1 at four dimensionless distances from the cathode of 2, 5, 7 and 11. The axial velocities decrease with increasing axial distance and the radial profiles are wider as the arc expands, as can be seen in Figure 2.4.17 (e) that presents a 36 KA and 35 cm arc velocities plotted at four dimensionless distances of 2, 5, 7, 11. The same plots as in Figure 2.4.17 but in dimensionless form are presented in Figure 2.4.18. The axial velocity is normalized by dividing over the maximum velocity at each axial distance,  $V_{max}^0$ , while the radius is normalized using the arc radius given by equation 2.4.4.  $V_{max}^0$  is always located at the symmetry axis. When all lines are plotted together, a single line again is obtained regardless the arc current, the arc length and the axial position (Figure 2.4.18 (f)). This expression may be expressed through the following relationship:

$$\frac{V_z}{V_{max}^0} = 1.02 \exp\left(-0.5\left(\frac{(Z/R_c) - 0.00647}{0.446}\right)^2\right) \quad (\text{eq. 2.4.11})$$

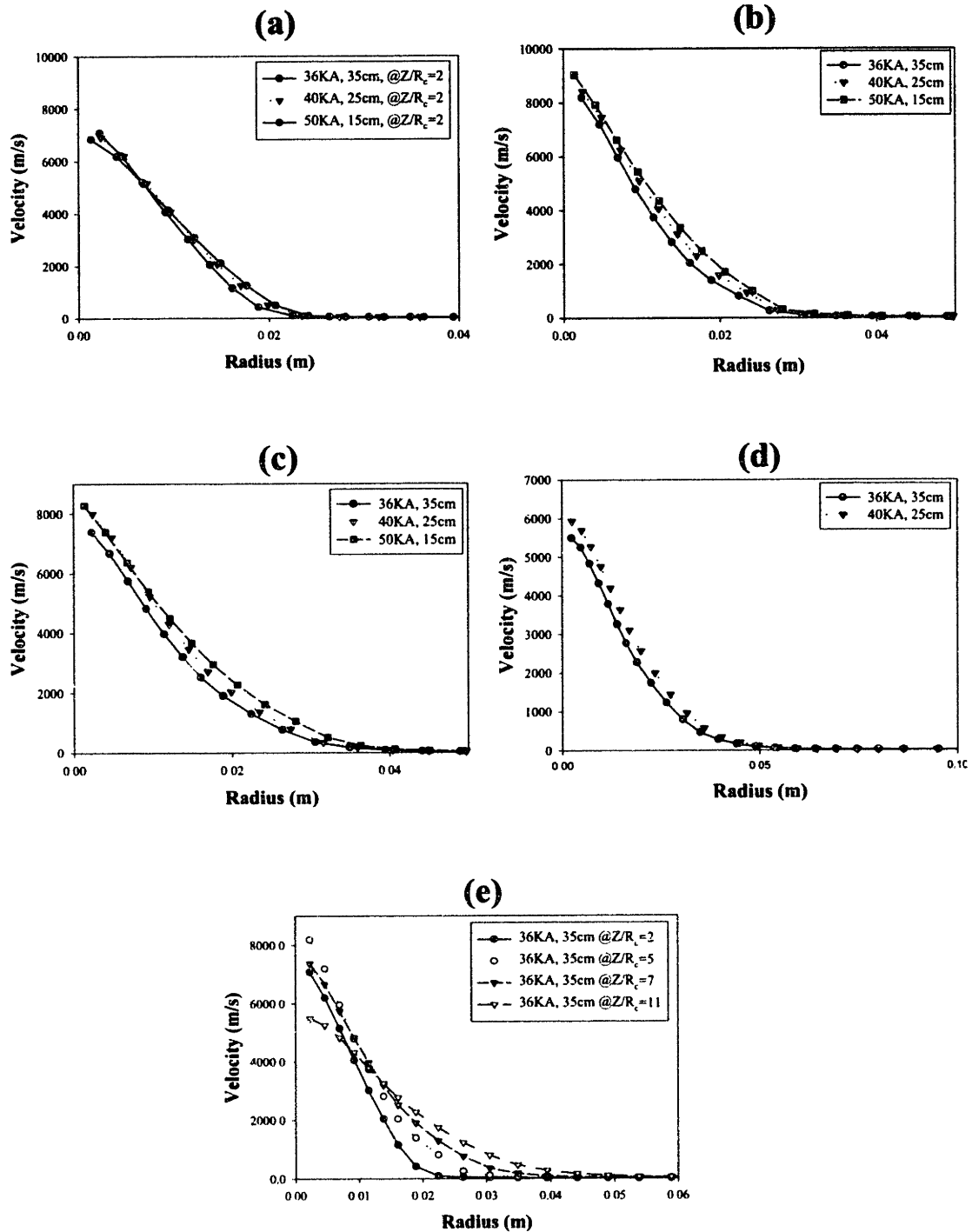


Figure 2.4.17 Axial velocity profiles along the radius for the arcs presented in Table 2.4.1. The profiles correspond to dimensionless distances of (a)  $Z/R_c=2$ . (b)  $Z/R_c=5$ . (c)  $Z/R_c=7$ . (d)  $Z/R_c=11$ . (e) Axial velocities along the radius at dimensionless distances of 2, 5, 7, and 11 (36 KA and 35 cm arc).



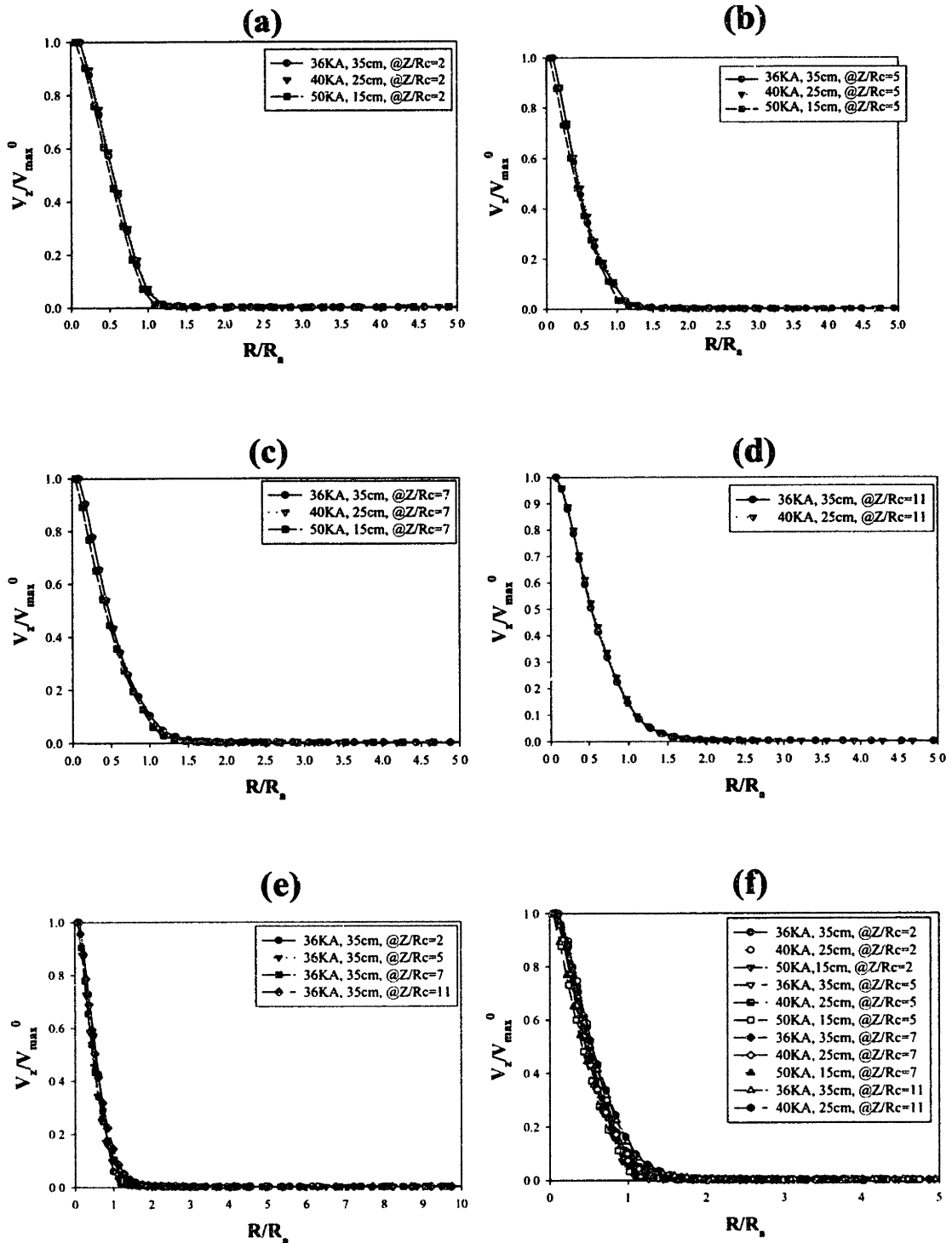


Figure 2.4.18 Dimensionless axial velocity profiles along the radius for the arcs presented in Table 2.4.1. The profiles correspond to dimensionless distances of (a)  $Z/R_c=2$ . (b)  $Z/R_c=5$ . (c)  $Z/R_c=7$ . (d)  $Z/R_c=11$ . (e) Dimensionless axial velocity profiles for the 36 KA and 35 cm arc. (f) All lines are plotted together to show the universal fashion of the profile.

In order to generate a universal axial velocity field, a unique expression for  $V_{max}^0$  must be obtained. In order to generate such a relation, a dimensionless axial velocity plot against dimensionless axial distance at the symmetry axis is presented in Figure 2.4.19 (b). Axial velocity is normalized by dividing over the maximum arc velocity,  $V_{MAX}$ . The figure presents three lines representing each of the arcs considered in Table 2.4.1. Lines are very similar, but differences are important close to the cathode and bath surface (impingement region), which may be explained since radial velocities dominate in those regions. Figure 2.4.19 (a) is the same plot presented in Figure 2.4.19 (b) but in dimensional form. This plot is presented to point out that despite the differences in the dimensionless curves, still the axial velocity profiles are very similar in dimensionless form when compared against dimensional curves. An interesting observation in the axial profile of the axial velocity is that the maximum velocities are located at the same dimensionless axial distance,  $Z/R_c$  of 5. The complex axial velocity field can only be expressed via rather complex polynomial function:

$$\frac{V_{max}^0}{V_{MAX}} = \frac{\left( 3.27 \left( \frac{Z}{R_c} \right) - 0.24 \left( \frac{Z}{R_c} \right)^2 + 0.0188 \left( \frac{Z}{R_c} \right)^3 \right)}{\left( 1 + 3.27 \left( \frac{Z}{R_c} \right) - 0.5 \left( \frac{Z}{R_c} \right)^2 + 0.052 \left( \frac{Z}{R_c} \right)^3 \right)} \quad (\text{eq. 2.4.12})$$

The closure would be the acquisition of the maximum arc velocity,  $V_{MAX}$ . This value can be obtained from the actual simulations or by employing the Maecker equation (equation 2.1.2) that estimates this value. Then, once  $V_{MAX}$  is estimated, the complete axial velocity field can be obtained by combining equations 2.4.11 and 2.4.10.

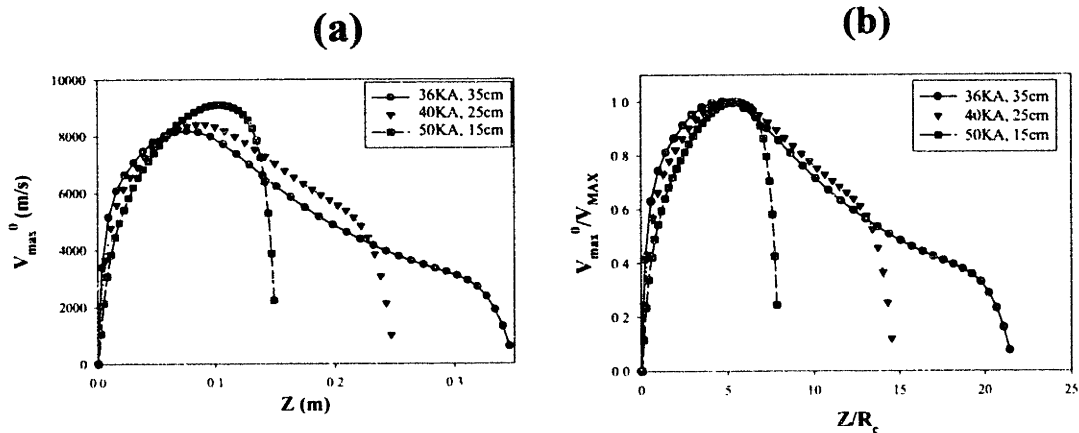


Figure 2.4.19 Axial velocity profiles along the symmetry axis for the arcs in Table 2.4.1. (a) Dimensional axial profiles. (b) Dimensionless profiles obtained when  $V_{max}^0$  is divided by the maximum velocity in the domain,  $V_{MAX}$ , while  $Z$  is divided by  $R_c$ .

Finally, it is important to analyze the heat transfer from the arc to the bath, which represents a practical aspect of the electric arc furnace operation that can be appreciated clearly with the help of the model. It has to be recognized that the main function of electric arcs is to melt scrap and heat up molten steel. Then, the total heat transfer from the arc is a function, as shown before, of the arc current and arc length, or in terms of practical variables, heat transfer is a function of arc power. Figure 2.4.20 shows total heat flow into the bath as a function of arc power ( $V \times I$ ). As expected, increasing arc power increases the total heat transfer for a constant circular bath area with a radius of 0.3 m. The heat transfer ranges from 2 MW for a total arc power of 16 MW to almost 5 MW for an arc power of almost 50 MW. It is interesting to calculate the thermal efficiency of the arc, defined as the percentage of heat produced in the arc (arc power) that actually reaches the bath (total heat flow) and this can be expressed by the following equation:

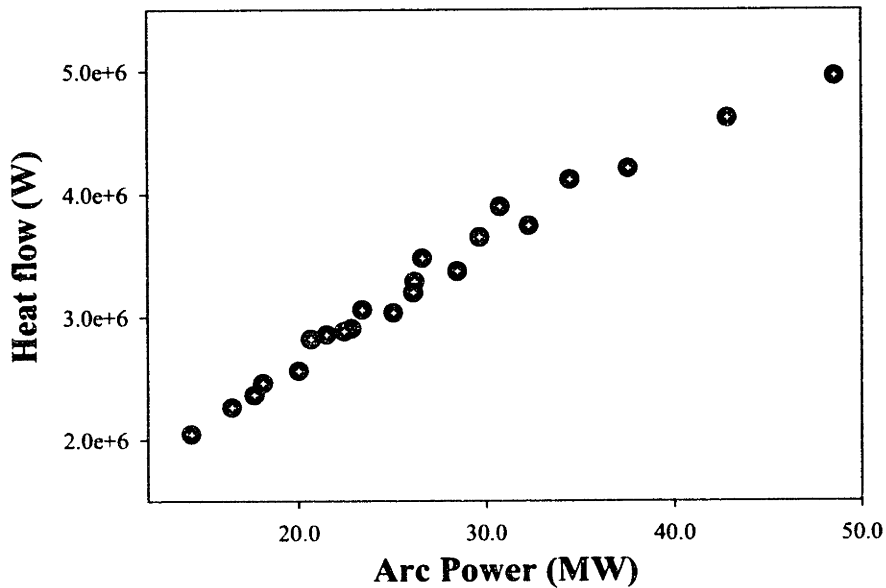


Figure 2.4.20 Total heat flow input to the bath from the arc as a function of arc power.

$$Efficiency = \left( \frac{HeatFlow}{ArcPower} \right) \cdot 100 \quad (eq. 2.4.13)$$

It can be seen in Figure 2.4.21 that the electric arc transfers heat more inefficiently to the bath as the arc power increases despite the fact that an increase in arc power results in higher heat input. It is also interesting to note that arc efficiencies are generally very low (10-20%) which indicates that most of the very expensive electric energy is not transferred to the bath but rather to the furnace walls, roof, and

exhaust gases. Actually, it can be said that the efficiency decreases linearly with arc power, although the rate of decrease is small. In other words, it can be said that long arcs are less efficient than short arcs for the same arc current. A linear regression gives an estimation of the arc efficiency as a function of the arc power as:

$$\text{Efficiency} = 15.49 - 0.111\text{Power} \tag{eq. 2.4.14}$$

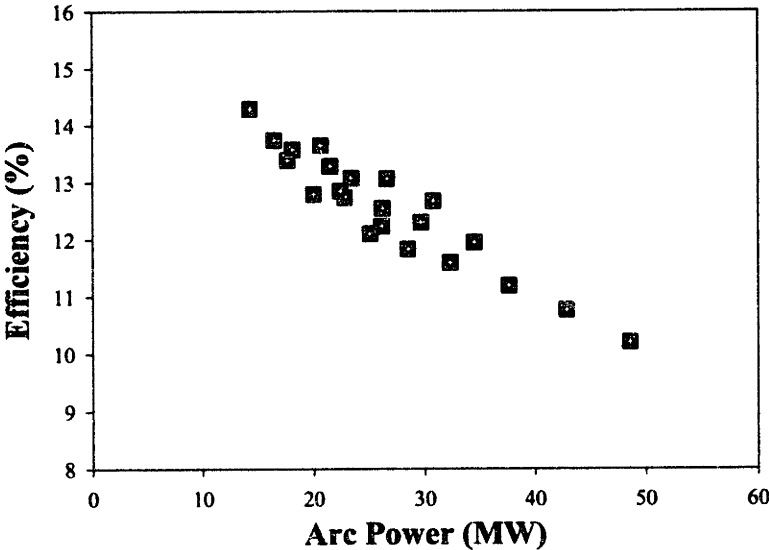


Figure 2.4.21 Electric arc heating efficiency. The efficiency is defined as the fraction of total arc power reaching the bath region.

## Chapter 3: Bath Modeling

In this chapter, bath modeling is presented following a similar sequence than that used in chapter 2 to describe the arc model. Primarily, a brief description of the main phenomena involved in the bath region is presented mathematically through the statement of governing equations and boundary conditions, with the help of some simplifying assumptions. The representation of the bath region includes some variations in order to represent different aspects such as gas injection and the presence of a top layer of slag, which add a degree of complexity in the statement of the problem. Then, validation of the models using some similar experimental physical models is presented followed by the results obtained from the models and their analysis, which constitutes the closure for chapter 3.

### Section 3.1: Physical Representation of the Bath

Once the main element in DC-EAF has been explained and characterized, i.e. the electric arc, the bath region can be described, since the boundary conditions (arc-bath interactions) at the top surface of the bath are now available from the arc results. The bath is in fact the most important element from the practical point of view, since it contains the steel phase that is a final product to be processed in the operation.

Figure 3.1.1 presents a schematic simplified representation of the bath region. The arc region is also placed above the cylindrical furnace container for completeness of the figure. The arc provides heat, current, shear stress, and pressure at the top bath surface. The bath phase in the refining stage is composed of liquid steel, liquid slag on top of the steel and gases evolved from carbon boil or injection from the bottom through porous plugs. Circulation of the bath is promoted by the electromagnetic forces produced by the pass of the current and the self induced magnetic field, by shear stress at the bath top surface and by buoyancy due to temperature gradients inside the melt. Heat is mainly transferred from the arc as described in chapter 2. Heat is also generated inside the melt by Joule effect due to the pass of current and the heat leaves the system through the furnace walls and by radiation from the melt top surface to the furnace wall panels and roof. In addition to these heat and momentum transfer phenomena, mass transfer is also critical in the bath region, where solute concentrations are determined by thermodynamics and kinetics of the steel-slag, steel-gas chemical reactions taking place.

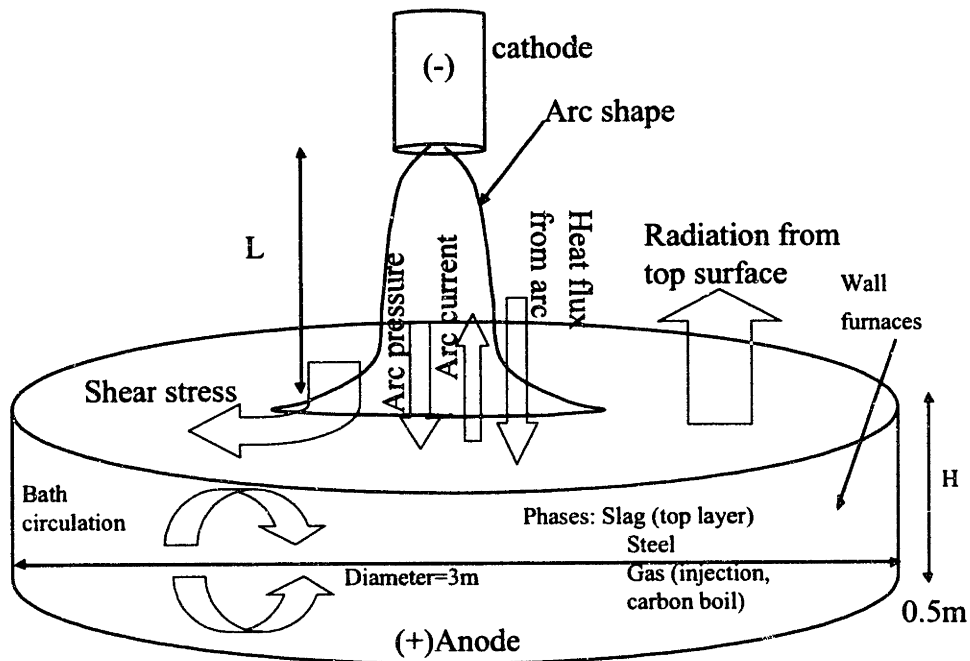


Figure 3.1.1 Schematic representation of the bath region in a DC-EAF.

### Section 3.2: Mathematical Model of the Bath Region

The bath model is developed based on the approach given in chapter 1 (section 1.5). As stated in that section, the arc model presented in chapter 2 is used to establish arc-bath interaction through boundary conditions at the top surface of the bath.

Several mathematical representations of the system with different levels of complexity are explored in this region. Three different models devoted to representing the bath are presented in this chapter:

- Bath model under the influence of the electric arc and considering only steel in the bath region
- Bath model under the effect of the arc and with bubbling stirring from the bottom of the reactor. This is a two-phase (gas-liquid) system
- Bath model under the effect of the arc with a layer of slag on top of the steel phase. This bath model is a two-liquid phase system

## Single-phase steel Model

In the mathematical representation of the bath region a general case dealing with a single phase is first described. The alternative formulations required to represent gas injection and the additional slag phase are discussed subsequently.

### *Assumptions and Governing Equations*

The simplest, single phase, model of steel bath is represented on a cylindrical axisymmetric coordinate system in which the arc-bath interface is assumed flat as shown in Figure 3.2.1 A list of the most important model assumptions include:

- Steel is the only phase present in the bath region
- Physical properties of all phases are independent of temperature
- The arc-bath interface is assumed to be flat
- The problem is considered to be in steady state represented by a cylindrical coordinate system
- Induced currents are neglected
- Wall temperatures are fixed at 1773 K, which is close to the liquidus temperature of low carbon steels
- Radiation from the furnace walls and roof is not considered

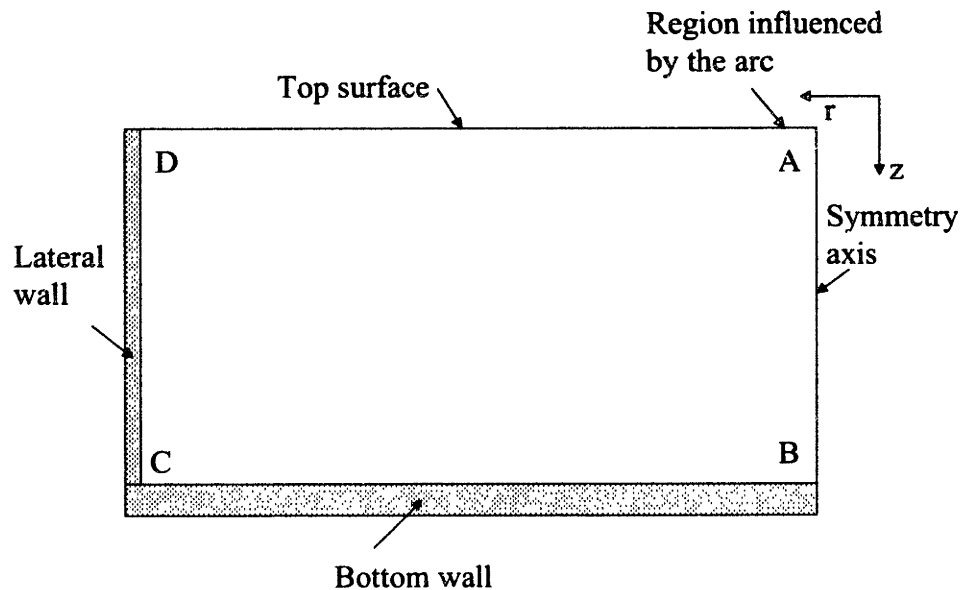


Figure 3.2.1 Schematic representation of the computation domain for the bath region in a DC-EAF.

From the list of assumptions presented above, the weakest ones are the flat surface adopted at the top of the bath as well as the fixed temperatures at the walls. Surface depression is not considered in the present work due to the increasing degree of complexity that would require the computation. The difficulty comes not only from the additional free surface problem required to compute the depression, but also due to the extra coupling between arc and bath that would force the computations of both regions to be performed simultaneously or in an iterative manner.

Fixing the temperature at the furnace walls is an artificial boundary condition that prevents the analysis of heat flux through the refractory walls. The proper boundary condition would require experimentally determined heat fluxes at the walls as a function of the position to realistically represent the heat transfer through the walls.

The governing equations include:

- The continuity equation:

$$\frac{\partial}{\partial z}(\rho v_z) + \frac{1}{r}(\rho r v_r) = 0 \quad (\text{eq. 3.2.1})$$

- The axial component of the turbulent Navier-Stokes equations:

$$\begin{aligned} \frac{\partial}{\partial z}(\rho v_z^2) + \frac{1}{r} \frac{\partial}{\partial r}(\rho r v_r v_z) = -\frac{\partial P}{\partial z} + \frac{2\partial}{\partial z} \left( \mu_{eff} \frac{\partial v_z}{\partial z} \right) \\ + \frac{1}{r} \frac{\partial}{\partial r} \left( r \mu_{eff} \left( \frac{\partial v_z}{\partial r} + \frac{\partial v_r}{\partial z} \right) \right) + F_z + F_{Buoyancy} \end{aligned} \quad (\text{eq. 3.2.2a})$$

- The radial component of the turbulent Navier-Stokes equations:

$$\begin{aligned} \frac{\partial}{\partial z}(\rho v_r v_z) + \frac{1}{r} \frac{\partial}{\partial r}(\rho r v_r^2) = -\frac{\partial P}{\partial r} + \frac{2}{r} \frac{\partial}{\partial r} \left( \mu_{eff} \frac{r \partial v_r}{\partial r} \right) - \frac{2v_r}{r^2} \mu_{eff} \\ + \frac{\partial}{\partial z} \left( \mu_{eff} \left( \frac{\partial v_r}{\partial z} + \frac{\partial v_z}{\partial r} \right) \right) + F_r \end{aligned} \quad (\text{eq. 3.2.2b})$$



where  $F_z$  and  $F_r$  are the axial and radial components of electromagnetic forces, and  $F_{buoyancy}$  is the effective buoyancy force. These equations are equivalent to those presented in chapter 2. Therefore, for a full description of symbols and terms in equations 3.2.1 – 3.2.2 the reader is referred to chapter 2.

- The turbulent energy conservation equation:

$$\frac{\partial}{\partial z}(\rho C_p v_z T) + \frac{1}{r} \frac{\partial}{\partial r}(\rho C_p r v_r T) = \frac{\partial}{\partial z} \left( k_t \frac{\partial T}{\partial z} \right) + \frac{1}{r} \frac{\partial}{\partial r} \left( r k_t \frac{\partial T}{\partial r} \right) + Q_{Joule} \quad (\text{eq. 3.2.3})$$

where  $T$  is the temperature. The last term at the right hand side of equation 3.2.3 is the Joule heat source term,  $Q_{Joule}$ .

- The Maxwell equations:

$$\nabla \times \vec{E} = 0 \quad (\text{eq. 3.2.4a})$$

$$\nabla \times \vec{H} = \vec{J} \quad (\text{eq. 3.2.4b})$$

$$\nabla \cdot \vec{B} = 0 \quad (\text{eq. 3.2.4c})$$

- The charge conservation equation:

$$\nabla \cdot \vec{J} = 0 \quad (\text{eq. 3.2.5})$$

- The Ohm's law:

$$\vec{J} = \sigma \vec{E} \quad (\text{eq. 3.2.6})$$

- The conservation equations for the turbulent kinetic energy,  $k$ , and the energy dissipation rate,  $\varepsilon$ , i.e. the standard k- $\varepsilon$  turbulence model:

$$\frac{\partial}{\partial z}(\rho v_z k) + \frac{1}{r} \frac{\partial}{\partial r}(\rho r v_r k) = \frac{\partial}{\partial z} \left( \frac{\mu_t}{\sigma_k} \frac{\partial k}{\partial z} \right) + \frac{1}{r} \frac{\partial}{\partial r} \left( r \frac{\mu_t}{\sigma_k} \frac{\partial k}{\partial r} \right) + S_k - \rho \varepsilon \quad (\text{eq. 3.2.7})$$

$$\frac{\partial}{\partial z}(\rho v_z \varepsilon) + \frac{1}{r} \frac{\partial}{\partial r}(\rho r v_r \varepsilon) = \frac{\partial}{\partial z} \left( \frac{\mu_t}{\sigma_\varepsilon} \frac{\partial \varepsilon}{\partial z} \right) + \frac{1}{r} \frac{\partial}{\partial r} \left( r \frac{\mu_t}{\sigma_\varepsilon} \frac{\partial \varepsilon}{\partial r} \right) + S_\varepsilon \quad (\text{eq. 3.2.8})$$

where  $S_k$  and  $S_\varepsilon$  are defined as:

$$S_k = \mu_t \left[ 2 \left\{ \left( \frac{\partial v_z}{\partial z} \right)^2 + \left( \frac{\partial v_r}{\partial r} \right)^2 + \left( \frac{v_r}{r} \right)^2 \right\} + \left( \frac{\partial v_z}{\partial r} + \frac{\partial v_r}{\partial z} \right)^2 \right] \quad (\text{eq. 3.2.9})$$

$$S_\varepsilon = C_1 \varepsilon \frac{S_k}{k} - C_2 \rho \frac{\varepsilon^2}{k} \quad (\text{eq. 3.2.10})$$

$C_1$  and  $C_2$  are constants for the k- $\varepsilon$  turbulent model, while  $\alpha_k$  and  $\alpha_\varepsilon$  are the Prandtl numbers for  $k$  and  $\varepsilon$  respectively. These constants were previously defined in Table 2.1.1.

The turbulent nature of the flow is describe by using the following equation for the effective viscosity:

$$\mu_{eff} = \mu + \mu_t \quad (\text{eq. 3.2.11})$$

The molecular viscosity is  $\mu$ , and the turbulent viscosity,  $\mu_t$ , is calculated directly from the solution of the standard k- $\varepsilon$  turbulence model according to:

$$\mu_t = C_D \rho \frac{k^2}{\varepsilon} \quad (\text{eq. 3.2.12})$$

Equations 3.2.1 - 3.2.12 define the mathematical statement of the bath region in DC-EAF for a single steel phase. As in the arc problem, a high degree of coupling exists between the governing equations. For this reason, a more detailed description of how the electric problem is actually implemented in the numerical model as well as its coupling to the transport equations is presented below.

#### *Electromagnetic Problem and Its Coupling with the Heat and Momentum Equations*

As explained in Chapter 2, the potential equation can be derived as:

$$\frac{1}{r} \frac{\partial}{\partial r} \left( \sigma r \frac{\partial \phi}{\partial r} \right) + \frac{\partial}{\partial z} \left( \sigma \frac{\partial \phi}{\partial z} \right) = 0 \quad (\text{eq. 3.2.13})$$

where  $\phi$  is the electric potential related to the electric field,  $E$ , through the following expression:

$$\bar{E} = -\nabla\phi \quad (\text{eq. 3.2.14})$$

Equation 3.2.13 is the conservation equation solved simultaneously with the rest of the conservation equations. The current density components can be obtained by using Ohm's law (equation 3.2.6):

$$J_r = -\sigma \left( \frac{\partial\phi}{\partial r} \right) \quad (\text{eq. 3.2.15a})$$

$$J_z = -\sigma \left( \frac{\partial\phi}{\partial z} \right) \quad (\text{eq. 3.2.15b})$$

The azimuthal component of magnetic flux density,  $B_\theta$ , can be derived from the Ampere's law:

$$B = \frac{\mu_o}{r} \int_0^R 2\pi r J_z dr \quad (\text{eq. 3.2.16})$$

Equations 3.2.13, 3.2.15 and 3.2.16 constitute the solution of the electric problem in the bath.

The electromagnetic body forces ( $JXB$ ) constitute the coupling between the electromagnetic phenomena and fluid flow (equations 3.2.17a and 3.2.17b). The coupling between the electromagnetic phenomena and heat transfer is through the Joule heat source (equation 3.2.17c). Finally, heat transfer and fluid flow phenomena are coupled through buoyancy forces expressed by the Boussinesq approximation (equation 3.2.17d):

$$F_r = -J_z B \quad (\text{eq. 3.2.17a})$$

$$F_z = J_r B \quad (\text{eq. 3.2.17b})$$

$$Q_{joule} = \left( \frac{J_z^2 + J_r^2}{\sigma} \right) \quad (\text{eq. 3.2.17c})$$

$$F_{Buoyancy} = -\rho\gamma_l g (T - T_o) \quad (\text{eq. 3.2.17d})$$

where  $T_o$  is the reference temperature,  $g$  is the gravitational vector, and  $\gamma_l$  is the thermal coefficient of volume expansion for steel.

### Boundary Conditions

The boundary conditions reflect zero velocities and zero turbulence values at the walls. The link between the laminar region (adjacent to the wall) and the fully turbulent region is given by the wall function approach. Two options for the implementation of the wall function are explored: equilibrium and non-equilibrium wall functions [89]. In this work the non-equilibrium wall function approach was used and wall temperatures were set to a constant value (1773 K). For the electromagnetic representation, the bottom wall is assumed to be a good conductor of the current and constitutes the anode, and thus, a zero potential value is assigned there, while the lateral wall does not conduct electricity. At the symmetry axis, all variables have zero flux conditions. Finally, at the top surface, the heat flux, the shear stress and current from the arc calculation are introduced as boundary conditions for the energy, radial momentum and potential equations, respectively. Also at the free surface, steel is allowed to lose heat by radiation. Table 3.2.1 presents all boundary conditions based on the geometry and symbols employed in Figure 3.2.1.

	$V_r$	$v_z$	$T$	$\phi$	$k$	$\varepsilon$
AB	0	$\frac{\partial v_z}{\partial r} = 0$	$\frac{\partial T}{\partial r} = 0$	$\left(\frac{\partial \phi}{\partial r}\right) = 0$	$\frac{\partial k}{\partial z} = 0$	$\frac{\partial \varepsilon}{\partial z} = 0$
BC	0	0	$T_{\text{wall}}=1773$ K (convective heat with non-equilibrium wall function)	$\phi = 0$	0 (non-equilibrium wall function)	$\frac{\partial \varepsilon}{\partial z} = 0$ (wall function)
CD	0	0	$T_{\text{wall}}=1773$ K (convective heat with non-equilibrium wall function)	$\left(\frac{\partial \phi}{\partial r}\right) = 0$	0 (non-equilibrium wall function)	0 (wall function)
DA	$\tau_a$ from arc model (eq.2.1.32)	0	$q_{\text{top}} = q_{\text{arc}} - \sigma \varepsilon T^4$ $q_{\text{arc}}$ from arc model eq. 2.1.31	$\left(\frac{\partial \phi}{\partial z}\right) = -\frac{J_{\text{arc}}}{\sigma}$ $J_{\text{arc}}$ from arc model	$\frac{\partial k}{\partial r} = 0$	$\frac{\partial \varepsilon}{\partial r} = 0$

Table 3.2.1 Boundary conditions in the bath region for a single steel phase model

### Physical Properties of Steel and Geometric Parameters of the Reactor

A list of the physical properties employed in the calculations for the single steel phase model together with the geometric parameters used is presented in Table 3.2.2.

Physical properties of steel	
Density, $\rho_l$ (kg/m <sup>3</sup> )	7200
Specific heat, $C_{p_l}$ (J/kg K)	670
Viscosity, $\mu_l$ (kg/m s)	$6.5 \times 10^{-3}$
Thermal conductivity, $k_{ll}$ (W/m K)	15
Electric conductivity, $\sigma$ (Ohm <sup>-1</sup> m <sup>-1</sup> )	$7.14 \times 10^5$
Thermal volume expansion coefficient, $\gamma_l$ (K <sup>-1</sup> )	$1.4 \times 10^{-4}$
Furnace parameters	
Furnace radius (m)	1.5
Liquid depth (m)	0.5
Arc length (m)	0.15 – 0.35
Arc current (KA)	36 – 50
Wall temperatures (K)	1773

Table 3.2.2 Physical properties of steel and numerical values of some geometric parameters of the reactor

### Gas-Steel Model

When injection of argon gas through a nozzle from the bottom is included in the DC-EAF, the bubbling process makes necessary some modifications to the model previously presented, in order to account for the effect of the bubbles ascending through the melt. Gas injection involves the solution of a complete set of conservation equations for both the gas and liquid phases. Then, the gas-steel system is handled with the Eulerian-Eulerian approach and implemented with the numerical technique called IPISA (Inter-Phase-Slip-Algorithm) [100]. Additionally, since the bubbling practice must be eccentric, at specific injection points, the gas-steel system must involve a 3D representation.

#### *Assumptions for the Gas-Steel Model*

The model is based on the Eulerian-Eulerian approach to solve the two-phase problem in the bath region, in which the two phases share the same domain. One phase is continuous (liquid) while the other is dispersed (gas). The approach comprises the solution of a complete set of conservation equations for each phase present in the domain. Additionally, the electric potential is associated with the steel, which is the conductive phase, and turbulence is associated to the liquid phase only. Also, all the other assumptions from the single steel phase model apply in this case.

#### *Governing Equations for the Gas-Steel Model*

The governing equations include a complete set of conservation equations for each phase: Continuity equation, the turbulent Navier-Stokes equations, the turbulent energy conservation equations, the Maxwell equations, the charge conservation equation and Ohm's law (only on steel, since steel is the conductive phase). The conservation equations for the turbulent kinetic energy,  $k$ , and the energy

dissipation rate,  $\epsilon$ , associated with the standard k- $\epsilon$  turbulence model. Finally, it is important to specify that in the IPSA technique only one pressure is solved and both phases share the same pressure.

### Interfacial and Special Sources

The same sources described by equations 3.2.17a – 3.2.17d are included in the liquid momentum and energy equations for this model. Additionally, an important momentum source for the gas phase is the buoyancy effect due to the difference of densities between the gas and liquid steel.

The link between the two phases is considered at the gas-liquid interface where both phases exchange momentum and heat. Expressions describing the exchange of momentum (friction between gas and liquid) and the heat transfer between the phases are given in Table 3.2.3. The interfacial sources in both gas and liquid momentum equations have the same value but opposite sign. The driving force in the friction term is the difference in velocities between the phases, while heat transfer at the interface is driven by temperature differences between the phases. Finally, the additional turbulence generated due to rising of bubbles through the melt is accounted with an extra source terms proposed by Lopez et al [101], and included in Table 3.2.3.

Friction force*	$F_{friction} = C_f (V_b - V_l)$ <p><math>C_f</math> is the friction coefficient, <math>V_b</math> is gas velocity, <math>V_l</math> is liquid velocity. The difference <math>V_b - V_l</math> is known as the slip velocity, <math>V_{slip}</math>.</p>
Heat transfer*	$S_{Hnt} = hA_b (T_g - T_l)$ <p>where <math>h</math> is the heat transfer coefficient, <math>A_b</math> is the bubble surface area per unit volume, <math>T_g</math> is gas temperature and <math>T_l</math> is steel temperature. The heat transfer coefficient is computed from the local Nusselt number</p> $Nu = \frac{hD_p}{k_t}$ <p>where <math>k_t</math> is the thermal conductivity and <math>D_p</math> is the bubble diameter. Nusselt number for bubble-liquid heat exchange are obtained from empirical correlations [102]</p>
Extra* Turbulence	$S_\epsilon = R_l P_b$ $S_k = R_l P_b \frac{\epsilon}{k}$ <p>where <math>S_\epsilon</math> and <math>S_k</math> are the sources for <math>\epsilon</math> and <math>k</math> respectively. <math>R_l</math> is the liquid volume fraction and <math>P_b</math> is the production rate of <math>k</math> due to the drag work that bubbles do as they move through the continuous phase.</p>

Table 3.2.3 Interfacial source terms for the momentum and energy equations

\*For details see [103].

### Boundary Conditions

The same boundary conditions applied for the liquid phase in the single-phase steel model, are valid for all variables in this gas-steel model. However, the gas phase require the setting of additional boundary conditions. At the inlet, vertical velocity for the gas is set according to the gas flow rate and nozzle diameter used in the calculations. Temperature of the gas entering is set equal to the wall temperature. At the top boundary, gas is allowed to escape as soon as it reaches the free surface and the enthalpy carried by the gas leaving is used as a negative source in the energy equation.

### Physical Properties of the Phases and Geometric Parameters of the Reactor

Table 3.2.4 shows the physical properties of the gas and some geometrical parameters used in the calculations.

Physical Properties of Argon Gas	
Density, $\rho_g$ (kg/m <sup>3</sup> )	1.18
Specific heat, $Cp_g$ (J/kg K)	520
Viscosity, $\mu_g$ (kg/m s)	$2.0 \times 10^{-5}$
Thermal conductivity, $k_g$ (W/m K)	$1.893 \times 10^{-4}$
Surface tension Ar-Steel, $\sigma_{nt}$ (J/m <sup>2</sup> )	1.8
Numerical values of parameters used in the model	
Number of nozzles	3 (symmetrically located)
Location of nozzle	@ $r/R_{furnace}=0.625$
Nozzle diameter (m)	0.005
Bubble diameter, $D_p$ , (m)	0.009
Gas flow rate, $Q$ , (m <sup>3</sup> /s)	$5.0 \times 10^{-4}$

Table 3.2.4 Physical properties of argon and numerical values of some geometric parameters of the reactor

### Slag-Steel Model

In this variation to the original single-phase model, the same geometric system presented in Figure 3.2.1 is again considered. However, instead of having only liquid steel, this model represents a two liquid system, where slag of lower density is above the steel. The steel and slag liquids are immiscible and the interface separating them is sharp and well defined due to the differences in density. The sharp interface makes this case totally different from the steel-gas case where the gas was dispersed into the liquid steel. For this fundamental difference at the interface, the problem is treated as a free surface problem between the two liquids. To handle the problem, a marker technique denominated the "Scalar Equation Method" (SEM) [104] is implemented. In this technique a one-phase fluid flow simulation is performed and the presence of the top liquid (slag) is determined by the solution of a marker variable. This marker, which has a unit value where steel is present and zero value in slag positions, is allowed to move by convection but is

not allowed to diffuse. The track in time of markers determines the free surface position, which is considered to appear where the marker has values between 0 and 1. Then, the marker value is used to assign the physical properties of the corresponding fluids.

### *Governing Equations, Boundary Conditions and Physical Properties Used in the Slag-Steel Model*

Basically the same formulation presented for the single-phase model holds in this case. The only difference is that the conservation equations are solved in transient mode since the marker history is required to track the interface between the two liquids. The Marker equation solved together with the set of equations in this technique is:

$$\frac{\partial M}{\partial t} + \frac{1}{r} \frac{\partial}{\partial r} (rMv_r) + \frac{\partial}{\partial z} (Mv_z) = 0 \quad (\text{eq. 3.1.18})$$

where  $M$  is the Marker variable. As initial condition, a layer of slag is placed on top of the steel and the marker is assigned zero values in the slag region and unit values in the steel region. Initial conditions also include zero velocities and a constant temperature of 1773 K for both phases. The boundary conditions and assumptions employed in the steel model hold here too. The main difference is that physical properties in each position must be calculated at each time step since their values depend on the phase present at each cell, which in turn depends on the Marker motion defining the interface. Physical properties for a common slag used in DC-EAF is presented in Table 3.2.5.

Physical properties of the slag	
Density, $\rho_{slag}$ (kg/m <sup>3</sup> )	2300
Specific heat, $Cp_{slag}$ (J/kg K)	1157
Thermal volume expansion coefficient, $\gamma_{slag}$ (K <sup>-1</sup> )	$2.7 \times 10^{-4}$
Viscosity, $\mu_{slag}$ (kg/m s)	0.43
Thermal conductivity, $k_{slag}$ (W/m K)	0.1509
Numerical values of parameters used in the model	
Thickness of slag layer (m)	0.05m

Table 3.2.5 Physical properties of slag and some geometric parameters of the reactor

### **Mixing Time Model**

One of the important elements to study is the ability of the reactor to homogenize concentration of solutes and temperature. The way to measure this characteristic or behavior is by determining the characteristic mixing time of the reactor. The mixing time is defined as the time required for a small amount of tracer added into the liquid to reach 95% of uniformity [105]. Mixing phenomena are represented by solving a tracer conservation equation in transient mode, where the solute is transported through the domain under steady state velocity and turbulence fields:



$$\frac{\partial}{\partial t}(R_l \rho_l C) + \nabla \cdot (V_l R_l \rho_l C) = \nabla \cdot (V_l \Gamma_{eff} \nabla C) \quad (\text{eq. 3.2.19})$$

where  $R_l$ ,  $\rho_l$ ,  $V_l$  and  $C$  are the liquid volume fraction, liquid density, liquid velocity and concentration of the tracer respectively.  $\Gamma_{eff}$  is the effective mass diffusion coefficient defined as:

$$\Gamma_{eff} = \frac{\mu}{Sc} + \frac{\mu_t}{Sc_t} \quad (\text{eq. 3.2.20})$$

where the laminar and turbulent Schmidt numbers are  $Sc = \mu/D$  and  $Sc_t = \mu_t/D_t$ , respectively.  $D$  and  $D_t$  are the laminar and turbulent diffusivities of the tracer, respectively. For this work a  $Sc_t$  equal to one is employed.

### Section 3.3: Bath Model Validation

In this section, an attempt to validate specific aspects of the phenomena taking place in the bath region is presented through the representation of experimental systems reported in the literature that present similar physics to the system under study. These experimental systems are:

- Kang's experimental system to study electromagnetic driven flows [29]
- Air-Water models of Ladles

#### Section 3.3.1: Electromagnetic Driven Flow (Kang's Experimental Setup)

In order to validate the numerical model regarding its capabilities to represent electromagnetically driven flows, the experimental work reported by Kang et. al. was used to compare against our model predictions. In their work, Kang measured velocities, and turbulent parameters such as kinetic energy and its dissipation rate, in a system where electric current flows between two electrodes through a Wood's metal pool. The experimental setup is shown schematically in Figure 3.3.1. The cathode is placed at the top touching the surface of the pool. The anode consists on the entire bottom surface while the lateral wall is isolated. Dimensions and currents employed in the experiments are also indicated in the figure. The current flows between the two electrodes through the Woods metal, but due to the differences in their conducting area, the current diverges. The passage of this current self induces a magnetic flux density in the azimuthal direction and the cross product  $J \times B$  drives the flow motion creating the circulation loops depicted in the figure. Joule heat is not considered since the electric conductivity of the Woods metal is extremely high (see Table 3.3.1). For this reason the melt can be considered to be isothermal.

Simulations were performed using a 2D steady state formulation in cylindrical coordinates and assuming an isothermal pool, a constant distribution of current over the entire surface of the cathode, and a flat free surface. Additionally, several approaches for the turbulence models are tested. The governing equations include the continuity, turbulent Navier-Stokes, Maxwell's, Ohm's law and the charge conservation equation. Different turbulence models are explored (standard k- $\epsilon$ , RNG, two scale k- $\epsilon$ ). The physical properties of Wood's metal are presented in Table 3.3.1.

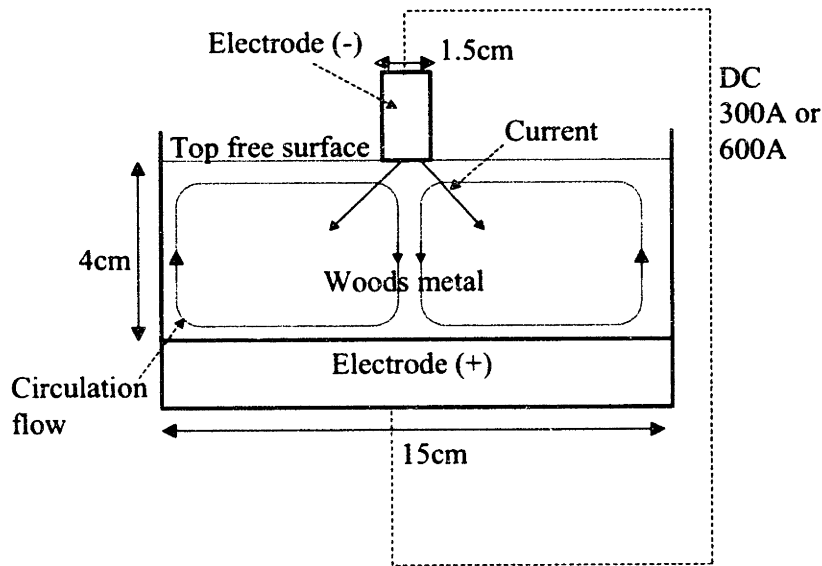


Figure 3.3.1 Schematic representation of the experimental setup by Kang. Phenomena occurring in the system are also shown in figure.

Physical properties of the slag	
Density (kg/m <sup>3</sup> )	8370
Viscosity (kg/m s)	0.00229
Electric conductivity (Ohm <sup>-1</sup> m <sup>-1</sup> )	9x10 <sup>5</sup>

Table 3.3.1 Physical properties of Woods metal

Figure 3.3.2 shows the predicted velocity fields for the 300 A and 600 A cases where only half of the system is presented. It is shown in both fields that a single circulation loop is formed extending from the symmetry axis to the lateral wall. The maximum velocities are located at the symmetry axis. This electromagnetically driven flow also shows that increasing the current increases the forces and as a consequence bigger velocities.

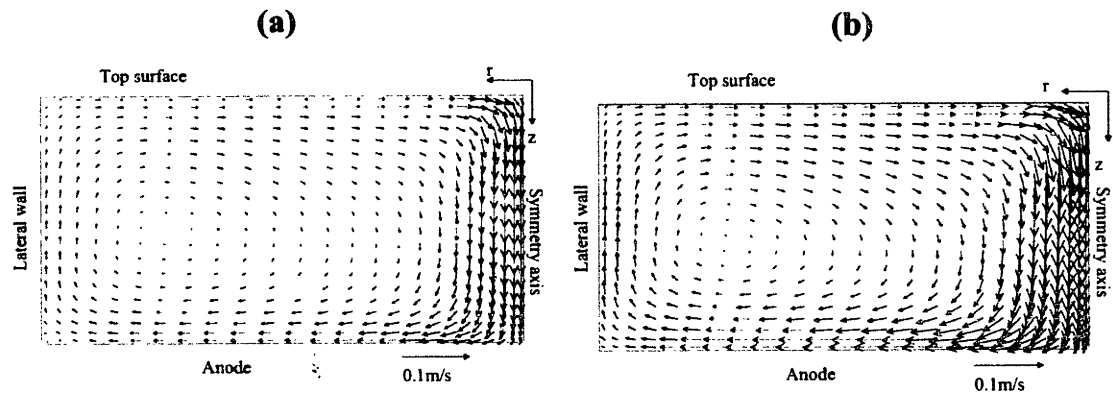


Figure 3.3.2 Velocity field computed for the Kang system. (a) Current of 300 A. (b) Current of 600 A.

Figure 3.3.3 shows a comparison between experimentally obtained and predicted mean velocities at 2 cm from the top surface along the radius for both 300 A and 600 A cases. In the plots, predictions are presented using different turbulence models, i.e. the standard  $k-\epsilon$ , RNG and the two-scale  $k-\epsilon$  model. Good agreement is observed between experiments and predictions. The different turbulence models predict different velocities close to the symmetry axis but after about 1 cm from the axis there are no big differences in the model predictions. The effect of increasing the current on velocities is clearly seen by comparing Figures 3.3.3 (a) and (b) where velocities increase about twice with an equivalent increasing in current.

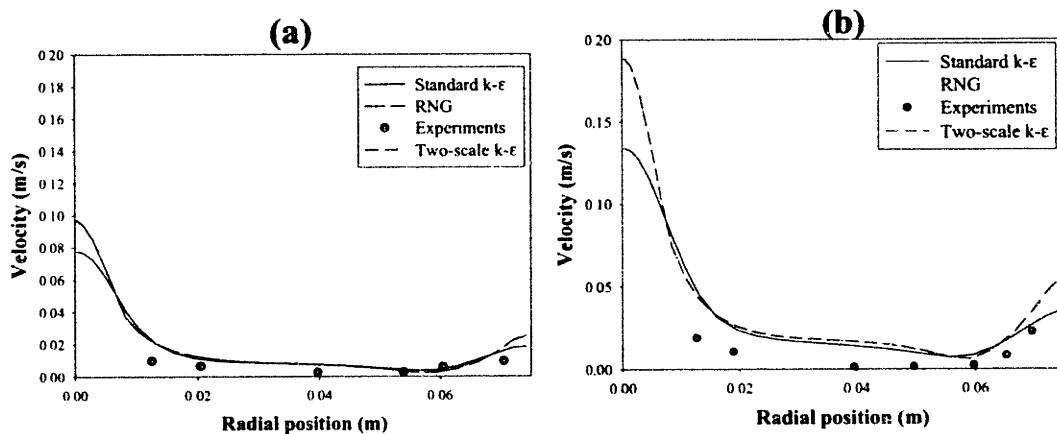


Figure 3.3.3 Comparison between experiments and predictions of mean liquid velocities at 2 cm from top surface along the radius. Three different turbulence models are presented: Standard  $k-\epsilon$ , RNG and Two-scale  $k-\epsilon$ . (a) Current of 300 A. (b) Current of 600 A.

Figure 3.3.4 presents the comparison between turbulent kinetic energy measured by Kang and predicted by the model along the radius at 0.5 cm from the top surface. Again, the three different turbulence models are presented in the plot. The two-scale k- $\epsilon$  model gives the best agreement while the standard k- $\epsilon$  seems to over predict the turbulent kinetic energy field. It is interesting to note that increasing the current produces a great increase in the magnitude of the turbulent kinetic energy.

Finally, Figure 3.3.5 presents a comparison between energy dissipation rate measured by Kang and predicted by the model along the radius at 2 cm from the top surface. The energy dissipation rate is plotted in a logarithmic scale due to the wide range of values in the system. Again, three different turbulence models are presented in the plot. The RNG and the two-scale k- $\epsilon$  models provide reasonable agreement with experiments for the energy dissipation rate, while the standard k- $\epsilon$  predicts much higher values of this turbulent parameter. The prediction presented for the 300 A case shows a better agreement between experiments and predictions. A difference of three orders of magnitude exists between the overall energy dissipation rate profiles between the 300 A and 600 A cases.

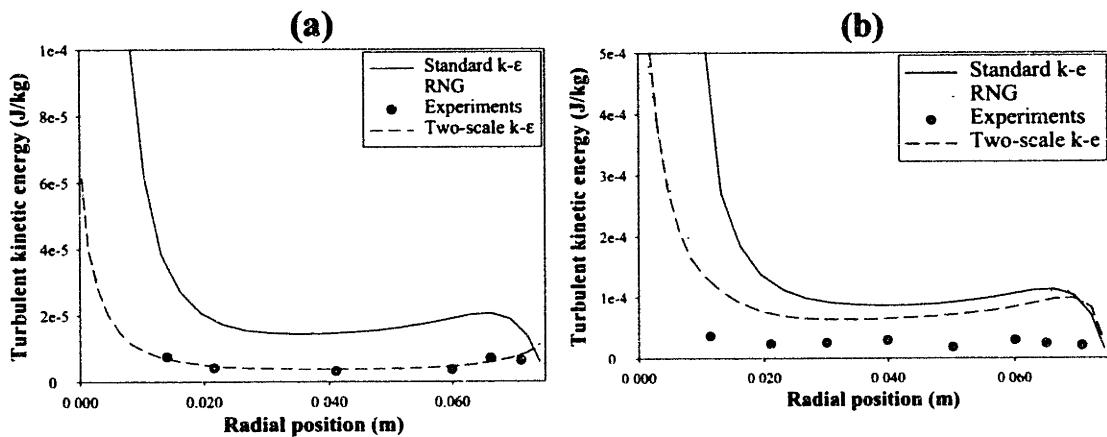


Figure 3.3.4 Comparison between experiments and predictions of turbulent kinetic energy at 0.5 cm from top surface along the radius. Three different turbulence models are presented: Standard k- $\epsilon$ , RNG and Two-scale k- $\epsilon$ . (a) Current of 300 A. (b) Current of 600 A.

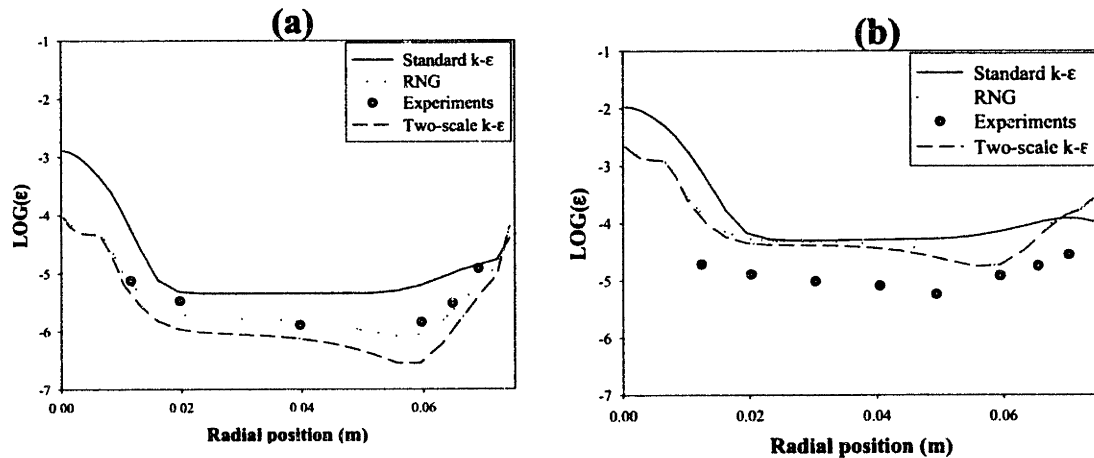


Figure 3.3.5 Comparison between experiments and predictions of energy dissipation rate (in logarithmic scale) at 2 cm from top surface along the radius. Three different turbulence models are presented: Standard k- $\epsilon$ , RNG and Two-scale k- $\epsilon$ . (a) Current of 300 A. (b) Current of 600 A.

### Section 3.3.2: Physical Models of Ladles

When injection of gases through the bottom in DC-EAF is practiced, the physical representation of the system is completely different as was expressed in the mathematical formulation. Experimental or theoretical studies regarding gas injection in DC-EAF are rather limited and more qualitative than quantitative [106]. However, for the last two decades there has been a growing interest in the understanding of fluid flow, mass and heat transfer in other metallurgical systems, such as metallurgical ladles. Considerable efforts can be found in the literature where both physical and mathematical model investigations are reported to represent ladle systems. The number of independent research groups around the world that have studied gas injection systems is significant [47]. Then, experimental studies in these systems are taken as the validation cases for our gas injection mathematical model representation.

Our Eulerian-Eulerian mathematical model is used to simulate experimental studies in centric (2D) and eccentric (3D) air-water systems as well as in gas metal systems ( $\text{N}_2$ -Woods metal) reported in the literature [51,49,107,69,57,71,70]. The model is capable to represent some of the most important bath characteristics such as liquid velocity, gas hold up, turbulent kinetic energy and also mixing phenomena via mixing times. The accurate description of mixing is very important for process analysis. The mixing process is essential in order to predict slag-metal and gas-metal reaction kinetics, which is the ultimate goal of the numerical simulations in ladles.

What follows is just the presentation of some illustrations of the comparison between calculations obtained from our model and experimental measurements.

Figure 3.3.6 shows a schematic representation of the experimental stirred ladles with centric or eccentric injection systems employed by Grevet [49], Sheng et. al. [107], Iguchi et. al. [51], and Oeters et. al. [71,70]. The conditions and parameters characterizing the experimental systems are given in Table 3.3.2 together with the corresponding physical properties.

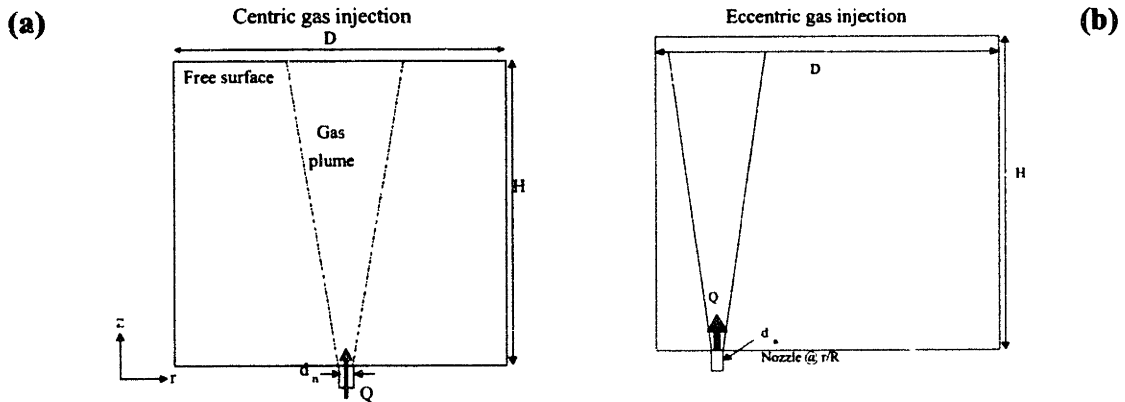


Figure 3.3.6 Schematic representation of the ladle systems simulated in this work.

Case	Vessel diameter $D$ (m)	Depth of liquid $H$ (m)	Nozzle diameter $d_n$ (m)	Flow rate $Q$ (m <sup>3</sup> /s)	Bubble diameter $D_p$ (m)
A) Iguchi [51] Centric Air-water	0.126	0.233	0.002	$4.14 \times 10^{-5}$	0.0125
B) Grevet [49] Centric Air-water	0.6	0.6	0.0127	$2.666 \times 10^{-4}$ $1.333 \times 10^{-4}$	0.02645 0.0229
C) Sheng & Irons [107] Centric Air-water	0.5	0.42	0.004	$1.5 \times 10^{-4}$ $5 \times 10^{-5}$	0.02013 0.0146519
D) Mietz & Oeters [84] Eccentric Air-water	0.63	0.58	0.005 (nozzle at $r/R=2/3$ )	$5 \times 10^{-4}$	0.02944
E) Xie and Oeters [71] Eccentric, N <sub>2</sub> -woods Metal	0.4	0.37	0.003 (nozzle at $r/R=1/2$ )	$5 \times 10^{-4}$	0.027
F) Xie and Oeters [70] Centric N <sub>2</sub> -woods metal	0.4	0.37	0.003	$2 \times 10^{-4}$	0.022
Physical Properties					
Substance	$\rho$ (kg/m <sup>3</sup> )	$\mu$ (kg/ms)	$\sigma_{nt}$ (J/m <sup>2</sup> )		
Water	1000	0.001	0.0727		
Air	1.18	$2.0 \times 10^{-5}$	-		
Woods metal	9400	0.004136	0.46		
Nitrogen	1.16	$2.0 \times 10^{-5}$	-		

Table 3.3.2 Geometric parameters of the simulated experimental systems

### **Centric Gas Injection in Air-Water Systems**

The first three experimental systems shown in Table 3.3.2 (cases A, B and C) were used to test the model against experimental measurements in air-water centric injection systems. A comparison of results of the radial profiles of axial liquid velocities for some of the conditions listed in Table 3.3.2 is presented in Figure 3.3.7 to compare the model predictions and experimental measurements. As seen in the plots, in most cases the agreement is very good. The behavior is similar in all the cases since the axial positions are above the middle ladle height.

### **Centric Gas Injection in Nitrogen-Woods Metal Systems**

The availability of experimental results for gas-stirred ladles with actual metals is important since the effect of buoyancy forces varies considerable from light water to heavy Woods metal or steel. Also, the effect of the gas expansion due to the rapid change in static pressure is higher in high-density metal, as compared to low-density water systems. Thus, the experimental measurements reported by Xie and Oeters [70] provide an excellent set up to validate the model on an actual metal systems.

Figure 3.3.8 shows a comparison between the model predictions and the experimental liquid velocity field measured by Xie and Oeters. As seen in the plots, a very good agreement is observed, not only in the shape and dimensions of the circulation loops, but also in the actual magnitude of the velocity values.

Figure 3.3.9 shows the calculated and measured liquid velocity profiles along the radius at distances of 5 cm, 15 cm, 25 cm and 35 cm from bottom. As seen in the figures, the flow profiles are narrow near the nozzle and become wide closer to the free surface. The maximum velocities are always located at the center and they decrease in magnitude at locations approaching the free surface. In comparing predictions with measurements, an excellent agreement is observed, except near the free surface (at 35 cm from the bottom), where lower velocities are predicted. Similar plots are presented in Figure 3.3.10 for the predicted and measured gas holdup profiles. It is noted that the gas fraction profiles also exhibit a maximum at the symmetry axis and the distribution follows a Gaussian form, which becomes wider as the distance from the nozzle increases. The maximum in the curves decreases rapidly as the distance from bottom increases. The comparisons presented in these curves also exhibit an excellent agreement, except again in the vicinity of the free surface, where lower gas fractions are predicted in the central region of the plume.

## **Eccentric Gas Injection in Nitrogen-Woods Metal Systems**

The modeling capability to represent and study systems with eccentric gas injection is even more important than in the previous (centric) case, since eccentric injection is the common practice in industrial ladle and DC-EAF operations. The reason for adopting eccentric injection is due to the apparent better mixing in the melt as compared to centric injection. This type of injection, however, inherently involves a 3D system with more complex flow patterns and less intuitive mixing characteristics.



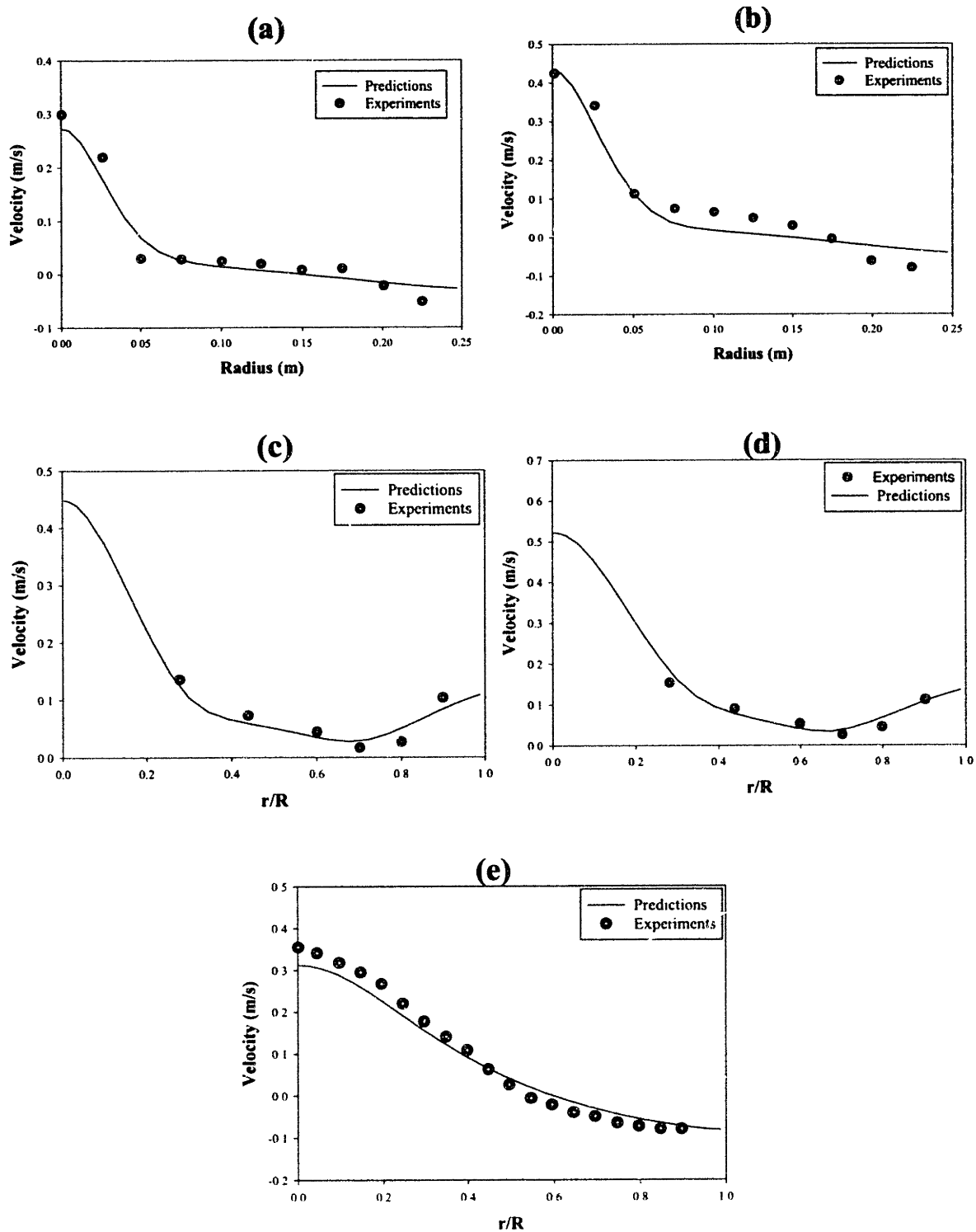


Figure 3.3.7 Predicted and experimental liquid axial velocity profiles as a function of the radial position for different experimental systems. (a) Sheng and Irons with  $0.5 \times 10^{-4} \text{ m}^3/\text{s}$  at 0.21 m from nozzle. (b) Sheng and Irons with  $1.5 \times 10^{-4} \text{ m}^3/\text{s}$  at 0.21 m from nozzle. (c) Grevet with  $1.33 \times 10^{-4} \text{ m}^3/\text{s}$  at 0.408 m from nozzle. (d) Grevet with  $2.66 \times 10^{-4} \text{ m}^3/\text{s}$  at 0.408 m from nozzle. (e) Iguchi at 0.1398 m from nozzle.

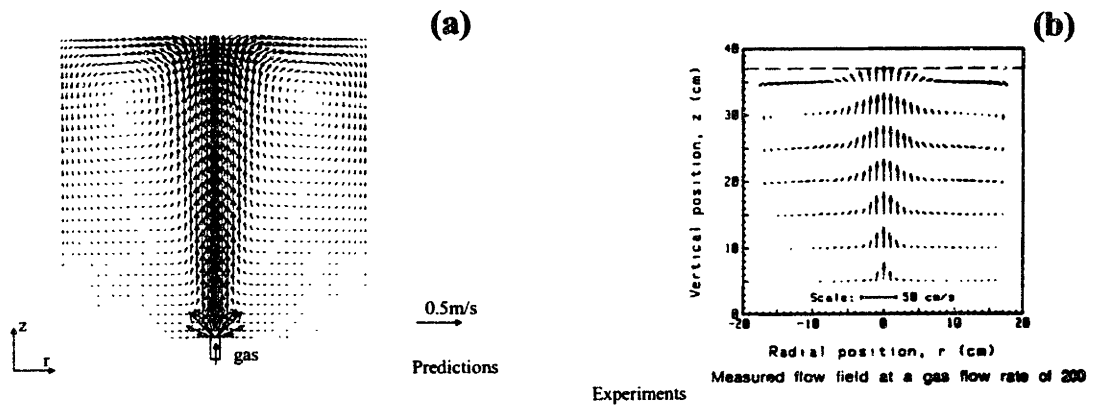


Figure 3.3.8 Comparison between predicted (a) and measured (b) liquid velocity fields (case F in Table 3.3.2)

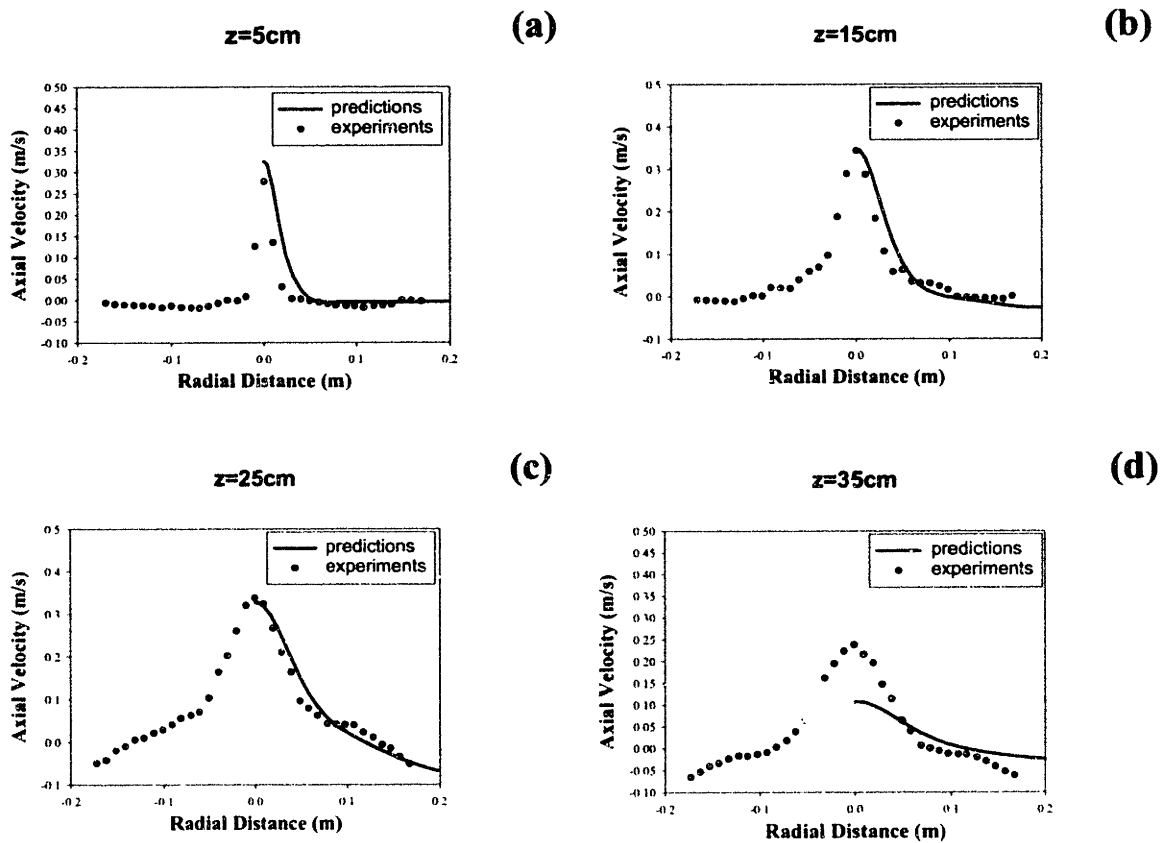


Figure 3.3.9 Radial profiles of liquid axial velocity at different axial positions (case F in Table 3.3.2). Distance from the bottom: (a) 5 cm; (b) 15 cm; (c) 25 cm; (d) 35 cm

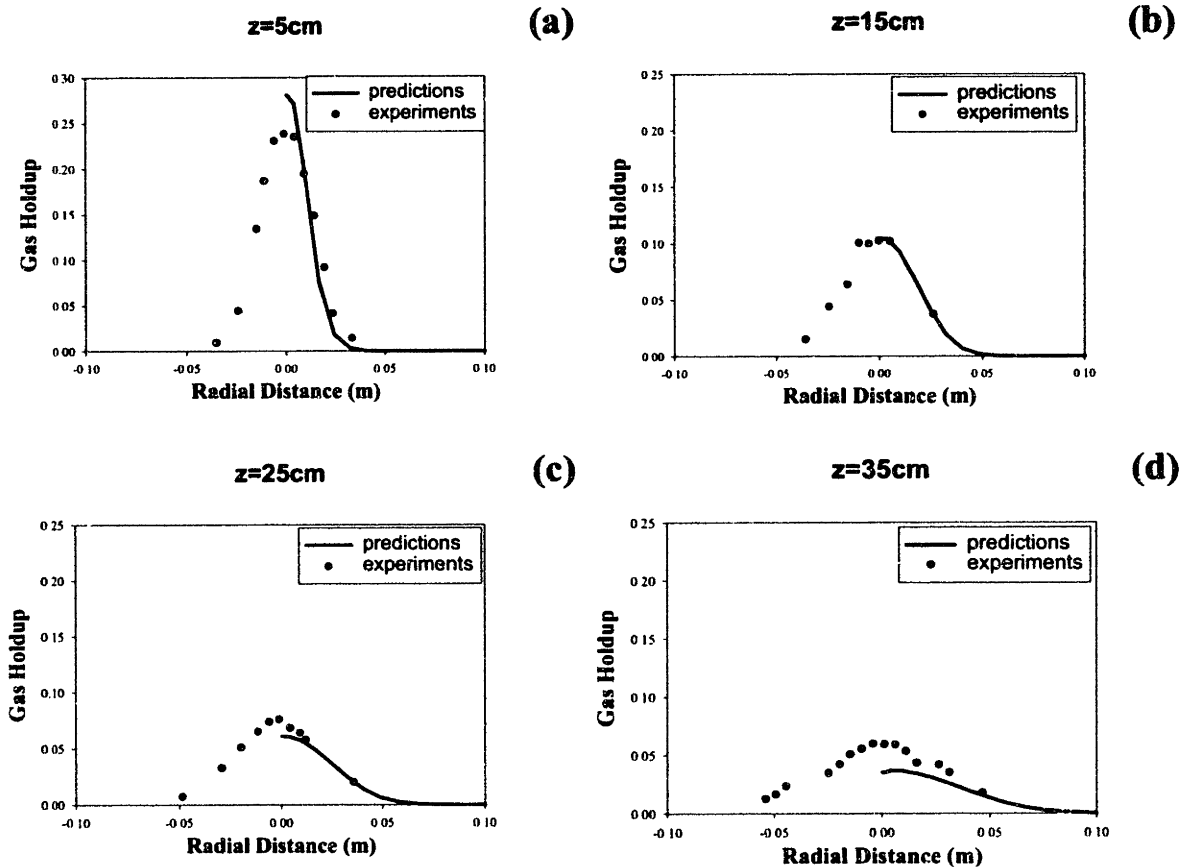


Figure 3.3.10 Radial profiles of gas hold up at different axial positions (case F in Table 3.3.2). Distance from the bottom: (a) 5 cm; (b) 15 cm; (c) 25 cm; (d) 35 cm

Figure 3.3.11 shows the predicted and experimental liquid velocity fields at the  $r$ - $z$  plane containing the symmetry axis and the center of the nozzle. It is seen that the agreement shown in this comparison is excellent in terms of both the flow patterns and the order of magnitude of the velocities. It is noted how significant the single loop shown in the figure forces the liquid to follow a deflected trajectory toward the wall. Although not presented in this section, the overall velocity patterns on different  $r$ - $z$  planes are significantly affected by the azimuthal velocity component, which affect the mixing behavior of the system.

The corresponding comparison between predicted and measured gas holdup is shown in Figure 3.3.12, on the same  $r$ - $z$  plane containing the symmetry axis and the nozzle center and at different height locations. The gas distribution profiles show the deflection of the plume promoted by the velocity field shown in Figure 3.3.11. It can be seen in the figure that a good overall agreement is observed between predicted and experimental radial profiles, although the predictions do not depict as high plume deflection as that shown in the experiments.

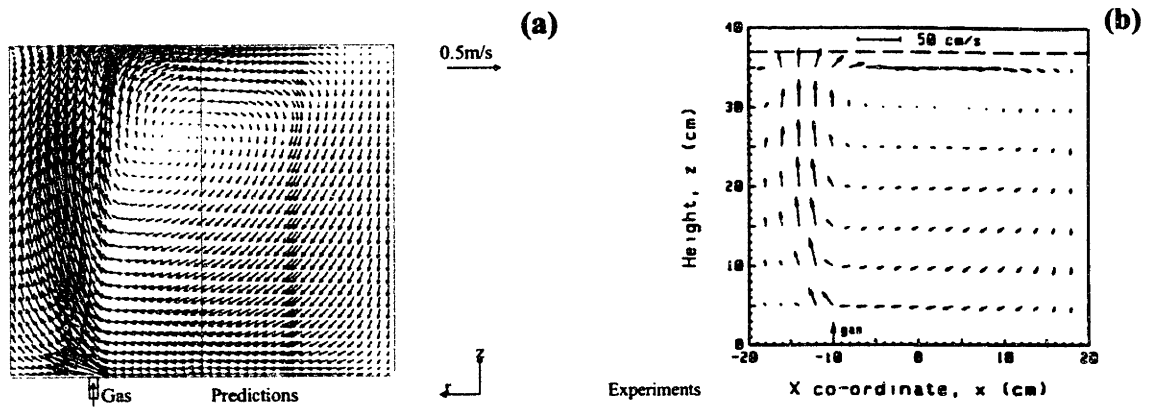


Figure 3.3.11 Comparison between predicted (a) and measured (b) liquid velocity fields for eccentric injection of nitrogen in Woods metal (case E in Table 3.3.2)

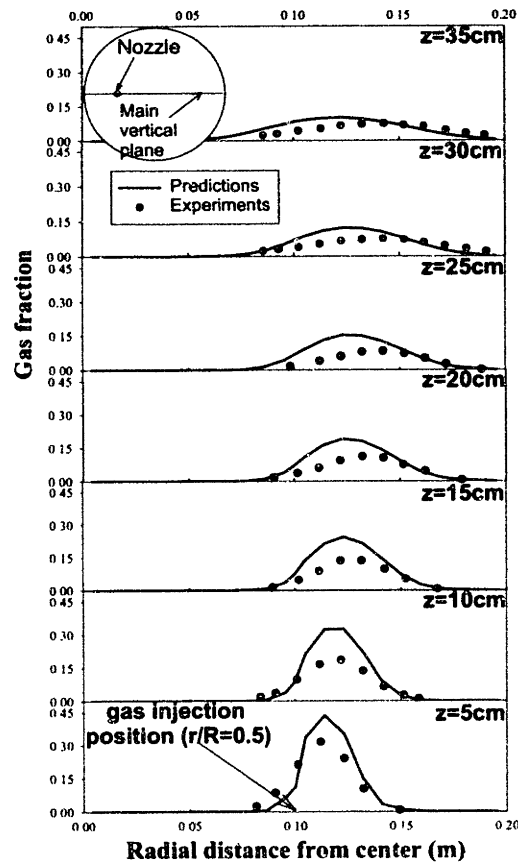


Figure 3.3.12 Comparison between predicted and measured gas fraction distributions for eccentric injection of nitrogen in Woods metal (case E in Table 3.3.2). The  $r$ - $z$  plane shown corresponds to the plane containing both the symmetry axis and the center of the nozzle. The different axial locations are 5, 10, 15, 20, 25, 30, and 35 cm from the bottom.

### **Eccentric Gas Injection in Air-Water Systems (Mixing Phenomena)**

The numerical analysis of mixing phenomena in eccentric gas injection systems can be conducted based on the experiments carried out by Mietz and Oeters [84] in which, in addition to velocity, gas holdup and turbulent fields, they also reported detailed measurements of tracer dispersion. In their experiments, they injected a fixed amount of a tracer substance (3 ml of 0.85 M solution of NaOH) at a fixed position in the central region of the plume. The tracer was introduced into a fully developed flow pattern for an eccentric gas injection of air into water. The evolution of the mixing process was then recorded by measuring the tracer concentration as a function of time at different positions in the ladle.

Simulations were performed in order to describe the motion and mixing of solute. This was achieved by solving a transient tracer conservation equation on a fully steady state two-phase Eulerian-Eulerian solution for the fluid and gas. The initial condition sets the concentration of solute corresponding to the injection position and zero concentration of solute everywhere else. For the computation a laminar Schmidt number was set with a value of diffusivity for NaOH in water of  $2.12667 \times 10^{-7} \text{ m}^2/\text{s}$  (computed from the ionic model for dilute solutes) and a turbulent Schmidt number equal to one.

Figure 3.3.13 shows the predicted and measured concentration profiles as a function of time for three different measuring positions. The tracer injection and measuring locations are also depicted schematically in the plots. As seen in the figure, the overall agreement between experimental measurements and predictions is quite reasonable. The tracer concentration history at the different measuring positions is a consequence of the two main factors controlling mixing in this system: the flow patterns and the turbulent characteristics. The knowledge of flow patterns and the turbulent structure in the system, combined with the analysis of tracer dispersion, provide means for the understanding and description of mixing phenomena in this type of reactors. The model validation, gives a reasonable confidence in the capabilities of the model to analyze gas-stirred systems.

The shape of the tracer concentration curves shown in Figure 3.3.13 depicts a cyclic behavior which is directly associated with the characteristic 3-D single loop of fluid that travels in the entire vessel. The circulation time of this loop (i.e., time taken by a concentrated “packet” of fluid to complete a cycle or time between consecutive maxima or minima in the curves) is between 8 to 9 seconds for the cases presented in Figure 3.3.13. As seen in the plots, the frequency in these cycles is nearly constant but their amplitude decreases with time as the mixing process takes place and the liquid becomes homogeneous. Closer inspection of the curves also indicates a delay time involved for a tracer-rich “packet” of fluid to travel from the injection to the corresponding measuring point. This time depends on the relative distance traveled along circulation loops (i.e., relative location between the injection and measuring points). These

delay times are 3, 8 and 10 seconds for the measuring positions a, b, and c shown in the figure, respectively. In the system under analysis, three cycles were required to completely mix the tracer, resulting in a total mixing time of about 35 seconds.

On a more fundamental level, interpretation of these results indicates that the maximum concentration at every cycle decreases as a result of eddy-diffusivity, which promotes lateral dispersion of solute. Thus, the combined effects of convection and eddy diffusion, which depend on the characteristic flow patterns and turbulence structure, play a key role in determining the mixing behavior in the system.

Simulation of mixing phenomena in gas-stirred systems is important since the ultimate goal of the models is to be able to represent slag-metal and gas-metal reactions in ladle metallurgy and DC-EAF operations. Such representations require the full description of complex transport phenomena aspects that include also a suite of auxiliary, semi-empirical, correlations that have resulted from numerous experimental investigations. Therefore, carefully validated models represent an important tool not only to provide process understanding but also to address the numerous critical aspects involved in process design.

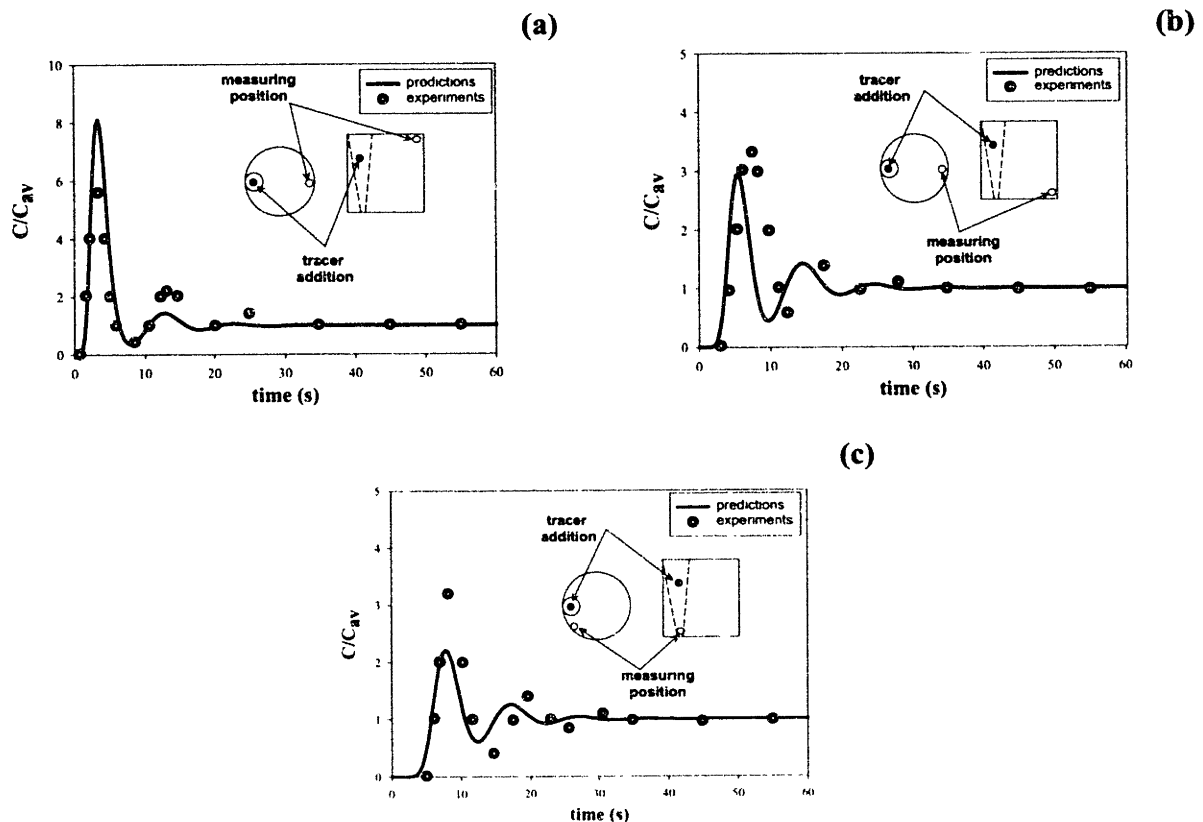


Figure 3.3.13 Tracer concentration history at three different positions for an eccentric injection of air into a water ladle (case D in Table 3.3.2). The concentration is represented in dimensionless form, where  $C_{av}$  is the concentration at full mixing condition and  $C$  is the instantaneous concentration.

## Section 3.4: Bath Model Results

In this section the computational results obtained from the model in the bath region of a DC-EAF are presented for the three different bath models developed, i.e. single-phase model, gas-steel and steel-slag models.

### Section 3.4.1: Results for Single-Phase Model

In this section, results and analysis of the fluid motion and heat transfer in the bath region are presented for the single-phase model. Grid sensitivity is presented followed by a full and detailed description of the bath region under the standard arc case of 40 KA and 25 cm. Finally, analysis of the process is performed to appreciate the effect of some important parameters such as the principal arc variables, i.e., arc current and arc length ( $I$  and  $L$ ). Also, the effect of some other aspects such as size of the anode surface, size of the reactor, and turbulence model are shown through this section. Analysis made on terms of mixing times and heat balances are described parallel to the presentation of results. Most of the analysis is performed under the standard arc case of 40 KA and 25 cm.

#### Section 3.4.1.1: Grid Sensitivity

The grid sensitivity was performed using five different non-uniform 2D grids for the bath region domain of Figure 3.2.1. The r-z non-uniform grids used for comparison are 15x10, 30x20, 45x30, 60x40 and 75x50 cells. These grids represent a cylindrical reactor of 1.5 m of furnace radius,  $R_{furnace}$ , and 0.5 m of liquid depth,  $H$ . More grid points are allocated close to the symmetry and top free surface where a better resolution is required to predict correctly the strong gradients in some bath properties appearing in those zones. Figure 3.4.1 shows the potential and axial velocity distributions along the symmetry axis for the grids tested. With the exception of the coarser grid (15x10) the rest of the grids show similar behaviors and values for the axial profiles. It is also interesting to note that increasing the number of cells makes the axial profiles to converge to the correct values.

In order to appreciate the sensitivity of the grid along the radial direction, the axial velocity profile along the radius at 0.25 m from top surface as well as the radial velocity along the radius but this time at the bottom of the reactor are presented in Figure 3.4.2. Again, most grids, except the coarser, predict almost the same values for both axial and radial velocities.

Apparently, the 45x30, 60x40 and 75x50 grids predict similar fields for the main characteristics of the bath region, being the finer the grid the better the accuracy. However, as accuracy is improved with an increase in the number of cells, the CPU times also increase significantly. Thus, the best grid must provide

a good accuracy but, at the same, should take reasonable CPU times to obtain a converged solution. For this reason, the 60x40 grid is the final choice from the grid sensitivity study.

Figure 3.4.3 presents the non-uniform 60x40 grid used in the rest of the computations for the single-phase model. The one-phase model was implemented in the CFD code PHOENICS-3.2. About 10000 iterations on this 60x40 grid required approximately 1hr of CPU time for convergence on a PentiumII/330.

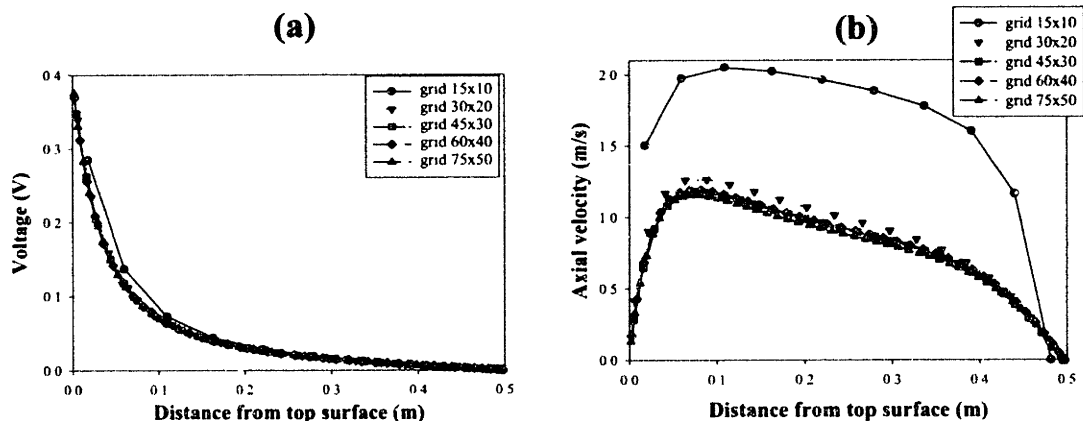


Figure 3.4.1 Grid sensitivity using 5 different non-uniform grids of 15x10, 30x20, 45x30, 60x40 and 75x50. (a) Potential distribution along the symmetry axis. (b) Axial velocity along the symmetry axis.

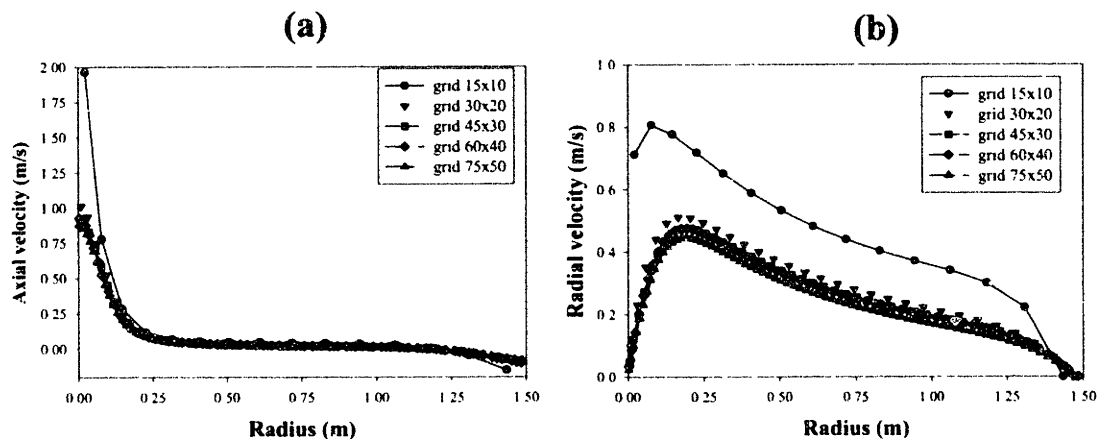


Figure 3.4.2 Grid sensitivity using 5 different non-uniform grids of 15x10, 30x20, 45x30, 60x40 and 75x50. (a) Axial velocity along the radius at 0.25 m from top surface. (b) Radial velocity along the radius at the cell next to the bottom of the reactor.



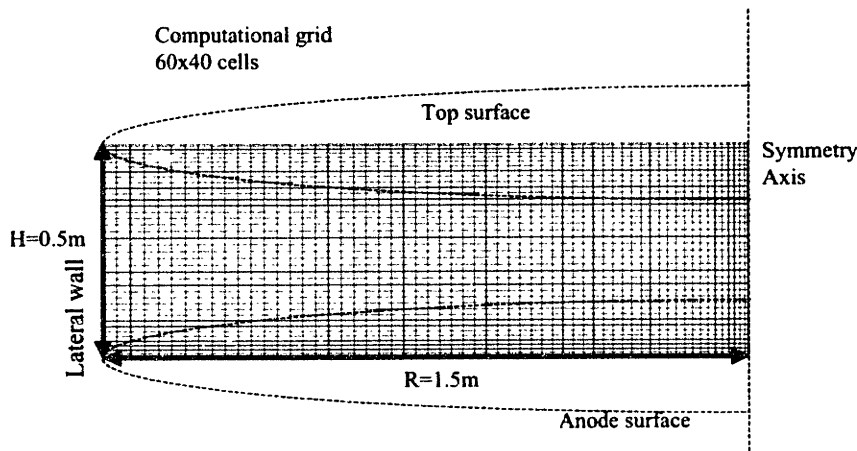


Figure 3.4.3 Computational grid of 60x40 cells selected for calculations based on the grid sensitivity analysis.

### Section 3.4.1.2: Standard Case (Arc Current of 40 KA and Arc Length of 25 cm): General Description

The main characteristics of the bath region are now presented under the effect of the standard arc case of 40 KA of current and 25 cm arc length. The first field presented in Figure 3.4.4 is the steel velocity (Figure 3.4.4 (a)), in which the flow pattern exhibits a circulation loop in the clockwise direction. The steel presents downward flow near the symmetry axis and upward flow near the lateral wall. The magnitudes of the velocities are large close to the symmetry axis (with a maximum velocity of 1.2 m/s) and small close to the lateral wall. Electromagnetic body forces drive the fluid motion leaving the other two driving forces, i.e. shear from the arc and buoyancy, in a secondary position (this point will be further discussed in the next section). The flow pattern is developed in a similar way to the jet formed in the arc region. In this case, a high concentration of forces located below the arc and close to the symmetry axis (called “arc attachment zone” or “AAZ” in the figures), creates a high-pressure zone that forces fluid to move downward to a lower pressure zone. Then, the fluid reaches the bottom wall and is forced to flow in the radial direction until it reaches the lateral wall, where it flows upwards. Eventually the free surface makes the liquid to flow in the radial positive direction until the loop is completed when fluid returns to the initial position in the arc attachment zone. Stream lines presented in Figure 3.4.2 (b) confirm the circulation flow pattern followed by the liquid under the effect of the arc, by forming a single clockwise loop, whose center is located closer to the lateral wall and midway between top and bottom surfaces.

The circulatory motion developed in the bath region can also be seen in Figures 3.4.4 (c) and (d), where axial and radial velocities are plotted as a function of the radius at five different axial positions from the top surface (0m or top surface, 0.125 m, 0.25 m, 0.375 m and 0.5 m or bottom surface). It can be seen that the axial velocities are very high close to the symmetry axis but in the rest of the reactor steel is practically static and, close to the lateral wall, the axial velocity changes sign (velocities in the upward direction). Radial velocities also show the circulatory pattern of fluid flow. At the top surface, large negative radial velocities (directed towards the symmetry axis) are found due to the electromagnetic body forces. In contrast, at the bottom surface radial velocities are also large, but positive due to the flow deflected coming from the top of the reactor at the symmetry axis.

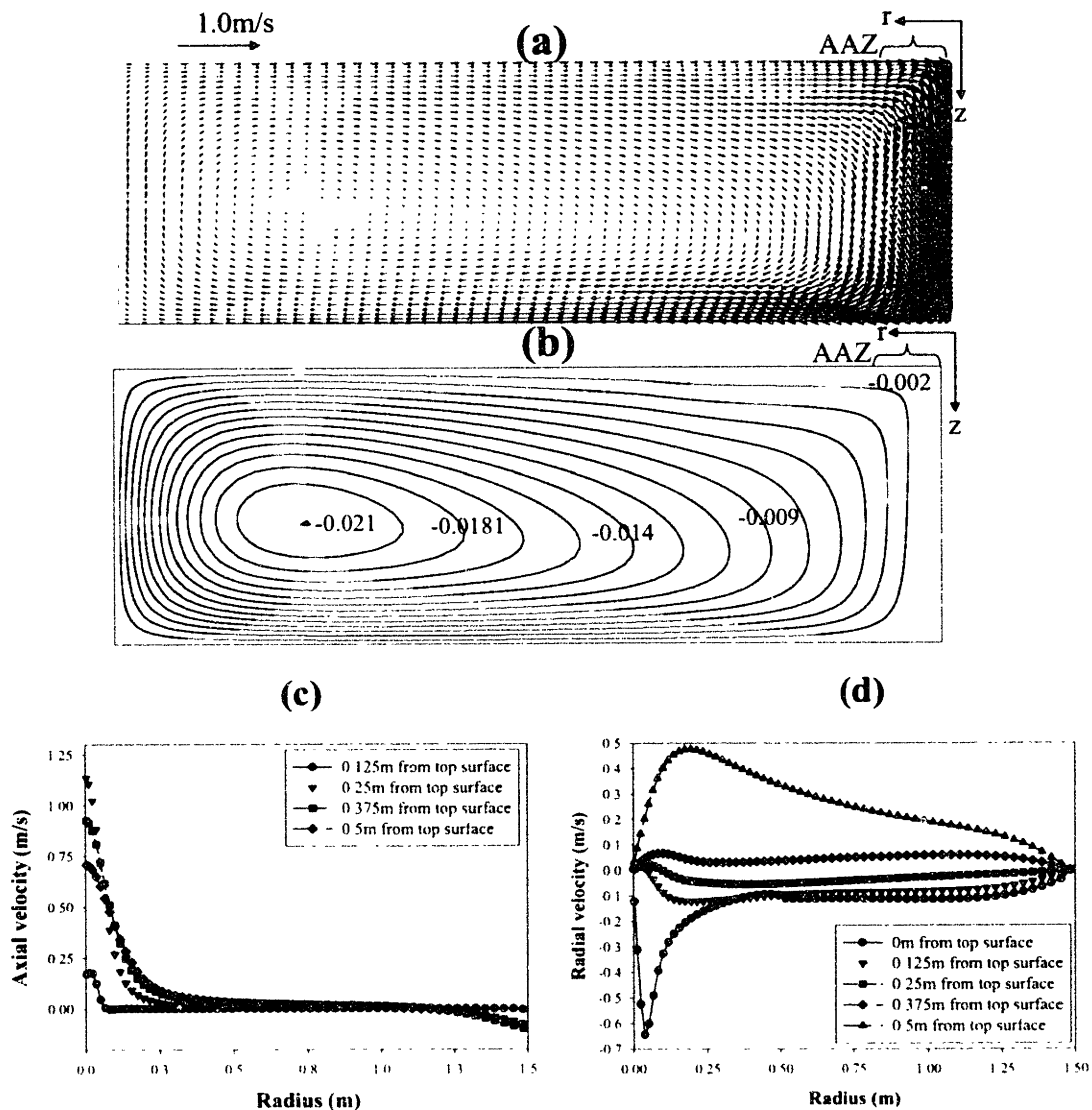


Figure 3.4.4 Bath region characteristics for the standard case (40 kA and 25 cm): (a) Velocity field. (b) Stream lines. (c) Axial velocity profiles along the radius at different axial distances of 0.125, 0.25, 0.375 and 0.5 m from top surface. (d) Radial velocity profiles along radius at different axial distances of 0, 0.125, 0.25, 0.375 and 0.5 m from top surface.

Figure 3.4.5 (a) shows the temperature field inside the bath region. The effect of the arc is evident since the highest temperatures are found at the top surface just below the arc (the “arc attachment zone”). In this zone, most of the heat, current, and shear are transferred from the arc to the bath. The velocity field shapes the temperature field. Liquid moving downwards close to the symmetry axis convects liquid enhancing the dissipation of heat received at the top surface from the arc. Temperature gradients are high close to the arc attachment zone but start decreasing as distance from the arc attachment zone increases. A maximum temperature of 1952 K is found at the center of arc attachment zone, where the highest heat flux is received. A minimum temperature of 1772 K is located close to the lateral wall and top surface, where the effect of the arc is not important and radiation losses predominate. A total temperature gradient of 180 K exists between the coldest and hottest region of the reactor. In Figure 3.4.5 (b) radial temperature profiles are plotted at five axial positions (0, 0.125, 0.25, 0.375 and 0.5 m from top surface). In this figure it can be better appreciated the effect of the arc on the arc attachment zone. Also, it is interesting to note that at the top surface, effectively, maximum and minimum temperatures are found (maximum at arc attachment zone and minimum at the lateral wall). It is interesting to note the higher overall temperatures along the radial temperature profile at the bottom in comparison with those along the radial profiles at about 0.1 m height from the bottom. These higher temperatures at the bottom can be explained as a consequence of the main circulation loop, which carries hot fluid from the arc attachment zone directly along the bottom of the bath.

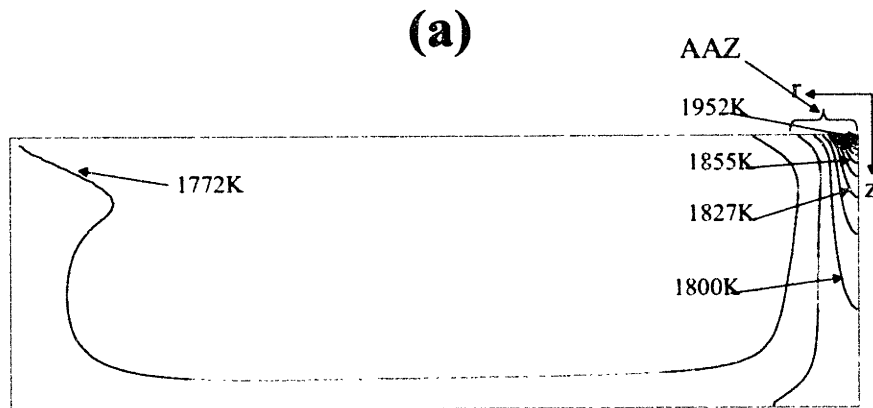


Figure 3.4.5 Bath region characteristics for the standard case (40 kA and 25 cm): (a) Temperature field.

(b)

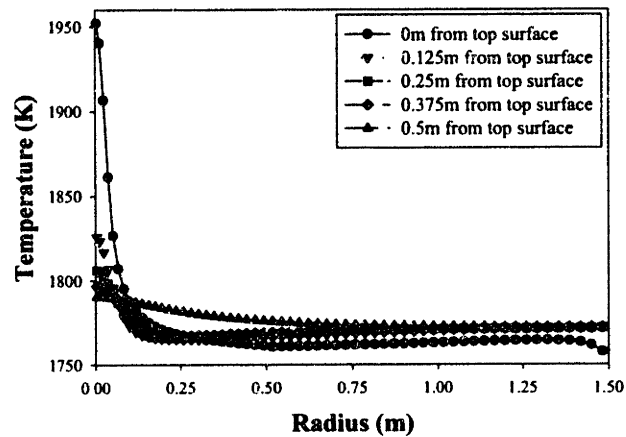


Figure 3.4.5 (cont.) Bath region characteristics for the standard case (40 kA and 25 cm): (b) Radial temperature profiles along radius at axial distances of 0.125, 0.25, 0.375 and 0.5 m from top surface.

Regarding electric parameters in the bath, Figure 3.4.6 (a) presents the potential field in this region. A potential difference of  $\sim 0.4$  V is found through the liquid steel. This small value (compared with the several hundreds of volts in the arc region) is explained due to the high electric conductivity of steel ( $7.14 \times 10^5 \Omega^{-1} \text{m}^{-1}$ ). Isopotential lines form semicircles and the gradient of potential strongly decreases as the distance from the top surface increases. Current density vectors (proportional to the potential gradient given by equations 3.2.15) are expected to decrease and spread from the arc attachment zone where the current density is exclusively in the axial direction and presents a Gaussian-like distribution as mentioned in Chapter 2. Figure 3.4.6 (b) presents the vector current density field in the bath region. In effect, current density vectors converge to the small circular area in the arc attachment zone at the top surface. Current density vectors are large in that zone, but deeper into the liquid their magnitude decreases significantly. This phenomenon occurs due to the big area differences between the small conduction area at the arc attachment zone and the large anode surface area at the bottom. Also, since steel is assumed to have a constant electric conductivity, thus helps to spread the current, and the radial components are predominant just outside the arc attachment zone. The magnetic flux density field is presented in Figure 3.4.6 (c). The largest value of 0.14 T is located at the top surface just at the edge of the arc attachment zone. This field corresponds to the integration of Ampere's law (equation 3.2.16). The main condition that allows using this expression, is that the current density must be aligned predominantly in the axial direction, which it is not clearly the case in the bath region, where due to the circular shape of the potential lines, the radial components of the current density are important. However, the advantage of computing the magnetic flux density field with equation 3.2.16 is its easy numerical implementation. Additionally, at the top surface and at the symmetry axis the assumption is valid, since current density vectors are actually axially directed. It is also important to mention that it is in those positions (top free surface and symmetry axis) where the biggest electromagnetic body forces are expected. Therefore, neglecting the presence of the radial

component of the current density is a reasonable assumption since does not affect the computation of the body forces and in consequence predicts accurately the fluid flow patters. The electromagnetic body force field is presented in Figure 3.4.6 (d). These forces are computed from the cross product between current density and magnetic flux density ( $J \times B$ ). Therefore, maximum values of the Lorentz forces are found at the arc attachment zone where maximum vales of both  $B_\theta$  and  $J$  are found.

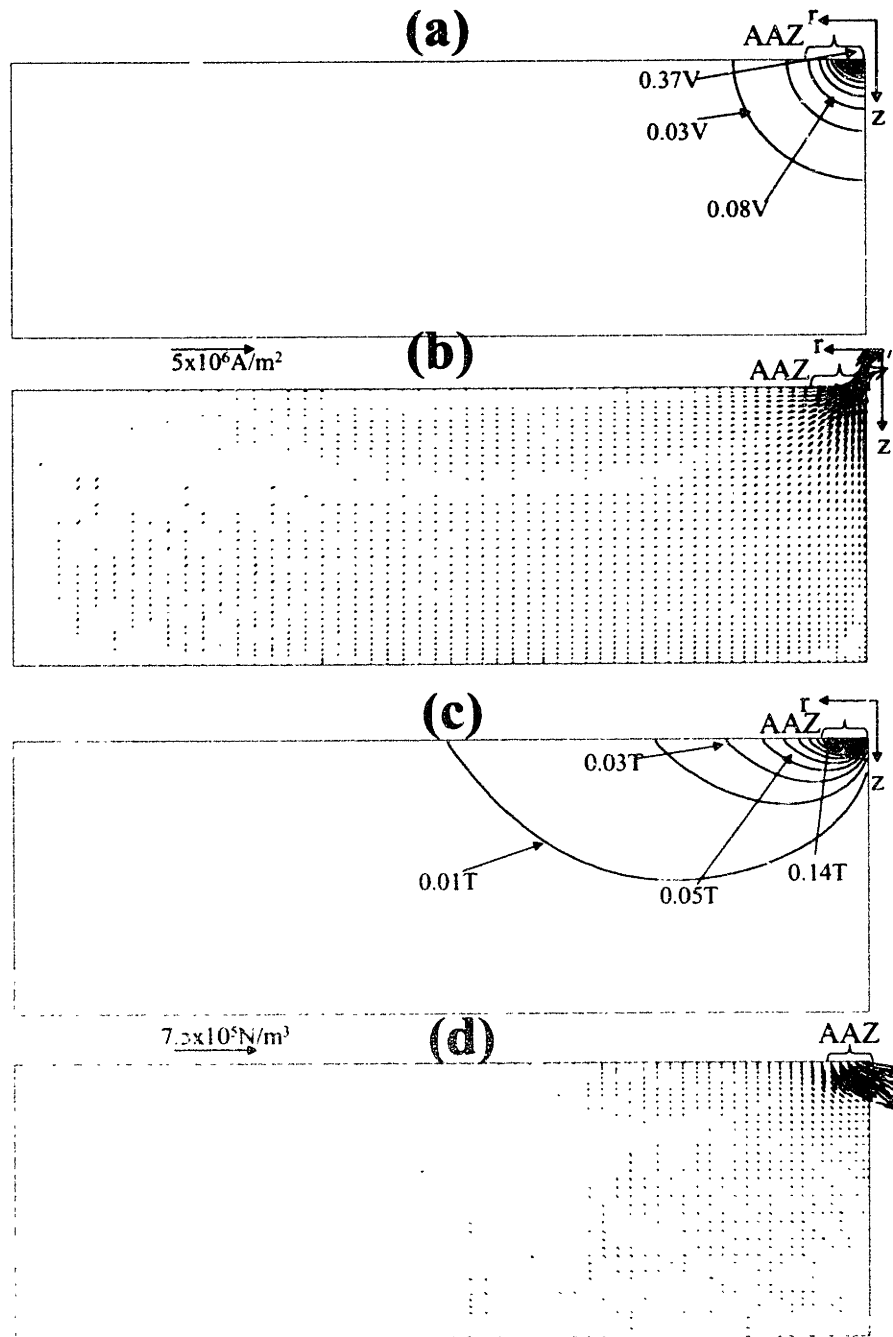


Figure 3.4.6 Bath region characteristics for the standard case (40 kA and 25 cm): (a) Potential field. (b) Temperature field. (c) Magnetic flux density field. (d) Electromagnetic body force field.

Finally, Figure 3.4.7 presents the turbulent parameters computed in the bath region. Turbulent kinetic energy and energy dissipation rate (Figures 3.4.7 (a) and (b)) present similar contour plots. The highest values and gradients are found at the arc attachment zone and then both (values and gradients) start decreasing as distances from this zone increases (in a similar behavior as presented for the temperature field in Figure 3.4.5 (a)). The turbulent kinematic viscosity,  $\mu$ , is presented in Figure 3.4.7 (c). Observing the turbulent kinematic viscosity field, a complex turbulent structure is found. However, several different regions can be distinguished in the bath. The first region is located below the arc attachment zone extending to almost the bottom of the furnace. The highest turbulence is found in this region as a consequence of the high electromagnetic forces as well as the high velocity gradients prevailing in this zone. However, this region occupies a very small volume fraction of the entire reactor. Another region extend for most of the reactor (but away from the symmetry line) presenting lower gradients of turbulent viscosity and eventually the turbulent viscosity drops to zero at the walls. Figure 3.4.7 (d) presents radial profiles of turbulent kinematic viscosity at 0, 0.125, 0.25, 0.375 and 0.5 m from the top surface where it can be appreciated that outside a radial cylinder of  $\sim 0.4$  m, most of the reactor has relatively the same levels of turbulence.

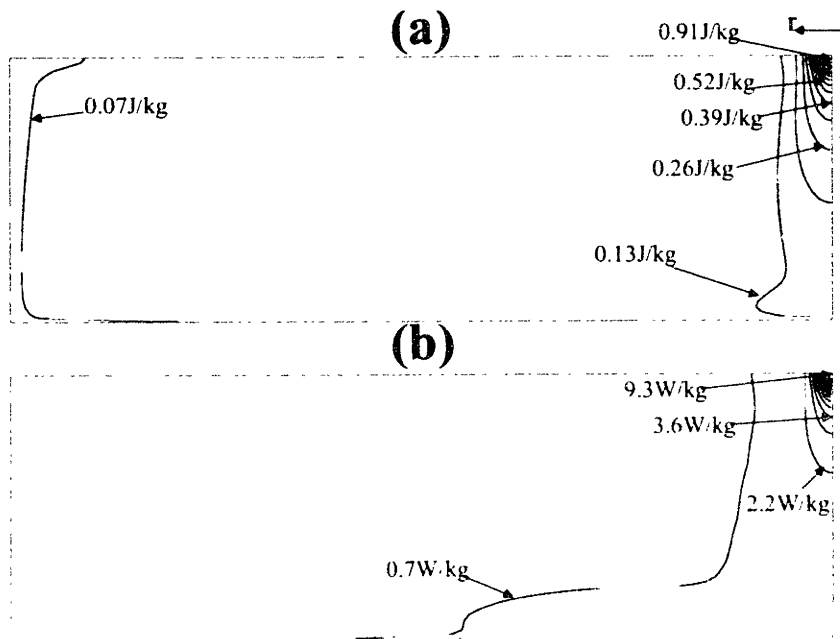


Figure 3.4.7 Bath region characteristics for the standard case (40 KA and 25 cm): (a) Turbulent kinetic energy field. (b) Energy dissipation rate field.

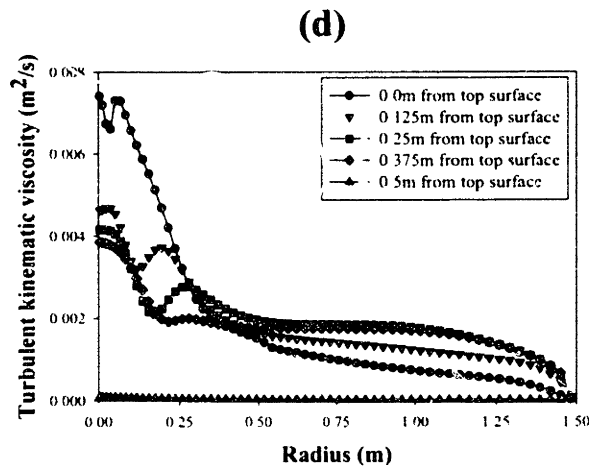
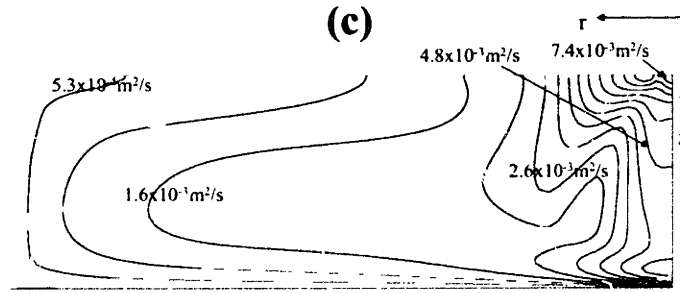


Figure 3.4.7 (cont.) Bath region characteristics for the standard case (40 KA and 25 cm): (c) Turbulent kinematic viscosity field. (d) Turbulent kinematic viscosity radial profiles at 0, 0.125, 0.25, 0.375 and 0.5 m from top surface.

The description presented above indicates that close to the arc attachment zone large gradients of some variables are present and as the distance from the top surface increases, these gradients decrease. To better appreciate this last statement, axial profiles of temperature, potential, and axial velocity along the symmetry axis are presented in Figure 3.4.8. In this plot, potential and temperature axial profiles clearly show that close to the arc attachment zone large gradients exist, but as the distance from the top surface increases, the profiles become smooth.

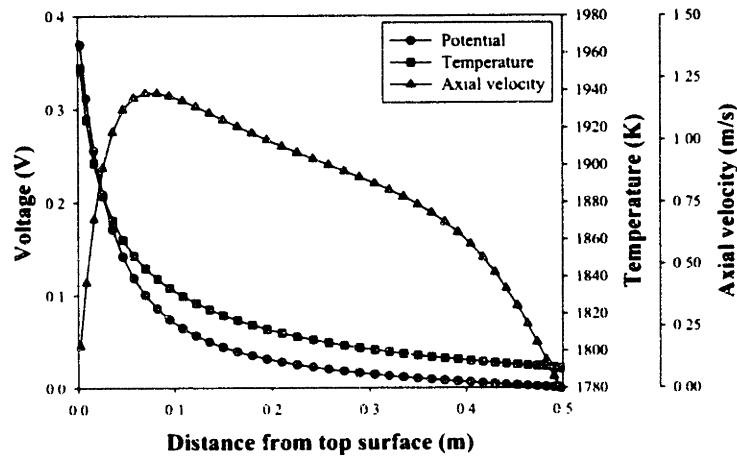


Figure 3.4.8 Axial bath properties along the symmetry axis: temperature, axial velocity and potential distributions.

### Section 3.4.1.3: Effect of Buoyancy, Shear Stress and Electromagnetic Body Forces on Fluid Dynamics and Heat Transfer in the Bath Region

Figure 3.4.9 (a) shows the velocity and temperature fields calculated under the combined effects of the shear stress from the arc, buoyancy, and electromagnetic forces. Temperature and velocity fields were already analyzed in the last section.

The effect of each driving force (shear, buoyancy, and electromagnetic) is analyzed separately in independent calculations and compared against the combined case. Figure 3.4.9 (b) shows the effect of buoyancy, where a single circulation loop is also formed, but where the direction is counter-clockwise in this case (i.e., fluid flow is upwards at the symmetry axis and downward close to the wall). As seen in the figure, very low velocities are predicted for this hypothetical case ( $\sim 0.1$  m/s) and, as a result, the temperature field shows an extremely high hot spot on the surface in the central region of the bath (arc attachment zone).

Figure 3.4.9 (c) shows the effect of the shear stress from the arc. This also results in a single circulation loop in the same direction as that for buoyancy, although higher maximum velocities ( $\sim 0.5$  m/s) are observed in the case. Poor heat dissipation results in temperature stratification and high thermal gradients in the bath.



Finally, the effect of electromagnetic forces is shown in Figure 3.4.9 (d). The calculated circulation loop and temperature distribution clearly shows that electromagnetic effects are dominant in establishing velocity and temperature distributions in the bath. An overall comparison among the four cases in the figure also shows that buoyancy and shear forces counteract the effect of electromagnetic forces. This produces less dissipation in the bath and higher overall temperature gradients.

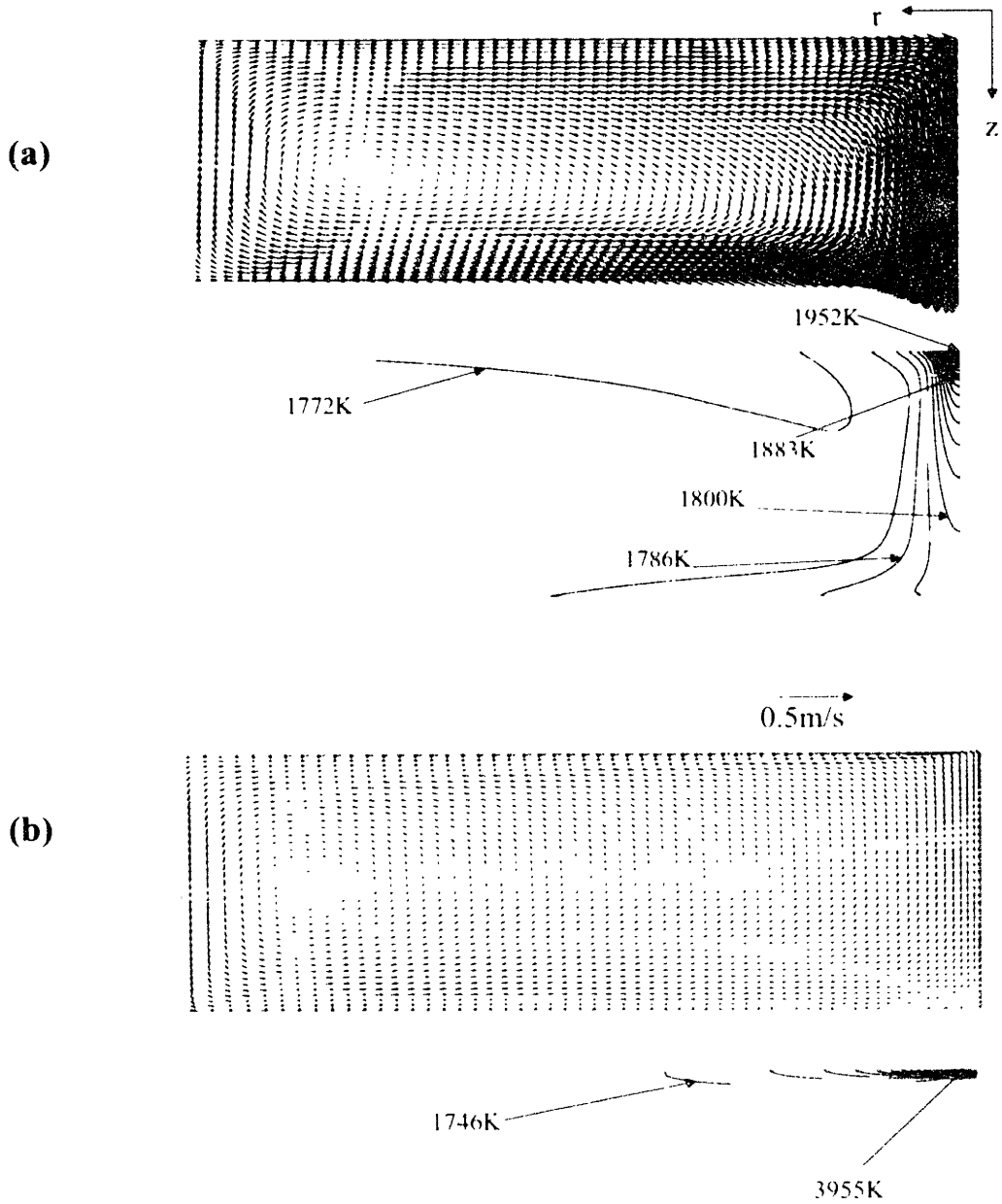


Figure 3.4.9 Temperature and velocity fields in the bath region under the influence of different effects driving the flow (a) Combined effect (shear stress, buoyancy, and electromagnetic forces), and (b) Buoyancy only

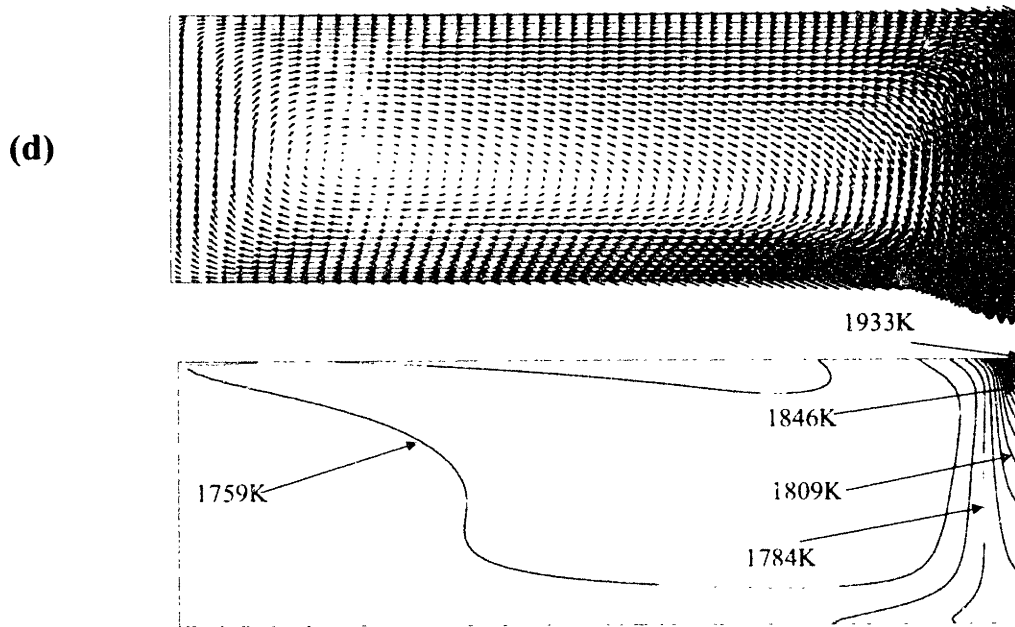
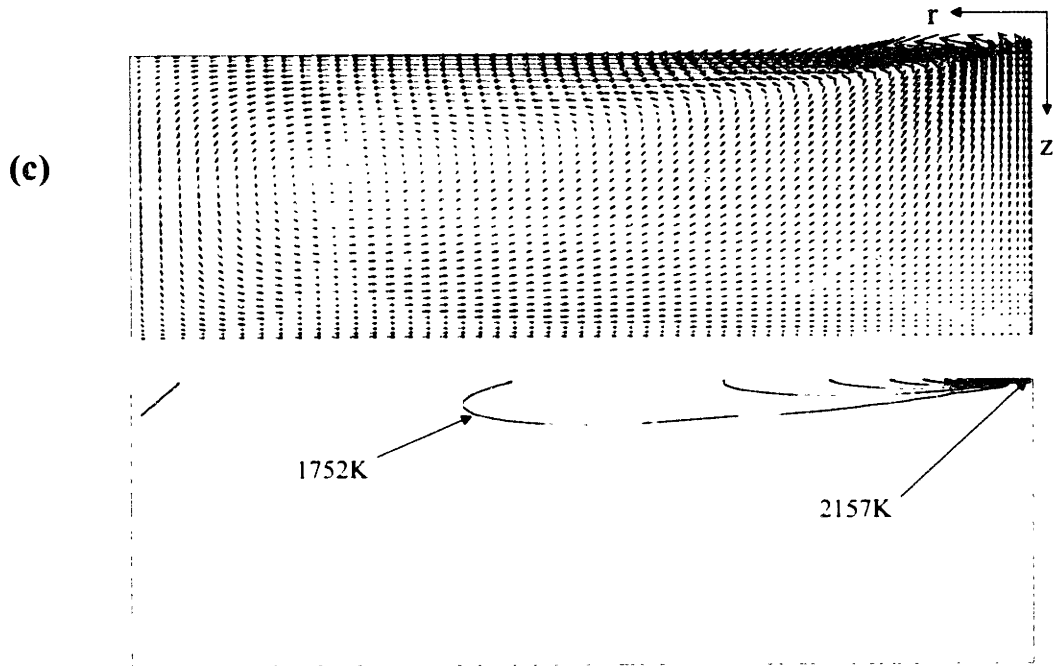


Figure 3.4.9 (cont.) Temperature and velocity fields in the bath region under the influence of (c) Shear stress only, and (d) Electromagnetism only.

### **Section 3.4.1.4: Effect of Arc Length and Arc Current on Fluid Dynamics and Heat Transfer in the Bath Region**

A sensitivity study is presented in this section to explore the effect that the arc length and the arc current have on the main bath characteristics.

#### **Arc length sensitivity**

To examine the effect of the arc length on the arc characteristics, a sensitivity study was conducted running computations of the bath region under electric arcs with a single arc current of 40 KA and five different arc lengths of 15, 20, 25, 30 and 35 cm.

The effect of the arc length on temperature and velocity at the symmetry axis is presented in Figures 3.4.10 (a) and (b) respectively. It can be seen in Figure 3.4.10 (a) that the bath temperature in the arc attachment zone is not very sensitive to arc length variations. However, it has to be remembered that an increase in the arc length is equivalent to an increase in the arc power and consequently more heat is transferred from the arc as the arc length increases. Therefore, below the arc attachment zone, it is clearly observed that bath temperatures are higher for longer arc lengths. In contrast, axial velocities at the symmetry axis in the bath region decrease as the arc length increases as can be observed in Figure 3.4.10 (b). Since the arc current is kept at a constant value of 40 KA, the same current must flow through the bath region. However, as the arc length increases, the current density profiles at the bath surface become wider and present lower maximum values at the center. This wider current density profiles are not able to concentrate strong enough electromagnetic body forces to move the liquid with the high velocities obtained for shorter arc lengths (narrow arc current density profiles). Maximum velocities of less than 1.0 m/s are obtained for an arc length of 35 cm arc length while maximum values of velocity of around 1.5 m/s are obtained for an arc length of 15 cm.

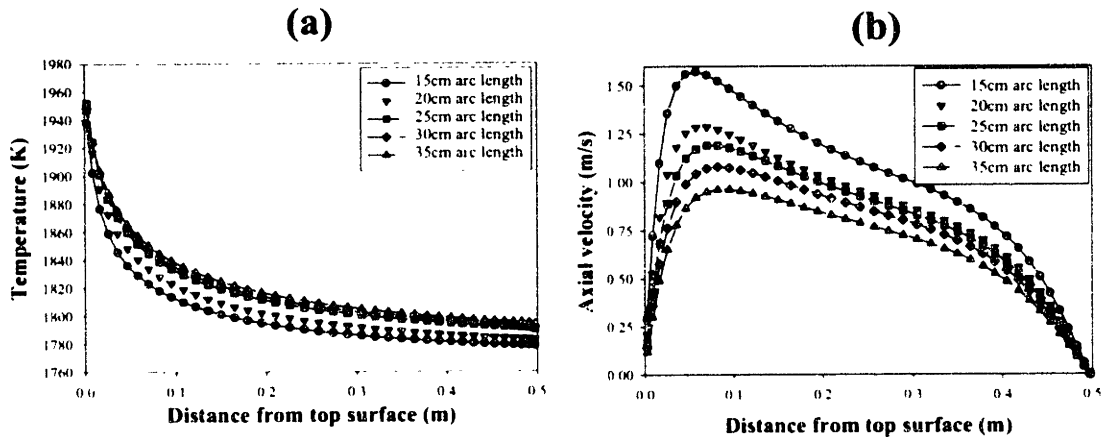


Figure 3.4.10 Axial profiles of bath characteristics along the symmetry axis for different arc lengths of 15, 20, 25, 30, and 35 cm and 40 KA of arc current. (a) Temperature. (b) Axial velocity.

Radial velocities also present a similar trend as can be seen in Figure 3.4.11 (a). In this figure, radial velocity profiles along the radius at the bottom surface are plotted for all arc lengths tested in this study. Again, short arc lengths give larger velocities than large arc lengths. Then, it can be generalized that as the arc length increases the bath velocities decrease, as can be seen in Figure 3.4.11 (b), where maximum velocities are plotted as a function of arc length.

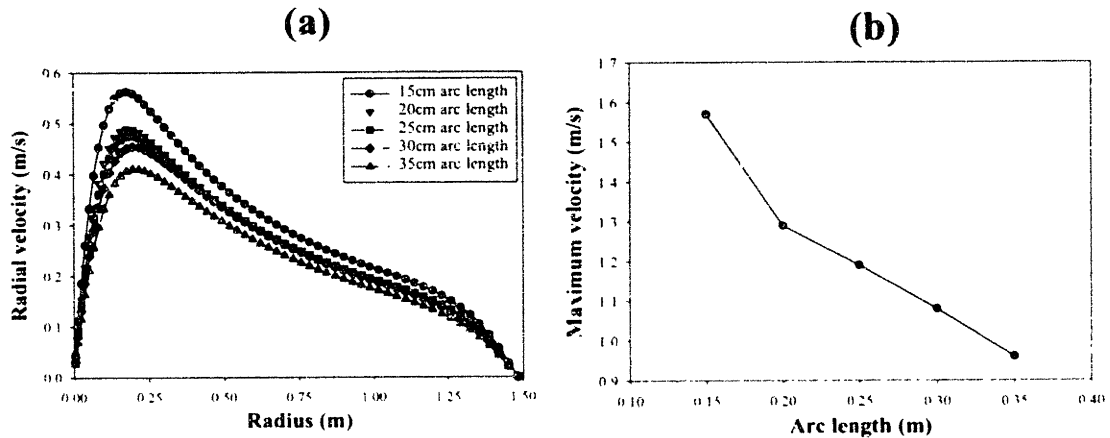


Figure 3.4.11(a) Radial steel velocities along radius at the bottom surface for different arc lengths of 15, 20, 25, 30, and 35 cm and 40 KA of arc current. (b) Maximum velocity in the domain as a function of the arc length.

Regarding turbulent parameters, in Figure 3.4.12 (a) and (b) the turbulent kinetic energy and energy dissipation rate are plotted along the radius at 0.25 m from the top surface for all arc lengths tested. Similar to the bath velocity behavior, both, the turbulent kinetic energy and energy dissipation rate,

decrease as the arc length increases. Figure 3.4.12 (c) presents the radial profiles of turbulent kinematic viscosity at 0.25 m from the top surface for the different arc lengths. The turbulent kinematic viscosity is relatively insensitive to arc length variations as can be appreciated in the figure, where a single profile is obtained regardless the arc length. Then, despite the strong sensitivity of the energy dissipation rate and turbulent kinetic energy on arc length, the combined effect results in rather insensitive turbulent viscosity to arc length variations.

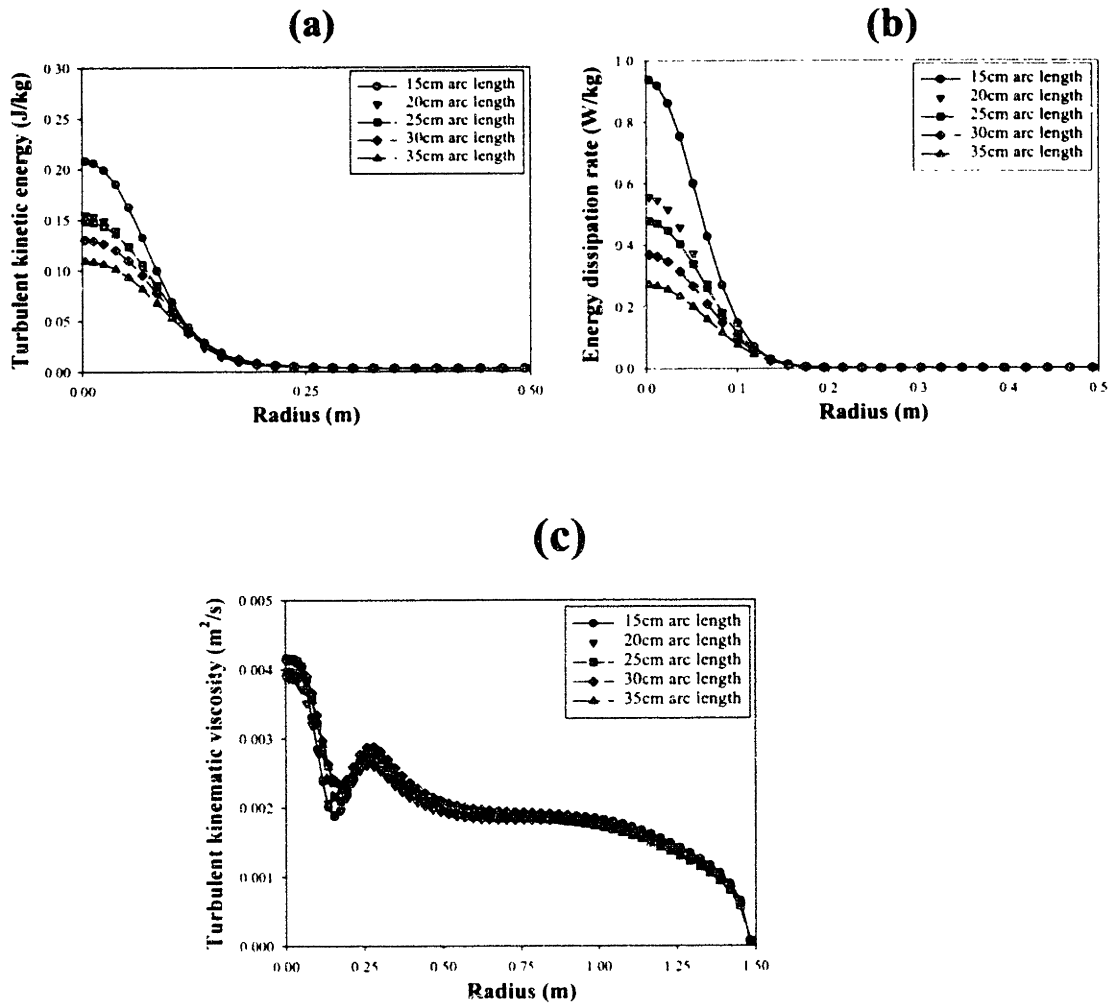


Figure 3.4.12 Radial profiles of the turbulent characteristics in the bath region at 0.25 m from top surface for different arc lengths of 15, 20, 25, 30, and 35 cm and 40 KA of arc current. (a) Turbulent kinetic energy. (b) Energy dissipation rate. (c) Turbulent kinematic viscosity.

Figure 3.4.13 shows the average temperature in the bath region as a function of arc length. The average temperature can be defined by the following equation:

$$T_{average} = \frac{\sum T_{cell} V_{cell}}{V_{total}} \quad (\text{eq. 3.4.1})$$

where  $T_{average}$  is the average temperature,  $V_{cell}$  and  $V_{total}$  are the cell volume and total volume respectively, and  $T_{cell}$  is the cell temperature. The average temperature can be related to the amount of energy being held in the bath region. Then, as indicated by Figure 3.4.13 an increase in the arc length, for a constant arc current, increases the arc power and also the total amount of energy transferred into the melt and hence more energy is present in the bath region (for a constant volume furnace occupied by steel).

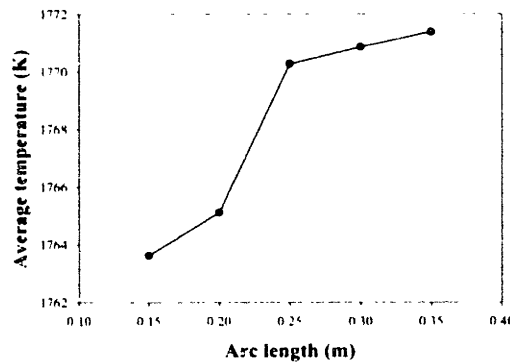


Figure 3.4.13 Average Temperature in the bath region as a function of arc length. The average temperature represents the enthalpy of the melt in the bath region.

Figures 3.4.14 (a)-(e) present mixing time maps for all cases tested in the arc length sensitivity study (Arc current of 40 KA and arc lengths of 15, 20, 25, 30, and 35 cm). The mixing times were obtained by injecting a fixed amount of tracer into a specific cell in the computational domain and then the time required to homogenize the whole domain is taken as the mixing time for the location where the tracer was injected. Homogenization was considered when all cells in the domain are within +/- 5% of the equilibrium concentration. The five maps show similar contours of mixing time, presenting the lowest mixing time just at the center of the circulation loop (see Figure 3.4.4 (b)). These contour lines follow the same pattern as the streamlines. The mixing time behavior results from the combined effect of two factors: fluid flow patterns (also magnitude of velocities) and turbulence structure. Since turbulent viscosity was found to be relatively insensitive to the arc length, the velocity field is the decisive factor when trying to explain the differences observed between the maps for different arc lengths. As arc length increases, mixing times increase due to the lower overall velocities obtained. An arc length of 15 cm presents minimum and maximum mixing times of 35 and 60 seconds respectively, while for an arc length of 35 cm a minimum mixing time of 40 and maximum of 75 seconds are obtained. Therefore, keeping the same arc current, an increase in arc power (increase in arc length) will result in an overall increase of the mixing times for worst mixed melts.

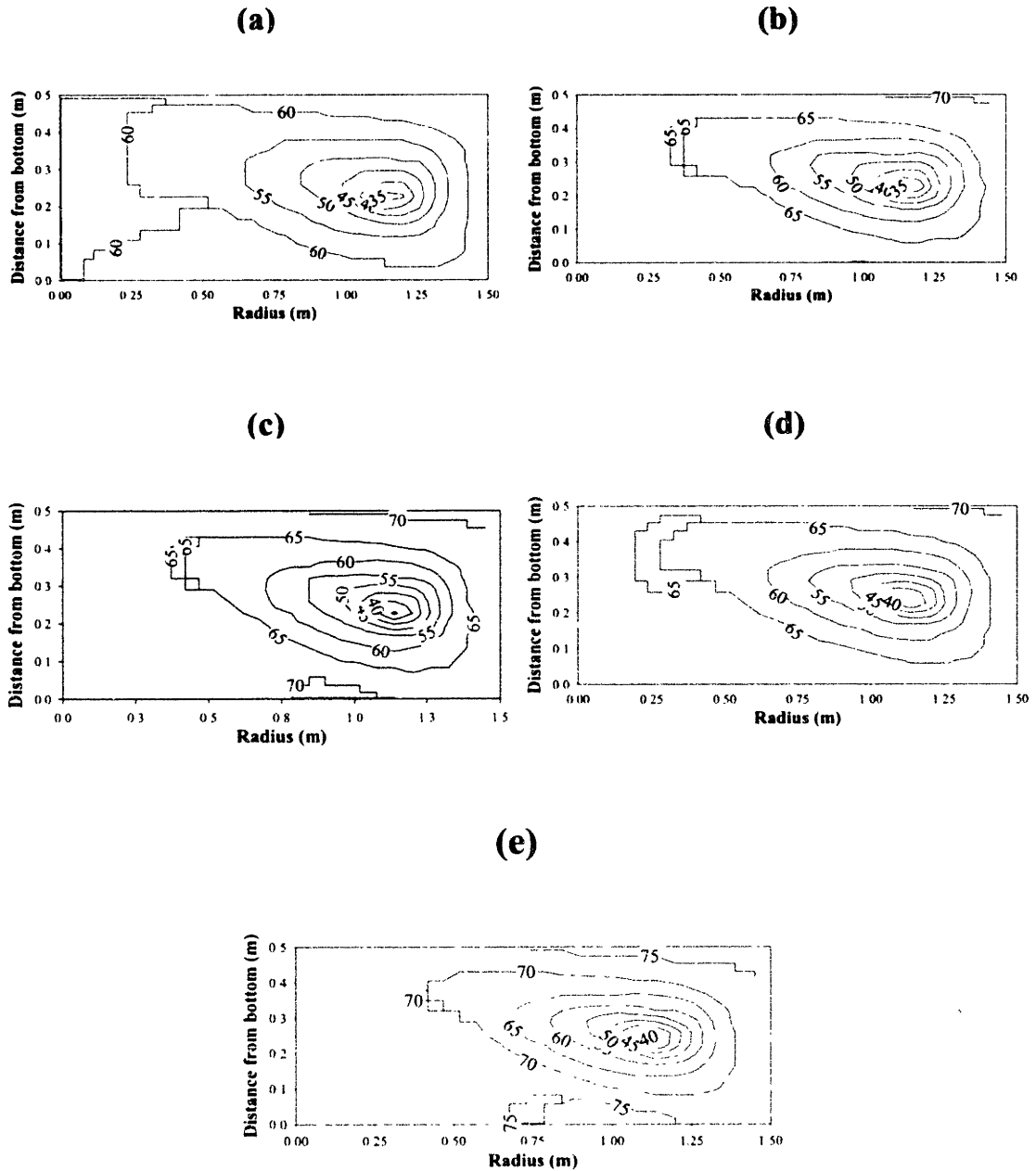


Figure 3.4.14 Mixing time maps for the bath regions under electric arcs current of 40 KA and arc lengths of (a) 15 cm, (b) 20 cm, (c) 25 cm, (d) 30 cm, and (e) 35 cm. Mixing times are expressed in seconds and 95% of uniformity is the criteria to define mixing.

An interesting finding is that maximum mixing times are found in the zones presenting maximum velocities. A solute addition injected in the top surface will take almost twice as much time for complete



mixing than if the same solute is injected in the center of the circulation loop. Figure 3.4.15 presents the concentration history at six different positions (schematically presented in the figure) when the tracer is injected at the center of the top free surface (a) and when the tracer is injected in the center of the circulation loop (b). Different behaviors are observed between the two plots. In the first case (injection at the top surface), a cyclic behavior is observed in the concentration history and almost three loops are needed to reach uniform concentration, but after each loop is completed, the amplitude is lower due to the lateral eddy diffusion that homogenizes the melt. The circulation time, defined as the time between two maxima, is of the order of 25 seconds for case (a) and mixing times of the order of 60 seconds are obtained in all monitored locations in this case. In contrast, in case (b) (injection of the tracer at the center of the loop) the concentration histories do not show the cyclic behavior (especially those locations outside the center of the loop) and instead, the concentration increases steadily until the equilibrium composition is reached. This behavior indicates that turbulence dominates in this case. Mixing times of the order of 30 seconds (half than in case (a)) are obtained in all locations monitored for case (b).

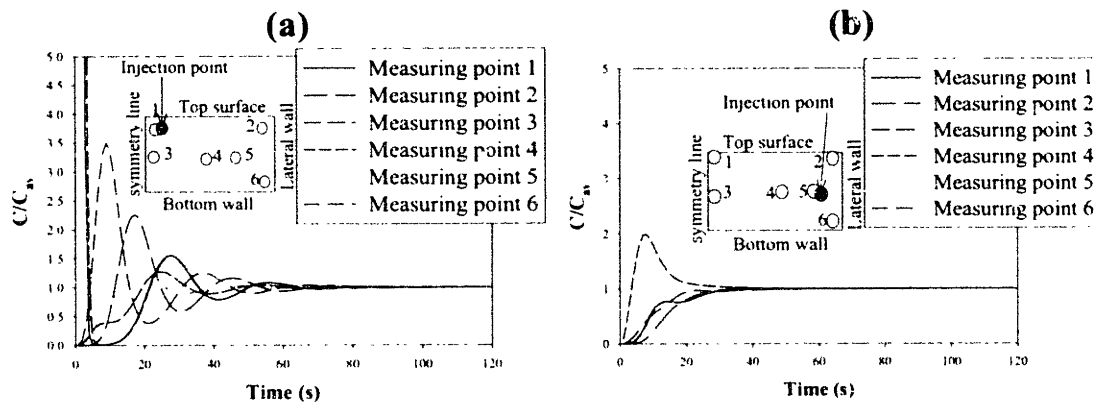


Figure 3.4.15 Concentration history at six different positions in the bath domain when injection is place in: (a) top free surface at the symmetry axis and (b) in the center of the circulation loop. The melt is influenced by an arc of 40 KA arc current and 25 cm arc length. The plots show a schematic representation of the injection and measuring positions.

Figure 3.4.16 shows the heat balance in the bath region for all cases considered. Five contributions are considered in this energy balance: (a) the heat transferred from the arc (ARC), (b) the radiation losses at the top surface (RADIATION), (c) the Joule heat (Joule), and (e) Heat flow from lateral and bottom walls (LATWALL and BOTWALL). Each contribution is quantitatively described through the bars, and the five bars plotted together at each contribution represent every arc length case. Joule heat can be considered to be insignificant. Radiation is not too sensitive to arc length variations. Obviously, heat from the arc increases as arc length increases since the arc power also increases. But the interesting part in Figure 3.4.16 is related to the heat flow through the walls. As arc length increases, heat flow through the bottom wall changes sign (from a positive value for arc lengths of 15 and 20 cm to negative values for the rest of

arc lengths) while positive heat flowing through the lateral wall decreases. It has to be remembered that the boundary conditions at the walls are fixed temperatures of 1773 K. Thus, as arc power is incremented (or arc length increases), more heat is extracted through the walls, since the steel is hotter. This is important, because it means that an increase in arc power may result in a damage to the refractory at the bottom wall, which is the surface that feels the most the aggressive effect of the arc.

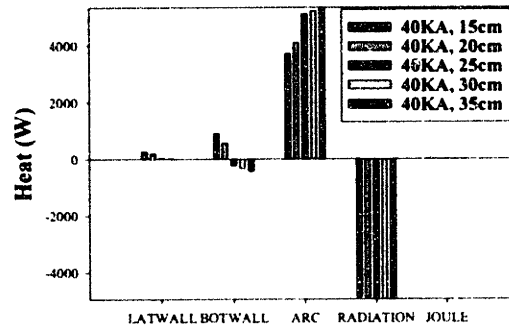


Figure 3.4.16 Comparison of the heat balances in the bath region for the different arc lengths tested (15, 20, 25, 30 and 35 cm) keeping the same arc current of 40 K.A. In the plot five elements contribute to the heat balance: (a) Heat from lateral wall, (b) Heat from bottom wall, (c) Heat from the arc, (d) Radiation losses and (e) Joule heat.

### Arc current sensitivity

The effect of arc current on arc characteristics is investigated by performing a sensitivity study of the bath region under electric arcs with a single arc length of 25 cm and four different arc currents of 36, 40, 44 and 50 KA.

Figures 3.4.17 (a) and (b) present the effect of the arc current on temperature and axial velocity at the symmetry axis respectively. The radial temperature profile at 0.25 m from the top surface and the radial velocity distribution at the bottom surface are presented in Figure 3.4.18 (a) and (b) respectively, where it can be seen that an increment in arc current produces higher temperatures and velocities.

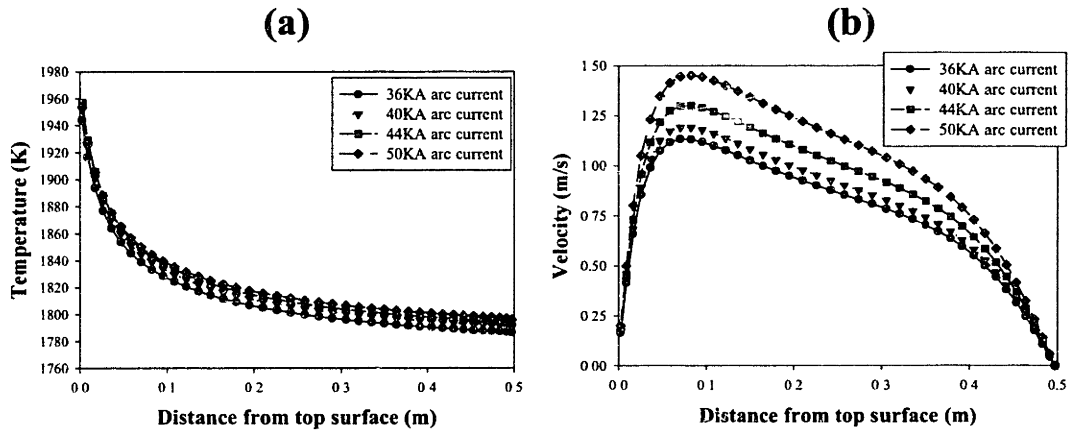


Figure 3.4.17 Effect of the arc current on several bath properties along the symmetry axis under the influence of electric arcs of 25 cm arc length and 36, 40, 44 and 50 KA arc currents. (a) Temperature. (b) Axial velocity.

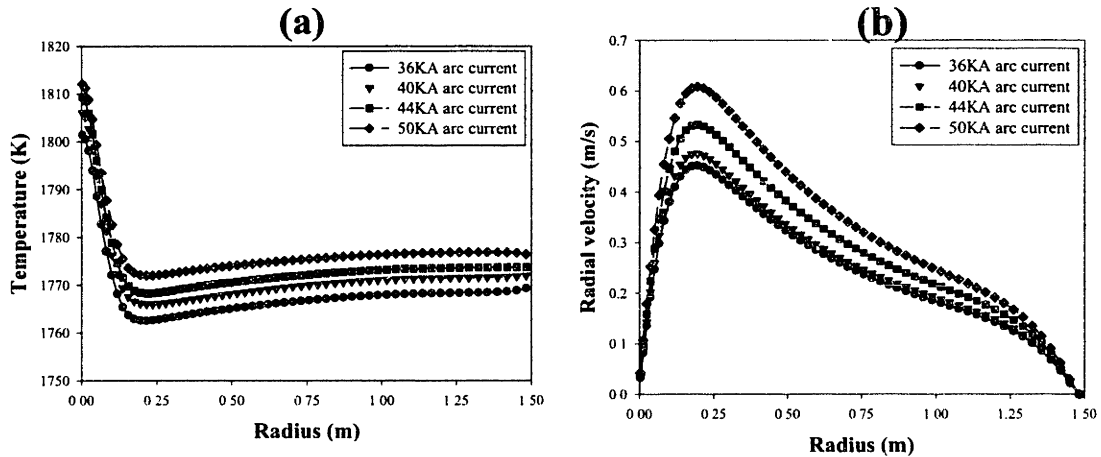


Figure 3.4.18 Effect of the arc current on several bath properties along the radius axis under the influence of electric arcs of 25 cm arc length and 36, 40, 44 and 50 KA arc currents. (a) Temperature radial profile at 0.25 m from top surface. (b) Radial velocity profile along the radius at the bottom surface.

Figures 3.4.19 (a) and (b) present the turbulent kinetic energy and energy dissipation rate plotted along the radius at 0.25 m from the top surface for all arc currents tested. Again, both turbulence parameters increase as arc current increases. Figure 3.4.19 (c) presents the radial profile of turbulent kinematic viscosity at 0.25 m from the top surface. Now, a different behavior than that shown in the arc length sensitivity is observed, i.e. the turbulent kinematic viscosity is very sensitive to arc current variations as can be appreciated in the figure, where the turbulent kinematic viscosity increases as arc current increases.

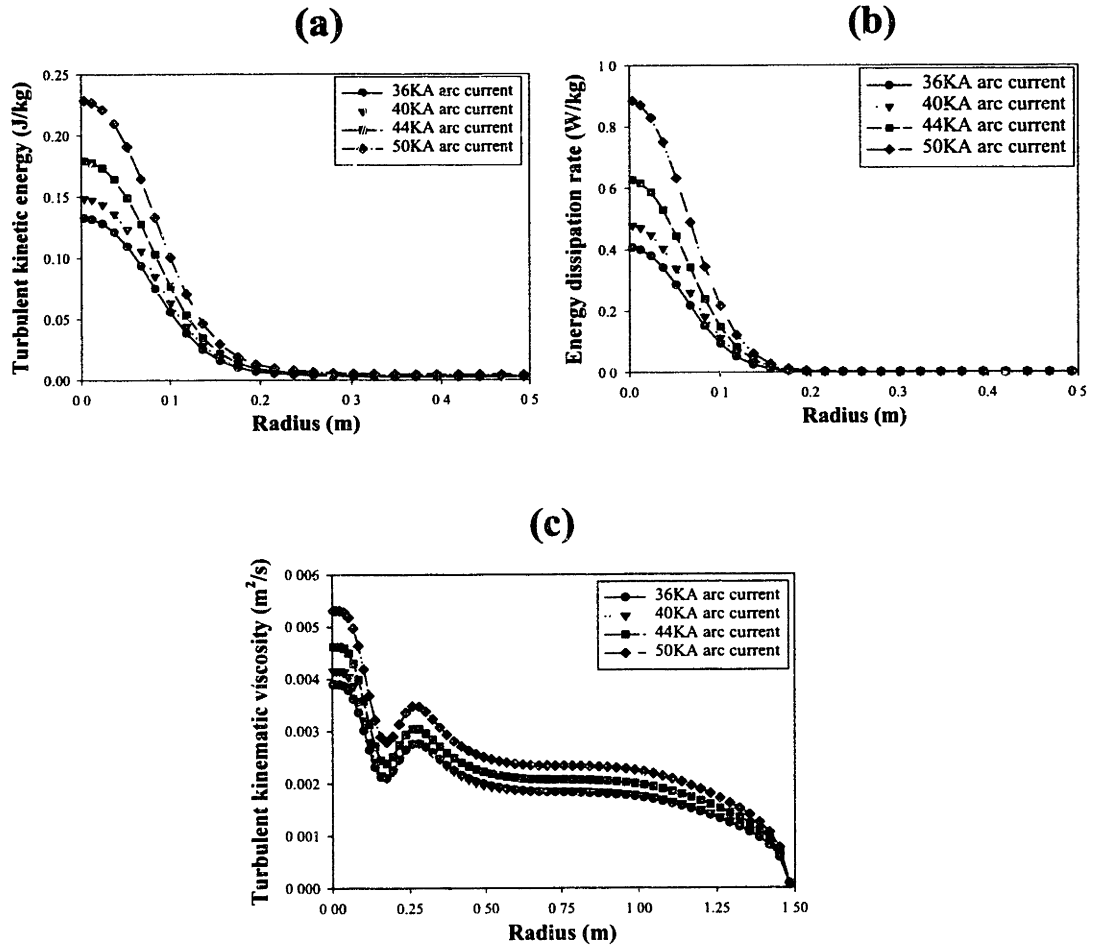


Figure 3.4.19 Radial profiles of the turbulent characteristics in the bath at 0.25 m from top surface for different arc currents of 36, 40, 44, and 50 KA, and 25 cm arc length. (a) Turbulent kinetic energy. (b) Energy dissipation rate. (c) Turbulent kinematic viscosity.

Figure 3.4.20 (a) shows the average temperature in the bath region as a function of the arc current. The figure indicates that an increment in arc current (keeping the same arc length) increases the average bath temperature or enthalpy (which is consistent with the fact that more heat is transferred to the bath from the arc by increasing the arc current). Figure 3.4.20 (b) shows the maximum velocity as a function of arc current. As arc current increases maximum velocities also increase. This is a very logical consequence, since more current (at the same arc length) is equivalent to higher electromagnetic body forces and hence greater velocities.

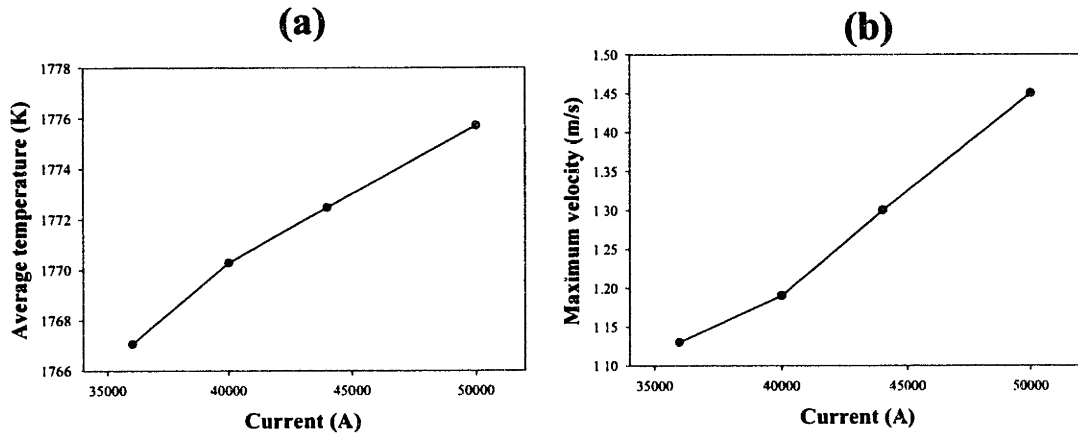


Figure 3.4.20 (a) Average temperature in the bath region as a function of arc current. (b) Maximum velocity in the bath region as a function of the arc current.

Figures 3.4.21 (a)-(d) present mixing time maps for all cases tested in this arc current sensitivity study (Arc length of 25 cm and arc currents of 36, 40, 44 and 50 KA). Again, the contour lines follow the shape of the streamlines and minimum mixing times are located at the center of the loop, while maximum mixing times are found at the top free surface. Then, since both, turbulent viscosity and velocities increase with arc current, mixing times decrease. An arc current of 36 KA presents minimum and maximum mixing times of 35 and 70 seconds respectively, which are lower than the minimum of 30 and maximum of 50 seconds obtained for an arc current of 50 KA.

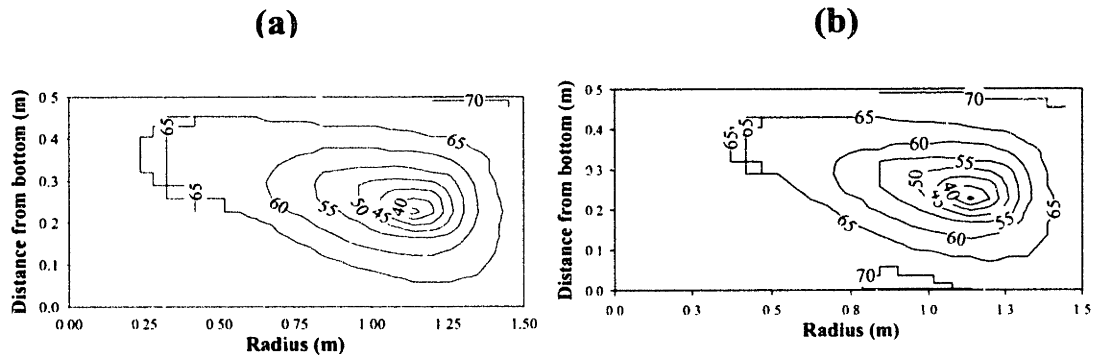


Figure 3.4.21 Mixing time maps for the bath regions under electric arcs with arc lengths of 25 cm and arc currents of (a) 36 KA. (b) 40 KA. Mixing times are expressed in seconds and 95% of uniformity is the criteria to define mixing.

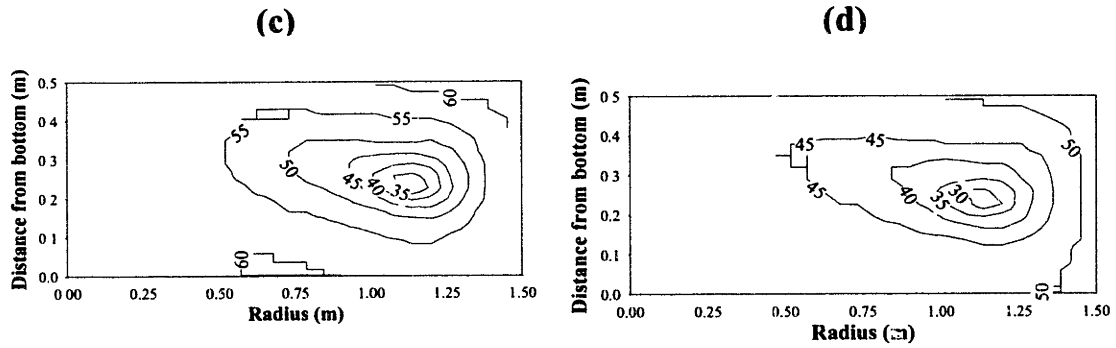


Figure 3.4.21 (cont.) Mixing time maps for the bath regions under electric arcs with arc lengths of 25 cm and arc currents of (c) 44 KA, and (d) 50 KA. Mixing times are expressed in seconds and 95% of uniformity is the criteria to define mixing.

Figure 3.4.22 shows the heat balance in the bath region for the cases considered in this arc current sensitivity study. Radiation is almost insensitive to arc current variations. Heat from the arc increases as arc current rises since the arc power also increases. As arc current increases, heat flowing through the bottom and lateral walls changes sign (from positive for small arc currents to negative for large arc currents). Thus, as arc power is incremented (or arc current increases), more heat is extracted through the walls, since the steel is hotter. Particularly for a 50 KA arc the heat flowing out from the bottom wall is significant and in this case damage to the refractory at the bottom wall could be an issue in the DC-EAF operation.

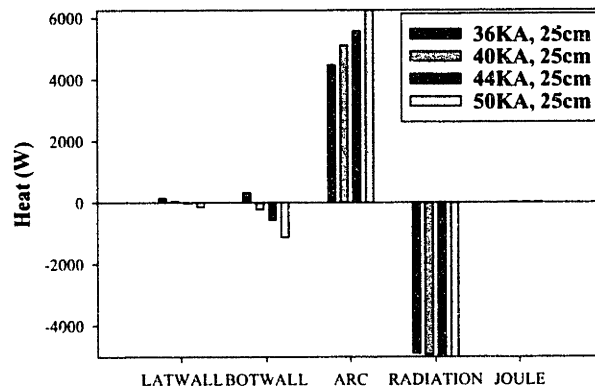


Figure 3.4.22 Comparison of the heat balances in the bath region for the different arc currents tested (36, 40, 44, and 50 KA) keeping the same arc length of 25 cm. In the plot five elements contribute to the heat balance: (a) Heat from lateral wall, (b) Heat from bottom wall, (c) Heat from the arc, (d) Radiation losses and (e) Joule heat.

### Section 3.4.1.5: Effect of the Wall Function: Equilibrium versus Non-Equilibrium Wall Function

In this section the effect of the diverse options available for the representation of the wall functions is analyzed in terms of the heat transferred from the melt to the walls. Two options are available for the implementation of wall functions: equilibrium and non-equilibrium [89]. In both approaches, the heat flux at the wall is computed as:

$$q_{wall} = \rho \cdot St \cdot abs(U_r) \cdot (T_w - T) \quad (\text{eq. 3.4.2})$$

where  $q_{wall}$  is the heat flux at the wall,  $U_r$  is the absolute value of the velocity parallel to the wall,  $T$  is the temperature in the cell next to the wall,  $T_w$  is the wall temperature (1773 K), and  $St$  is the Stanton number. The difference between the two approaches comes from the Stanton number computation. For the equilibrium wall function, the Stanton number is expressed according to:

$$St = \max(St_{turb}, St_{lam})$$

$$St_{lam} = \frac{1}{Pr_t Re} \quad (\text{eq. 3.4.3a})$$

$$St_{turb} = \frac{s_{turb}}{\left( Pr_t \left( 1 + Pm \sqrt{s_{turb}} \right) \right)}$$

where  $St_{lam}$  and  $St_{turb}$  are laminar and turbulent Stanton numbers.  $Pr_t$  is the turbulent Prandtl number,  $Re$  is the Reynolds number,  $Pm$  is the smooth-wall sub-layer-resistance function of Jayatilke [108], and  $s_{turb}$  is the turbulent friction factor [89]. In contrast, the non-equilibrium wall function computes the turbulent Stanton number as:

$$St_{turb} = \frac{s_{turb}}{\left( Pr_t \left( 1 + \frac{Pm \cdot s_{turb} \cdot U_r}{0.5477 \sqrt{k}} \right) \right)} \quad (\text{eq. 3.4.3b})$$

In order to see the effect of the wall function on some bath properties Figure 3.4.23 (a) presents axial profiles of temperature, axial velocity and potential along the symmetry axis. No difference is observed between the two approaches in this region of the reactor. Figure 3.4.23 (b) shows the radial profiles of velocity and temperature along the radius at the bottom surface. In these profiles, the variation in wall function approach produces some differences in the temperature close to the center of the furnace. The non-equilibrium wall function extracts more heat through the bottom wall than the equilibrium wall

function and, therefore, lower temperatures are predicted. Radial velocity is not greatly affected by the wall function approach. However, slightly bigger velocities at the bottom wall are predicted with the non-equilibrium wall function. Figure 3.4.24 shows the heat balance in the bath region using the bar plots, where effectively, the non-equilibrium wall function extracts a little more heat through the bottom wall than the equilibrium wall function.

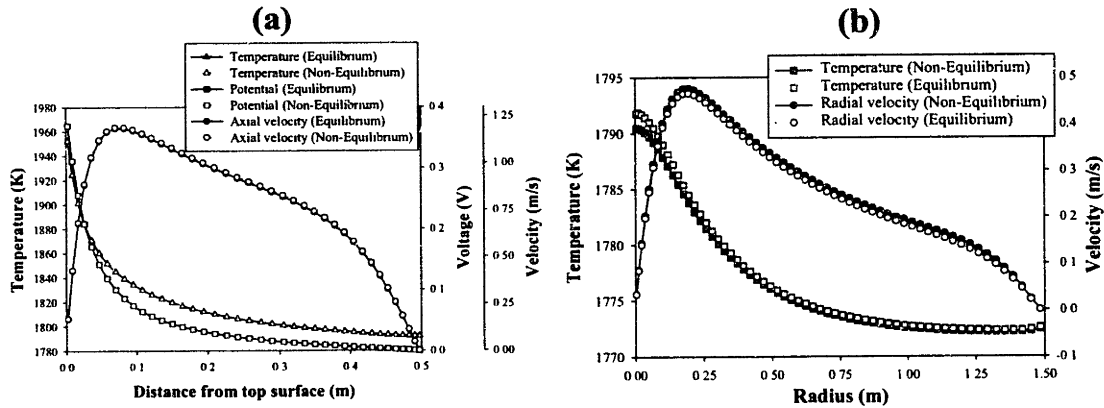


Figure 3.4.23 Effect of the wall function approach on the bath properties. (a) Axial profiles along the symmetry axis for potential, temperature, and axial velocity. (b) Temperature and radial velocity profiles along the radius at the bottom surface.

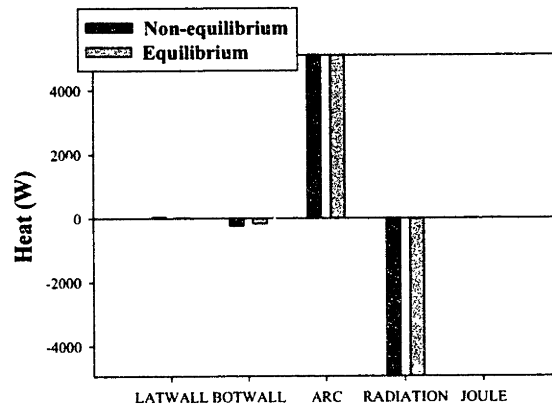


Figure 3.4.24 Comparison of the heat balances in the bath region for the different wall function approaches tested (equilibrium and non-equilibrium) keeping the same arc length of 25 cm and arc current of 40 kA. In the plot five elements contribute to the heat balance: (a) Heat from lateral wall, (b) Heat from bottom wall, (c) Heat from the arc, (d) Radiation losses and (e) Joule heat.

### Section 3.4.1.6: Effect of the Turbulence Models

In the mathematical formulation turbulence was accounted for by the prescription of the standard k-ε model. Unfortunately, there is no physical evidence showing that the standard k-ε model provides the



best representation for the turbulence structure in the bath region. Thus, the evaluation of several options available for the representation of turbulence is presented in this section. These options are the RNG and the two-scale k- $\epsilon$  model (section 2.3.3.2).

Figures 3.4.25 (a) and (b) show the axial velocity and temperature profiles along the symmetry axis respectively, for the standard k- $\epsilon$ , RNG and two-scale k- $\epsilon$  turbulence models. RNG and the two-scale k- $\epsilon$  models predict much higher overall velocities (almost twice) and temperatures along the symmetry axis than the standard k- $\epsilon$  model. Those obtained with the RNG model being the highest. Figures 3.4.26 (a) and (b) shows temperature and radial velocity profiles along the radius at the bottom surface. Again, much higher temperature and velocity profiles are obtained with the RNG and the two-scale k- $\epsilon$  model than with the standard k- $\epsilon$  model. Turbulent parameters are presented in Figure 3.4.27 (a) - (c), where radial profiles at 0.25 m from top surface of the turbulent kinetic energy, energy dissipation rate and turbulent kinematic viscosity are plotted for the three turbulence models considered. The standard k- $\epsilon$  model predicts much higher turbulent parameters than the other two models. It is interesting to appreciate that turbulent viscosity is much higher at the symmetry axis for the k- $\epsilon$  model. The higher velocities and temperatures predicted with the RNG and two-scale k- $\epsilon$  models at the axis, can be explained in terms of the lower turbulent viscosity computed from these models than with the standard k- $\epsilon$ , where velocities and the temperatures spread more as a consequence of the large eddy diffusivity.

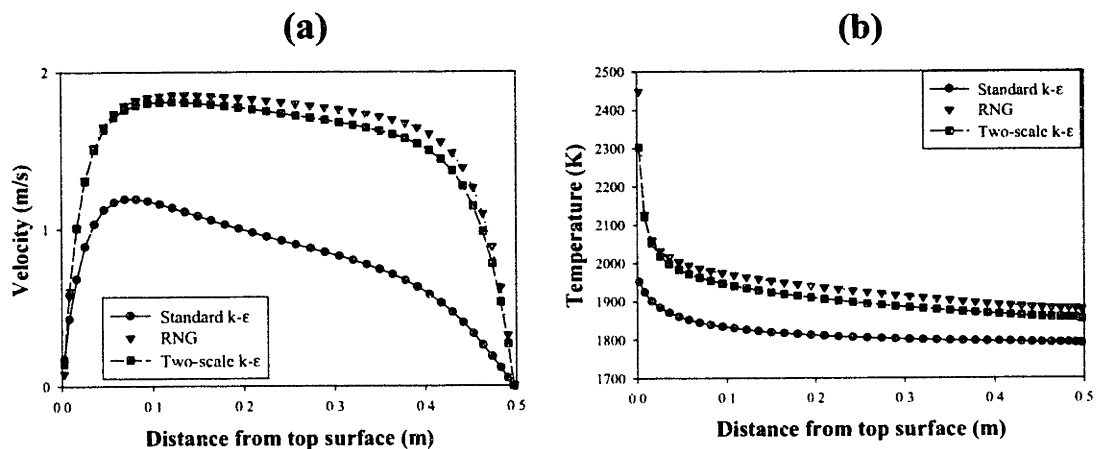


Figure 3.4.25 Effect of the turbulence model approach on the bath properties along the symmetry axis. (a) Axial velocity. (b) Temperature. Three different turbulence models are compared (standard k- $\epsilon$ , RNG, and the two-scale k- $\epsilon$  turbulence models).

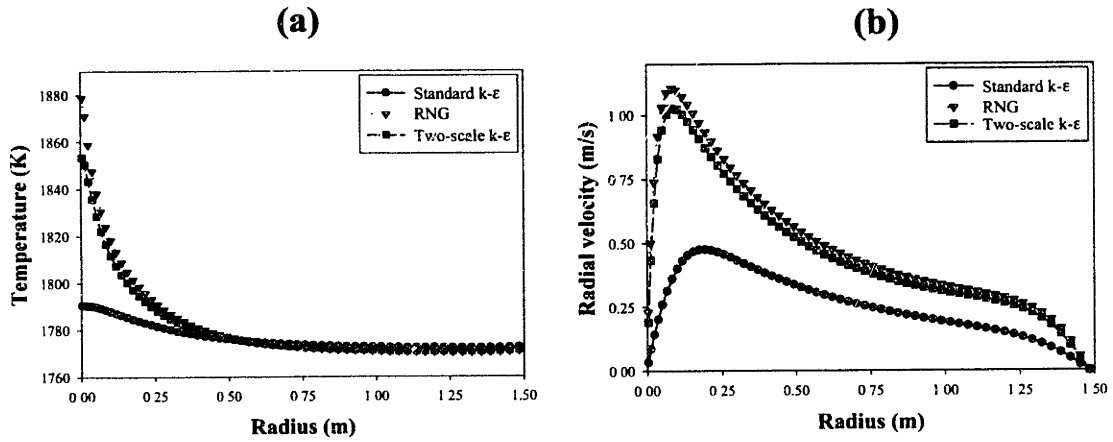


Figure 3.4.26 Effect of the turbulence model approach on the bath properties along the radius from the top surface. (a) Radial velocity. (b) Temperature. Three different turbulence models are compared (standard k-ε, RNG, and the two-scale k-ε turbulence models).

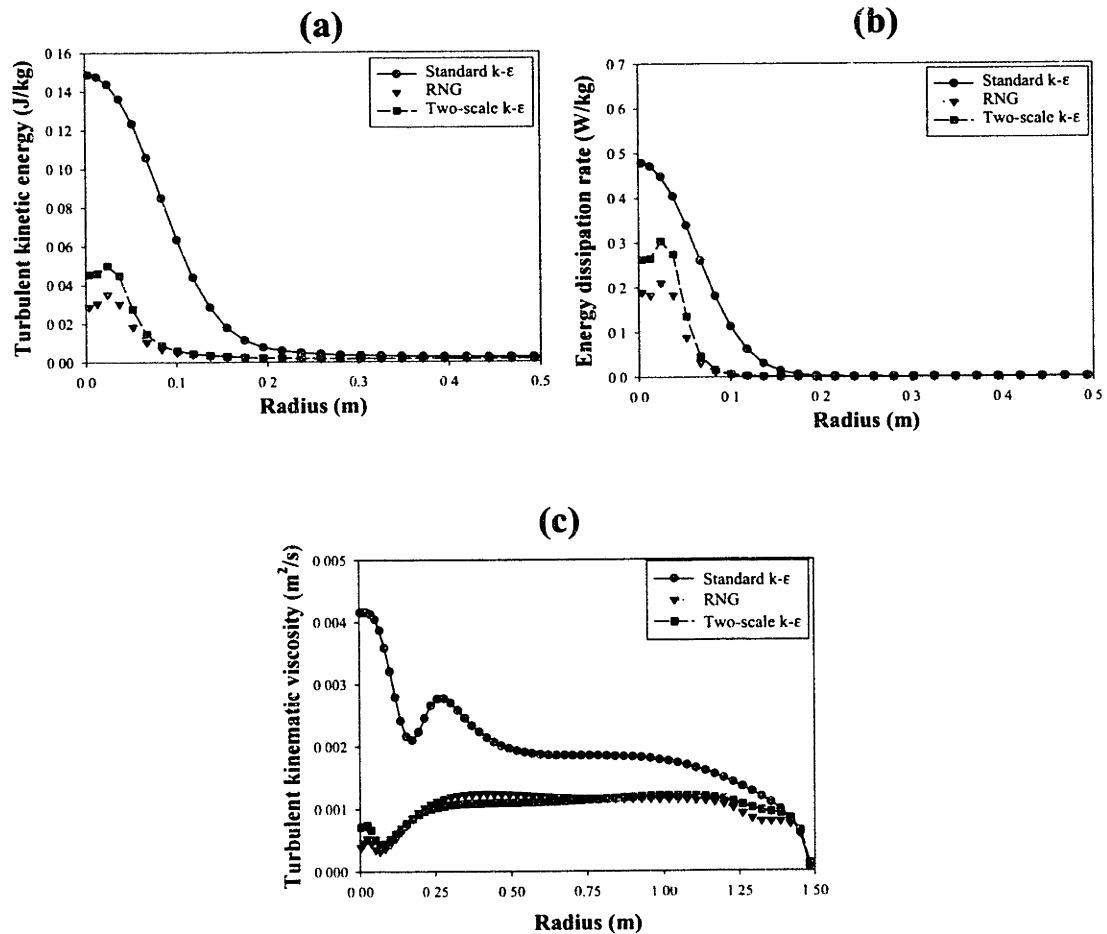


Figure 3.4.27 Effect of the turbulence model approach on the bath turbulent properties along the radius at 0.25 m from top surface. (a) Turbulent kinetic energy. (b) Energy dissipation rate. (c) Turbulent kinematic viscosity.

Figure 3.4.28 presents mixing times maps for the three turbulence models tested. The RNG and the two-scale k- $\epsilon$  model predict very uniform mixing times of 42 to 45 seconds in comparison to the wider range of 35 to 70 seconds predicted with the standard k- $\epsilon$  model. Then, despite the fact that both RNG and two-scale k- $\epsilon$  models predict lower turbulent viscosity field, they present low mixing times due to the high velocities obtained with these models.

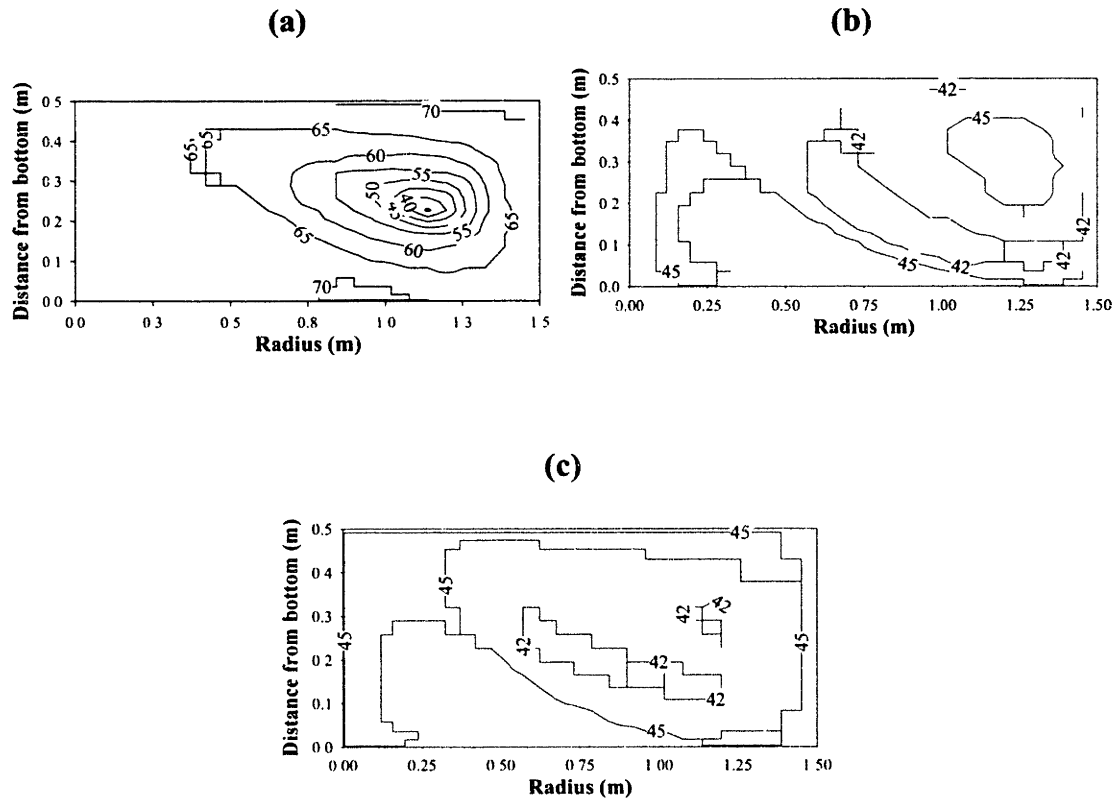


Figure 3.4.28 Mixing time maps for the bath regions under electric arcs current of 40 KA and arc lengths of 25 cm for the three different turbulence models. (a) Standard k- $\epsilon$ . (b) RNG. (c) Two-scale k- $\epsilon$ . Mixing times are expressed in seconds and 95% of uniformity is the criteria to define mixing.

Finally, Figure 3.4.29 presents bar plots showing comparative heat balances between the different turbulence model predictions. The heat coming from the arc, as well as the radiation at the top surface, and the Joule heat are all insensitive to the formulation of the turbulence model. However, higher velocities and temperatures obtained from the RNG and the tow-scale turbulence model result in higher heat flows through the bottom wall surfaces than with the standard k- $\epsilon$  model.

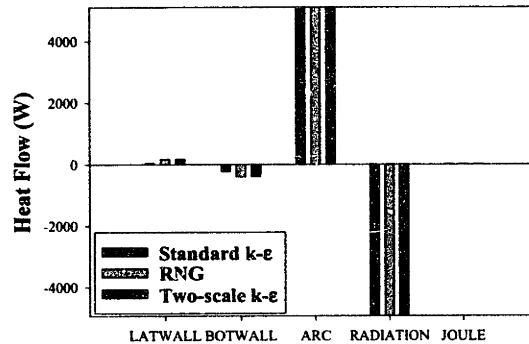


Figure 3.4.29 Comparison of the heat balances in the bath region for the different turbulence models tested (standard k-ε, RNG, and the two-scale k-ε) keeping the same arc length of 25 cm and arc current of 40 KA. In the plot five elements contribute to the heat balance: (a) Heat from lateral wall, (b) Heat from bottom wall, (c) Heat from the arc, (d) Radiation losses and (e) Joule heat.

### Section 3.4.1.7: Effect of the Size of the Reactor on the Fluid Dynamics and Temperature Field

The size of the furnace is a design variable that may be varied to meet the required productivity in the steelmaking factory. The results presented in this section are devoted to providing the effect of the furnace radius  $R_{furnace}$  and bath depth  $H$  on the bath characteristics such as velocities, temperatures and mixing times.

#### Bath depth sensitivity

The effect of the bath depth was analyzed by including computations using bath depths of 0.35, 0.5 and 0.7 m, but keeping the same furnace radius of 1.5 m. Results for the furnace bath depth of 0.5 m were presented in Figures 3.4.4 and 3.4.5. Figure 3.4.30 shows the velocity (a), temperature (b) and streamline (c) fields for the furnace with a liquid depth of 0.35 m. Figure 3.4.31 shows corresponding results for a bath depth of 0.7 m. Decreasing the aspect ratio  $H/R_{furnace}$  produces a double circulatory loop in the liquid steel bath. The consequence of this complex fluid flow pattern for the smaller bath depth of 0.35 m is an increase in mixing times as shown in the Figure 3.4.32, where mixing time maps for furnaces with 0.35 and 0.7 m of bath depths are compared. It can be deduced from this figure that the best mixing behavior is promoted by the highest furnace aspect ratio  $H/R_{furnace}$  (mixing times between 50 - 65 seconds for 0.7 m of bath depth, 40 - 70 seconds for the standard depth of 0.5 m and 60-140 seconds for 0.35 m of bath depth). The fact that mixing improves by increasing the bath depth is important, since it means that increasing the volume of the furnace (enhancing productivity) improves the mixing phenomena. Figure

3.4.33 shows the average temperature (or enthalpy) as a function of the bath volume produced by the increase in bath depth. It can be noted that the energy inside the bath increases as the volume of the melt increases for a constant arc current and arc length (constant arc power). This finding further indicates that the melt is not only better homogenized but also retains more heat from the arc as the bath depth increases. In the comparative heat balance shown in Figure 3.4.34, it is seen that heat from the arc, the Joule heat, and radiation losses are insensitive to bath depth variations. But it is the bottom wall heat flow that changes the most with the bath depth variations. As the bath depth increases less heat is extracted from the bottom, therefore, more heat is retained in the bath, which explains the behavior shown in Figure 3.4.33. The explanation of the last statement is that since the top surface is farther away from the bottom as the depth increases, the liquid steel coming from the hot spot reaches the bottom at a lower temperature than when the bath is shallow. The effect of the arc attachment zone on the bottom wall is increased as the bath depth decreases.

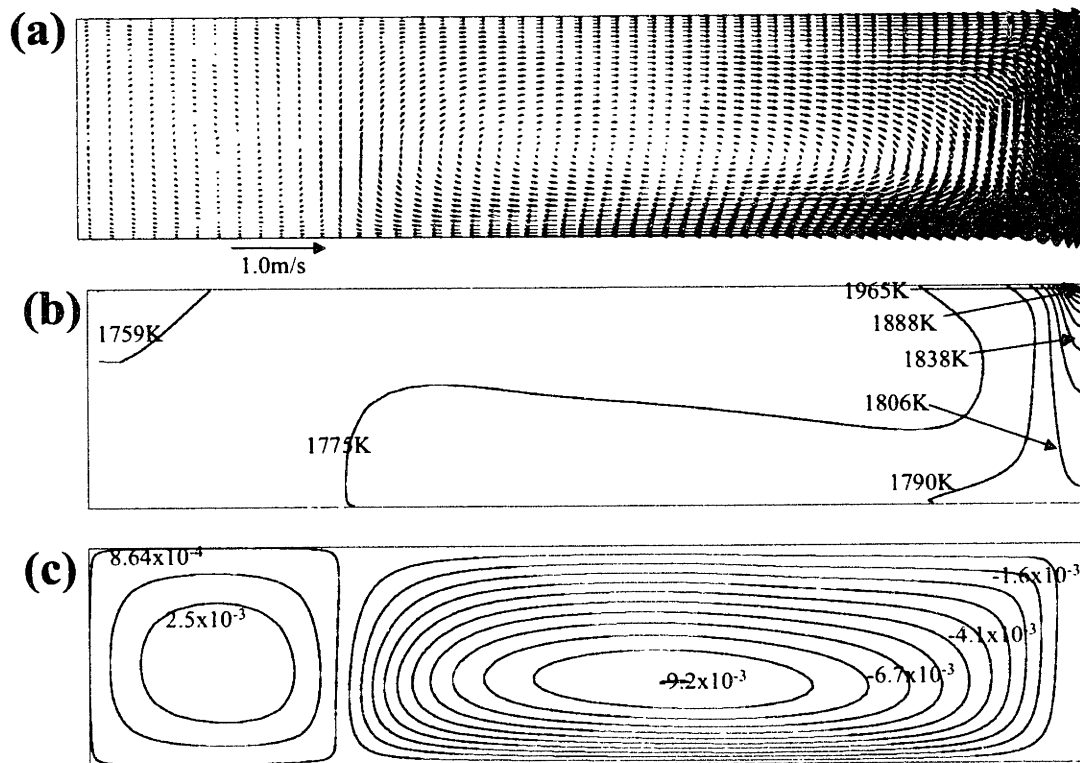


Figure 3.4.30 (a) Velocity, (b) temperature and (c) streamlines field in the bath region for a furnace radius of 1.5 m and a bath depth of 0.35 m, keeping the same arc length of 25 cm and arc current of 40 kA.

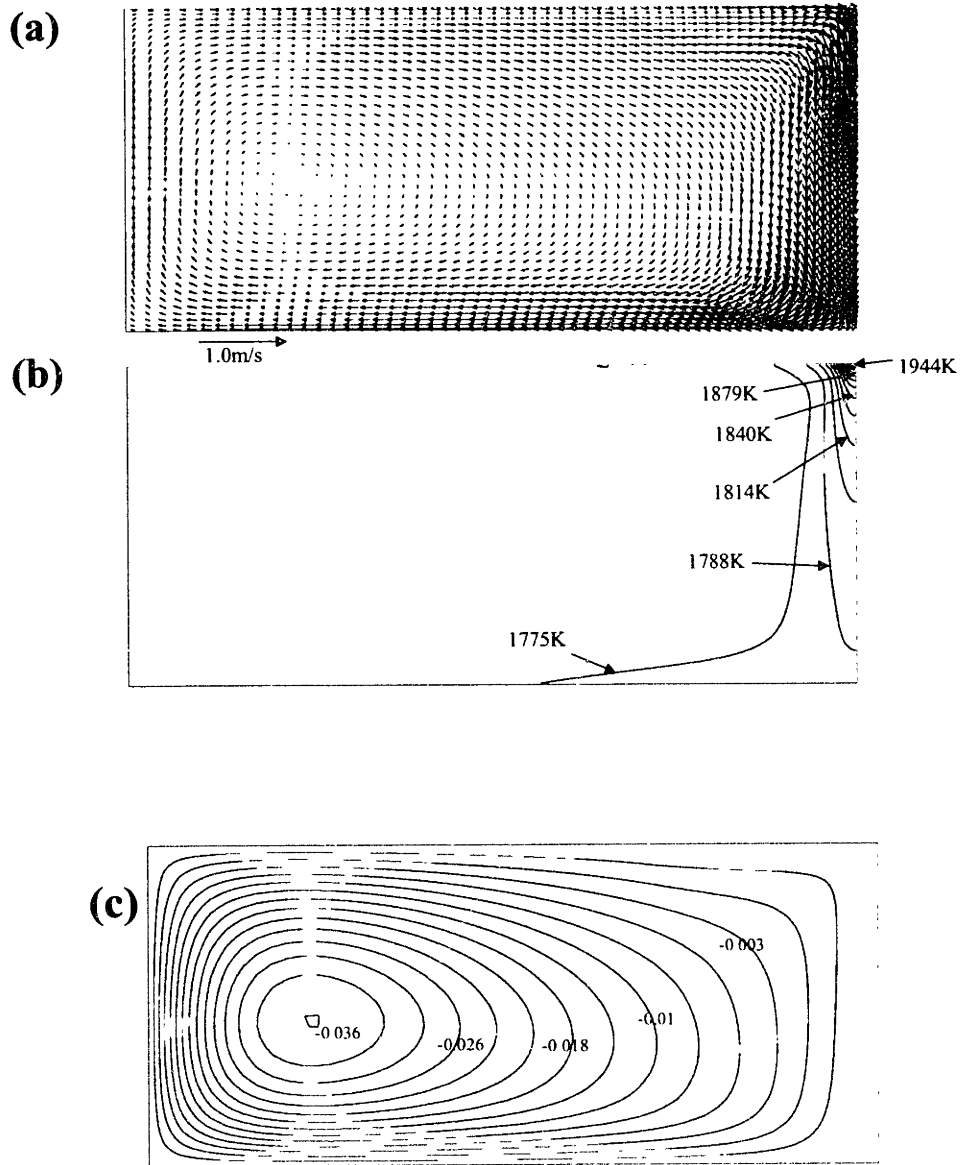


Figure 3.4.31 (a) Velocity, (b) temperature and (c) streamlines field in the bath region for a furnace radius of 1.5 m and a bath depth of 0.7 m, keeping the same arc length of 25 cm and arc current of 40 KA.

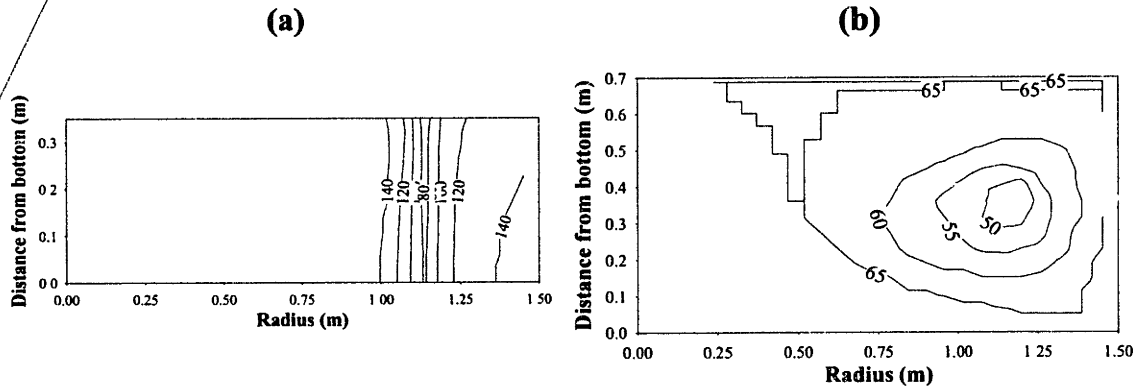


Figure 3.4.32 Mixing time maps for the bath regions under electric arc currents of 40 KA and arc lengths of 25 cm for the different steel bath depths. (a)  $H=0.35$  m. (b)  $H=0.7$  m. Mixing times are expressed in seconds and 95% of uniformity is the criteria to define mixing.

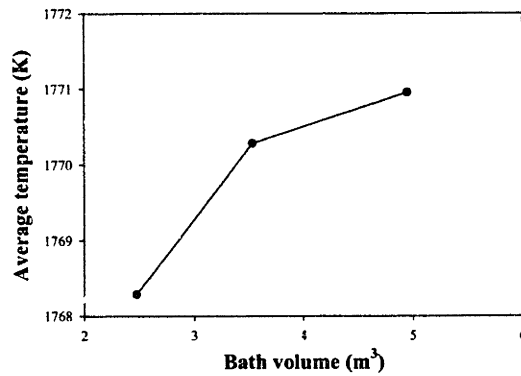


Figure 3.4.33 Average temperature as a function of the bath volume keeping the arc length and current in their standard values of 40 KA and 25 cm respectively. Bath volume increments are due bath depth variations.

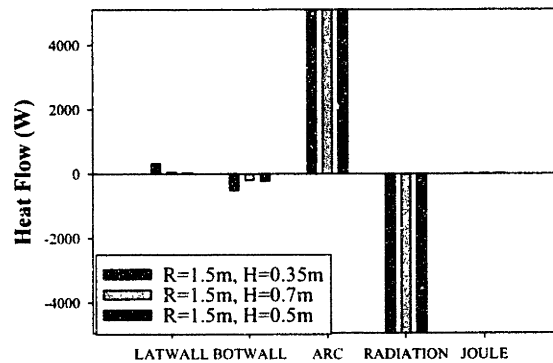


Figure 3.4.34 Comparison of the heat balances in the bath region for the different bath depths tested ( $H=0.35$  m,  $H=0.5$  m,  $H=0.7$  m) keeping the same arc length of 25 cm and arc current of 40 KA.

## Furnace Radius Sensitivity

The effect of the furnace radius was analyzed by performing computations on the bath region employing furnace radii of 1.5, 2.0 and 2.5 m and keeping the same bath depth of 0.5 m. Results for the furnace radius of 1.5 m were presented in Figures 3.4.4 and 3.4.5. Figures 3.4.35 and 3.4.36 show the velocity (a), temperature (b), and streamline (c) fields for furnaces with radii of 2.0 and 2.5 m respectively. A single loop is maintained in these two cases, but it is noted that the maximum temperature drop significantly from 1952 K for 1.5 m radius to 1902 K for 2.5 m radius. In this case, the aspect ratio  $H/R_{furnace}$  decreases as the furnace radius increases. Figures 3.4.37 (a) and (b) show the mixing time maps for furnace radii of 2.0 and 2.5 m respectively. Mixing time maps for the 1.5 m furnace radius were presented in Figure 3.4.14 (c). Overall mixing times increase as the furnace radius increases (40 – 70 seconds for  $R_{furnace}=1.5$  m, 60-110 seconds for  $R_{furnace}=2.0$  m and 80 – 120 seconds for  $R_{furnace}=2.5$  m), indicating that an increase in the furnace radius produces more poorly mixed melts.

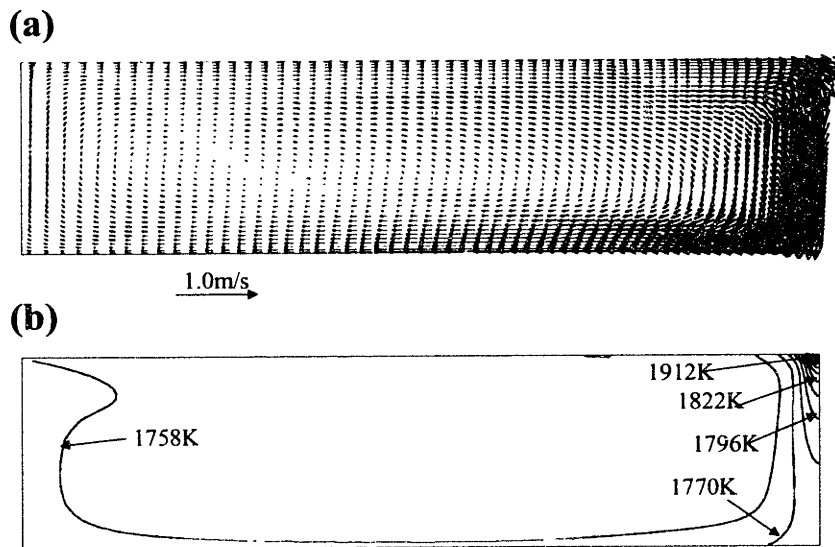


Figure 3.4.35 (a) Velocity, and (b) temperature fields in the bath region for a furnace radius of 2.0 m and bath depth of 0.5 m, keeping the same arc length of 25 cm and arc current of 40 KA.



(c)

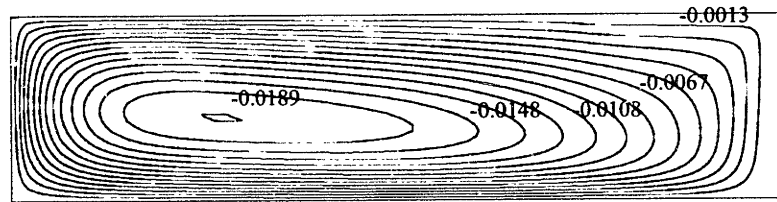
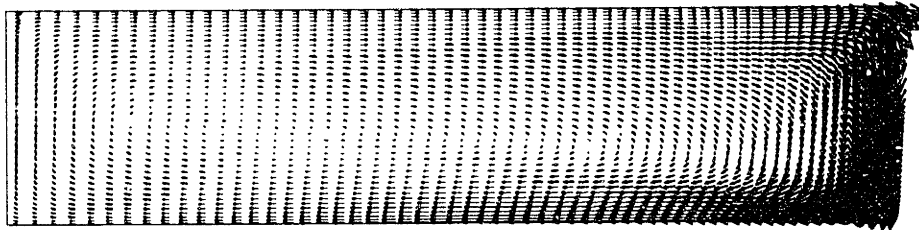


Figure 3.4.35 (cont.) (c) streamlines field in the bath region for a furnace radius of 2.0 m and bath depth of 0.5 m, keeping the same arc length of 25 cm and arc current of 40 kA.

(a)



(b)

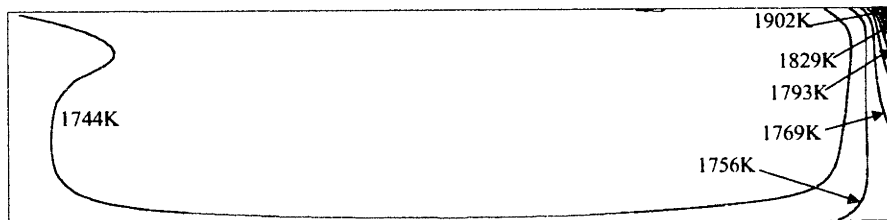


Figure 3.4.36 (a) Velocity, and (b) temperature fields in the bath region for a furnace radius of 2.5 m and bath depth of 0.7 m, keeping the same arc length of 25 cm and arc current of 40 kA.

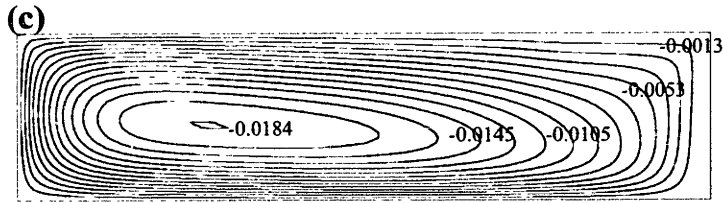


Figure 3.4.36 (cont.) (c) streamlines field in the bath region for a furnace radius of 2.5 m and bath depth of 0.7 m, keeping the same arc length of 25 cm and arc current of 40 KA.

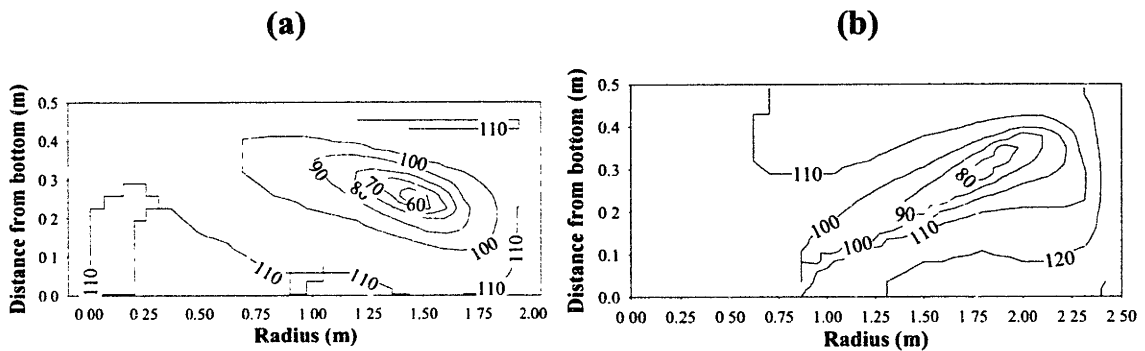


Figure 3.4.37 Mixing time maps for the bath regions under electric arc current of 40 KA and arc length of 25 cm for different furnace radii. (a)  $R_{furnace}=2.0$  m. (b)  $R_{furnace}=2.5$  m. Mixing times are expressed in seconds and 95% of uniformity is the criteria to define mixing.

Figure 3.4.38 shows the average temperature variations with respect to the furnace volume (due to changes in furnace radius). Enthalpy in the bath decreases as volume of the furnace increases. This behavior contradicts the trend presented in Figure 3.4.33, where bath enthalpy increases as volume increases (or a bath depth increases). But this time, an increase in the furnace radius increases the top surface area, and hence radiation losses are much higher. Therefore, radiation losses increase as furnace radius increases and consequently the bath enthalpy presents this decay shown in Figure 3.4.38.

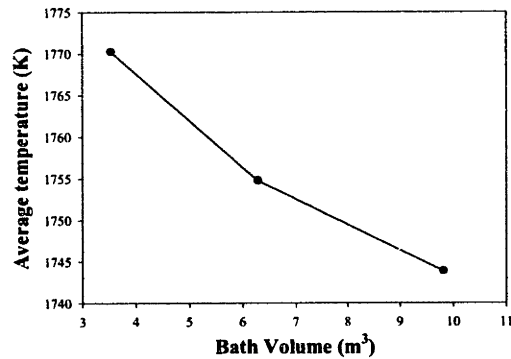


Figure 3.4.38 Average temperature as a function of the bath volume keeping the arc length and current in their standard values of 40 KA and 25 cm respectively. Bath volume increments are due furnace radius variations.

The comparative heat balances presented in Figure 3.4.39 shows that radiation increases significantly when furnace radius is increased. These radiation losses are compensated in some extent by the heat introduced into the bath through the walls. Despite the fact that this positive heat coming from the walls is physically incorrect (heat must flow out through the walls not in), it reflects the fact that bath temperatures are much lower than the wall temperatures, producing the positive heat flows shown in Figure 3.4.39. Therefore, in actual conditions, the decay shown in Figure 3.4.38 could be more prominent.

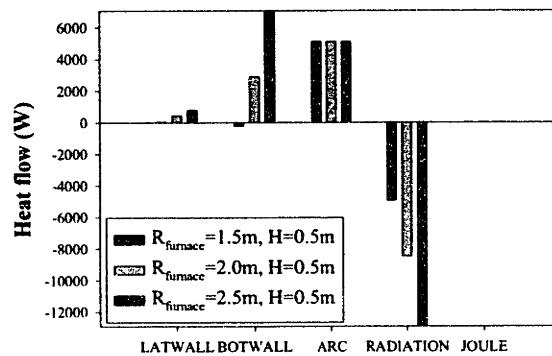


Figure 3.4.39 Comparison of the heat balances in the bath region for the different furnace radii tested ( $R_{furnace}=1.5\text{ m}$ ,  $R_{furnace}=2.0\text{ m}$ ,  $R_{furnace}=2.5\text{ m}$ ) keeping the same arc length of 25 cm and arc current of 40 KA.

### Section 3.4.1.8: Effect of the Anode Electrode Configuration on Fluid Dynamics and Temperature field

The last aspect analyzed in the single-phase system is the effect of the anode size on the bath behavior. By default, the whole bottom surface was considered to conduct the electric current. In order to

see the effect of the anode surface, the bottom surface is now restricted to the passage of current in certain sections, leading to three different anode surface configurations: (a) Anode ring located at 1.062 m from the center and 0.06 m width. (b) Circular anode at the center with a radius of 0.1 m. (c) Circular anode at the center with a radius of 0.05 m.

Figure 3.4.40 shows the velocity (a), temperature (b), current density (c), body force (d) and potential (e) fields for the anode ring case. The fields are similar to the fields obtained when the whole bottom surface is used as anode. The potential field presented in Figure 3.4.40 (e) presents potential lines perpendicular to the bottom surface close to the center, which indicates that no current is flowing through the bottom surface, with the exception of the anode ring.

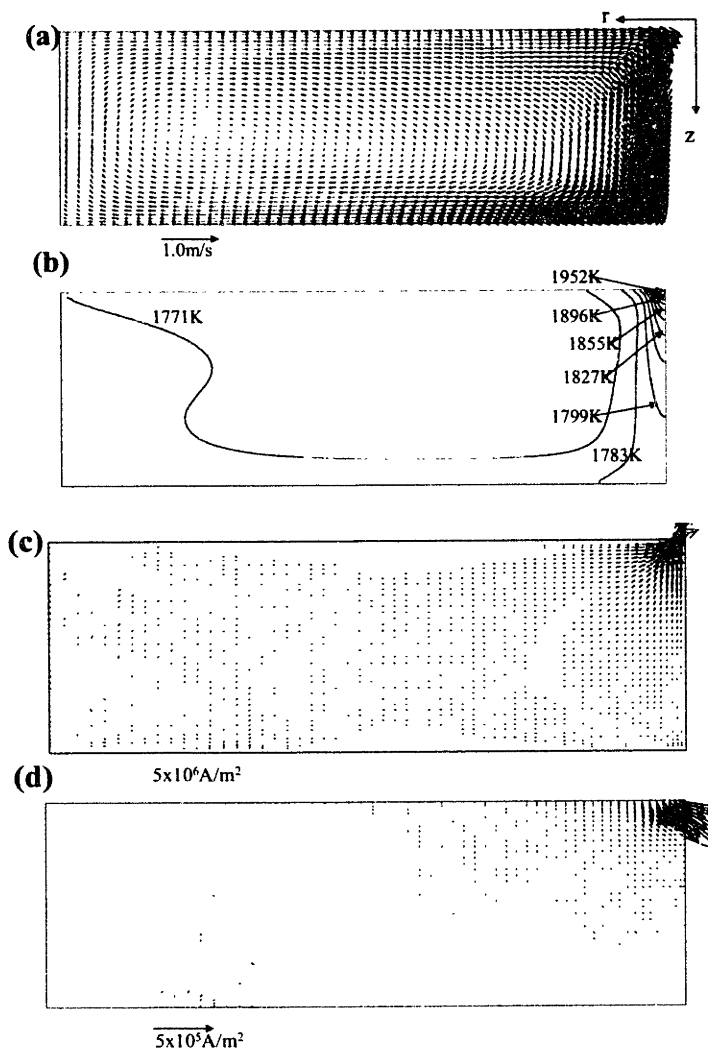


Figure 3.4.40 (a) Velocity, (b) temperature, (c) current density, and (d) body force fields in the bath region for a furnace with a radius of 1.5 m and a bath depth of 0.5 m under the standard arc (25 cm and 40 KA) and using an anode ring as indicated in the figure (e).

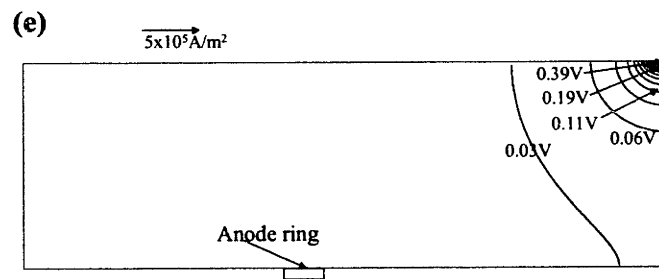


Figure 3.4.40 (cont.) (e) potential field in the bath region for a furnace radius of 1.5 m and bath depth of 0.5 m, under the standard arc (25 cm and 40 KA) and using an anode ring as indicated in the figure (e).

Figure 3.4.41 shows the corresponding quantities for the circular anode area with radius of 0.1 m. In this case, strong differences appear in all fields when comparing them against the case with whole bottom surface anode. The velocity field (Figure 3.4.41 (a)) presents a complex flow pattern shown by the streamlines presented in Figure 3.4.41 (c). Obviously this flow pattern affects the temperature field (Figure 3.4.41 (b)) since convection plays an important role in shaping the temperature field. The small anode area is the factor that creates all these changes in the bath behavior. The potential gradient (Figure 3.4.41 (d)) decreases when distance from the top surface increases, but as the anode is closer, the potential gradient increases again. This behavior promotes divergence of current just below the arc attachment zone, but as the axial distance approaches the anode, the current density converges due to the small anode area, as shown in the current density field of this Figure 3.4.41 (f). Other fields, such as magnetic flux density (Figure 3.4.41 (e)) and electromagnetic body forces (Figure 3.4.41 (g)), are also consistent with this current density field. The body force field presents two regions of dominance, i.e. in the arc attachment zone and in the vicinity of the anode surface. These two zones are in opposition to each other. In this particular case, the arc attachment zone dominates, and therefore the liquid steel is mainly directed downward close to the symmetry line.

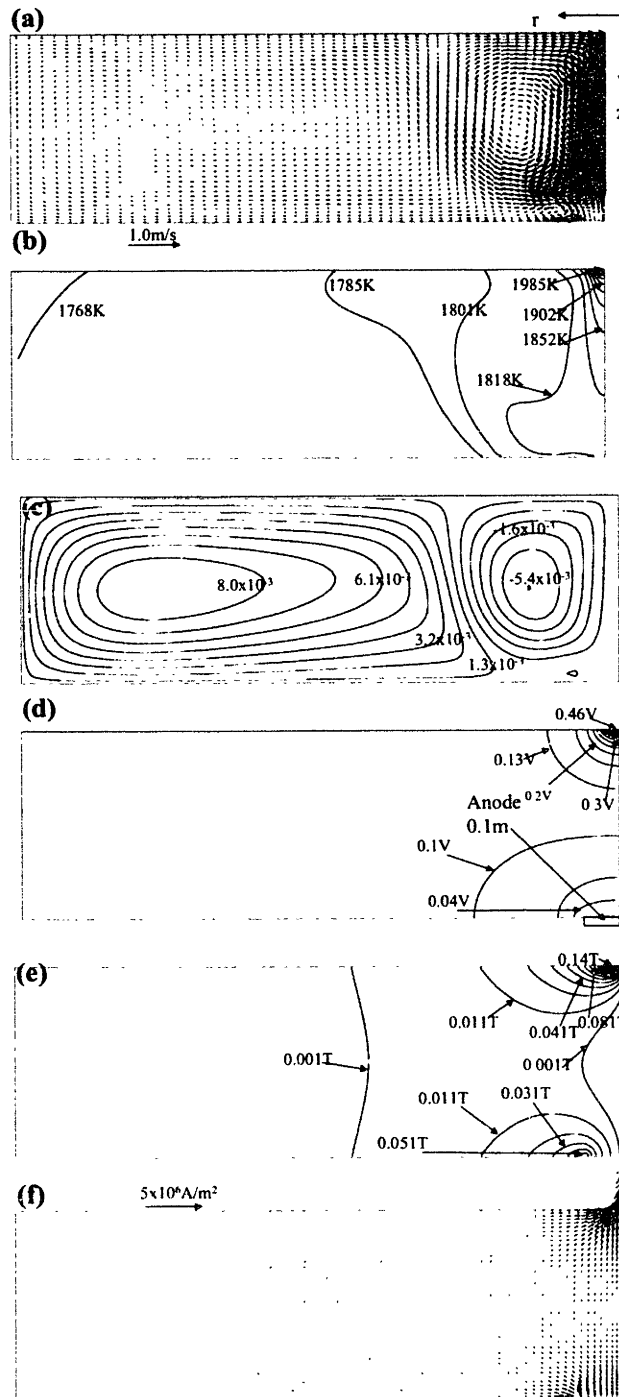


Figure 3.4.41 (a) Velocity, (b) temperature, (c) streamlines, (d) potential, (e) magnetic flux density, and (f) current density fields in the bath region for a furnace radius of 1.5 m and bath depth of 0.5 m, under the standard arc (25 cm and 40 kA) and using a circular anode with a radius of 0.1 m.

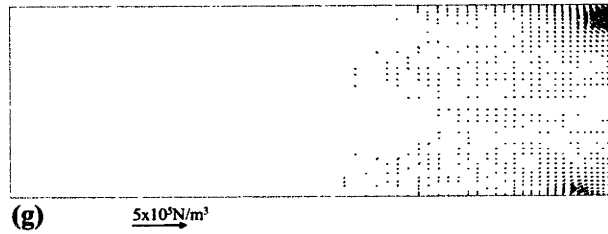


Figure 3.4.41 (cont.) (g) body force field in the bath region for a furnace radius of 1.5 m and bath depth of 0.5 m, under the standard arc (25 cm and 40 KA) and using a circular anode with a radius of 0.1 m.

Figure 3.4.42 shows the velocity (a), temperature (b), streamline (c), potential (d), current (e), magnetic flux density (f) and body force (g) fields for the furnace with a smaller anode circular area and a radius of 0.05 m. This time the velocity field presents two circulation loops the largest being in the opposite direction (counter-clockwise) to the normal loop formed when the whole bottom surface acts as anode. Under this velocity pattern, the temperature field shows that hot steel at the top does not penetrate deep into the bath and most of the reactor is well homogenized, the arc attachment zone being the region where high temperature gradients are present. This temperature field could be beneficial to prevent wear the bottom refractory. The potential field, is similar to the previous case (anode radius of 0.1 m), and shows isopotential lines concentrated in the arc attachment zone and in the vicinity of the anode. But since the anode area is smaller, the current density converges even more at the anode (larger current density vectors) and consequently stronger body forces are located at the anode, rather than in the arc attachment zone. As a result, liquid moves upward since forces at the anode overcome the opposite forces located at the arc attachment zone. The magnetic flux density field also indicates the convergence of current in the anode region.

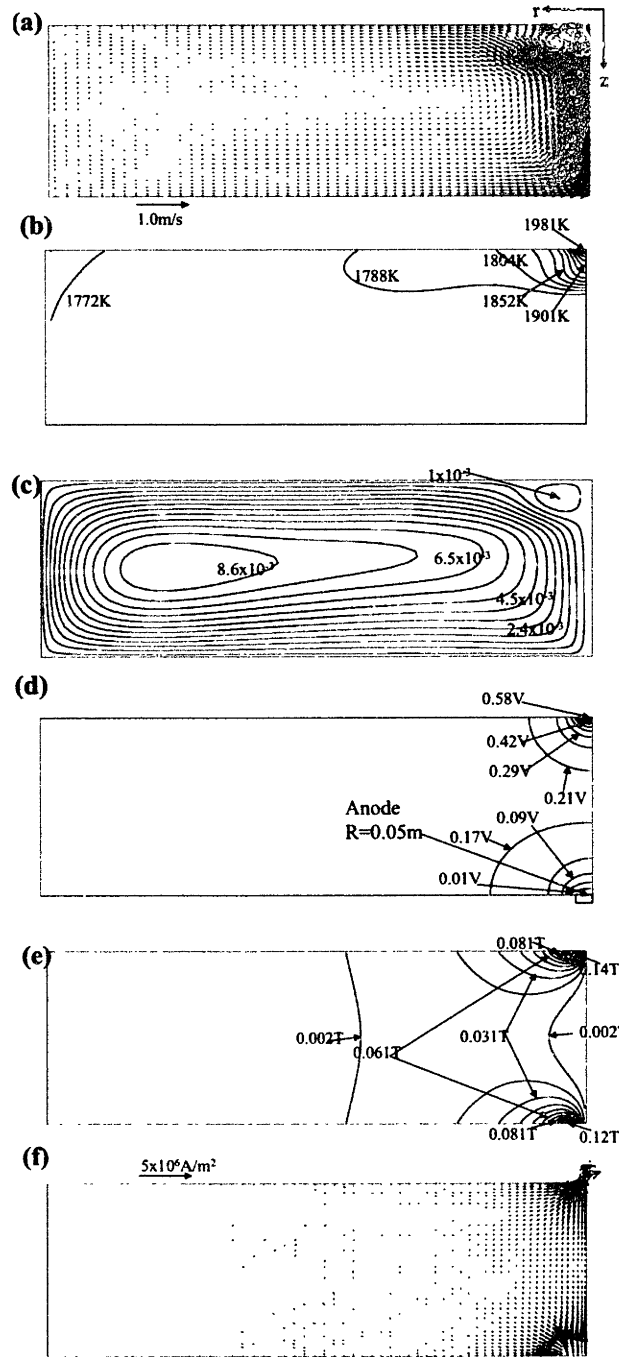


Figure 3.4.42 (a) Velocity, (b) temperature, (c) streamlines, (d) potential, (e) magnetic flux density, and (f) current density force fields in the bath region for a furnace radius of 1.5 m and bath depth of 0.5 m, under the standard arc (25 cm and 40 KA) and using a circular anode with a radius of 0.05 m.



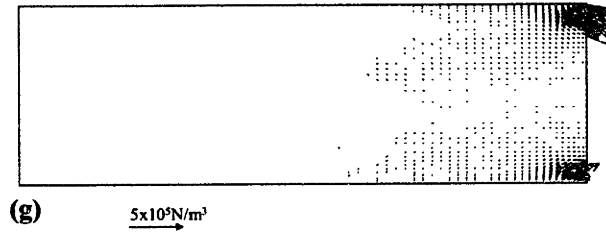


Figure 3.4.42 (cont.) (g) body force field in the bath region for a furnace radius of 1.5 m and bath depth of 0.5 m, under the standard arc (25 cm and 40 KA) and using a circular anode with a radius of 0.05 m.

The temperature, axial velocity and potential profiles along the symmetry axis for the different anode surfaces configurations considered in the study (including the whole bottom surface anode) are presented in Figure 3.4.43 (a) - (c). The effect of the anode surface on the axial profiles is enormous as indicated by the plots. All of the axial profiles along the axis present similar behavior for both normal and anode ring configurations. When the anode configuration changes to a small circular area at the center of the reactor (0.1 m or 0.05 m), the temperature behaves differently depending if the fluid is directed downward or upward close to the symmetry axis. Velocities are very similar in all cases except for the smallest circular anode area, where the axial velocity profile along the axis changes sign, being positive close to the top free surface and negative in the rest of the axis. The potential profiles along the axis for the circular anode area configurations presents the two high gradient zones (one close to the anode and the other close to the top surface), but the smaller the anode area, the larger the potential gradient close to the anode.

Figure 3.4.44 (a) – (d) show the mixing time maps for the different anode configurations tested in this sensitivity study. The anode ring configuration is the most beneficial in terms of shorter mixing times (35 – 65 seconds). In contrast, the smaller circular anode produces the longer mixing times (50 – 100 seconds for 0.05 m of anode radius and 56-88 seconds for the anode surface with a 0.1 m radius).

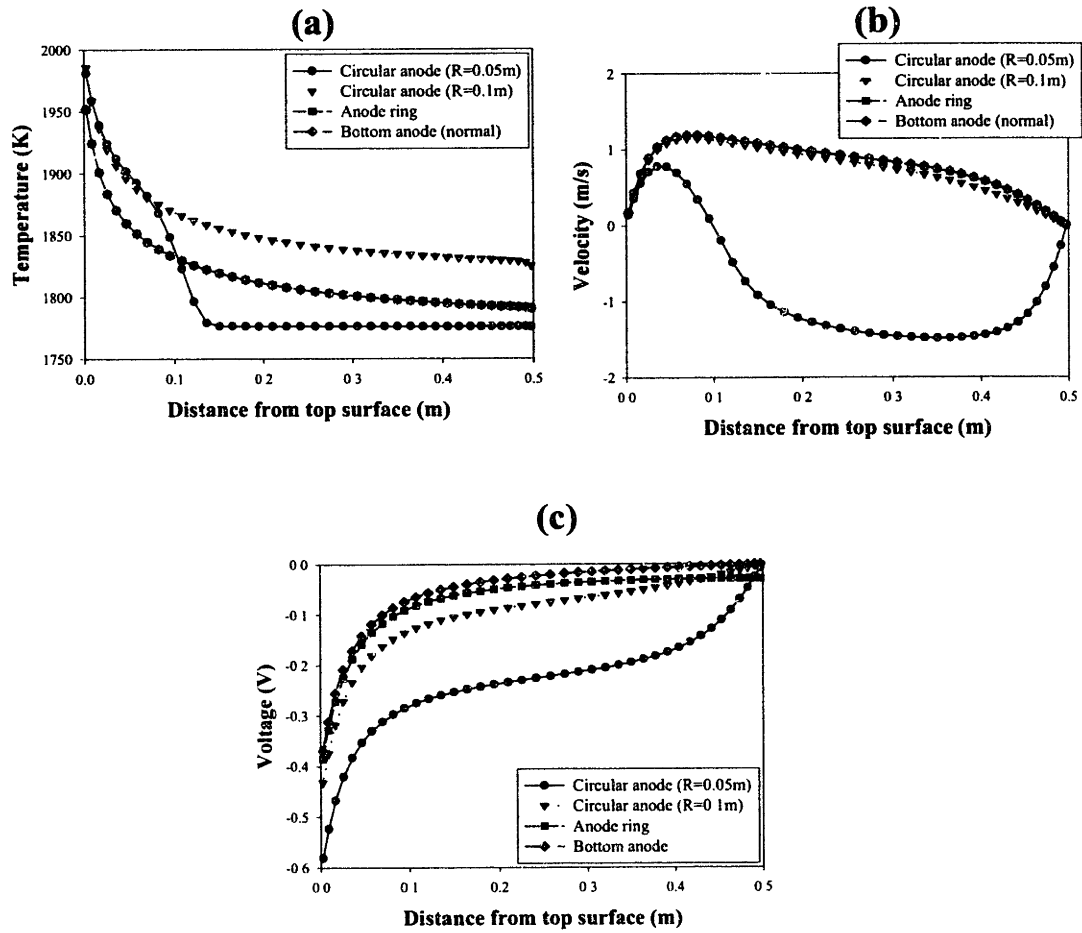


Figure 3.4.43 Effect of the anode configuration on the bath properties along the symmetry axis. (a) Temperature. (b) Axial velocity. (c) Potential.

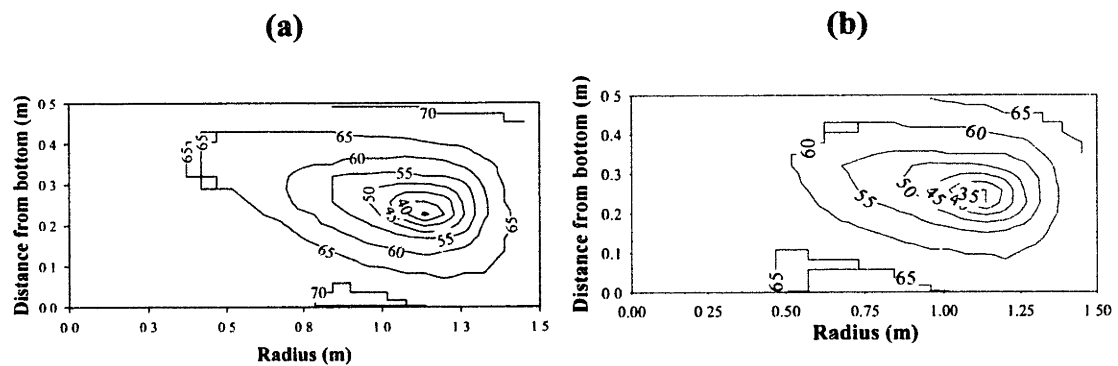


Figure 3.4.44 Mixing time maps for the bath regions under the standard electric arc (40 kA and 25 cm) for the four different anode configurations. (a) Bottom anode (normal). (b) Anode ring.

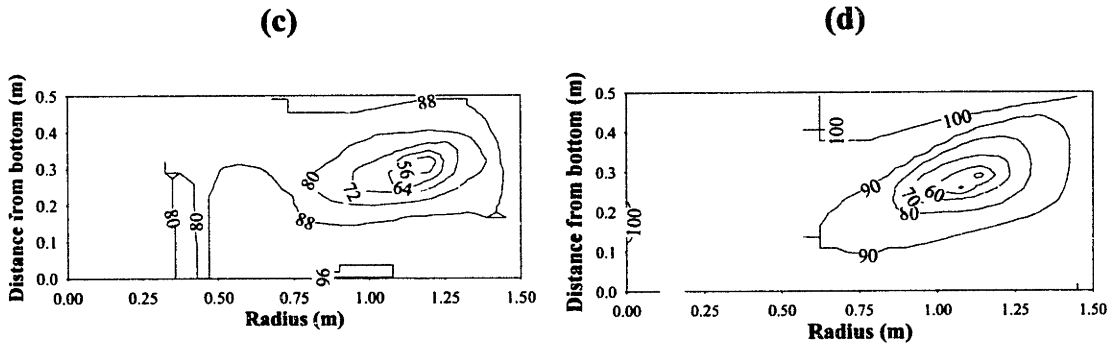


Figure 3.4.44 (cont.) Mixing time maps for the bath regions under the standard electric arc (40 kA and 25 cm) for the four different anode configurations. (c) Circular anode with radius of 0.1 m. (d) Circular anode with radius of 0.05 m.

In terms of the heat balance, it is seen that no major differences are obtained when the anode surface is changed, as shown in the Figure 3.4.45 where the heat balance is presented for all anode configurations used in the sensitivity study. In this plot, less heat is extracted from the bottom wall with the circular configuration of 0.05 m anode radius, which confirms the beneficial effect that this configuration has on the bottom refractory wall.

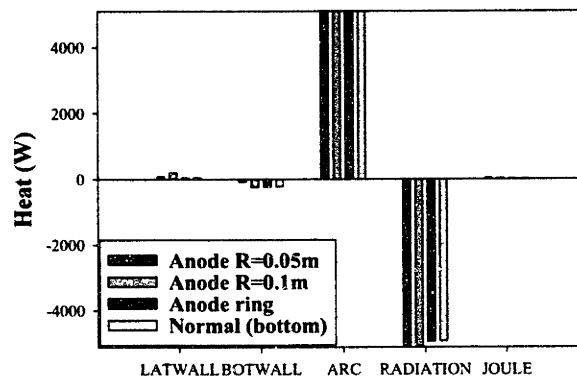


Figure 3.4.45 Comparison of the heat balances in the bath region for the different anode configurations tested (bottom anode (normal), anode ring, circular anode with radius of 0.1 m, circular anode with radius of 0.05 m) keeping the same arc length of 25 cm and arc current of 40 kA.

### Section 3.4.2: Results of the Gas Injection Model

In this section, results and analysis of fluid flow and heat transfer in the bath region are presented for the Gas-Steel model. First, the isolated effect of gas injection through three nozzles located at radial distances of 0.94 m from the center and separated one from the other by  $120^\circ$  for the same standard case of

40 KA and 25 cm. Then, the other driving forces are included together with gas injection and fluid flow and temperature fields are fully described. Finally, the effect of the gas flow rate on the bath behavior and characteristics is presented through a sensitivity study.

### Section 3.4.2.1: Isolated Effect of Inert Gas Injection on Velocity and Temperature Fields of the steel (Gas-Steel Model)

Figure 3.4.46 shows the computed fluid flow patterns and temperature distribution on different planes in a 3D domain for a 3-nozzle gas-stirred EAF system. The domain only represents a 1/6 th. symmetric section of the entire furnace. Since the purpose of this result is to examine the specific role of gas injection in determining flow patterns and temperature distributions in the bath, the results shown in the figure do not include the effects of shear, buoyancy or electromagnetic forces. Only the heat input from the arc and the Joule heat effect are considered in the calculation. Under the conditions of this simulation, the flow patterns indicate that gas injection can promote reasonable fluid circulation in the regions close to the wall, with typical velocities of the order of 0.1 m/s (much higher velocities are appreciated in the plume region, >1 m/s). In contrast, the central portion of the bath is relatively stagnant. The temperature field shown in the figure reflects this situation, where a uniform temperature region is observed near the wall and significant temperature gradients are predominant in the center of the bath. It should be stressed, however, that a different mixing situation in this central region would be expected if electromagnetic effects were included in the calculation.

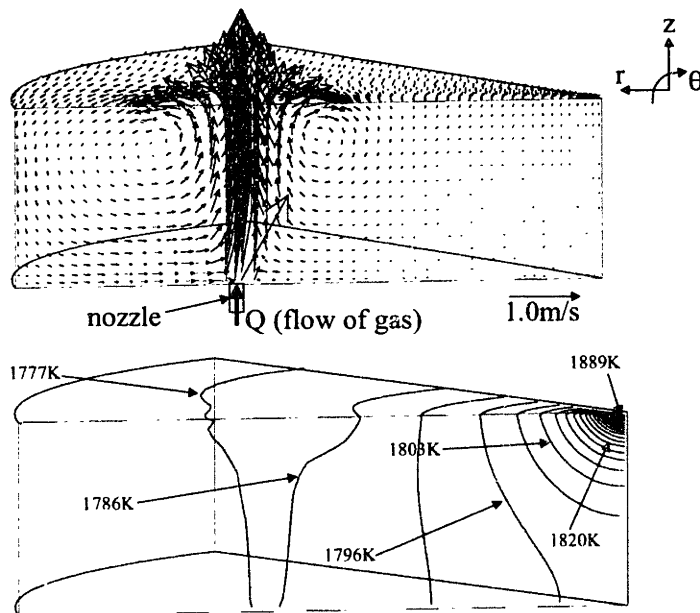


Figure 3.4.46 Velocity and temperature fields in the bath region under the effect of bottom gas injection.

### Section 3.4.2.2: Effect of Inert Gas Injection on the Bath Behavior (Gas-Steel Model)

When gas injection is combined with the additional driving forces for fluid motion, the relative importance of the injection and the electromagnetic body forces can be studied. Figure 3.4.47 shows the computed liquid velocity (a), liquid temperature (b), gas volume fraction (c), magnetic flux density (d), current density (e) and electromagnetic body force (f) fields on different planes in a 3D domain for the 3-nozzle gas-stirred EAF system presented in the last section. Again, the domain only represents a 1/6th symmetric section of the entire furnace. The liquid velocity field is similar to that presented in Figure 3.4.46, but now the effect of the electromagnetic stirring is present and then, close to the symmetry line, the flow motion is dominated by the electromagnetic body forces. Therefore, the combination of all forces seems to eliminate dead zones in the reactor. The temperature field also shows the effect of the electromagnetic stirring close to the symmetry axis where temperature contours are different from those presented in the previous case (Figure 3.4.46). In the zone where gas injection predominates, homogenous liquid temperatures are found (17 K temperature difference in this zone). In the gas volume fraction field, the gas plume formed above the nozzle is appreciated. The top surface also presents some concentration of gas, but the rest of the reactor is almost free of gas. The magnetic flux density field presented in the figure represents a 3D extrapolation from a 2D representation of the electromagnetic problem, i.e. the injection of gas does not eliminate the 2D nature of the electric problem. Then, the current density and electromagnetic body force fields are also 3D representations of the 2D fields already shown in the previous section (single-phase steel results). Actually, only two components of both current density and body force fields are computed (the axial and radial components), while only the azimuthal component of the magnetic field is considered.

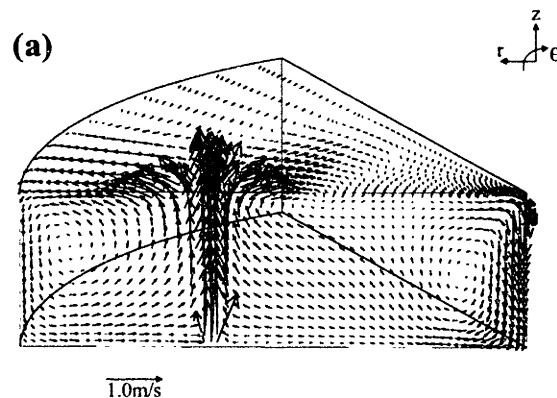


Figure 3.4.47 (a) Liquid velocity field in the bath region under the influence of the standard electric arc and the gas injection through 3 nozzles. Only 1/6th of the system is presented due to symmetry.

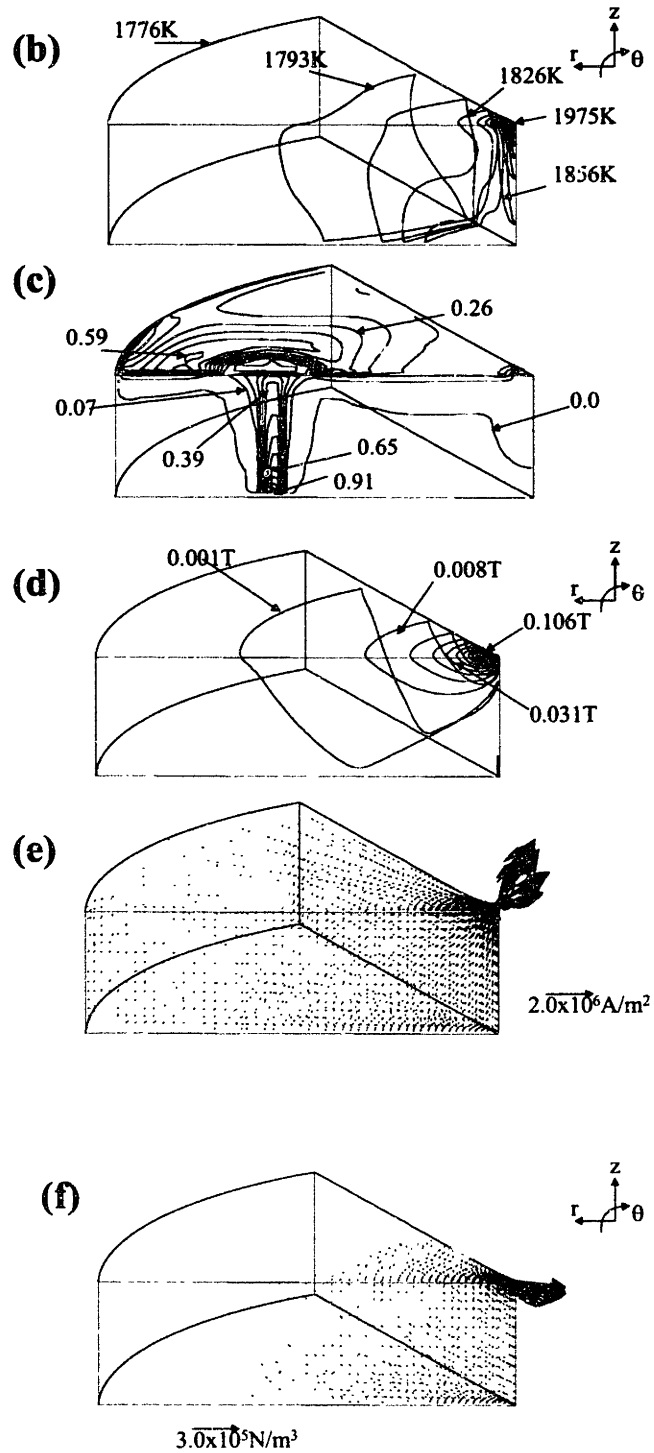


Figure 3.4.47 (cont.) (b) liquid temperature, (c) gas volume fraction, (d) magnetic flux density, (e) current density, and (f) body force fields in the bath region under the influence of the standard electric arc and the gas injection through 3 nozzles. Only 1/6th of the system is presented due symmetry.

### Section 3.4.2.3: Effect of Gas Flow Rate on the Velocity and Temperature Fields (Gas-Steel Model)

In this section we present a sensitivity study performed to examine the effect that the gas flow rate has on the velocity and temperature fields for the gas injection system. The sensitivity study is obtained considering the standard arc case (40 KA, 25 cm), for different gas injection flow rates of  $5.0 \times 10^{-4}$  (standard),  $2.5 \times 10^{-4}$ ,  $1.6666 \times 10^{-4}$ ,  $1 \times 10^{-3}$  and  $1.5 \times 10^{-3} \text{ m}^3/\text{s}$  at each nozzle.

Figure 3.4.48 shows the velocity fields obtained when different gas flow rates are employed. As expected, an increase in the gas flow rate produces higher liquid velocities, especially for the liquid being in contact with or in the vicinity of the plume region. Overall liquid velocities increase as the gas flow rates increase. For a gas flow rate of  $1.66 \times 10^{-4} \text{ m}^3/\text{s}$  a maximum liquid velocity of 0.8 m/s is obtained at the exit of the nozzle, while at the same location a liquid velocity of 4 m/s is obtained when the gas flow rate is  $1.5 \times 10^{-3} \text{ m}^3/\text{s}$  (one order of magnitude higher). However, it should be noted that an extremely high value of 4 m/s is predicted at the nozzle location, where the gas volume fraction is around 97% (almost no liquid at that point).

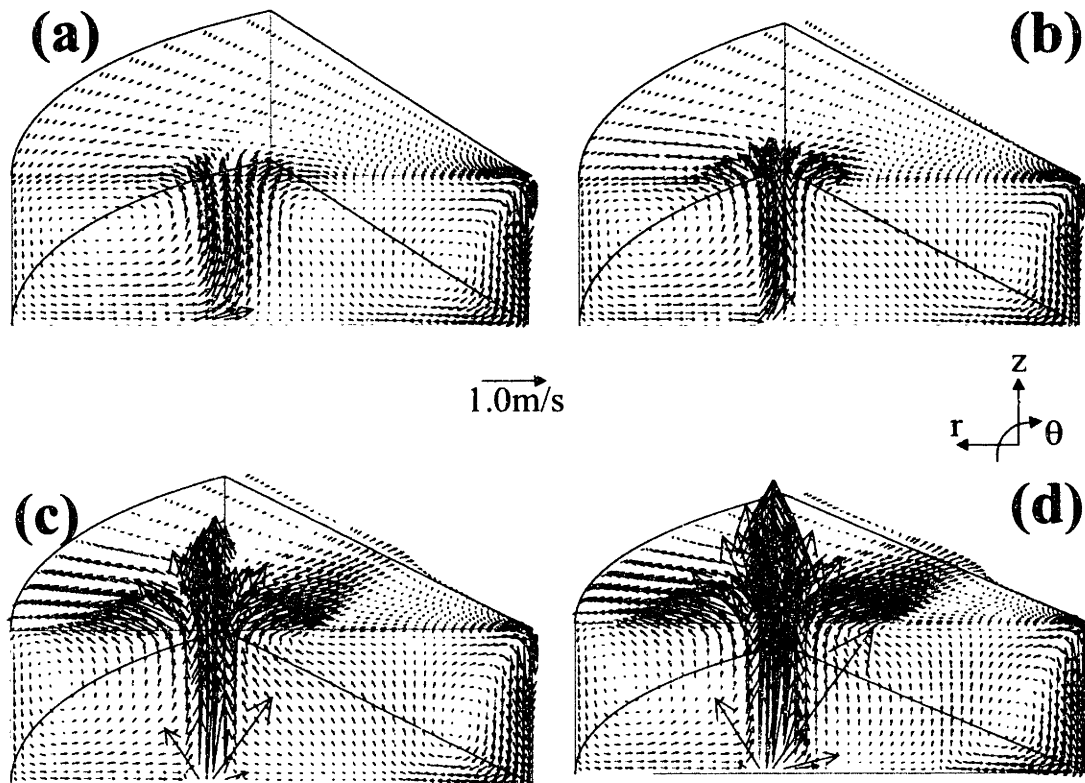


Figure 3.4.48 Effect of varying the gas flow rate on the liquid velocity field. (a)  $Q=1.6666 \times 10^{-4} \text{ m}^3/\text{s}$ . (b)  $Q=5.0 \times 10^{-4} \text{ m}^3/\text{s}$ . (c)  $Q=1 \times 10^{-3} \text{ m}^3/\text{s}$ . (d)  $Q=1.5 \times 10^{-3} \text{ m}^3/\text{s}$ .

Figure 3.4.49 shows the temperature fields produced when the gas flow rates are varied from  $1.66 \times 10^{-4} \text{ m}^3/\text{s}$  to  $1.5 \times 10^{-3} \text{ m}^3/\text{s}$ . Two main findings can be noted from this figure. The first is that the maximum temperature in the arc attachment zone increases as the gas flow rate increases, which is a surprising result, since as the mixing increases due to gas injection one would expect lower temperature gradients. Maximum temperatures of 1966, 1971, 1975, 1987 and 1999 K are obtained from the lowest to the highest gas flow rates. The second important observation is that the well-homogenized region expands to a bigger portion of the reactor as the gas flow rate increases. Then, despite the fact that the arc attachment zone is hotter as the gas flow rate increases most part of the reactor is well homogenized. Hence, combining these two main findings, it can be said that as the gas flow rate increases, the region dominated by electromagnetic forces is reduced to a smaller portion but this promotes a hotter arc attachment zone. This is mainly because there is no chance to dissipate the heat coming from the arc due to the reduce zone where electromagnetic stirring is dominating. Therefore, gas injection is beneficial (homogenizing temperature and species in the reactor), but care must be taken to avoid the formation of excessively hot regions. These hot spots (or the isolated region where the electromagnetic effects dominate) will lead to a poor dissipation of the heat coming from the arc, being the dissipation of the heat one of the most important objectives of the gas injection.

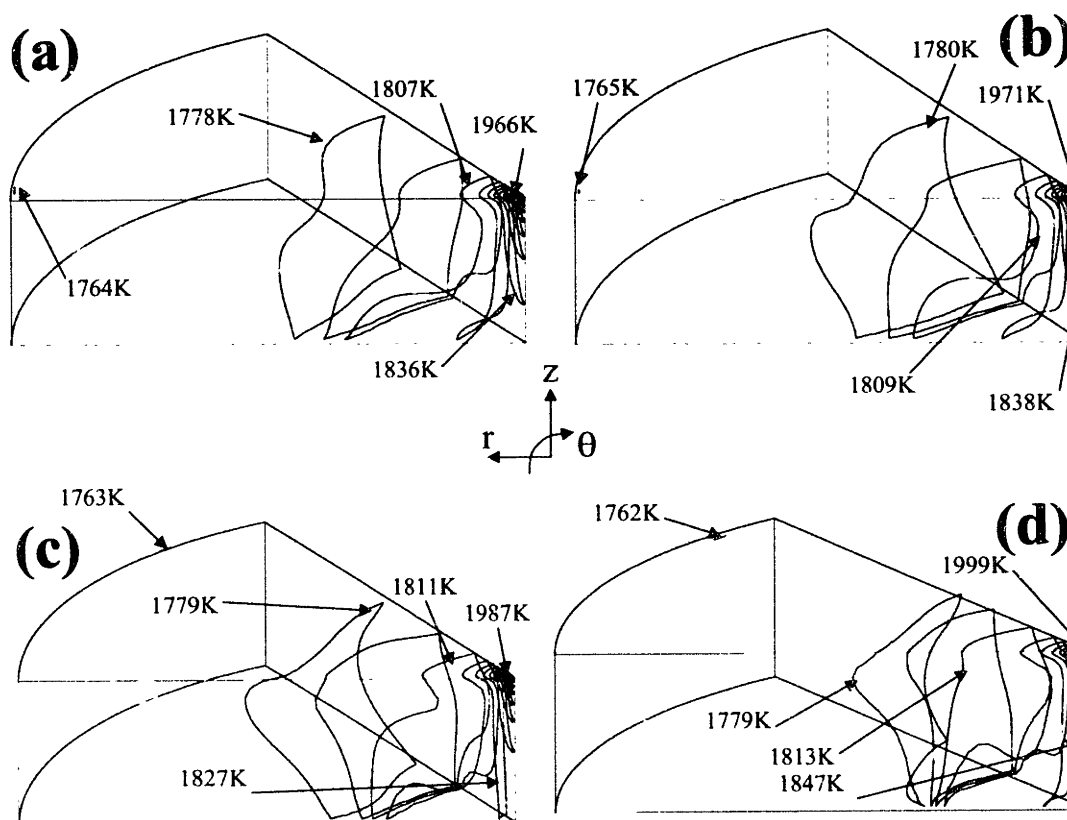


Figure 3.4.49 Effect of varying the gas flow rate on the liquid temperature field. (a)  $Q = 1.6666 \times 10^{-4} \text{ m}^3/\text{s}$ . (b)  $Q = 5.0 \times 10^{-4} \text{ m}^3/\text{s}$ . (c)  $Q = 1. \times 10^{-3} \text{ m}^3/\text{s}$ . (d)  $Q = 1.5 \times 10^{-3} \text{ m}^3/\text{s}$ .



### **Section 3.4.3: Simplified Formulation to Represent a Top Slag Layer**

In representing slag-steel systems, numerous complexities are involved and simplifications are required to tackle the problem. It is considered that in actual operation the high pressure generated by the arc (i.e., the arc thrust) causes a bath depression on the steel surface [21], pushing the non-conducting slag layer away from the central region and, thus, maintaining the electrical connection. Furthermore, the steel and slag are immiscible liquids and, due to their differences in density, the interface separating them can be considered sharp and well defined as was stated in the mathematical formulation. As a first approximation the volume and location of the top slag are arbitrarily imposed a priori. Numerically, the slag layer is prevented from moving toward the central region of the furnace by an artificial retainer, but is allowed to exchange momentum and heat with the steel along a horizontal interface.

#### **Section 3.4.3.1: Effect of the Slag Layer on Velocity and Temperature Fields (Slag-Steel Model)**

Figure 3.4.50 shows the temperature and velocity fields in a two-liquid (slag-steel) system. As mentioned above, these results involve an idealized situation and therefore only a comparative analysis is attempted. The slag layer affects the behavior of the system by decreasing the velocity in the steel phase and reducing the bath circulation. A maximum velocity of 0.4 m/s is calculated, in contrast to the 1.2 m/s obtained when no slag is present. The top slag layer also forms a circulation loop, moving in the opposite direction to the steel, but with a much lower velocity. The presence of the slag layer also has a critical effect on the bath temperature field. There is an overall temperature difference of about 70 K across the layer of slag and higher temperatures are observed in the central region of the furnace, compared to the standard case with no slag, described in Figure 3.4.4 (a).

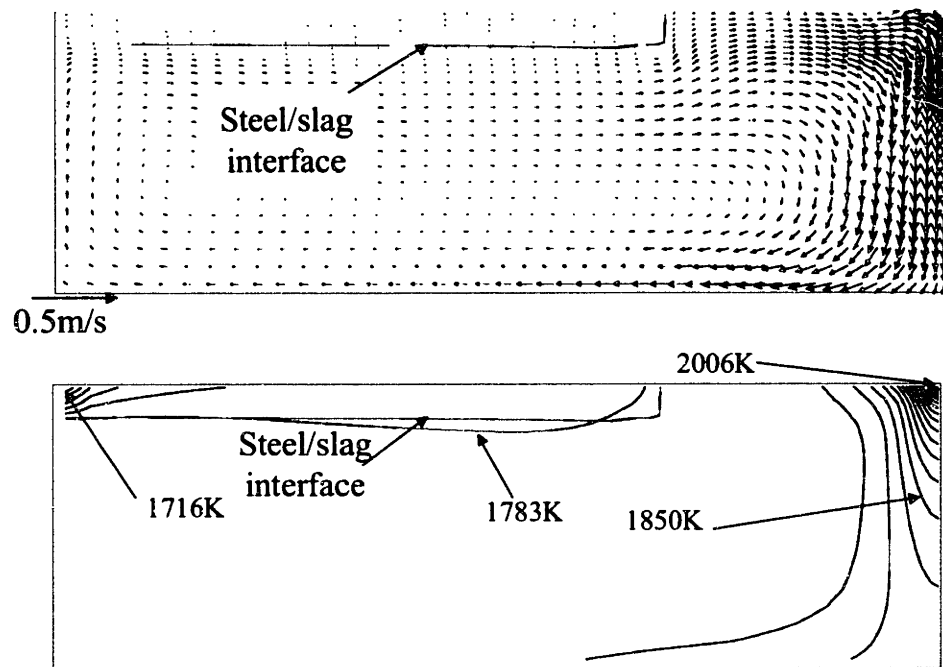


Figure 3.4.50 Velocity and temperature fields in the bath region under the effect of a layer of slag.

## Chapter 4: Conclusions

A mathematical model has been developed to represent DC-EAF refining operations. The model involves the simultaneous solution of Maxwell's equations for the electromagnetic field, and the turbulent fluid flow and heat transfer equations. In solving the arc and bath regions it was assumed (and justified) that the arc-bath interactions are dominated by the behavior of the arc. In contrast to previous modeling investigations, this work relaxes some critical assumptions and provides a more realistic and comprehensive representation of the system. This work also examines and compares the relative merits of alternative electromagnetic and turbulence formulations, and addresses the role of induced currents and compressibility effects in representing the arc. Furthermore, due allowance was made to represent and analyze the effect of gas injection, the presence of a slag layer in the bath and the differences in anode configurations. Finally, a detailed analysis was carried out to examine the effect of process parameters (e.g., arc current, arc length, bath dimensions, anode arrangements, etc) on the behavior of the furnace (i.e., heat transfer to the bath, heating efficiency, mixing times in the bath, etc). Despite limitations in available experimental information on actual or pilot plant DC-EAF systems, different aspects of the model are validated using several sources of experimental data reported for related systems in the literature.

### **Main conclusions drawn from the arc model:**

#### **Arc physics:**

1. Two mathematical descriptions of the electromagnetic field were compared: the magnetic and the electric potential approaches. It was found that for argon arc welding systems predictions based on the potential approach agreed better with experimental results than those obtained using the magnetic approach. Also, the potential approach exhibited better convergence behavior and was selected as the preferred description of the electromagnetic fields.
2. The model was further validated using experimental velocity measurements in a high-intensity carbon arcs. Good agreement was obtained.
3. The “anatomy” of the arc region was fully described using the model. The results in the arc region show that all the arc characteristics are strongly coupled. It was found that the boundary of the arc region could be unambiguously defined as the location of the 10000 K, the radial location of the point of maximum magnetic flux density, the inflection points in the iso-potential lines, and the current density or conductivity fields.

4. A standard value of  $4.4 \times 10^7 \text{ A/m}^2$  was used for the current density at the cathode spot,  $J_c$ , as measured by Jordan. Changes in the value of this parameter had little effect on the electrical properties at the bath surface but a large effect on the cathode jet velocity, both in the arc and at the surface of the bath.
5. It was found that the choice of turbulence model had a big effect on the model predictions. Higher levels of turbulence were predicted with the standard k- $\epsilon$  model in comparison to the RNG and two-scale k- $\epsilon$  models. However, no conclusions can be drawn as to which model better represents the system, since no experimental measurements are available. Arc characteristics and arc-bath interactions are sensitive to the turbulence model selected for the calculations.
6. The bath temperature does not affect the arc region, and this permits a convenient decoupling between arc and bath regions.
7. Compressibility effects are likely to play an important role in industrial DC-EAF. The overall effect of compressibility is to decrease the arc velocity and temperature and some arc-bath interactions (shear stress and heat fluxes at the bath surface). However, convergence becomes a critical issue when compressibility is considered.
8. The effect of including induced currents in the mathematical representation is to further expand the arc region and the predicted shape of the arc is in better agreement with experimental measurements.
9. Maecker's asymptotic expressions for maximum velocity and arc pressure are consistent with our model predictions in both trends and values. The expression obtained for maximum arc pressure at the cathode in this work is as follows:

$$P_{\max} = 1.13 \cdot \frac{\mu_o I J_c}{4\pi}$$

10. The most important contribution of this thesis, regarding the arc physics, is the definition of a universal arc shape in dimensionless form (valid for any arc current and arc lengths within the range of conditions studied before the impingement region close to the bath). The arc shape is the fundamental parameter that permits the prediction of the axial velocity, temperature and magnetic flux density through simple mathematical expressions. These expressions are limited to free-burning arcs with graphite cathode electrodes in air and are presented below:

a) Arc shape or arc radius (before the impingement region):

$$\frac{R_a}{R_c} = \left( 0.863747 - 0.2527 \frac{Z}{R_c} \right)^{0.5} \quad (\text{eq. 2.4.4})$$

where  $R_a$  is the arc radius,  $R_c$  is the cathode spot radius and  $Z$  is the axial distance from the cathode.

**b) Magnetic flux density:**

$$\frac{B_\theta}{B_{\max}^0} = 1.8632 \left( \frac{R}{R_a} \right) - 0.5874 \left( \frac{R}{R_a} \right)^2 - 0.19117 \left( \frac{R}{R_a} \right)^3 \quad \text{for } R \leq R_a \quad (\text{eq. 2.4.5})$$

$$\frac{B_\theta}{B_{\max}^0} = \frac{1}{\left( \frac{R}{R_a} \right)} \quad \text{for } R > R_a \quad (\text{eq. 2.4.6})$$

$$B_{MAX} = \frac{\mu_o I}{2\pi R_c} \quad (\text{eq. 2.4.7})$$

$$\frac{B_{\max}^0}{B_{MAX}} = \exp \left( 0.0363 - 0.1959 \left( \frac{Z}{R_c} \right)^{0.5} \right) \quad (\text{eq. 2.4.8})$$

where  $B_\theta$  is the magnetic flux density,  $B_{\max}^0$  is the maximum magnetic flux density value (located at the arc radius), and  $B_{MAX}$  is the maximum magnetic flux density value in the domain (always located at the edge of the cathode spot radius).

**c) Temperature field:**

$$\frac{T}{T_{\max}^0} = 0.0425 + \frac{0.9744}{\left( 1 + \exp \left( -\frac{(R/R_a) - 1.079}{0.2647} \right) \right)} \quad (\text{eq. 2.4.9})$$

$$\frac{T_{\max}^0}{T_{MAX}} = 0.4352 + 0.55366 \exp \left( \frac{-(Z/R_c)}{12.9745} \right) \quad (\text{eq. 2.4.10})$$

where  $T$  is the arc temperature,  $T_{\max}^0$  is the temperature along the symmetry axis and  $T_{MAX}$  is the maximum temperature in the domain (which varies from ~25000 K to ~28000 K for the whole range of conditions analyzed in this work).

**d) Axial velocity field:**

$$\frac{V_z}{V_{\max}^0} = 1.02 \exp \left( -0.5 \left( \frac{(Z/R_c) - 0.00647}{0.446} \right)^2 \right) \quad (\text{eq. 2.4.11})$$

$$\frac{V_{max}^0}{V_{MAX}} = \frac{\left( 3.27 \left( \frac{Z}{R_c} \right) - 0.24 \left( \frac{Z}{R_c} \right)^2 + 0.0188 \left( \frac{Z}{R_c} \right)^3 \right)}{\left( 1 + 3.27 \left( \frac{Z}{R_c} \right) - 0.5 \left( \frac{Z}{R_c} \right)^2 + 0.052 \left( \frac{Z}{R_c} \right)^3 \right)} \quad (\text{eq. 2.4.12})$$

where  $V_z$  is the axial velocity,  $V_{max}^0$  is the axial velocity along the axis and  $V_{MAX}$  is the maximum velocity, which can be determined from the Maecker equation (eq. 2.1.2).

All of the physical properties in the arc can be obtained from the temperature field. The magnetic field can be used to obtain the current densities and the electric potential using Ampere's and Ohm's laws.

### Sensitivity of the main two process parameters

The principal process parameters in the arc region that were investigated in this work were the arc length and the arc current. The following conclusions can be drawn:

Aspect examined	Arc length effect ( $L$ )	Arc current effect ( $I$ )
Arc characteristics (arc temperature, arc velocity, pressure, current density, etc.)	No effect	Increasing arc current increases arc velocities, temperatures, pressures, current densities, magnetic flux densities, etc. in the arc column
Arc-bath interactions (current density, shear stress, heat fluxes and arc pressure at the bath surface)	Very sensitive to arc length effects: Wider distributions with lower maximum values when arc length increases	Sensitive to arc current variations: Distributions are unaffected but values are increased with arc current increments
Voltage drop in the arc	Very sensitive: arc voltage increases greatly with an arc length increase	Minor influence on arc voltage
Heat flow from the arc to the bath	Increases with an increase in arc length, but for large arc lengths an asymptotic behavior is observed	Linear dependence between heat flow to the bath and arc current
Heat transfer mechanisms (convection, electronic, radiation)	Radiation is greatly affected by arc length. Increasing arc length increases arc resistance and therefore increases radiation. Convection is slightly affected by arc length. Increasing arc length increases the convective heat transfer. Electronic heat is not affected at all.	Electronic contribution is the most sensitive of the heat transfer mechanisms to arc current (increasing arc current increases the electronic contribution). Convection is also increased with an increment in arc current. Radiation is not sensitive to arc current variations
Arc power (Voltage x Current)	An increase in arc length greatly increases arc resistance and, consequently, arc power	Since does not affect arc resistance, an increase in arc current linearly increases arc power

11. The heat transferred from the arc to the bath is controlled by convection, although radiation can become an important mechanism, especially for large arc lengths. It is also recognized that increasing the arc power (increasing arc current or arc length) increases the amount of energy transferred into the bath, but the heat transfer efficiency decreases. Therefore, the shorter the arc the more efficient is the heat transfer to the bath..

**The main conclusions obtained from the bath model are as follows:**

12. Results of the model illustrate that, in the absence of inert gas stirring and with no slag present in the system, electromagnetic forces dominate and are responsible for a single, clockwise, circulation loop in the bath, with high velocities in the central region (downward flow) and relatively low velocities in the vicinity of the lateral wall (upward flow). Buoyancy and shear stress effects partially counteract the electromagnetic driven flow. The arc also controls temperature stratification in the bath. In fact, the largest gradients of almost all bath variables are located just below the arc, in the region called the “arc attachment zone”. Outside this zone a more uniform region is found.

Regarding the effect of some of the process parameters and design variables on bath characteristics the following can be concluded:

Aspect examined in the bath	Arc length effect	Arc current effect	Furnace aspect ratio ( $H/R_{furnace}$ )	Anode configuration
Heat introduced from the arc and kept in the steel	Heat in the steel increases asymptotically with an increase in arc length (consistent with the effect of arc length on heat transfer from the arc)	Heat in the steel increases linearly with an increase in arc current (consistent with the effect of arc current on heat transfer from the arc)	More heat is kept in the steel if the aspect ratio increases using the same arc (taller and lower hearth diameters recommended). Large furnace radius increases significantly the radiation losses	Small circular bottom anode (0.05 m radius) takes better advantage of the heat coming from the arc than the other anode configurations
Mixing phenomena	Increasing the arc length increases the mixing time (decreased mixing)	Increasing the arc current decreases the mixing time (increased mixing)	The higher the aspect ratio, the better the mixing in the bath	The anode ring configuration provides the best mixing followed by the whole bottom anode. Small circular anodes do not promote mixing

Velocity field	Increasing the arc length reduce velocities in the steel. Arc length do not affect turbulence in the melt	Increasing the arc current increases velocities and the degree of turbulence in the melt	Velocity field is not affected greatly with the aspect ratio. But if the aspect ration decreases too much, complex flow pattern can be appreciated	Flow patters are greatly affected by the anode configuration. Small circular area anodes change the direction of the circulation loops in the steel
Temperature stratification	An increase in arc length reduces the presence of the hot spot below the arc (arc attachment zone) but an overall increase of temperature in the steel	An increase in arc current promotes the formation of the hot spot and increases overall temperatures in the steel	Increasing the bath volume leads to a decrease in average temperature for the same arc. But an increase in aspect ratio tends to promote homogenization of the melts	Bath region with high temperature gradients is reduced with small circular anodes, but at the same time higher temperatures are present in the hot spot (arc attachment zone)
Refractory wall wear	Increasing the arc length moderately increases the possibility of refractory wear	Increasing the arc current increases strongly the possibility of refractory wear	Increasing the aspect ratio prevents refractory wear. Aspect ratio effect on refractory wear is important	Small circular anode prevents hot steel from the arc attachment zone to reach directly the bottom refractory.

13. Turbulence models are very important in obtaining a more accurate fluid flow pattern. Since there is no physical or experimental evidence, it is impossible to determine which model is the best option to represent turbulence in this type of systems. However, in general, the standard k- $\epsilon$  predicts much higher turbulence in the bath and arc regions than the RNG and the two-scale k- $\epsilon$  models.
14. The effect of a slag cover is to reduce the velocity in the bulk of the bath, away from the arc region, and to raise the average bath temperature.
15. The effect of stirring by inert gas injection, considered in isolation, indicates that sufficient mixing can be promoted in the periphery of the bath to prevent temperature stratification in that region, and to help dissipate the heat being supplied by the arc in the central region of the bath. Gas injection increases mixing in the bath and the larger the gas flow rate, the larger the mixing observed. The combination of gas injection and electromagnetic body forces can effectively eliminate dead zones in the reactor.



The model will also be potentially useful to address the study of other important issues in EAF operation, such as the position at which additions (for example ferroalloys) are more rapidly mixed and better recovered. Also, the locations for addition of DRI can be optimized to increase its dissolution rate.

Although further efforts are required in order to validate the model under actual steelmaking conditions, the author feels that the bath model presented in this thesis can be used as a useful tool for gaining process understanding of DC-EAF operations.

## Chapter 5: Future Work

It is the author's opinion that the model developed in this thesis is robust and capable to representing the most important aspects involved in EAF operations and that the trends shown by the calculations can be readily applicable to better understand the behavior of these systems. However, it is also clear that in order to obtain absolute confidence in the results, additional experimental information is required to fully validate the models. This, despite the effort invested in using any available experimental information reported for related systems.

An ideal experimental system would be one similar to Bowman's setup (see section 2.2.2.1), but using larger arc currents ( $> 10,000$  A) and arc lengths (10 – 50 cm), and where allowance can be made for specific measurements. For studies of the arc region, these measurements should include:

- Temperature fields and shapes of the arcs (through spectroscopic measurements and high-speed photography), as well as velocity distributions and turbulence characteristics in the arc region (using interferometry and laser-doppler techniques).
- Heat and current fluxes at the anode surface. For this purpose, it can be proposed to use the same experimental anodes described in [109]: (a) A water-cooled copper plate where the coolant inlet and outlet temperatures can be measured with thermocouples while the coolant flow can be measured with a flowmeters (i.e., a calorimetric techniques). (b) A "split plate" anode or (c) a "point probe" anode incorporated into a water-cooled copper holder. The point probe was designed as a calorimeter, whose cooling circuit was separated from that of the surrounding holder. By traversing the probe in lateral direction, flux values can be measured.
- Current density at the cathode spot,  $J_c$ , by visual examination through high-speed films where the luminosity of the arc allows the measurement of the spot as indicated in [22].

For the bath region, construction of laboratory or pilot plant scale experimental systems would be needed to obtain measurements of steel circulation and be able to corroborate:

- Temperature, velocity and turbulence distributions predicted by the model. These measurements would require the use of thermocouples, as well as hot-film or hot-wire anemometers, or electromagnetic or Vives probes [110].
- Mixing characteristics in the system. The addition and continuous recording of radioactive tracers can be employed to determine the rate of bath homogenization.
- Temperatures or heat fluxes at or across the wall furnace. These could be readily obtained from experiments using arrays of thermocouples.

With regard to the mathematical modeling aspects, other areas that need further exploration are:

- Representation and analysis of the role of the free surface deformation produced at the arc jet-bath interface.
- Implementation and study of chemical reactions taking place during DC-EAF operations (i.e., decarburization, desulphurization, etc).

- Representation of other operations being used in current practice, such as the use of lances for injection of oxygen, formation of foaming slags, dissolution of raw materials and additions (e.g., DRI, ferroalloys, etc), and the like.
- Development and implementation of three-dimensional electromagnetic codes to be able to represent more rigorously non-axisymmetric furnace geometries.
- Development of more precise representations of turbulence in electromagnetically driven plasma and metallic systems.
- Analysis of compressibility effects in the arc and development of suitable strategies to perform such calculations under the whole range of conditions typical for EAF operations.

## References

1. *Crude Steel Production*, 1999, International Iron & Steel Institute.
2. Fruehan, R.J., ed. *The Making, Shaping and Treating of Steel*. 11th ed. Steel-making and Refining volume, ed. T.A.S. Foundation. 1998: Pittsburgh.
3. Szekely, J. and G. Trapaga, Some perspectives on new steel-making technologies. *MPT Metallurgical Plant and Technology International*, 1987. No. 4(August).
4. Fritz, E. and J. Steins, New technologies for the production of stainless steel. *MPT Metallurgical Plant and Technology International*, 1998. 4(August): p. 74-80.
5. McIntyre and L.E. R., EAF Steel-making-Process and Practice Update. *Iron & Steelmaker*, 1993(May): p. 61-66.
6. Mathur and D. G., Oxygen injection for effective post-combustion in the EAF. *Iron & Steelmaker*, 1994(May): p. 53-57.
7. Greis, P., DC arc furnaces of the world. *MPT Metallurgical Plant and Technology International*, 1998. 4(August): p. 84-88.
8. Taylor, C.R., ed. *Electric Furnace Steelmaking*. . 1985, Iron and Steel Society.
9. Linninger, A.A., M.A. Hofer, and A.A. Patuzi, DynEAF - a dynamic modeling tool for integrated electric steelmaking. *Iron and Steel Engineer*, 1995(March): p. 43-53.
10. Ushio, J. Szekely, and C.W. Chang, Mathematical modeling of flow field and heat transfer in high-current arc discharge. *Ironmaking and Steelmaking*, 1981. 6: p. 279-286.
11. Szekely, J., J. Mckelliget, and M. Choudhary, Heat-transfer fluid flow and bath circulation in electric-arc furnaces and DC plasma furnaces. *Ironmaking and steelmaking*, 1983. 10(4): p. 169-179.
12. McKelliget, J. and J. Szekeiy, A mathematical model of the cathode region of a high intensity carbon arc. *J. Phys. D: Appl. Phys.*, 1983. 16: p. 1007-1022.
13. Qian, F., B. Farouk, and R. Mutharasan, Modeling of fluid flow and heat transfer in the plasma region of the dc electric arc furnace. *Metallurgical and Materials Transactions B*, 1995. 26B(October): p. 1057-1067.
14. Paik, S. and H.D. Nguyen, Numerical modeling of multiphase plasma/soil flow and heat transfer in an electric arc furnace. *Int. J. Heat Mass Transfer*, 1995. 38(7): p. 1161-1171.
15. Gu, L. and J.A. Bakken. *Mass, Heat and Momentum Transfer at the Plasma-Metal Pool Interphase in a Plasma Arc Reactor*. in ISHMT. 1994. Turkey.
16. Larsen, H.L. and J.A. Bakken. *Modeling of industrial AC arcs*. in TPP-4. 1996. Athens.
17. Wanping, H. and J.D. Lavers, Coupled electro-thermal-flow model for very long electric arcs. *IEEE Transactions on Magnetics Proceedings of the 1996 7th Biennial IEEE conference on electromagnetic field computation*, 1996. 33(2).
18. Saevarsdottir, G., H.L. Larsen, and J.A. Bakken. *Modelling og AC arcs in three-phase submerged arc furnaces*. in INFACON 8. 1998.
19. Larsen, H.L., G. Saevardottir, and J.A. Bakken. *Improved channel arc model for high-current AC arcs*. in TPP-5. 1998. St. Pb.
20. Bowman, B., Measurements of plasma velocity distributions in free-burning DC arcs up to 2160 A. *J. Phys. D: Appl. Phys.*, 1972. 5: p. 1422-1432.
21. Bowman, B. *Properties of arcs in DC furnaces*. in Electric furnace conference proceedings. 1994: ISS.
22. Jordan, G.R., B. Bowman, and D. Wakelam, Electrical and photographic measurements of high-power arcs. *J. Phys. D: Appl. Phys.*, 1969. 3: p. 1089-1099.
23. Kurimoto, H., H.N. Mondal, and T. Morisue, Analysis of velocity and temperature fields of molten metal in DC electric arc furnace. *Journal of Chemical Engineering of Japan*, 1996. 29(1): p. 75-81.
24. Lee, M.D. and W.J. McKenzie, Bottom refractory performance in Consteel and top charged DC furnaces. *Iron and Steelmaker*, 1998(February): p. 47-52.
25. Gu, L. and G.A. Irons. *Physical and mathematical modeling of fluid flow in electric arc furnaces*. in Electric furnace conference proceedings. 1998.
26. Gu, L. and G.A. Irons. *Physical and mathematical modeling of oxygen lancing and arc jetting in electric arc furnaces*. in 57th Electric Furnace Conference. 1999. Pittsburgh, PA: Iron & Steel Society.

27. Deneys, A.C. and D.G.C. Robertson. *Fluid flow phenomena in a laboratory scale DC arc furnace for slag cleaning*. in Electric furnace conference proceedings. 1998. New Orleans.
28. Deneys, A.C. and D.G.C. Robertson. *Flow visualization and temperature measurements close to the arc attachment zone of a laboratory scale DC arc furnace for slag cleaning*. in Fluid Flow Phenomena in Metals Processing. 1999. San Diego, CA: TMS.
29. Kang, T., *Experimental and computational study of electromagnetically driven flow due to the passage of a current between two electrodes*, Ph.D. in *Materials Science and Engineering*. 1987, Massachusetts Institute of Technology: Cambridge. p. 291.
30. Murthy, A., *Physical and numerical simulation of turbulent recirculating flows in materials processing operations*, Ph.D. in *Materials Science and Engineering*. 1984, Massachusetts Institute of Technology: Cambridge. p. 309.
31. Maecker, H., *Z. Phys.*, 1955. **141**: p. 198-216.
32. Lowke, J.J. and H.C. Ludwing, A simple model for high-current arcs stabilized by forced convection. *Journal of applied physics*, 1975. **46**(8): p. 52-60.
33. Squire, H.B., The round laminar jet. *Quart. Journal Mech. and Applied Math.*, 1951. **IV**(3): p. 321-329.
34. Ramakrishnan, S. and A.D. Stokes, An approximate model for high-current free-burning arcs. *J. Phys. D: Appl. Phys.*, 1978. **11**: p. 2267-2280.
35. Ramakrishnan, S. and B. Nuon, Prediction of properties of free burning welding arc columns. *J. Phys. D: Appl. Phys.*, 1980. **13**: p. 1845-1853.
36. Allum, C.J., Gas flow in the column of a TIG welding arc. *J. Phys. D: Appl. Phys.*, 1981. **14**: p. 1041-1059.
37. Hsu, K.C., K. Etemadi, and E. Pfender, Study of the free-burning high-intensity argon arc. *J. Appl. Phys.*, 1982. **54**(3): p. 1293-1302.
38. McKelliget, J. and J. Szekely, Heat transfer and fluid flow in the welding arc. *Metallurgical Transactions A*, 1986. **17A**(July): p. 1139-1148.
39. Choo, R.T.C., *Mathematical modeling of heat and fluid flow phenomena in a mutually coupled welding arc and weld pool*, Ph.D. in *Materials Science and Engineering*. 1990, Massachusetts Institute of Technology: Cambridge. p. 260.
40. Kim, W.H., H.G. Fan, and S.J. Na, A mathematical model of gas tungsten arc welding considering the cathode and the free surface of the weld pool. *Metallurgical and Materials Transactions B*, 1997. **28B**(August).
41. Nestor, O.H., Heat intensity and current density distributions at the anode of high current, inert gas arcs. *Journal of applied physics*, 1961. **33**(5): p. 1638-1648.
42. Lee, Y.S. and S.J. Na, A numerical analysis of a stationary gas tungsten welding arc considering various electrode angles. *Supplement of the welding journal*, 1996(September): p. 269-279.
43. Goodarzi, M., R. Choo, and J.M. Toguri, The effect of the cathode tip angle on the GTAW arc and weld pool: I. Mathematical Model of the Arc. *Journal of Physics D-Applied Physics*, 1997. **30**(5): p. 2744-2756.
44. Lowke, J.J., R. Morrow, and J. Haidar, A simplified unified theory of arcs and their electrodes. *J. Phys. D: Appl. Phys.*, 1997. **30**: p. 2033-2042.
45. Ushio, M., M. Tanaka, and C.S. Wu, Analytical approach to anode boundary layer of gas tungsten arcs. *Trans. JWRI*, 1996. **25**(2): p. 9-21.
46. Haidar, J. and J.J. Lowke, Effect of CO<sub>2</sub> shielding gas on metal droplet formation in arc welding. *IEEE Transactions on Plasma Science*, 1997. **25**(5): p. 931-936.
47. Mazumdar, D. and R.I.L. Guthrie, The physical and mathematical modeling of gas stirred ladle systems. *ISIJ international*, 1995. **35**(1): p. 1-20.
48. Sheng, Y.Y. and G.A. Irons, Measurement and modeling of turbulence in the gas/liquid two-phase zone during gas injection. *Metallurgical Transactions B*, 1993. **24B**(August): p. 695-705.
49. Grevet, J.H., J. Szekely, and N. EL-Kaddah, An experimental and theoretical study of gas bubble driven circulation systems. *Int. J. Heat Mass Transfer*, 1982. **25**(4): p. 487-497.
50. Castillejos, A.H. and J.K. Brimacombe, Physical characteristics of gas jets injected vertically upward into liquid metal. *Metallurgical Transactions B*, 1989. **20B**(October): p. 595-601.
51. Iguchi, M., H. Takeuchi, and Z. Morita, The flow field in air-water vertical bubbling jets in cylindrical vessel. *ISIJ International*, 1991. **31**(3): p. 246-253.

52. Castillejos, A.H. and J.K. Brimacombe, Measurement of physical characteristics of bubbles in gas-liquid plumes: part II. Local properties of turbulent air-water plumes in vertically injected jets. *Metallurgical Transactions B*, 1987. **18B**(December): p. 659-671.
53. Iguchi, M., *et al.*, Velocity and turbulence measurements in a cylindrical bath subject to centric bottom gas injection. *Metallurgical and Materials Transactions B*, 1995. **26B**(April): p. 241-247.
54. Johansen, S.T., *et al.*, Fluid dynamics in bubble stirred ladles: Part I. Experiments. *Metallurgical Transactions B*, 1988. **19B**(October): p. 745-754.
55. Iguchi, M., K. Nakamura, and R. Tsujino, Mixing time and fluid flow phenomena in liquids of varying kinematic viscosities agitated by bottom gas injection. *Metallurgical and Materials Transaction B*, 1998. **29B**(June): p. 569-575.
56. Mazumdar, D. and R.I.L. Guthrie, Mixing models for gas stirred metallurgical reactors. *Metallurgical Transactions B*, 1986. **17B**(December): p. 725-733.
57. Mietz, J. and F. Oeters, Model experiments on mixing phenomena in gas-stirred melts. *Steel Research*, 1988. **59**(52): p. 52-59.
58. Bessho, N., S. Taniguchi, and A. Kikuchi, Mass transfer between gas and liquid in a gas-stirred vessel. *ISIJ*, 1985: p. 55-61.
59. Hirasawa, M., *et al.*, Rate of mass transfer between molten slag and metal under gas injection stirring. *Transactions ISIJ*, 1987. **27**: p. 277-282.
60. Jonsson, L. and P. Jonsson, Modeling of the fluid conditions around the slag metal interface in a gas-stirred ladle. *ISIJ International*, 1996. **36**(9): p. 1127-1134.
61. Kim, S., R.J. Fruehan, and R.I.L. Guthrie, Physical model studies of slag/metal reactions in gas stirred ladles - Determination of critical gas flow rate. *I&SM*, 1993(November): p. 71-76.
62. Mazumdar, D., A correlation for estimation of mass transfer rates of solids in gas stirred ladle systems. *Steel Research*, 1996. **67**(7): p. 263-267.
63. Mietz, J., S. Schneider, and F. Oeters, Model experiments on mass transfer in ladle metallurgy. *Steel Research*, 1991. **62**(1): p. 1-9.
64. Taniguchi, S., *et al.* Characteristics of mass transfer at the free surface of liquid in a gas-stirred system. in Proceedings of the Sixth International Iron and Steel Congress. 1990. Nagoya.
65. Xie, Y.K., S. Orsten, and F. Oeters, Behavior of bubbles at gas blowing into liquid Wood's metal. *ISIJ International*, 1992. **32**(1): p. 66-75.
66. Iguchi, M., *et al.*, Measurement of bubble characteristics in a molten iron bath at 1600C using an electroresistivity probe. *Metallurgical and Materials Transactions B*, 1995. **26B**(February): p. 67-74.
67. Iguchi, M., *et al.*, Heat transfer between bubbles and liquid during cold gas injection. *ISIJ International*, 1992. **32**(7): p. 865-872.
68. Tokunaga, H., M. Iguchi, and H. Tatemichi, Heat transfer between bubbles and molten Wood's metal. *ISIJ International*, 1995. **35**(1): p. 21-25.
69. Mietz, J. and F. Oeters, Flow field and mixing with eccentric gas stirring. *Steel research*, 1988. **60**(9): p. 387-394.
70. Xie, Y. and F. Oeters, Experimental studies on the flow velocity of molten metals in a ladle model at centric gas blowing. *Steel Research*, 1992. **63**(3): p. 93-104.
71. Xie, Y. and F. Oeters, Measurements of bubble plume behavior and flow velocity in gas stirred liquid Wood's metal with an eccentric nozzle position. *Steel Research*, 1994. **65**(8): p. 315-319.
72. Guthrie, S.J.a.R.I.L., Modeling flows and mixing in steel-making ladles designed for single and dual plug bubbling operations. *Metallurgical Transactions B*, 1992. **23B**: p. 765-778.
73. Ilgbusi, O.J. and J. Szekely, The modeling of gas-bubble driven circulations systems. *ISIJ International*, 1990. **30**(9): p. 731-739.
74. Schwarz, M.P. and W.J. Turner, Applicability of the standard k- $\epsilon$  turbulence model to gas-stirred baths. *Appl. Math. Modelling*, 1988. **12**(June): p. 273-279.
75. Johansen, S.T. and F. Boysan, Fluid dynamics in bubble stirred ladles: Part II. Mathematical modeling. *Metallurgical Transactions B*, 1988. **19B**(October): p. 755-764.
76. Sheng, Y.Y. and G.A. Irons, The impact of bubble dynamics on the flow in plumes of ladle water models. *Metallurgical Transactions B*, 1995. **26B**(June): p. 625-635.
77. Neifer, M., *et al.* Numerical simulation and operating trials of melt flow and mixing behavior of alloying agents. in SCANINJECT VII. 1995. Lulea, Sweden: 283-309.

78. Turkoglu, H. and B. Farouk, Numerical computations of fluid flow and heat transfer in a gas-stirred liquid bath. *Metallurgical Transactions B*, 1990. **21B**(August): p. 771-781.
79. Szekely, J., T. Lehner, and C.W. Chang, Flow phenomena, mixing, and mass transfer in argon stirred ladles. *Ironmaking and Steelmaking*, 1979(6): p. 285-293.
80. Koh, P.T.L., N.C. Markatos, and M. Cross, Numerical simulation of gas stirred liquid baths with a free surface. *PCH PhysicoChemical Hydrodynamics*, 1987. **9**(1/2): p. 197-207.
81. Turkoglu, H. and B. Farouk, Mixing time and liquid circulation rate in steel-making ladles with vertical gas injection. *ISIJ International*, 1991. **31**(12): p. 1371-1380.
82. Jonsson, L., *Three-phase (steel-gas-slag) modeling of the CAS-OB process*. in 80th Steelmaking Conference. 1997. Chicago: ISS.
83. Richter, h.J., J.T. Laaspere, and J.M. Fitzpatrick. *Experimental and numerical modeling of mixing and settling in continuous metal production*. in Metallurgical Processes for Early twenty-first Century. 1994: The Minerals, Metals & Materials Society.
84. Mietz, J. and F. Oeters, Model studies of mixing phenomena in stirred melts. *Canadian metallurgical quarterly*, 1989. **28**(1): p. 19-27.
85. Boulos, M.I., P. Fauchais, and E. Pfender, *Thermal plasmas - Fundamentals and applications*. Vol. 1. 1994, New York: Plenum press. 452.
86. Strachan, D.C. and M.R. Barrault, Axial velocity variations in high-current free-burning arcs. *Journal of Physics D: Appl. Phys.*, 1976. **9**: p. 435-446.
87. Schoeck, P.A., ed. *An investigation of the anode energy balance of high intensity arcs in argon*. Modern developments in heat transfer, ed. W. Ibele. 1963, Academic Press: New York and London. 352-400.
88. Murphy, A.B., Transport coefficients of air, argon-air and oxygen-air plasmas. *Plasma chemistry and plasma processing*, 1995. **15**(2): p. 279-307.
89. Malin, M.R. and D.B. Spalding, *Turbulence Models in PHOENICS*. 1995, CHAM: London. p. 1-18.
90. Quigley, M.B.C., P.H. Richards, and D.T. Swift-Hook, *J. Phys. D. Appl Phys.*, 1973. **6**: p. 2250-2258.
91. Eckert, E.R.G. and E. Pfender, *Advanced Heat Transfer*, 1967. **4**: p. 229-316.
92. Yos, J.M., *Thermodynamic data for air*, . 1963, Avco RAD-Tm-63-7.
93. Morris, J.C., *J. Am. Inst. Aeronaut. Astronaut.*, 1966. **4**: p. 1223-1226.
94. Choo, R.T.C., J. Szekely, and R.C. Westhoff, On the calculation of the free surface temperature of gas-tungsten-arc weld pools from first principles: part I. Modeling the welding arc. *Metallurgical Transactions B*, 1992. **23B**(June): p. 357-369.
95. Evans, D.C. and R.S. Tankin, *Phys. Fluids*, 1967. **10**: p. 1137-1144.
96. Patankar, S.V., *Numerical Heat Transfer and Fluid Flow*. first ed. Series in Computational Methods in Mechanics and Thermal Sciences, ed. W.J. Minkowycz and E.M. Sparrow. 1980, Ney York: McGraw-Hill. 197.
97. McKelliget, J. and J. Szekely. *The modeling of fluid flow and heat transfer in arc furnaces*. in 5th Arc furnace meeting. 1985. Budapest, Hungary.
98. Szekely, J. and N.J. Themelis, *Rate Phenomena in Process Metallurgy*. first ed. 1971, New York: John Wiley & Sons, Inc. 784.
99. Courses, C., *PHOENICS Instruction Course CHAM/TR/300*, . 1990, CHAM Limited: Atlanta, Georgia. p. 9.2 (1-8).
100. Spalding, D.B., *IPSA 1981: New Developments and Computed Results (Report HTS/81/2)*, . 1981, Imperial College CFDU: London.
101. Lopez, M., Phase distribution in bubbly two-phase flow in vertical ducts. *Int. J. Multiphase Flow*, 1994. **20**(5): p. 805-810.
102. Kuo, J.T. and G.B. Wallis, Flow of bubbles through nozzles. *Int. J. Multiphase Flow*, 1988. **14**(5): p. 547.
103. Ramirez, M.A. and G. Trapaga. *Mathematical modeling of mixing of solute in centric and eccentric gas-stirred ladles*. in Brimacombe Memorial Symposium. 2000. British Columbia.
104. Spalding, D.B., Numerical simulation of flows with moving interfaces. *PCH PhysicoChemical Hydrodynamics*, 1988. **10**(5/6): p. 625-637.

105. Li, L., *Mathematical modeling of fluid flow and mixing in metallurgical reactors with bottom gas injection*, Ph.D. in *Materials Science and Engineering*. 1996, Massachusetts Institute of Technology: Cambridge. p. 178.
106. Anderson, S.H., *et al.* *Worldwide experience of electric arc furnace bottom stirring*. in *Electric Furnace Conference*. 1990.
107. Sheng, Y.Y. and G.A. Irons, Measurements of the internal structure of gas-liquid plumes. *Metallurgical Transactions B*, 1992. **23B**(December): p. 779=788.
108. Jayatilike, C.L.V., ed. *The influence of the Prandtl number and surface roughness on the resistance of the sublayer to momentum and heat transfer*. Prog. in Heat & Mass Transfer, ed. P. Press. Vol. 1. 1969.
109. ibele, W., ed. *Modern developments in heat transfer*. . 1963, Academic Press: New York and London.
110. Szekely, J., J.W. Evans, and J.K. Brimacombe, *The Mathematical and physical Modeling of Primary Metals Processing*.



## Appendix A: DC Arc Furnaces of the World

The first modern DC arc furnace was developed in the 1980's. Since then, this technology has gained acceptance in the steel-making industry and up to 1998 more than 130 DC arc furnaces had been built or are under construction worldwide. In Table A.1 a list of the DC arc furnaces in the world is presented. In the table, the geographic location, supplier and year of commissioning are provided as well as technical information of the furnace such as its hearth diameter, tapping weight and transformer rating.

Company	Location	Supplier (Licensor)	Hearth diameter m	Tapping weight t	Transformer rating <sup>1)</sup> MVA	Year of commissioning <sup>2)</sup> Remarks
<b>Australia</b> Graham	Yagoona	Kvaerner Metals <sup>3)</sup>	2.7	10	7.5	1995 - Revamp
<b>Belgium</b> Cockerill Sambre	Charleroi	Wurth/Fuchs/Clocim	6.8	165	110	1996 - Finger shaft furnace
<b>Uaines G. Bol</b>	La Louvière	Mannesmann <sup>4)</sup>	6.6	85	95	1991
<b>Brazil</b> Sipasa	São Paulo	Concast <sup>5)</sup>	5.2	60	54	1997
<b>Canada</b> Inco	Mississauga	Concast	2.5	5	2	1987 - FeNi dust
<b>China</b> Baosteel Baij Steel Berman Special Steel Changcheng Special Steel Daye Steel Guangzhou Iron & Steel Corp Hangzhou Iron & Steel Works Jiang yin Xing Cheng Special steel works Lanzhou Steel Shanghai No. 5 Steelworks Shanghai Pudong Iron & Steel Shanghai Pudong Iron & Steel Suzhou Steel Yanshan	Baoshan n.a. Qiqihar Jiangyou Huangshi Guangzhou Hangzhou Jiangyin Lanzhou Shanghai Shanghai Shanghai Suzhou Jiangyin	Kvaerner Metals Mannesmann Mannesmann Kvaerner Metals Concast Concast Kvaerner Metals Mannesmann Concast SMS <sup>6)</sup> Concast Concast Mannesmann Kvaerner Metals	7.3 5.8 6.6 6.7 5.2 5.2 6.1 6.6 5.6 6.5 6.1 6.1 6.6 5.5	150 70 90 100 70 70 90 100 70 45 100 100 100 100 60	100 60 85 90 56 50 90 90 45 40 74 74 100 50	1996 - Twin vessel 1998 1997 1997 1998 1998 1997 1998 1996 1995 1995 1994 1995
<b>Egypt</b> Misco - Misr Steel	Port-Said	Concast	5.2	60	36	1998
<b>France</b> Laminés Marchands Européens Unimétal	Tnith St Leger Gandrange	Kvaerner Metals Kvaerner Metals	5.8 7.3	80 150	84 150	1985 1994 - Twin vessel
<b>Germany</b> Arbed/Stw Thüringen Degussa Georgsmannhütte Salzgitter Stahl RWTH Aachen SMS Schloemann-Siemag AG	Unterwellenborn Hanau Georgsmannhütte Peine Aachen Kreuztal	VAI/DVAI Concast SMS SMS SMS SMS	6.5 1.5 7.3 7.3 1.2 3.0	120 5 125 100 0.2 12	120 2.0 80 90 0.375 6	1995 1989 - Pt 1994 1995 1981 - Pilot furnace 1982 - shut down
<b>Greece</b> Helyvourgia Thessalas	Velesino	Mannesmann	7.4	80	65	1998 - Coniarc
<b>India</b> Essar Essar Essar	Hazira Hazira Hazira	Kvaerner Metals Kvaerner Metals Kvaerner Metals	7.3 7.3 7.3	150 150 150	160 160 160	1994 1994 1994
<b>Indonesia</b> PT Krakatau Steel/Posco	Cilegon	NKK (SMS)	7.3	150	130	1999
<b>Italy</b> ABS - Acciaiere Bertoli Safau ASO Siderurgica ASO Siderurgica Rubera	Urdine Ospitaletto Ospitaletto Modena	Danieli <sup>7)</sup> Concast Concast Tagliaferri	5.8 2.4 4.3 n.a.	90 35 40 60	90 6 25 44	1997 - Danarc Plus M <sup>8)</sup> 1990 - Ladle furnace 1997 1994
<b>Japan</b> Daido Steel Dawwa Steel Dawwa Steel Oji Steel Itoh Iron & Steel Kansas Billet Center Kobe Steel Kotobuki Steel Kyoeri Steel Kyoeri Steel Mitsubishi Metal Industries Mitsubishi Steel Nakayama Steel Nakayama Steel Shimizu Steel	Hoshizaki Mizushima Mizushima Gunma Ishinomaki Sakai Takasago Kure Nagoya Wakayama Nigata Muroran Osaka Funamachi Tomakomai	Daido/NSC <sup>9)</sup> /U+S <sup>10)</sup> Kvaerner Metals Kvaerner Metals Daido/NSC/U+S NSC/Daido/U+S Sakai NKK (SMS) IHI (Concast) NKK (SMS) NKK (SMS) NKK (SMS) IHI (Concast) NKK (SMS) NSC/Daido/U+S NKK (SMS)	4.0 7.0 6.7 6.1 6.0 7.0 4.6 5.3 7.0 5.4 (6.1) 6.1 6.1 6.7 6.4 5.3	25 120 100 80 75 120 30 71 110 60 60 100 70 75 40 (60)	15 100 100 80 60 102 20 31 60 50 50 92 50 88.6 50	1989 1994 1990 1999 - Scrap preheater 1997 - Twin vessel 1992 - Twin vessel 1991 1996 1992 - Consteel 1990 1994 1994 1992 1991 1996

Table A.1 DC arc furnaces of the world (July 1998) [7]

Company	Location	Supplier (License)	Hearth diameter (m)	Capacity (metric t)	Temperature (metric t)	Year of commissioning
Sumitomo Metal Industries	Kansai	Daido/NSC/U+S	4.9	40	35	1996 - Twin vessel
Takunan Steel	Naha	Daido/NSC/U+S	5.8	70	52	1995 - Twin vessel
Toa Steel	Kashima	NKK (SMS)	7.2	150	80	1995 - Twin vessel
<b>Japan</b>						
Tokyo Steel	Utsunomiya	IHI (Concast)	8.1 x 10.7	140	100	1996 - 2 electrodes
Tokyo Steel	Kyushu	NKK (SMS)	7.0	130	65	1989
Tokyo Steel	Okayama	NKK (SMS)	8.3	220 (150)	90	1992
Tokyo Steel	Takamatsu	IHI (Concast)	5.2	66	55	1996
Topy Kogyo	Toyohashi	NKK (SMS)	4.6	35	15	1988
Yamato Kogyo	Himeji	Daido/NSK/U+S	7.0	130	90	1996 - Multi stage preheater
<b>Luxembourg</b>						
Profilarbed	Differdange	Mannesmann	7.6	155	140	1994 - Twin vessel
Profilarbed	Esch-Belval	Mannesmann	7.6	155	140	1995 - Twin vessel
<b>Malaysia</b>						
Arnsteell Mills	Kualalngat	Daido/NSC/U+S	7.0	160	140	1998 - Multi stage preheater
Malayawata Steel	Prai	Concast	5.5	80	85	1994
Megasteel	Kuala Lumpur	SMS/Fuchs	7.3	160	95	1998 - Finger shaft furnace
Megasteel	Kuala Lumpur	SMS/Fuchs	7.3	160	95	1998 - Finger shaft furnace
Perwaja Steel	Kemaman	NKK (SMS)	5.8	75	50	1996
Perwaja Steel	Kemaman	NKK (SMS)	5.8	75	50	1996
Southern Steel	Penang	Concast	5.5	80	67	1991
Southern Steel	Penang	Concast	6.1	90	85	1997 - Twin vessel
<b>Mexico</b>						
Hylsa	Monterrey	Nippon Steel Corp.	7.0	135	156	1994
Hylsa	Monterrey	NSC/Daido/U+S	7.0	135	156	1994
Hylsa	Monterrey	Fuchs/NSC	6.8	135	150	1995 - Finger shaft furnace
Hylsa	Monterrey	Danieli	7.3	150	208	1998 - 2 electrodes
Hylsa	Puebla	Daniel/Fuchs	7.3	135	180	1998 - Finger shaft furnace + 2 electrodes
<b>Philippines</b>						
Milwaukee Industries	Manila/Pampanga	VAI	4.7	40/50	30	1994
<b>Singapore</b>						
NatSteel	Singapore	Concast	5.2	55	53	1993
NatSteel	Singapore	Concast/Fuchs	5.2	55	53	1992
NatSteel	Singapore	Concast/Fuchs	5.2	55	53	1993
NatSteel	Singapore	Fuchs/VAI	5.9	80	83	1997 - Finger shaft furnace
<b>South Africa</b>						
Anglo American Corp.	Krugersdorf	Concast	9.0	110	40	1989 - FeCr
Anglo American Corp.	Saldanha	Concast	10.2	500	40	1994 - Fe + TiO <sub>2</sub>
Anglo American Corp.	Saldanha	Concast	11.6	800	50	1998 - Fe + TiO <sub>2</sub>
<b>South Korea</b>						
Dongkuk Steel Mill Co. Ltd.	Inchon	NKK (SMS)	6.7	100	65 (100)	1992
Dongkuk Steel Mill Co. Ltd.	Pohang	NSC	7.0	140	105	1997 - Twin vessel
Dongkuk Steel Mill Co. Ltd.	Pohang	NSC/Daido/U+S	7.0	140	105	1997 - Twin vessel
Hanbo Steel	Asan	NKK (SMS)	7.6	155	80 (120)	1994
Hanbo Steel	Asan	NKK (SMS)	7.6	155	80 (120)	1994
Hanbo Steel	Asan	NKK (SMS)	7.6	155	80 (120)	1995
Hanbo Steel	Asan	NKK (SMS)	7.6	200	90 (120)	1997
Hanbo Steel	Asan	NKK (SMS)	7.6	200	90 (120)	1997
Hwan Young Steel	Chung Nam	Concast	5.8	100	107	1993
Inchon Iron & Steel	Inchon	NKK (SMS)	7.0	120	65 (95)	1998 - Twin vessel
Korea Iron & Steel	Chang Won	NKK (SMS)	7.0	120	65 (100)	1992
Posco	Kwangyang	NSC/Daido/U+S	7.0	130	102	1996 - Twin vessel
Posco	Kwangyang	NSC/Daido/U+S	7.0	130	102	1996 - Twin vessel
Posco	Kwangyang	NSC/Daido/U+S	7.0	130	102	1999 - Twin vessel
Posco	Kwangyang	NSC/Daido/U+S	7.0	130	102	1999 - Twin vessel
<b>Spain</b>						
A.C.B.	Bilbao	Kvaerner Metals	6.7	130	130	1996
A.C.B.	Bilbao	Kvaerner Metals	6.7	130	130	1996
Siderurgica Balboa	Jérez de los Caballeros	Danieli	5.6	80	35/45 (2 x)	1992
Siderurgica Balboa	Jérez de los Caballeros	Danieli	5.6	100	70	1998 - Danarc Plus M <sup>2</sup>

Table A.1 (cont.) DC arc furnaces of the world (July 1998) [7]

Company	Location	Supplier (Licensor)	Hearth diameter m	Tapping weight <sup>1)</sup> t	Transformer rating <sup>2)</sup> MVA	Year of commissioning <sup>3)</sup> Remarks
<b>Sweden</b>						
Mefos	Luleå	Concast	2.0	5	2.5	1990 – Pilot plant
<b>Taiwan</b>						
Feng Hsin Iron & Steel	Taichung	Daido/NSC/U+S	6.1	80	82	1995
Kuei Hung Steel	Tainan	Concast	6.7	160	100	1993
Kuei Yi Industrial Co	Lung Ching	NKK (SMS)	7.3	150	85 (120)	1998
Tung Ho Steel	Miao Lu	Kvaerner Metals	6.7	100	100	1993
Wei Chin Steel	Tainan	NKK (SMS)	6.1	90	50 (82)	1994
<b>Thailand</b>						
Namheng Steel	Lopburi	Concast <sup>4)</sup>	5.2	60	50	1996
<b>Turkey</b>						
Diler Demir Çelik	Iskenderun	Concast <sup>4)</sup>	5.5	80	67	1993
Kroman Çelik	Gebze	Concast <sup>4)</sup>	5.5	80	75	1992
<b>USA</b>						
Bethlehem Steel	Steelton, PA	NKK (SMS)	7.0	150	80 (126)	1994
Charter Steel	Saukville	Concast <sup>4)</sup>	5.2	70	42	1991
Florida Steel	Tampa	DVAI	5.2	54	40	1991
Gallatin Steel	Warsaw, KY	NKK (SMS)	7.8	180	90 (150)	1995 – Twin vessel
Ipsco Steel Inc	Muscatine, IO	Mannesmann	7.5	135	140	1995
North Star Steel	St Paul, MN	VAI	6.0	85	80/88	1994
North Star Steel	Kingman, AZ	Fuchs	6.0 SSF <sup>4)</sup>	95	80	1996
North Star Steel	Kingman, AZ	Concast <sup>4)</sup>	6.1	82	80	1996 – Partial
Nucor Steel	Darlington, SC	SMS	3.8	32	11.5	1985 – Modification
Nucor Steel	Darlington, SC	SMS	6.5	100	45	1993 – Consteel
Nucor Steel	Norfolk, NB	SMS	6.5	91	65	1997 – Twin vessel
Nucor Steel	Hickman, AR	SMS	7.3	150	80–100	1992/97
Nucor Steel	Hickman, AR	SMS	7.3	150	80–100	1992/97
Nucor Steel	Armored, AR	SMS	7.3	150	80	1992
Nucor Steel	Berkeley County, SC	SMS	7.8	150	110	1996 – Twin vessel
SMI Steel Inc	Birmingham, AL	NKK (SMS)	5.8	70	60 (66)	1994
Trco Steel	Decatur, AL	NKK (SMS)	7.6	155	90 (150)	1997 – 2 cathodes
Trco Steel	Decatur, AL	NKK (SMS)	7.6	155	90 (150)	1997 – 2 cathodes
Tuscaloosa Steel	Tuscaloosa, AL	SMS	7.1	136	75	1996 – Twin vessel
Sources: Reference lists and announcements of Concast, Daido Steel, Danieli, Fuchs Systemtechnik, Kvaerner Metals, Mannesmann Demag AG, Nippon Steel Corporation, NKK Corporation, SMS, Tagliaferm, Voest-Alpine Industrieanlagenbau, Paul Wurth						
1) Maximum or tapping weight			7) Formerly MAN GHH, now SMS			
2) Maximum or nominal transformer rating			8) Danieli CentroMet			
3) Year of construction or year of commissioning			9) Tagliaferm, now part of the Techint Group			
4) Formerly ABB; now Concast			10) NSC – Nippon Steel Corp			
5) Formerly Clecim, now Kvaerner Metals			11) U+S – Usinor Sacilor			
6) Formerly Mannesmann-Demag Hüttentechnik MDH, now Mannesmann Metallurgy						

Table A.1 (cont.) DC arc furnaces of the world (July 1998) [7]

## **Biographical Note**

Marco Aurelio Ramírez was born on October 27, 1970, in Mexico city, Mexico, to María Nelly Argáez and Aurelio Ramírez Carballido. He attended elementary school in the “República de Iraq” school. He subsequently attended Preparatory School No. 2 in Mexico City.

In 1988 he was admitted to the School of Chemistry in the National University of Mexico (UNAM), to pursue an undergraduate education in Chemical Metallurgical Engineering. He obtained his B.S. in September 1993 with the thesis titled: “Application of the micro-macro modeling of the solidification to the analysis of the variables affecting the tendency to obtain white iron using gravitational casting in sand molds”. After obtaining the best academic record of his class (Chemical Metallurgical Engineering), he was awarded the “Gabino Barreda” Medal by the National University of Mexico in 1994 and also received the prize “The Best Student of Mexico” granted by the president of Mexico.

Thereafter, he was admitted to CINVESTAV in Saltillo, Mexico, to study the masters program in Metallurgical Engineering. He obtained his M.S. in July 1996 with his thesis titled: “Mathematical modeling of the solidification of multi-component Co-Cr-Mo alloys”.

In 1996, he was admitted to MIT where he was enrolled in the doctoral program in the Department of Material Science and Engineering in the area of Metallurgy.

# THESIS PROCESSING SLIP

FIXED FIELD: ill. \_\_\_\_\_ name \_\_\_\_\_

index \_\_\_\_\_ biblio \_\_\_\_\_

► COPIES: Archives Aero Dewey Barker Hum  
Lindgren Music Rotch Science Sche-Plough

TITLE VARIES: ►  \_\_\_\_\_

NAME VARIES: ►  Ramirez-Argáez,  
Marco Aurelio

IMPRINT: (COPYRIGHT) \_\_\_\_\_

► COLLATION: \_\_\_\_\_

► ADD: DEGREE: \_\_\_\_\_ ► DEPT.: \_\_\_\_\_

► ADD: DEGREE: \_\_\_\_\_ ► DEPT.: \_\_\_\_\_

SUPERVISORS: \_\_\_\_\_

NOTES:

cat'r: \_\_\_\_\_ date: \_\_\_\_\_  
page: 512  
► DEPT: Música  
► YEAR: 1977 ► DEGREE: M.A.  
► NAME: RAMÍREZ, Marco Aurelio